D 2014

U.PORTO
INSTITUTO DE CIÊNCIAS BIOMÉDICAS ABEL SALAZAR
UNIVERSIDADE DO PORTO

CYCLIC NUCLEOTIDE REGULATION IN A POTASSIUM CHANNEL

LIGAND SELECTIVITY AND CONFORMATIONAL CHANGE

JOÃO PEDRO ABREU PESSOA

TESE DE DOUTORAMENTO APRESENTADA

AO INSTITUTO DE CIÊNCIAS BIOMÉDICAS ABEL SALAZAR

DA UNIVERSIDADE DO PORTO EM

CIÊNCIAS BIOMÉDICAS

João Pedro Abreu Pessoa

Cyclic nucleotide regulation in a potassium channel: ligand selectivity and conformational change

Tese de Candidatura ao grau de Doutor em Ciências Biomédicas submetida ao Instituto de Ciências Biomédicas Abel Salazar da Universidade do Porto

Orientador – Doutor João Morais Cabral

Categoria – Investigador Principal

Afiliação – Instituto de Biologia Molecular e Celular da Universidade do Porto

Co-orientador Doutor Luís Gales

Categoria – Professor Associado

Afiliação – Instituto de Ciências Biomédicas Abel Salazar da Universidade do Porto

Illustration on the next page: arrangement obtained from eight repetitions of the binding curve represented in Fig. 2.4 B.

The present work was financially supported by Fundação Para a Ciência e a Tecnologia and co-financed by the European Social Fund, through the PhD Fellowship SFRH/BD/60274/2009 and the Research Fellowship PTDC/BBB-BEP/2017/2012.

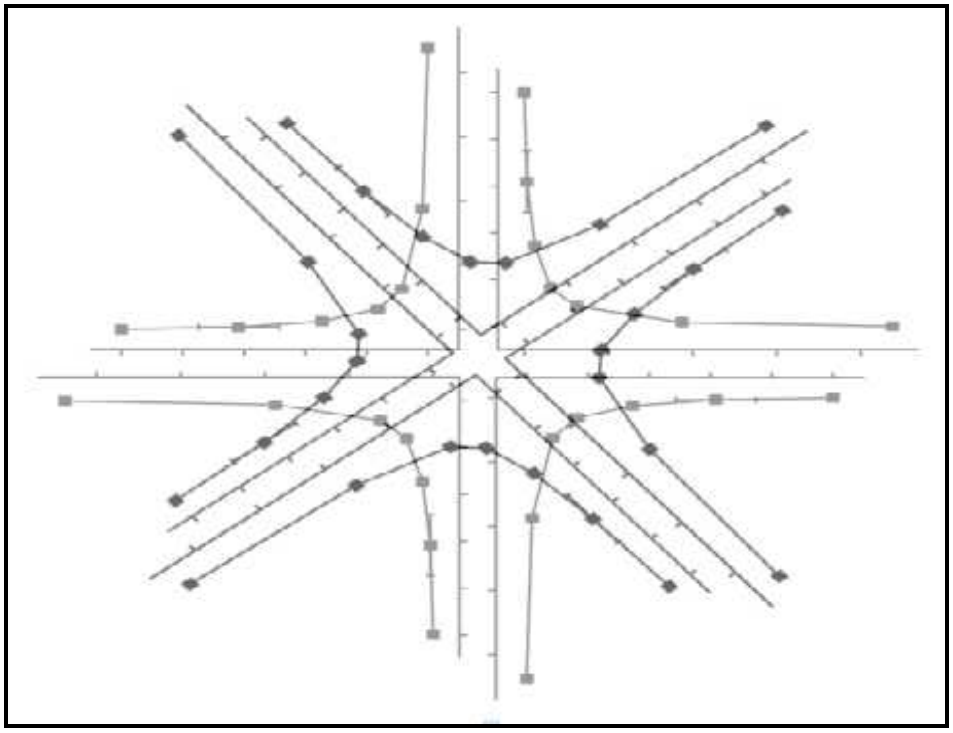

Dedicated to my family

i. Acknowledgements

First, I am going to mention the most important people who helped me in the “making of” of this thesis. Sorry to those not mentioned, you are not forgotten. Some of the contributions acknowledged might seem little, but they were not. The importance of things is not only on what they are, but also, on what they mean. (Forgive me the philosophical start, respectable reader. It will not happen again.)

To start, I wish to thank my supervisor, Dr. João Morais Cabral, for training me at all levels and for providing one additional year of financial support. I do appreciate his permanent concern about the work conditions of his team. I wish to thank also my co-supervisor, Dr. Luís Gales, for taking charge of such task.

I am truly grateful to Dr. Carol Harley, for her permanent concern and dedication, which keep the lab up and running (as well as tidy and organized). She has saved me a lot of time, especially while ordering things.

Fátima, thank you for sharing your crystallographic talent and for being one of the most important players in this story. Dear reader, please go to section 2, for the thrilling details!

Thank you Ricardo, for all your help, not only in the lab, but also on the computer. Thank you also for our many interesting discussions and for always having a suggestion or a piece of advice to share with me.

Thanks to Maria for being the owner of excellent teaching skills (and sense of humour!). Learning ITC from you was quite inspiring! I am sure that your thesis will be a very good one and I wish you great success in the final exam.

Thanks/köszönöm to András, for scientific (and non-scientific) discussions, excellent technical guidance, lessons about Hungarian language, touristic information about Budapest and delightfully delicious Hungarian cookies.

Rita is the ultimate “mood booster”. No mater how bad things may go, she always has a bit of joy to spare. Having her nearby simply makes the work (even) more pleasant.

Mood boosting qualities are also found in Artur, not only while expanding my knowledge about music and the English society, but also during any discussion about anything else.

Thank you Andreia, for being another great lab partner, for your nice presence, great company, both in the lab and during lunchtime, and interesting discussions.

Thanks also to Celso, João S. and Santiago. The former group members Ricardo Adaixo, Beatriz Teixeira, Ana Margarida Pereira, Ricardo Carvalho and Sofia Alves are not forgotten. It was enjoyable to meet each one of you and I wish you every success.

Much of the content here presented is due to our external collaborators. I am truly indebted to Dr. Shashi Bhushan, whose patience made true my wish of an EM collaboration and also to Mr. Cristian Kraft, for doing sample imaging. Without you both, part of this thesis would be incomplete and my curiosity about this technique would remain unsatisfied. Thank you so much!

I am also grateful to our AFM collaborators (section 3). Dr. Stefania Mari and Dr. Daniel Müller showed remarkable productivity and efficiency, which resulted in getting a paper accepted only one year after the beginning of the experiments (seriously!).

Other colleagues who I am most pleased to acknowledge are coming on! Thank you Inês, for the privilege of being part of your wonderful dissertation party! Thank you to the many colleagues who shared their experiences as PhD students and advised me on such matter!

Thanks to the IBMC technical staff, for their services, which facilitate the work of scientists. Thanks to all colleagues, group leaders and staff members who got involved in the events I organized for my guest speakers. Thanks to FCT, for the financial support that made this thesis possible.

Foremost, I wish to thank all my family, whose support and encouragement were the “secret” behind the pages that follow. I gratefully thank my parents, who put more effort on me than many would do and to whom I owe much in my achievements. I kindly thank my sister Ana, physician and scientist, whose inspiring example and success simply make me proud.

Well, now, the style is going to change. I hope you will enjoy reading the story at least as much as I enjoyed writing it. Sorry about the cliché.

“We urge the reader to bear in mind the imperfection of our current knowledge. Science is never finished. It proceeds by successive approximations, edging closer and closer to a complete and accurate understanding of Nature, but it is never fully there.”

Carl Sagan and Ann Druyan, *Shadows of Forgotten Ancestors*, 1993

ii. Abstract

Cyclic nucleotide regulated ion channels are membrane pores that permeate ions in the presence of the cyclic nucleotides adenosine 3', 5'-cyclic monophosphate (cAMP) or guanosine 3', 5'-cyclic monophosphate (cGMP). These channels play essential roles in vision and olfaction, as well as in cardiac and neuronal pacemaking. Heterologous expression of these eukaryotic membrane proteins, necessary for structural studies, is usually difficult. Such difficulty is commonly overcome by studying their prokaryotic homologues.

MlotiK1 is a bacterial cyclic nucleotide regulated potassium channel from *Mezorhizobium loti*. This homotetramer contains a transmembrane region and a cytoplasmic cyclic nucleotide binding (CNB) domain. The present thesis addresses recent research on this potassium channel, especially concerning its ligand selectivity determinants and global conformational change.

The molecular determinants of ligand selectivity were explored through a comprehensive set of point mutations in the CNB domain binding pocket. By combining three specific point mutations, ligand selectivity was inverted. While the wild-type CNB domain is known to favour binding of cAMP over cGMP, the triple mutant favours binding of cGMP over cAMP. Such inversion in ligand selectivity is reflected in the channel activation by cyclic nucleotides. The crystal structure of the triple mutant CNB domain showed that the change in selectivity is related to the establishment of an extensive water-mediated hydrogen bond network in the binding pocket. In contrast to the apolar wild-type binding pocket, this hydrophilic binding pocket is more flexible, allowing the accommodation of a variable number of water molecules that mediate cGMP binding through an hydrogen bond network.

The conformational change induced by cAMP in the full-length channel was visualized by atomic force microscopy, using a mutant with decreased ligand affinity. Such mutant was shown to be functionally active. The conformational change was found to be reversible and dependent on cAMP concentration. In the presence of cAMP, the CNB domains were organized in a four-fold arrangement, while in its absence they became highly unorganized and could not be visualized individually.

iii. Sumário

Os canais iónicos regulados por nucleótidos cíclicos são proteínas membranares que permeiam iões na presença dos nucleótidos cíclicos 3', 5'-monofostato cíclico de adenosina (cAMP) ou 3', 5'-monofosfato cíclico de guanosina (cGMP). Estes canais desempenham funções essenciais na visão e no olfacto, bem como no estabelecimento dos ritmos cardíaco e neuronal. A expressão heteróloga destas proteínas membranares eucarióticas, necessária para estudos estruturais, é frequentemente difícil. Esta dificuldade é geralmente superada através do estudo dos seus homólogos procarióticos.

O MlotiK1 é um canal de potássio regulado por nucleótidos cíclicos, proveniente da bactéria *Mezorhizobium loti*. Este homotetrâmero contém uma região transmembranar e um domínio de ligação a nucleótidos cíclicos citoplasmático. A presente tese aborda investigação recente neste canal de potássio, com ênfase nos determinantes moleculares de selectividade para o ligando e na sua alteração conformacional global.

Os determinantes moleculares de selectividade para o ligando foram explorados a partir de um conjunto abrangente de mutações pontuais no domínio de ligação. A selectividade para o ligando foi invertida através da combinação de três mutações específicas. Enquanto o domínio de ligação original favorece a ligação de cAMP relativamente a cGMP, o mutante triplo obtido favorece a ligação de cGMP sobre cAMP. Esta inversão de selectividade reflecte-se na activação do canal por nucleótidos cíclicos. A estrutura cristalina do domínio de ligação do mutante triplo revelou que a inversão de selectividade está relacionada com a formação de uma extensa rede de ligações de hidrogénio mediadas por moléculas de água no local de ligação. Em contraste com o local de ligação original, apolar, o local de ligação do mutante triplo é hidrofílico e mais fexível, permitindo acomodar um número variável de moléculas de água. Estas moléculas mediam a ligação de cGMP através de uma rede de ligações de hidrogénio.

A alteração conformacional induzida por cAMP no canal foi visualizada utilizando microscopia de força atómica e um mutante com baixa afinidade para cAMP. O referido mutante é funcionalmente activo. A alteração conformacional é reversível e dependente da concentração de cAMP. Na presença de cAMP, os domínios de ligação distribuem-se num arranjo tetragonal, ficando altamente desorganizados na sua ausência, não podendo ser visualizados individualmente.

iv. List of publications

The results described on this thesis are based on the following publications, which will be referred to in the text as Paper I and Paper II.

Paper I:

Pessoa J, Fonseca F, Furini S and Morais-Cabral J H (2014) “Determinants of ligand selectivity in a cyclic-nucleotide regulated potassium channel” *J. Gen. Physiol.* 144 (1): 41-54

Paper II:

Mari S A, Pessoa J, Altieri S, Hensen U, Thomas L, Morais-Cabral J H and Müller D J (2011) “Gating of the MlotiK1 potassium channel involves large rearrangements of the cyclic nucleotide-binding domains” *Proc. Natl. Acad. Sci. USA* 108 (51): 20802-20807

Contents

v. Abbreviations

2D crystal	Two-dimensional crystal
AFM	Atomic force microscopy
Apo A-1	Apolipoprotein A-1
ATP	Adenosine 5’-triphosphate
BK	Large conductance calcium-gated potassium channels
cAMP	Adenosine 3’, 5’-cyclic monophosphate
CAP	Catabolite gene activator protein
CCCP	Carbonyl cyanide 3-chlorophenyl hydrazone
cCMP	Cytidine 3’, 5’-cyclic monophosphate
cGMP	Guanosine 3’, 5’-cyclic monophosphate
CHAPS	[(3-Cholamidopropyl)dimethylammonio]-1-propanesulfonate hydrate
cIMP	Inosine 3’, 5’-cyclic monophosphate
CNG	Cyclic nucleotide-gated
DM	n-decyl-β-D-maltopyranoside
DTNB	5,5’-dithiobis-(2-nitrobenzoic acid)
DTT	Dithiothreitol
EM	Electron microscopy
Epac	Exchange protein directly activated by cAMP
GDP	Guanosine 5’-diphosphate
GEF	Guanine nucleotide exchange factor
GPCR	G-protein-coupled receptor
GTP	Guanosine 5’-triphosphate
HCN	Hyperpolarization-activated cyclic nucleotide-modulated
HDL	High-density lipoprotein
K_D	Dissociation constant
MD	Molecular dynamics
MSP	Membrane scaffold protein
MW	Molecular weight
NABB	Nanoscale apolipoprotein-bound bilayer particle
ndHDL	Nascent discoidal high-density lipoprotein
NMG	N-methyl-β-D-glucamine
PBC	Phosphate-binding cassete
PBFI	Potassium-binding benzofuran isophtalate
PBS	Phosphate-buffered saline

PDB	Protein data bank
PDE	Cyclic nucleotide phosphodiesterase
PKA	cAMP-dependent protein kinases
PKG	cGMP-dependent protein kinases
POPC	1-palmitoyl-2-oleoyl-sn-glycero-3-phosphocholine
SD	Standard deviation
SDS-PAGE	Sodium dodecylsulphate polyacrylamide gel electrophoresis
SK	Small conductance calcium-gated potassium channels
STM	Scanning tunneling microscopy
Zap1	Zebrafish apolipoprotein A-1

1. Introduction

1.1. Cyclic nucleotides

The cyclic nucleotides adenosine 3', 5'-cyclic monophosphate (cAMP) and guanosine 3',5'-cyclic monophosphate (cGMP) are universal signalling molecules, found in all organisms. They are involved in many physiological processes, including vision, olfaction, sugar metabolism and neuronal function.

1.1.1. Identification of cAMP and cGMP

cAMP was first identified as a "heat stable factor" produced in membrane fractions of dog or cat liver homogenates, upon addition of the hormones epinephrine or glucagon. Adenosine 5'-triphosphate (ATP) and magnesium were required and the "heat stable factor" could not be produced in the corresponding soluble fractions under the same conditions. When added to the supernatant, the "heat stable factor" induced glycogen breakdown by stimulating the liver phosphorylase activity (Berthet et al., 1957). The factor was later purified and identified as an adenine ribonucleotide (Sutherland and Rall, 1958). Its structure was determined (Lipkin, 1959) and it was named "adenosine 3',5'-phosphoric acid", cyclic 3,5-AMP (cAMP). cAMP was shown to be quantitatively synthesized from ATP and produced not only in the liver, but also in the heart, skeletal muscle and brain (Rall and Sutherland, 1958). The enzyme catalyzing this reaction requires magnesium and was named adenyl cyclase. Its distribution, preparation and properties were described (Sutherland et al., 1962) and pyrophosphate was shown to be another reaction product (Rall and Sutherland, 1962). Importantly, the discovery of cAMP led to the introduction of the concept of secondary messenger. The hormone (primary messenger) activated the membrane-bound adenyl cyclase, increasing the production of cAMP (secondary messenger) from ATP.

cGMP was first isolated from rat urine (Ashman et al., 1963) and animal tissue (Goldberg et al., 1969) (Ishikawa et al., 1969). Unlike cAMP, cGMP biosynthesis could not be initiated by epinephrine or glucagon, showing that it should result from another metabolic pathway (Hardman and Sutherland, 1969). It was shown that cGMP was produced from guanosine 5'-triphosphate (GTP) by a guanyl cyclase (White and Aurbach, 1969), which is largely soluble, has a preference for manganese instead of magnesium and is inhibited by several nucleotides, including ATP (Ishikawa et al., 1969).

1.1.2. Cyclic nucleotide synthesis, degradation and effectors

cAMP and cGMP are produced by adenyl and guanyl cyclases, respectively, and degraded by cyclic nucleotide phosphodiesterases (PDEs) (Rehmann et al., 2007). Physiological responses elicited by cyclic nucleotides are mostly mediated by cAMP-dependent protein kinases (PKA) (Walsh et al., 1968) (Kuo and Greengard, 1969a) (Kuo and Greengard, 1969b) (Miyamoto et al., 1969) and cGMP-dependent protein kinases (PKG) (Kuo and Greengard, 1970). These two homologous protein families are recognized as the main effectors of cAMP and cGMP-mediated responses (Lincoln and Corbin, 1977).

Other effectors are the bacterial Catabolite gene Activator Protein (CAP) (Emmer et al., 1970), which promotes gene transcription in the presence of cAMP (Zubay et al., 1970), ion channels, which are mostly studied in vision (Cook et al., 1987; Kaupp et al., 1989) and olfaction (Nakamura and Gold, 1987), a microbial cAMP receptor expressed on the surface of the eukaryotic microorganism *Dictyostelium discoideum* (slime mold) (Klein et al., 1988) and a protein family with Guanine nucleotide Exchange Factor (GEF) activity called Exchange Protein directly Activated by cAMP (Epac) (de Rooij et al., 1998; Kawasaki et al., 1998).

1.1.3. Generating cyclic nucleotides: adenyl cyclases and guanyl cyclases

In mammals, there are at least ten groups of adenyl cyclases (also known as adenylyl cyclases or adenylate cyclases), divided into one soluble and nine membrane-bound subgroups (Taussig and Gilman, 1995). The membrane bound adenyl cyclases are homologous, containing two catalytic domains that form the catalytic site and are attached to two membrane-embedded domains (Hanoune and Defer, 2001). The whole unit converts ATP into cAMP. Adenyl cyclase activity is controlled by a membrane-bound G-protein-coupled receptor (GPCR) and a heterotrimeric G protein (formed by α, β and γ subunits). Adenyl cyclase activity can be triggered by several molecules, including hormones and neurotransmiters, which bind to their specific GPCR. Upon activation by the GPCR, the guanosine 5'-diphosphate (GDP) in the G-protein α subunit is exchanged by guanosine 5'-triphosphate (GTP). The β and γ subunits are dissociated form it and regulate downstream processes (Taussig and Gilman, 1995), including activation of adenyl cyclase. During this process, the extracellular signal is amplified: one activated GPCR can activate several adenyl cyclases and each adenyl cyclase can synthesize many cAMP molecules. Besides G proteins, adenyl cyclases are regulated by protein

kinases, forskolin (a plant diterpene) and the calcium-binding protein calmodulin (Hanoune and Defer, 2001). Several human diseases are related to defective or excessive cAMP biosynthesis (Sutherland, 1972) (Costache et al., 2013).

There are two groups of guanyl cyclases (also known as guanylyl cyclases or guanylate cyclases): membrane-associated and soluble. Both have one catalytic domain per subunit (Tesmer, 2008). Membrane-associated guanyl cyclases are homodimers containing an extracellular binding domain, whose best known ligands are natriuretic peptides (peptide hormones), a transmembrane region with one or more segments and an intracellular catalytic domain (Wedel and Garbers, 2001) (Rehmann et al., 2007). Soluble guanyl cyclases are heterodimers formed by a α and a β subunit, existing two and three kinds of α and a β subunits, respectively (Friebe and Koesling, 2003). They contain a heme group and are activated by nitric oxide (Rehmann et al., 2007). Like adenyl cyclases, guanyl cyclases also amplify the extracellular signal during its transduction process.

1.1.4. Degrading cyclic nucleotides: Cyclic nucleotide phosphodiesterases

The intracellular concentrations of cAMP and cGMP are regulated mainly by the activities of adenyl/guanyl cyclase and cyclic nucleotide phosphodiesterases (PDEs). PDEs catalyze the conversion of cAMP or cGMP to AMP or GMP, respectively (Beavo et al., 1994). PDEs form a diverse protein family of dimers and multimeric complexes. Their function is achieved by a conserved catalytic domain usually located at the C-terminus. PDEs can be unspecific or specific for cAMP or cGMP (Manganiello et al., 1995). In some PDEs, a N-terminal GAF domain has been identified, whose function is cyclic nucleotide binding (Zoraghi et al., 2004). There are GAF domains specific for cAMP and for cGMP (Gross-Langenhoff et al., 2006). In cGMP-specific GAF domains, ligand binding is favoured through a conserved aspartate. GAF domains are not restricted to PDEs (Aravind and Ponting, 1997) and can bind other small molecules besides cyclic nucleotides (Zoraghi et al., 2004).

1.1.5. Proteins containing CNB domains

“The great variety of actions that involve adenosine 3’,5’-monophosphate (cyclic AMP), including mediation of the effects of many hormones in vertebrates as well as stimulation of enzyme synthesis in bacteria, raises the question as to the mechanism by

which this low molecular weight compound achieves its diversity of effects" (Kuo and Greengard, 1969b).

When the sequences of CAP, PKA and PKG were determined, a common structural motif was found: the cyclic nucleotide-binding (CNB) domain (Shabb and Corbin, 1992). CNB domains are recognized as the main common link among proteins regulated by cyclic nucleotides. The first structure of a CNB domain was obtained when *E. coli* CAP was crystallized in complex with cAMP (McKay and Steitz, 1981; McKay et al., 1982).

1.1.5.1. Protein kinases activated by cAMP or cGMP

PKAs are divided into several groups (Canaves and Taylor, 2002), which may have different subcellular locations (Theurkauf and Vallee, 1982). Eukaryotic PKAs are heterotetramers composed of two identical regulatory (where cAMP binds) and two identical catalytic subunits, existing four types of each one (Johnson et al., 2001). Each regulatory subunit has two tandem CNB domains (Titani et al., 1984; Diller et al., 2001). The regulatory subunits dimerize through a narrow region and a catalytic subunit is attached to each one of the regulatory subunits (Zhao et al., 1998). In the absence of cAMP, PKA is inhibited through high-affinity binding of the regulatory subunits to the catalytic subunits (Hofmann, 1980). In the presence of cAMP, two ligand molecules bind cooperatively to each regulatory subunit, disrupting the interaction with catalytic subunits and activating the kinase (Johnson et al., 2001) (Anand et al., 2002). cAMP-binding and interaction with a catalytic subunit are achieved through separate regions (Corbin et al., 1978; Herberg et al., 1994). PKA effects are mostly related to stimulation of glycolysis and glycogen breakdown in muscle and liver (Nelson, 2005).

There are at least two types of PKG: PKG1, found mostly in vascular smooth muscle cells, endothelium and platelets and PKG2, found mostly in the intestine, kidneys and brain (Vaandrager and de Jonge, 1996). PKG1 enzymes are homodimers, where each monomer contains one regulatory domain with two CNB domains, plus a C-terminal catalytic domain with kinase activity (Francis et al., 2010), which forms interactions within each monomer (Wolfe et al., 1989). The regulatory domain also forms the dimerization interface. In the absence of cGMP, the enzyme is inhibited by internal contacts, as in PKA (Francis et al., 2010). PKG1 mediates the vasodilation effect of nitric oxide and is, as a consequence, involved in vascular smooth muscle relaxation. Other effects include decrease in endothelial permeability, inhibition of platelet aggregation (Vaandrager and de

Jonge, 1996) and activation of potassium channels regulated by calcium and voltage (Alioua et al., 1998).

1.1.5.2. Ion channels

Ion channels regulated by cyclic nucleotides are best studied in the vision and in the olfaction mechanisms. Cyclic nucleotide gated (CNG) channels are usually heterotetramers, containing one C-terminal CNB domain per monomer. Their specificity for cAMP or cGMP varies (Kaupp and Seifert, 2002). Both visual and olfactory ion channels are specific for cations and permeate calcium (mostly) and also sodium and potassium (Menini, 1995). Unlike other ligand-gated ion channels, they do not desensitize in the continued presence of ligand (Kaupp and Seifert, 2002). They are also regulated by calcium/calmodulin (Trudeau and Zagotta, 2003), pH and phosphorylation (Kaupp and Seifert, 2002).

Light is sensed through closure of cGMP-gated ion channels and consequent termination of neurotransmitter release into neighbouring cells. In the dark, these channels are open. Rod cells in the retina have large amounts of the GPCR rhodopsin, which contains constitutively bound retinal, a photosensitive derivative of vitamin A. Light is sensed through isomerization of retinal, activating rhodopsin. Activated rhodopsin will relay the light signal through the G-protein transducin, exchanging its GDP to GTP and activating it. The α-subunit of activated transducin will activate a PDE, resulting in a decrease in cGMP concentration and consequent closure of cGMP-gated calcium channels, decreasing their current and the release of neurotransmitter. Conversely, the decrease in intracellular calcium concentration stimulates guanyl cyclase activity, enhancing cGMP synthesis by a feedback mechanism (Hille, 1992) (Matulef and Zagotta, 2003). A similar mechanism exists in cones, the cells in the retina responsible for colour vision; however, they are less sensitive and adapt to a wider range of light intensities, possibly because of differences in calcium homeostasis. Mutations in genes encoding these channels can lead to blindness or loss of colour discrimination (Kaupp and Seifert, 2002).

Binding of an odorant to its GPCR in an olfactory neuron stimulates adenyl cyclase, increasing the intracellular concentration of cAMP. cAMP will open calcium channels and the consequent increase in intracellular calcium concentration will open calcium-gated chloride channels. The current generated will stimulate neurotransmitter release into neighbouring cells, resulting in odour perception (Hille, 1992); (Craven and Zagotta, 2006). The ability to discriminate among many odours is due to the existence of a

vast array of odorant receptors. Mice lacking functional cAMP-sensitive olfactory channels exhibited no detectable response to odorants (Kaupp and Seifert, 2002).

1.1.5.3. Guanine nucleotide exchange factor, Epac

Epac is a monomer and contains a regulatory region with a CNB domain, plus a C-terminal catalytic region that mediates GEF activity. GEF activity consists in the transfer of GTP to the GTPase proteins Rap1 and Rap2, which cycle between GDP-bound (inactive) and GTP-bound (active) forms (Gloerich and Bos, 2010). In the absence of cAMP, Epac is inactive, since access of the catalytic domain to Rap is blocked by interactions with the regulatory regions in Epac (Rehmann et al., 2006). cAMP binding causes the CNB domain to swing away from its blocking position, allowing access to Rap proteins (Rehmann et al., 2008).

In mammalian cells, there are two isoforms of Epac: Epac1 and Epac2 (Gloerich and Bos, 2010). Epac2 contains an additional CNB domain at the N-terminus whose binding affinity is lower (de Rooij et al., 2000). This additional CNB domain has a non-canonical sequence and different phosphate-binding cassete (PBC) architecture (Rehmann et al., 2003). Its function may not be cAMP-binding. Repac, the other member of the family, lacks a CNB domain and is a constitutive activator of Rap proteins (de Rooij et al., 2000). Both Epac1 and Epac2 are abundant in the central nervous system and have neuronal functions (Gloerich and Bos, 2010). Epac1 is also abundant in blood vessels, kidney or adipose tissue and is involved in cardiac function, vascular permeability and inflammation (Fukuhara et al., 2005; Gloerich and Bos, 2010). Epac2 is also found in the adrenal gland and pancreas and is involved in insulin secretion (Shibasaki et al., 2007; Gloerich and Bos, 2010).

1.2. Potassium channels

Potassium channels are most likely the fundamental controllers of the cellular electrical homeostasis (Torres et al., 2007). Their diversity is of great importance to understand the variety of electrical responses of cells when subjected to stimuli.

1.2.1. The beginning of ion channel research

The ion channel research field has its foundations in the study of electrical activity of squid giant axons. The unusually large dimensions of these cells allowed measuring their electrical properties by using microelectrodes. Such electrical properties were found to be dependent on ion channels.

1.2.1.1. Electrical measurements in squid giant axons

Squid giant axons were prepared by removing fibers and branches under an optical microscope, after washing with sea water. Prepared axons usually had 6 to 8 centimetres in length and a uniform diameter between 530 and 580 µm. Recordings were done in elongated chambers with circulating sea water. Axons whose electrical properties stabilized within one hour were used in the following 6 to 8 hours, as their electrical properties were constant during such period (Cole and Curtis, 1939).

This system was used for measuring the electrical currents that resulted of applying voltage to giant axons. Such currents resulted mainly of changes in sodium and potassium permeabilities. Upon stimuli, the conductance changed differently and reversibly for each ion. Based on these recordings, an empirical kinetic model was presented to describe sodium and potassium permeability changes upon stimuli, in squid giant axons (Hodgkin and Huxley, 1952b, a, c). Such model became an explanation for their electrical excitability.

1.2.1.2. Early structural insights

Electrical recordings using inhibitory compounds in squid giant axons (Armstrong, 1971) or frog nerve fibers (Armstrong and Hille, 1972) suggested that potassium permeation should be achieved by permeation pores. Such pores should have two distinct regions: a cavity wide enough to accommodate an ion or an inhibitor molecule and a narrower inner region that could accommodate only the ion.

Perfusion of squid giant axons with proteases indicated that sodium and potassium permeation should be carried out by distinct channels and that those should be proteins (Armstrong et al., 1973). Other inhibition results were consistent with a potassium channel structure with multiple ion binding sites, crossed by ions in a single file (Adelman and French, 1978), as previously predicted (Hodgkin and Keynes, 1955). Moreover, potassium

channels should contain at least three potassium binding sites occupied by a minimum of two ions at a time (Hille and Schwarz, 1978) and their narrowest region should be a circle of oxygen atoms forming a 3 Å wide pore (Hille, 1973).

1.2.2. The potassium channel selectivity filter

Each potassium channel sequence contains a highly conserved segment called potassium channel signature sequence, which forms the narrow region responsible for selective potassium permeation, known as the selectivity filter (MacKinnon, 2003). Mutations in this segment can severely affect ion discrimination (Heginbotham et al., 1994).

Potassium ions permeate through these channels down their concentration gradient at rates that can be close to 10^6 ions per second, corresponding to the translocation of one ion every 0.1 millisseconds (Hille, 1992).

1.2.3. Important models of potassium channels: Shaker and KcsA

The Shaker potassium channel (Pongs et al., 1988) cloned from *Drosophila melanogaster*, the fruit fly, was found to be a tetramer (MacKinnon, 1991). Its external entryway was described as a shallow conical vestibule formed by loops, with the selectivity filter in the apex (Ranganathan et al., 1996). The channel function is affected by pore blockers, which can be trapped inside its cavity by the channel gate (Holmgren et al., 1997). This mechanism is called “gating” and is associated with changes in volume and accessibility in the cavity (Liu et al., 1997).

The KcsA channel from *Streptomyces lividans*, a filamentous soil bacterium, was shown to be selective for potassium and predicted to have two transmembrane helices per subunit (Schrempf et al., 1995). Purified KcsA is a remarkably stable tetramer in solution (Heginbotham et al., 1997) and was the first ion channel whose structure was determined by X-ray crstallography (Doyle et al., 1998). The structure showed a tetrameric assembly, where each subunit contains two long α-helices that cross the membrane and surround a shorter α-helix. The pore is located at the center of the four subunits (Fig. 1.1 A). The selectivity filter is formed by a loop located between the shorter and the C-terminal α-helices (Fig. 1.1 B). The selectivity filter contains four identical potassium binding sites, where each potassium ion is coordinated by eight oxygen atoms from main chain carbonyl groups and from side-chain hydroxyl groups (Fig. 1.1 C).

Although crystal structures show one ion bound to each of the four potassium binding sites, in fact, only two of those sites are occupied by ions at the same time (Zhou and MacKinnon, 2003). Each pair of ions is separated by one water molecule, alternating rapidly between two configurations, which are potassium-water-potassium-water and water-potassium-water-potassium. When a potassium ion enters in one side of the line, it displaces another potassium ion in the other side, resulting in potassium translocation (Morais-Cabral et al., 2001).

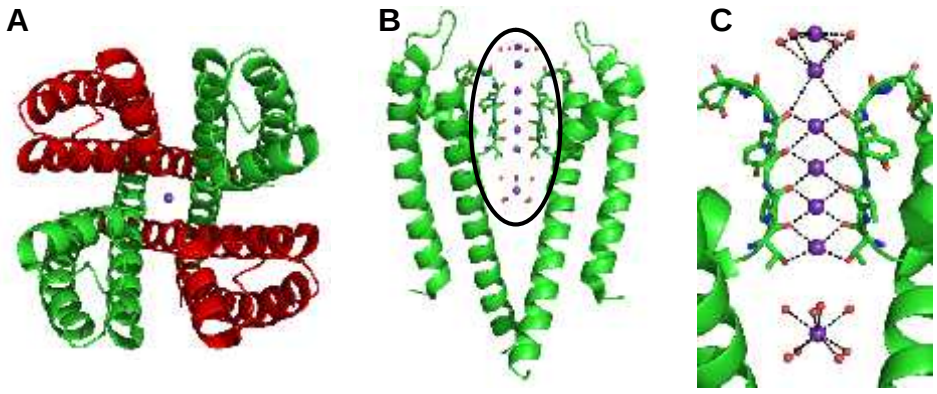

Figure 1.1: Crystal structure of the KcsA potassium channel in ribbon representation. Potassium ions and water molecules are represented as purple and red spheres, respectively. (A) Extracellular view, neighboring subunits are represented in different colors. (B) Side view, only two subunits are shown for clarity and the selectivity filter is indicated by oval. (c) Zoom over selectivity filter, where polar contacts between potassium ions and water molecules or carbonyl groups from the selectivity filter are indicated by black dashed lines. Protein data bank (PDB) code: 1K4C (Zhou et al., 2001).

1.2.4. Rapid and selective potassium permeation

The pore structure present in KcsA is conserved in eukaryotic potassium channels (MacKinnon et al., 1998). Evolutionary optimization of the potassium channel selectivity filter resulted in very high rates of potassium permeation and very high selectivity (MacKinnon, 2003). The very high permeation rate is explained by the weak binding of the ions to the selectivity filter. It has been postulated that such binding is weak for two reasons: 1) repulsion between two consecutive ions separated by one water molecule; 2) the presence of two potassium ions changes the conformation of the selectivity filter, causing an energetic penalty that reduces the total binding energy (MacKinnon, 2003). Potassium permeation is facilitated also because the cavity and pore allow the ions to remain hydrated inside the membrane and stabilized by the negative charges at the end

of α-helices (Roux and MacKinnon, 1999). It has also been postulated that high ion selectivity is achieved because the selectivity filter has several “tailor-made” binding sites that perfectly mimic the hydration shell of potassium (MacKinnon, 2003). The presence of potassium should impose a large energy barrier to other ions, as lithium or sodium, to bind to the selectivity filter (Thompson et al., 2009). Potassium, or another permeable cation, is required for structural stability of the selectivity filter and overall stability of the tetramer (Krishnan et al., 2005). Its removal causes pore dilation, loss of ion selectivity and ultimately loss of function (Loboda et al., 2001). Potassium channel diversity is due to the different mechanisms for gating (opening and closing of the pore) and regulation, which can be voltage or a ligand (MacKinnon, 2003).

The main families of potassium channels will be discussed below. The members of these families are homo or heterotetramers.

1.2.5. Voltage-gated potassium channels

When the membrane electrical field is altered, voltage-gated potassium channels detect the alteration. They become activated, letting potassium ions cross the membrane and restoring the electrical field to its resting state. In these channels, each monomer has six transmembrane segments divided into two domains (Fig. 1.2): the first four helices form the voltage sensor domain and the last two helices form the pore domain, identical to the one seen in KcsA (Fig. 1.1). Gating is directly controlled by the transmembrane electrical field, which is sensed in real time by a voltage sensor, located in the voltage sensor domain. The fourth helix in each voltage-sensor domain is an essential element in voltage sensing. It contains four to eight positively charged residues, mostly arginines, every third position (Tombola et al., 2006). The Shaker channel is a voltage-gated potassium channel and a useful model to explore the voltage sensing mechanism. During voltage sensing, positive charges in the fourth helix accessible on one side of the membrane change their accessibility to the other side by translation and most likely also rotation of the fourth helix (Yellen, 2002; Tombola et al., 2006).

In the structures of Shaker channels (Long et al., 2005; Long et al., 2007), the fourth helix adopts a 3_{10} helix conformation over seven to ten residues. 3_{10} helices are formed when main chain hydrogen bonds are established between residues separated by two other residues, while in α-helices the separation is of three residues. Therefore, 3_{10} helices are more tightly wound and less stable than canonical α-helices. These helices are relatively rare and most are short (usually with three or four residues). Longer 3_{10} helices are even rarer, since they have specific packing requirements, rarely seen over

long extensions (Vieira-Pires and Morais-Cabral, 2010). As mentioned above, voltage sensing should involve translation and most likely, also rotation of the fourth helix across the membrane. A 3_{10} helix conformation would place the positively charged residues all in the same side and the switch to a α-helical conformation would provide the rotation mentioned above. Such transition is possible and has been reversibly observed in isolated peptides upon changes in solvent polarity (Karle et al., 1994; Bellanda et al., 2007). Therefore, it has been proposed that voltage sensing might involve transition between the two conformations in part of the fourth helix (Vieira-Pires and Morais-Cabral, 2010). It is still unclear how voltage sensing is coupled to channel gating; however, several studies indicate that the linker between both transmembrane domains and the C-terminal portion of the C-terminal helix is involved (Tombola et al., 2006).

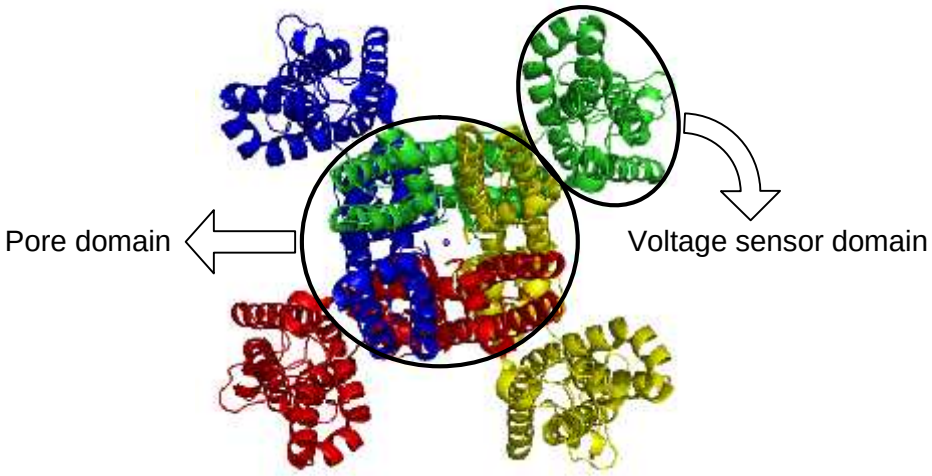

Figure 1.2: Crystal structure of the Shaker potassium channel in a ribbon representation (extracellular view). Each subunit is represented in a different color. The pore is indicated by a potassium ion represented by a sphere. The pore domain and the voltage sensor domain are indicated. PDB code: 2R9R (Long et al., 2007).

1.2.6. Ligand-gated potassium channels

There are two main families of potassium channels regulated by ligands: inward rectifier and calcium-gated, which will be described below.

1.2.6.1. Inward rectifier potassium channels

Inward rectifier potassium channels conduct potassium more efficiently towards the intracellular side (inward) than in the opposite direction (outward), due to pore blocking in the intracellular side by magnesium or polyamines (Hibino et al., 2010). Such blocking is mediated by their regulatory cytoplasmic domain formed by the N- and C-termini from each subunit, which provides a favorable environment for binding of polyamines (Nishida and MacKinnon, 2002). These channels lack a voltage sensor domain. They contain only the pore domain (Tao et al., 2009) and the overall structure is similar to KcsA. Their activity is regulated by a vast array of ligands, mostly ions, phospholipids or proteins, like GPCRs. Their functions include controlling the resting membrane voltage of cells, insulin release and neurotransmitter action (Hibino et al., 2010).

1.2.6.2. Calcium-activated potassium channels

This family is subdivided into large conductance (maxi-K or BK) and small conductance (SK) channels (McCoy and Nimigean, 2012). While both are activated by intracellular calcium, BK channels are also activated by voltage (Rothberg, 2012) (Adelman et al., 2012). Both types have six transmembrane helices, but BK channels have an additional N-terminal helix, which is part of the voltage sensor and also involved in oligomerization (Rothberg, 2012).

In SK channels, calcium regulation is mediated by calmodulin, which binds to the C-terminus of each subunit (Adelman et al., 2012). In BK channels, calcium is sensed by a cytoplasmic C-terminal regulator of conductance of potassium (RCK) domain (Rothberg, 2012), which has a regulatory function in various potassium channels and transporters (Roosild et al., 2009). BK channels are essential to control action potentials and neurotransmitter release, as well as in the control of smooth muscle contraction, triggered by calcium release from the endoplasmic reticulum (Rothberg, 2012). SK channels are expressed in the central nervous system and their activity has rapid effects in excitability and synaptic transmission, as well as in long term changes that affect memory and learning (Adelman et al., 2012).

1.3. Channels activated by cyclic nucleotides

Cyclic nucleotide activated ion channels are divided into two main families: cyclic nucleotide-gated (CNG) and hyperpolarization-activated cyclic nucleotide-modulated (HCN) channels. Both are homo or heterotetrameric, containing six putative α-helices and a cytoplasmic C-terminal CNB domain (Craven and Zagotta, 2006). Despite CNG, HCN channels are also regulated by voltage (Kaupp and Seifert, 2001). CNG channels are non-selective cation channels, permeating mostly sodium and calcium (Kaupp and Seifert, 2002). On the contrary, HCN channels are about 4-fold more permeant to potassium than sodium. The CNG and HCN families are believed to be similar in structure and mechanism; however, they play different physiological roles (Craven and Zagotta, 2006).

1.3.1. CNG channels

Although CNG channels are best studied in vertebrate photoreceptors and olfactory neurons, they are not restricted to these tissues. Another important function of CNG channels is mobility and chemoattraction in sperm cells. They are also found in heart, kidney, pancreas, adrenal gland and colon (Kaupp and Seifert, 2002; Matulef and Zagotta, 2003). Their importance in the central nervous system is being increasingly recognized, since they are probably involved in several processes, including neuronal excitability, neurotransmission and pain perception (Podda and Grassi, 2013). CNG channels have also been studied in plants (Zelman et al., 2012).

In CNG channels, the four N-terminal helices form a domain with homology to the voltage sensor domain of voltage-gated channels; however, these channels are not sensitive to voltage. It has been proposed that although the fourth helix contains some of the positive charges required for voltage sensing, some of the necessary counter charges are missing (Bellanda et al., 2007). Consistently with this hypothesis, the fourth helix of a CNG channel (voltage insensitive) was shown to work as a voltage sensor, by transferring it to a voltage-gated channel (Tang and Papazian, 1997). In CNG channels, this helix might also be “locked” in a fixed conformation by hydrophylic residues of its upstream loop (Kaupp and Seifert, 2002). It was proposed that the CNG channels pore opens through a translation and possible rotation of the intracellular ends of the C-terminal helices, increasing its internal diameter (Flynn and Zagotta, 2001).

1.3.2. HCN channels

In mammals, HCN channels are expressed in the heart and nervous system, where they regulate heart rate and neuronal excitability. Due to such function, they are also called pacemaker channels (Kaupp and Seifert, 2001). Strikingly, and unlike other voltage gated channels, which are activated by membrane depolarization, membrane hyperpolarization activates HCN channels. Nevertheless, the voltage sensing mechanism in HCN channels is probably similar to those of voltage-gated channels (Bell et al., 2004). HCN channel activation is also regulated by cyclic nucleotides, especially cAMP.

Rhythmic contraction of the cardiac muscle results of a cycle of membrane depolarization and hyperpolarization mediated by at least four different types of ion channels, including HCN channels (Kaupp and Seifert, 2001). Some neurotransmitters accelerate the heartbeat rate through an increase in cAMP concentration, favouring activation of HCN channels (Craven and Zagotta, 2006). In neurons, these channels work through a similar, but faster mechanism, and therefore the neuronal action potentials are faster (Craven and Zagotta, 2006). In the nervous system, they control neuronal excitability, synaptic transmission, among other functions (Benarroch, 2013). They are associated with learning and memory and misregulation may be involved in chronic pain and epilepsy (Lewis and Chetkovich, 2011). HCN channels have been explored as potential drug targets (Postea and Biel, 2011).

1.3.3. MlotiK1, a bacterial cyclic nucleotide-regulated potassium channel

The physiological and medical relevance of both CNG and HCN ion channels are important reasons for their study. Functionally, they have been well characterized through electrical recordings. However, structural studies require expression and purification of significantly large amounts of protein. For these eukaryotic membrane proteins, this is frequently not feasible and their prokaryotic homologues, such as MlotiK1, have been a valuable alternative. MlotiK1 is a cyclic nucleotide regulated potassium channel from *Mesorhizobium loti*, a symbiotic bacterium involved in nitrogen fixation (Kaneko et al., 2000). Both the full-length channel and its isolated CNB domain can be expressed and purified with good yield and purity. Protein folding is facilitated in the presence of a cyclic nucleotide, since ligand depletion during purification causes extensive protein aggregation (Nimigean et al., 2004).

1.3.3.1. Structural data

MlotiK1 is a homotetramer and its sequence predicts a transmembrane topology containing six α-helices and a cytoplasmic C-terminal CNB domain. Electron microscopy (EM) of single particles in the bound state shows that the CNB domains are organized with a four-fold symmetry, without any obvious interactions between them (Chiu et al., 2007). The structure of its transmembrane region has been determined at 3.1 Å by X-ray crystallography (Clayton et al., 2008), showing an arrangement similar to those of voltage-gated potassium channels. In each subunit, the four N-terminal α-helices form a voltage sensor-like domain and the two C-terminal α-helices form the pore domain (Fig. 1.3 A). In the voltage sensor-like domain, the fourth helix contains an unusually long 3_{10} helix, with eleven residues (Clayton et al., 2008). This helix does not have positively charged residues at the necessary positions for voltage sensing (Clayton et al., 2008) and therefore, it is unlikely to sense the transmembrane electrical field. Although it has structural homology to voltage-sensor domains, its role, if any, is unclear. Electron crystallography suggests that, in the membrane, the position of the voltage sensor-like domain relative to the pore domain is highly variable, adopting multiple orientations (Clayton et al., 2009). The pore domain has the typical structure found in potassium channels; however, it contains two bulky residues, F203 and Y215, which partially occlude the pore (Fig. 1.3 B) (Clayton et al., 2008). Although the crystals were grown in the presence of cAMP, the structure shows a closed state. The CNB domains were highly disorded and could not be resolved.

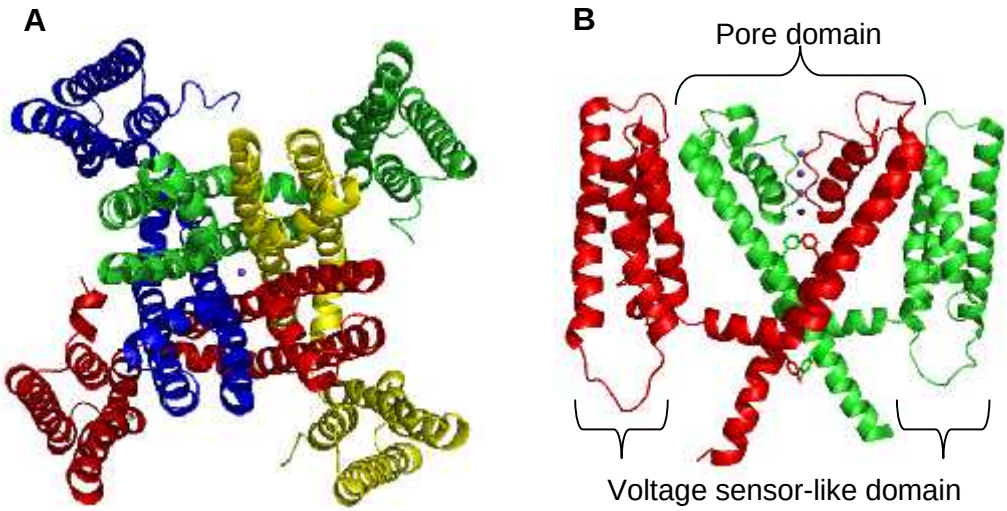

Figure 1.3: Crystal structure of the MlotiK1 potassium channel transmembrane region, in a ribbon representation. (A) Extracellular view, where each subunit is represented in a different color. The pore is indicated by a potassium ion represented by a sphere. (B) Side-view, only two subunits are shown for clarity. In the pore domain, the selectivity filter is indicated by four potassium ions (represented by spheres) and F203 and Y215 are represented in stick. PDB code: 3BEH (Clayton et al., 2008).

There are several crystal structures of the isolated CNB domain: four structures in complex with cAMP, two structures in complex with cGMP and six apo structures (Clayton et al., 2004; Altieri et al., 2008). There are also nuclear magnetic resonance (NMR) structures: one in complex with cAMP (Schunke et al., 2009) and an apo structure (Schunke et al., 2011). Both show that the isolated CNB domain is a monomer in solution. The structure of MlotiK1 CNB domain in complex with cAMP consists of an antiparalel β-roll and five helices, comprising a helical linker to the transmbrane region and four α-helices, αA, αB, αC and αP (Fig. 1.4 A). Superposition of bound and unbound structures of the CNB domain shows that the β-roll is essentially unchaged in both states, except in the β4-β5 hairpin loop. The linker that connects the CNB domain to the transmembrane region and the other helices are in different positions. Importantly, αC helix covers the binding pocket as a lid in the bound state and is deviated in the unbound state (Fig. 1.4 B). The different positions of αC helix in different crystal structures of the unbound state suggest that this helix is highly mobile in the absence of ligand (Clayton et al., 2004; Altieri et al., 2008); however NMR data indicates that the CNB domain is rigid in the unbound state (Schunke et al., 2011).

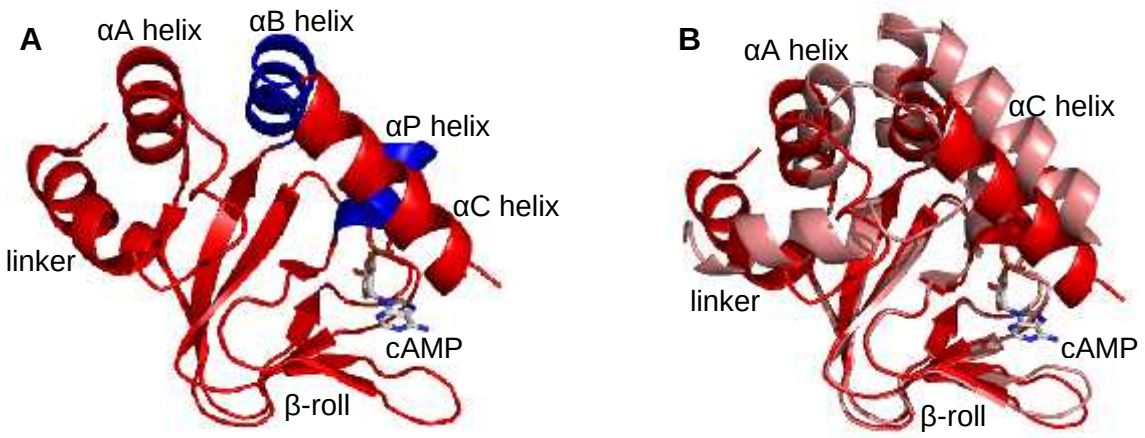

Figure 1.4: Crystal structures of MlotiK1 CNB domain in ribbon representations, with bound cAMP represented in stick. (A) Structure in complex with cAMP colored in red or blue (for αB and αP helices). (B) Superposition of cAMP-bound (red) and unbound (light red) structures through the β-roll. PDB codes: 1VP6 (bound) and 1U12 (unbound) (Clayton et al., 2004).

1.3.3.2. Functional data

MlotiK1 has remarkably slow permeation kinetics (Clayton et al., 2004); (Silverman and Heginbotham, 2007), partly due to the occlusion of the pore by the bulky residues F203 and Y215 (Clayton et al., 2008). It has not been possible to study MlotiK1 function through electrical recordings, most likely because of its slow permeation kinetics. Alternatively, a radioactive flux assay (Nimigean, 2006) has been used to functionally characterize this potassium channel. MlotiK1 is selective for potassium over sodium or lithium, but accurate estimates of the selectivity ratios could not be determined (Nimigean et al., 2004). MlotiK1 mediated potassium transport is enhanced by a cyclic nucleotide, but not totally dependent of it (Silverman and Heginbotham, 2007). The maximum stimulatory effect of cAMP is only about 2-fold (Clayton et al., 2004; Silverman and Heginbotham, 2007). The channel can also be activated by cGMP, but the necessary concentration for half of maximum activity is approximately 10-fold higher than for cAMP (Nimigean et al., 2004; Altieri et al., 2008). The determinants that define this 10-fold selectivity for cAMP versus cGMP are not completely known; however, CNB domain structures in complex with cAMP or cGMP provide some insights. Due to the different conformation of the ligand in the binding pocket, V288 makes van der Waals interactions with cAMP, but not with cGMP (Altieri et al., 2008). The same structures show that a

residue in the PBC, S308, establishes hydrogen bonds with cGMP, but not with cAMP. Mutating S308 to a valine decreases the affinity for cGMP by 3-fold, without significant effect in cAMP (Nimigean and Pagel, 2007). In CNG channels, an aspartate in αC helix was proposed to be important for the discrimination between cAMP and cGMP (Varnum et al., 1995). In MlotiK1, the equivalent residue is an alanine, which is not resolved in the crystal structures (Clayton et al., 2004; Altieri et al., 2008) and is disordered in the NMR structures (Schunke et al., 2009; Schunke et al., 2011). Mutating it to an aspartate increases affinity for cGMP by 3-fold, without detectable effect in cAMP (Nimigean and Pagel, 2007).

Cyclic nucleotide binding in MlotiK1 is not cooperative (Cukkemane et al., 2007) and is well coupled to channel opening (Nimigean and Pagel, 2007). Upon cAMP binding, the MlotiK1 CNB domain conformational change occurs through an induced-fit mechanism (Peuker et al., 2013) that affects virtually all residues in the CNB domain (Schunke et al., 2007; Schunke et al., 2010; Cukkemane et al., 2012). In the αC helix, the R348 residue establishes important interactions with the ligand (Clayton et al., 2004; Altieri et al., 2008; Schunke et al., 2009). Mutating it to an alanine significantly decreases binding affinity (Cukkemane et al., 2007).

MlotiK1 cannot be included either into the CNG or HCN families. It is selective for potassium, like HCN channels; however, it is most likely not voltage-gated. It should therefore be simply considered as separate family of prokaryotic potassium channels regulated by cyclic nucleotides (Nimigean et al., 2004).

1.3.3.3. State of the art and objectives

In contrast to the well characterized conformational change occurring in the CNB domain upon ligand binding/unbinding, the structural data available for MlotiK1 has shown its transmembrane region only in the closed state. It would be of interest to gain insights into the structural differences between the the open and closed states. Additionally, the molecular mechanism that determines ligand selectivity in CNB domains is still poorly understood and the MlotiK1 CNB domain is a good model to investigate it.

The main objectives of the present project are:

- To define the molecular determinants of ligand selectivity in MlotiK1 CNB domain.
- To visualize the cAMP-induced conformational change in the full length channel.

2. Inverting ligand selectivity in MlotiK1 (Paper I)

In the present section, a study on the molecular determinants of ligand selectivity in the MlotiK1 channel is described.

2.1. Introduction

The function of cyclic nucleotide dependent effectors is partly determined by the ligand selectivity properties of the CNB domain. These properties have not been completely characterized. One of the difficulties in the study of ligand selectivity is to distinguish the effects related to binding of nucleotide from the effects that are related to efficiency of ligand in fuctional activation. In this study, this difficulty has been overcome by studying the isolated CNB domain. The amino acids of the CNB domain binding pocket that specifically affect binding of either cAMP or cGMP are critical for ligand selectivity. Using site-directed mutagenesis and a fluorescence-based binding assay, we have screened a comprehensive set of point mutations in the binding pocket residues known to interact with the nucleotide base. From the single mutants tested, we generated a triple mutant, which displayed inverted ligand selectivity, so that the mutant has higher affinity for cGMP than for cAMP. This triple mutant was structurally and functionally characterized.

The binding pocket of CNB domains consists of a shallow cavity formed by side chains from several structural motifs, which are the β4-β5 hairpin, the αP helix, the PBC region and a lid, which in MlotiK1 is formed by αC helix (Fig. 2.1 A). Inspection of crystal structures of the MlotiK1 CNB domain binding pocket in complex with cAMP or cGMP shows the residues that interact with the ligand base. V282 and T284 in the β4-β5 hairpin, R348 in the lid of the αC helix, M299 in αP helix and F296 and S308 in the PBC. Comparing the structures in complex with cAMP and in complex with cGMP, the most obvious difference is in another residue in the β4-β5 hairpin: V288, which establishes van der Waals interactions with cAMP (Fig. 2.1 B), but not with cGMP (Fig. 2.1 C), making it a promising candidate in our search for determinants of ligand selectivity. Nevertheless, the other residues in the binding pocket were also explored, except F296, since it is highly conserved and therefore is probably not involved in ligand discrimination.

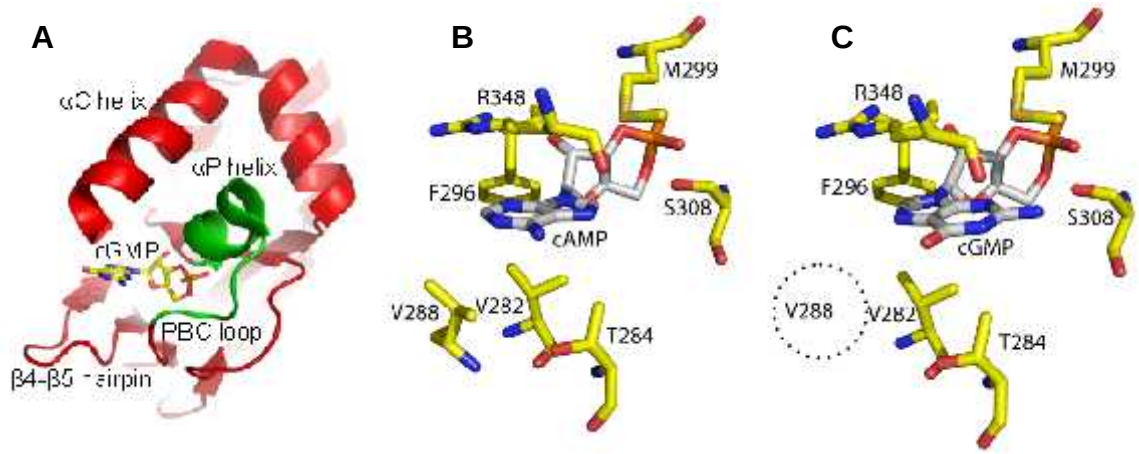

Figure 2.1: Cyclic nucleotide binding to the MlotiK1 CNB domain. (A) The CNB domain structural elements (in red and green) that form the ligand binding pocket are indicated. cGMP is shown as stick. (B) and (C) Residues interacting directly with ligand bases in the MlotiK1 CNB domain crystal structures bound to (B) cAMP (PDB code: 1VP6) and (C) cGMP (PDB code: 3CL1). Dotted circle indicates that V288 is not one of the residues interacting with cGMP.

2.2. Materials and methods

2.2.1. Expression and purification of ligand-free MlotiK1 CNB domain mutants

MlotiK1 CNB domain mutants were expressed and purified as described previously (Clayton et al., 2004). Phosphate-buffered saline (PBS) buffer containing 2 mM dithiothreitol (DTT) (purification buffer) was used throughout purification. Size-exclusion chromatography was performed in a Superdex 75 column (GE Healthcare). For preparation of apo-domain, freshly purified protein was incubated overnight with cAMP agarose beads (Sigma-Aldrich), and bound protein was extensively washed with purification buffer. cAMP-free protein was eluted by unfolding with purification buffer that included 3 M guanidinium chloride (unfolding buffer). cAMP removal was monitored by determining the OD_{260}/OD_{280} ratio, as described previously (Peuker et al., 2013). Typical values varied between 0.65 and 0.90 for nucleotide-free CNB domain. Protein was first diluted to 0.3 mg/ml with unfolding buffer and then diluted threefold into refolding buffer (100 mM NaCl, 10 mM sodium phosphate, pH 7.0, 5 mM glutathione [reduced], 0.5 mM glutathione [oxidized], 0.5 mM L-arginine and 10 mM EDTA) (Cukkemane et al., 2007) to a final concentration of 0.1 mg/ml protein and 1 M guanidinium chloride. This solution was

gently stirred at 4°C for 3 h, and then the protein was concentrated to ~0.3 mg/ml. The refolded protein was further dialyzed against refolding buffer to lower guanidinium chloride concentration to ~50 mM. Dialyzed protein was concentrated and loaded onto a Superdex 75 size-exclusion column to remove misfolded protein (Peuker et al., 2013) (folded protein elutes at 12.0–12.5 ml, and misfolded protein elutes at 16.0–17.0 ml). Finally, refolded apo-protein was dialyzed against 10 mM HEPES buffer, pH 7.5, and 100 mM NaCl before binding assays.

2.2.2. Cyclic nucleotide–binding assays

Dissociation constants (K_D) were determined at room temperature in 10 mM HEPES pH 7.5, and 100 mM NaCl, with a fluorescence assay that uses the fluorescent nucleotide analogue 8-NBD cAMP (Biolog) (Cukkemane et al., 2007; Altieri et al., 2008). Cyclic nucleotides (cAMP and cGMP [both from Sigma-Aldrich]), were purchased as acids or as sodium salts. For each mutant, the K_D of the fluorescent analogue was determined by titrating 50 nM 8-NBD cAMP with increasing protein concentrations and collecting fluorescence emission spectra (excitation at 471 nm) in a spectrofluorometer (Fluoromax-4; Horiba Scientific). For each protein concentration tested, emission at 536 nm was normalized as described previously (Altieri et al., 2008), and data were fitted with the following equation:

$$y = \frac{1}{1 + \frac{2}{-1 - \frac{L}{K} + \frac{P}{K} + \sqrt{\left(1 + \frac{L}{K} - \frac{P}{K}\right)^2 + 4 \times \frac{P}{K}}}},$$

where y is the normalized fluorescence intensity, K is the dissociation constant of 8-NBD cAMP, P is protein concentration, and L is 8-NBD cAMP concentration. For determination of the dissociation equilibrium constants of cAMP or cGMP, the above assay was repeated in the presence of a competing fixed concentration of cAMP or cGMP in each sample. For determination of the competing concentration, the protein concentration that resulted in 70–80 % of the maximum signal was selected and titrated with increased ligand concentrations. The ligand concentration that decreased the signal to 40–50 % was then chosen for the competition assay. Data were fitted with the following equation:

$$y = G \times L1 \times \frac{2\sqrt{a^2 - 3b}\cos\left(\frac{c}{3}\right) - a}{3K1 + 2\sqrt{a^2 - 3b}\cos\left(\frac{c}{3}\right) - a} + y0,$$

where:

$$a = K1 + K2 + L1 + L2 - P$$

$$b = K2(L1 - P) + K1(L2 - P) + K1K2$$

$$c = \arccos\frac{-2a^3 + 9ab + 27K1K2P}{2\sqrt{(a^2 - 3b)^3}},$$

where y is the fluorescence intensity, $K1$ is the dissociation constant of 8-NBD cAMP, $K2$ is the dissociation constant of cAMP or cGMP, $L1$ is the 8-NBD cAMP concentration, P is total protein concentration, $L2$ is total concentration of cAMP or cGMP, G is signal gain, and $y0$ is signal offset. For mutants displaying 8-NBD cAMP dissociation constants higher than 5 µM, a modified assay was used (Altieri et al., 2008). The concentrations of the protein and 8-NBD cAMP were fixed at approximately the K_D value and two times the K_D value, respectively, and titrated with increasing cAMP or cGMP concentrations. Data were fitted with the previous equation but with a varying cyclic nucleotide concentration.

The effect of point mutations on ligand binding was screened using the isolated CNB domain. The approach was a binding assay that uses the fluorescent cAMP derivative 8-NBD cAMP (Biolog). It is well known the the local environment has important effects on fluorescent molecules (Lakowicz, 2006). The intrinsic fluorescence of 8-NBD cAMP is enhanced upon protein binding (Kraemer et al., 2001). For determination of the dissociation constant (K_D) values of each CNB domain mutant for cAMP and cGMP, the first step was a protein titration at a fixed concentration of 8-NBD cAMP, usually 50 nM. Affinity for 8-NBD cAMP varied among the mutants screened, resulting on different ranges of protein concentrations required for saturation. If saturation occurs at relatively low (1-2 micromolar) protein concentrations, the mutant has high affinity for the cAMP analog (Fig. 2.2 A). If saturation requires higher protein concentration (tens of micromolar), the mutant has low affinity for the analogue (Fig. 2.2 B). We used different approaches for each of these two groups, as described below.

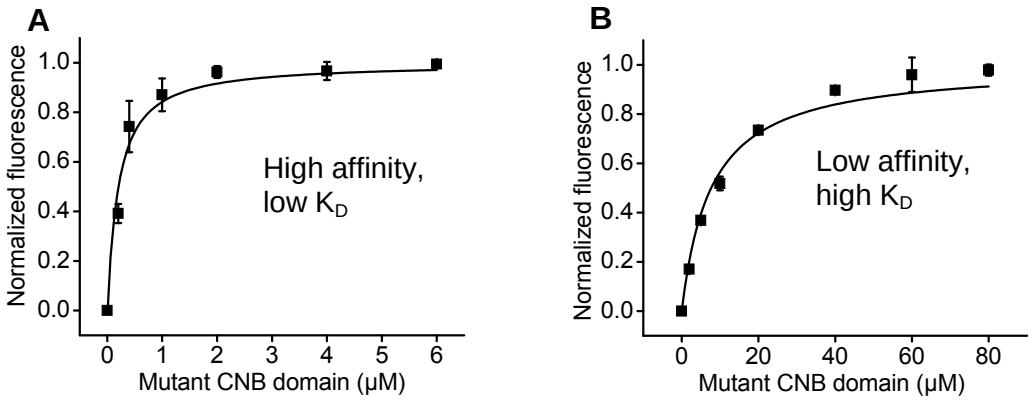

Figure 2.2: Titrations of MlotiK1 CNB domain with 50 nM 8-NBD cAMP (A) T284S and (B) R348A mutants. Determined K_Ds were 212 ± 22 nM and 7673 ± 818 nM for T284S and R348A, respectively.

2.2.2.1. High affinity mutants

For high affinity mutants, K_Ds for cAMP and cGMP were determined by repetition of the protein titration with 8-NBD cAMP in the presence of a fixed concentration of cAMP or cGMP. Using the T284S mutant as an example, the procedure used was the following. To determine the concentration of cAMP or cGMP to add to the protein titration curve, first, the fluorescence titration curve is analyzed to identify the protein concentration that resulted in approximately 70-80 % of the maximum signal (indicated by arrow in Fig. 2.3 A). Second, the protein concentration is fixed at that value and mixed with the fluorescent analogue. Incresing concentrations of cAMP or cGMP are added (Fig. 2.3 B), so that fluorescence decreases. The ligand concentration that results in a decrease of the signal to 40-50 % (indicated by arrows in Fig. 2.3 B) is chosen for the assay. The final titration involves adding increasing amounts of protein to a mix of fluorescent cyclic nucleotide analogue with cyclic nucleotide at the concentration determined in the previous step. The competition effect is evident when the binding curves in the absence and presence of cAMP or cGMP are superposed, as saturation is reached at higher concentrations of protein in the presence of non-fluorescent ligand (Fig. 2.3 C). The K_D for 8-NBD cAMP is determined (Fig. 2.3 D) and its value is used to calculate the K_Ds for cAMP (Fig. 2.3 E) and cGMP (Fig. 2.3 F), taking into account ligand concentrations.

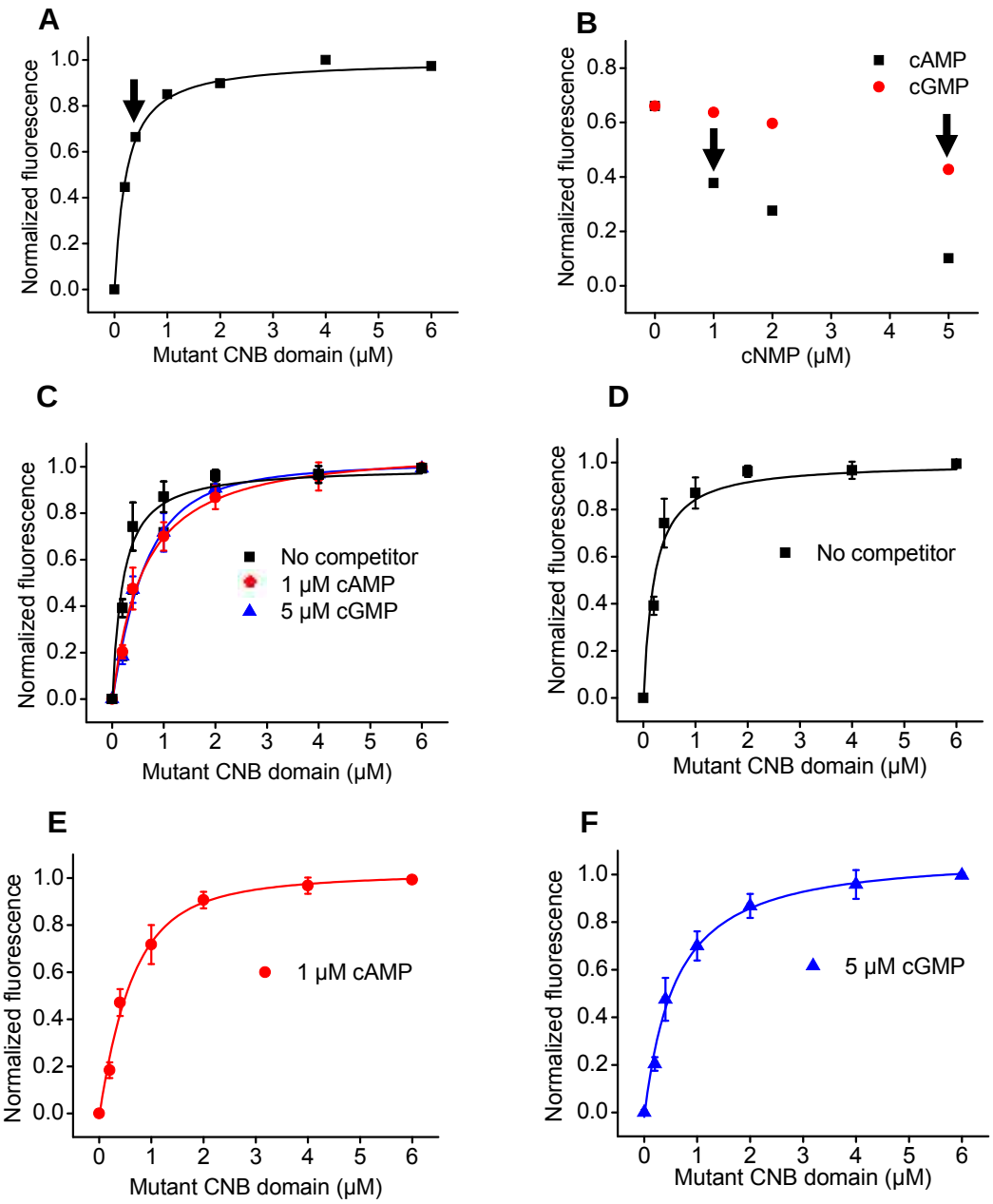

Figure 2.3: Determination of the K_D for cAMP and cGMP in MlotiK1 CNB domain T284S. (A) Initial protein titration with 50 nM 8-NBD cAMP. The protein concentration used in (B) was determined and is indicated by arrow. (B) Competition between 50 nM 8-NBD cAMP and different concentrations of cAMP or cGMP for binding to 400 nM MlotiK1 CNB domain T284S. Concentrations of cAMP and cGMP chosen for the final tritration are indicated. (C) Superposition of the protein titration curves in the absence and in the presence of 1 μM cAMP and 5 μM cGMP. (D) Final titration curve for determination of the K_D for 8-NBD cAMP, 212 ± 22 nM. (E) and (F) are the final titration curves for determination of the K_Ds for cAMP (E) and cGMP (F), 464 ± 58 nM and 2984 ± 379 nM, respectively. These were performed in the presence of the indicated concentrations of non-fluorescent ligand.

2.2.2.2. Low affinity mutants

For low affinity mutants, the procedure described above could not be used reliably, due to the high protein concentrations required to reach saturation. The alternative approach used was fixing protein concentration and increasing the concentrations of cAMP or cGMP. The procedure is exemplified for R348A. The K_D for 8-NBD cAMP is determined from a triplicate binding curve (Fig. 2.4 A), as described above. Then, protein and 8-NBD cAMP concentrations are fixed at one and two-fold of the K_D determined, respectively and the concentrations of cAMP (Fig. 2.4 B) or cGMP (Fig. 2.4 C) are varied. From each curve, K_D for cAMP or cGMP is determined taking into account the K_D for 8-NBD cAMP and ligand concentrations.

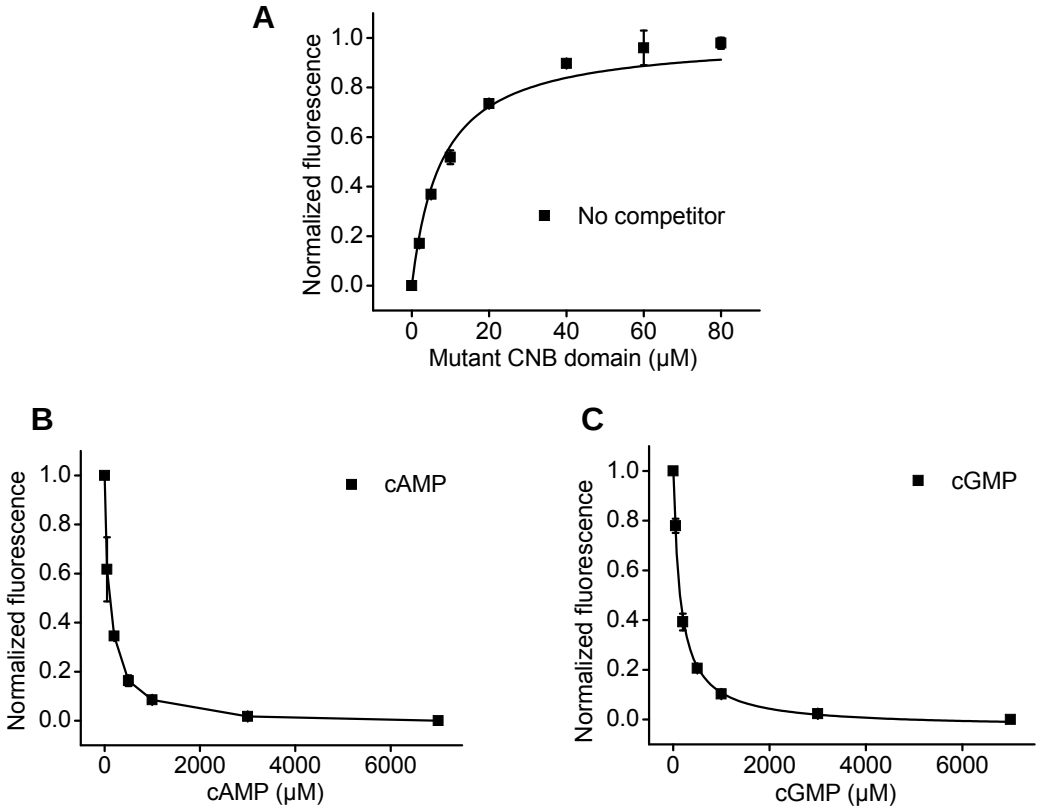

Figure 2.4: Determination of the K_Ds for cAMP and cGMP in the R348A CNB domain mutant. (A) Triplicate protein titration with 50 nM 8-NBD cAMP, for determination of the 8-NBD cAMP K_D, 7.7 ± 0.5 µM. Triplicate titration of (B) cAMP or (C) cGMP at 10 µM R348A and 20 µM 8-NBD cAMP. K_D values of 24.8 ± 3.2 µM and 38.8 ± 2.4 µM were determined for cAMP and cGMP, respectively.

2.2.3. Expression and purification of full-length MlotiK1 channel

Full-length MlotiK1 T284S/V288S/A352D was expressed, purified, and reconstituted as described previously for the wild-type channel (Clayton et al., 2004; Nimigean et al., 2004). In brief, MlotiK1 expressed in C41 (DE3) cells was extracted at 4°C for 30 min with PBS buffer, pH 7.4, containing 50 mM n-decyl-β-D-maltopyranoside (DM; Anatrace), 200 µM cAMP, 5 mM β-mercaptethanol. During purification and until gel filtration, the same buffer was used, but cAMP was excluded and the DM concentration decreased to 5 mM, unless stated otherwise. Detergent-extracted proteins were incubated with nickel beads and first washed with 50 mM imidazole to remove nonspecifically bound proteins, followed by a 200-ml wash in 2 mM DM. This ensured that cAMP bound to the triple mutant channel, which has micromolar affinity for cAMP, would dissociate from the protein. MlotiK1 was eluted in 500 mM imidazole and further purified by gel filtration on a Superdex 200 column (GE Healthcare) equilibrated in 20 mM Tris-HCl, pH 7.5, 150 mM KCl, 5 mM DM, and 3 mM DTT. Protein was immediately reconstituted in the presence of different ligand concentrations.

2.2.4. Liposome reconstitution and radioactive uptake assay

Proteoliposome preparation followed previously described procedures (Clayton et al., 2004; Nimigean et al., 2004; Altieri et al., 2008). In brief, 7.5 µg MlotiK1 protein was mixed with 1.5 mg *Escherichia coli* polar lipids (Avanti Polar Lipids, Inc.) in 10 mM HEPES, 5 mM N-methyl-β-D-glucamine (NMG), pH 7.6, and 150 mM KCl for a total volume of 150 µl. The detergent was removed by hydrophobic adsorption using Bio-Beads SM-2 (Bio-Rad Laboratories). Samples were gently stirred for 1 h at room temperature at a Bio-Beads/detergent (wt/wt) ratio of 10-15. This step was repeated twice and followed by an overnight incubation at 4°C with at a Bio-Beads/detergent (wt/wt) ratio of 20-30. Proteoliposomes were not frozen at any stage. A potassium concentration gradient was established by exchanging the external buffer to 10 mM HEPES, 5 mM NMG, pH 7.6, 20 µM KCl, and 150 mM sorbitol (sorbitol buffer) in the presence of the appropriate cAMP or cGMP concentrations, using spin columns. Uptake assays (Nimigean, 2006) were started by mixing one third of the final reaction volume of buffer-exchanged proteoliposomes with two thirds of sorbitol buffer containing 5 cps/µl $^{86}Rb^{+}$ (PerkinElmer) and the appropriate ligand concentration. Uptake was monitored after 90 min in 100-µl aliquots and normalized as described previously (Nimigean, 2006). Normalized uptake by MlotiK1

reconstituted into liposomes was plotted as a function of ligand concentration and fitted with the following Hill equation:

$$y = \frac{x^n}{k_{1/2} + x^n},$$

where y is the normalized uptake, x is the ligand concentration and n is the Hill coefficient. The $K_{1/2}$ of activation was determined.

2.2.5. Purification and crystallization of T284S/V288S/A352D mutant CNB domain

Expression and purification of T284S/V288S/A352D CNB domain was performed as described previously for the wild-type domain (Clayton et al., 2004). For nucleotide removal, the protein bound to GST beads was washed with 200 ml buffer (PBS buffer containing 3 mM DTT) before incubation with thrombin. Size-exclusion chromatography was performed on a Superdex 75 column equilibrated in 10 mM Tris, pH 7.0, 100 mM NaCl, and 4 mM DTT. Crystals of T284S/V288S/A352D mutant domain were grown using the vapor diffusion method in 24-well hanging-drop trays with a 500-µl reservoir solution of 0.15 M sodium citrate, pH 5.6, 0.9 M ammonium sulfate, and 100 mM lithium sulfate. Protein at 10 mg/ml was combined with cGMP (final concentration of 1.5 mM) and mixed with the reservoir solution at a 1:1 ratio for a final drop volume of 4 µl. Crystals appeared within 10 d at 25°C. Crystals were cryoprotected in well solution supplemented with 25 % glycerol and 1.5 mM cGMP before flash cooling in liquid nitrogen. Diffraction data were collected at 100 K at the beamline 14-4 of the European Synchrotron Radiation Facility (ESRF) and processed with XDS (Kabsch et al., 2010) and SCALA (Evans et al., 2006). Mutant CNB domain crystals grew in space group $P2_12_12_1$ with two molecules in the asymmetric unit. The structure of the mutant CNB domain–cGMP complex was solved by molecular replacement with Phaser (McCoy et al., 2007) using chain A of the cGMP-bound structure (Protein Data Bank accession no. 3CL1) (Altieri et al., 2008) as the search model. Model building and refinement were performed with Coot (Emsley et al., 2010) and Phenix (Afonine et al., 2012), respectively. Ligand restraints were generated using Phenix. Figures were generated using PyMOL software (Schrödinger, LLC).

2.2.6. Molecular dynamics (MD) simulations

Two models were defined as corresponding to the CNB domain of wild-type MlotiK1 and of the T284S/V288S/A352D mutant, respectively. The atomic coordinates of the wild-type domain were taken from the Protein Data Bank (accession number 3CL1) (Altieri et al., 2008). Residues 350–354 are missing in 3CL1, whereas their structure was solved in the mutant. Because these residues are close to the nucleotide-binding site, we decided to include them in both models. The initial structure of residues 350–354 in the wild-type domain was defined as an elongation of the αC helix. The final models included residues 320–354 for the wild-type CNB domain and residues 314–355 for the T284S/V288/A352 mutant domain. N and C terminals were acetylated and amidated. The default protonation state was assumed for all the ionizable residues, and histidine residues were protonated at the epsilon position. All of the water molecules that are present in the crystallographic structures were retained. The systems were solvated by ~6,000 water molecules, and the necessary number of chloride ions was added to guarantee electrical neutrality. The atomic models were first equilibrated in the NVT ensemble (600 ps), with harmonic restraints applied to all of the heavy atoms of the protein, of cGMP, and of the crystallographic water molecules. The harmonic restraints were gradually removed in the course of 10-ns equilibration trajectories in the NPT ensemble. Production trajectories of 100 ns followed. MD trajectories were simulated using NAMD version 2.9 (Phillips et al., 2005), with the CHARMM27 force field with CMAP corrections (MacKerell et al., 1998), and the TIP3P model for water molecules (Jorgensen et al., 1983). Pressure was kept at 1 atm by the Nosé–Hoover Langevin piston method (Martyna et al., 1994; Feller et al., 1995), with a damping time constant of 50 fs and a period of 100 fs. Temperature was kept at 300 K by coupling the system to a Langevin thermostat, with a damping coefficient of 5 ps^{-1} (Feller et al., 1995). Electrostatic interactions were treated by the particle mesh Ewald algorithm, with a grid spacing below 1 Å (Essmann et al., 1995). Van der Waals interactions were truncated at 12 Å and smoothed at 10 Å. Hydrogen atoms were restrained by the SETTLE algorithm (Miyamoto et al., 1992). A time step of 2 fs was adopted to integrate the equations of motion.

2.2.7. Energy calculations

The energy of binding, ΔG, is defined as:

$$\Delta G = G_{complex} - G_{protein} - G_{cGMP},$$

where $G_{complex}$, $G_{protein}$, and G_{cGMP} are the energies of the complex, the isolated protein, and the nucleic acid, respectively. These energies were estimated with the MM-PBSA approach, using the single-trajectory paradigm; i.e., the structures of complex, protein, and nucleic acid were taken from the same MD trajectory. As a general rule, the single-trajectory paradigm provides accurate energy estimates only if the ligands and the protein do not change structure upon binding. However, in this study, we are interested only in energetic differences between the wild-type and the triple mutant, and not in the absolute value of the binding energies. Therefore, a less stringent condition applies to MM-PBSA calculations with the single-trajectory paradigm. Even if the structure of the protein or of the ligand changes upon binding, the estimated difference in binding energy between the wild type and the mutant is still accurate, provided that these structural changes have similar energetic effects in the two systems. The free energy (G) of each species was calculated as:

$$G = E_{VDW} + G_{SA} + E_{COUL} + G_{PB},$$

where E_{VDW} is the van der Waals energy, E_{COUL} is the coulombic energy, and G_{PB} and G_{SA} are polar and apolar contributions to the solvation energy. The apolar contribution to the binding energy is given by the sum of E_{VDW} and G_{SA}, whereas the sum of E_{COUL} and G_{PB} defines the polar component of the binding energy. Solvation energies were calculated with the APBS software (Baker et al., 2001). The probe radius for the definition of the molecular surfaces was 1.4 Å. The relative dielectric constants were 80 and 2, respectively, for solvent and solutes. The apolar solvation energy was assumed proportional to the solvent-accessible surface area, with proportionality constant equal to 0.0072 kcal $mol^{-1}Å^{-2}$. Binding energies were calculated as average values over the 100 ns MD trajectories. The time series of the various energy terms was tested for the presence of correlation with the Ljung–Box lack of correlation statistical test with a confidence level of 95%, as described in Furini et al. (2013). A sampling period for the MD trajectories equal to 1 ns guaranteed lack of correlation among samples in the time series of all the energy terms. This lack of correlation is necessary for defining a safe (over) estimation of the standard error affecting the calculated binding energies.

2.3. Results

2.3.1. Single mutants

Using the assays described in section 2.2.2, the K_D values for cAMP and cGMP were determined for the set of single-point mutants listed in Table 2.1. As a control, we also determined the K_D values for the wild-type protein, obtaining 148 ± 22 nM and 1731 ± 264 for cAMP and cGMP, respectively. The CNB domain is 12-fold selective for cAMP (Table 2.1).

In the β4-β5 hairpin, we mutated three positions: V282, T284 and V288. Increasing the length of the V282 side chain, by mutating to a leucine decreased affinity for both ligands with no change in their selectivity. In T284, the mutation to serine resulted in a selectivity decrease relative to wild-type protein, 6-fold preference for cAMP (Table 2.1). The structural analysis of the wild-type domain bound to cGMP or cAMP (see above) suggested that V288 is the residue responsible for determining ligand selectivity (Altieri et al., 2008). Four mutations were generated at this position: alanine, leucine, isoleucine and serine. The first three mutants displayed decreased ligand selectivity, to about 6-fold. Interestingly, the mutation V288S decreased cAMP affinity by 8-fold with insignificant effect on cGMP, so that the domain is almost non-selective (Table 2.1).

In the αP helix, M299 was also mutated to cysteine and glutamine. In the first case, selectivity was slightly decreased and in the second, it increased slightly (Table 2.1).

The C-terminus contains a residue, A352, in a position shown to affect ligand selectivity in CNG channels (Varnum et al., 1995). In MlotiK1, it is not defined in the crystal structures (Clayton et al., 2004; Altieri et al., 2008) and is disordered in the NMR structures (Schunke et al., 2009; Schunke et al., 2011). Mutating this alanine to aspartate increased the affinity for cGMP 3-fold, with an insignificant effect on cAMP (Nimigean and Pagel, 2007). We generated two mutants at this position: A352S, which decreased selectivity to 4-fold and A352D, which decreased selectivity to 3-fold. In both cases, affinity for cGMP increased, with no effect (A352S) or a slight decrease (A352D) in cAMP binding affinity (Table 2.1).

In αC helix, R348 was mutated to five residues with different properties, but all had identical effects. They all severely decreased affinity and lowered selectivity to approximately 1-2-fold (Table 2.1). This shows that, at this position, the specific properties of arginine are essential for binding and discrimination between cAMP and cGMP.

Table 2.1: cAMP and cGMP dissociation constants (K_D) for the wild-type and single mutant CNB domain mutants.

Structural motif	Mutant	cAMP K_D (nM)	cGMP K_D (nM)	K_Ds ratio	N
	WT	148 ± 22	1731 ± 264	11.7	6
β4-β5 hairpin	V282L	1008 ± 53	8951 ± 743	8.9	3
	T284N	342 ± 41	6556 ± 633	19.2	3
	T284Q	731 ± 90	6952 ± 1312	9.5	3
	T284S	464 ± 58	2984 ± 379	6.4	6
	V288A	393 ± 50	2544 ± 355	6.5	3
	V288L	201 ± 19	996 ± 163	5.2	3
	V288I	138 ± 39	797 ± 118	5.8	6
	V288S	1205 ± 160	2105 ± 128	1.7	4
αP helix	M299C	501 ± 99	2942 ± 357	5.9	3
	M299Q	734 ± 134	11649 ± 2621	15.9	3
C-terminus	A352S	174 ± 23	727 ± 160	4.2	3
	A352D	256 ± 29	850 ± 121	3.3	6
αC helix	R348A	24822 ± 3182 *	38781 ± 2449 *	1.6	3
	R348N	19142 ± 507 *	32106 ± 3844 *	1.7	3
	R348Q	25097 ± 2216 *	46062 ± 5609 *	1.8	3
	R348K	16446 ± 842 *	23547 ± 982 *	1.4	3
	R348Y	24174 ± 2214 *	33172 ± 4771 *	1.4	3

K_Ds were determined as described for high affinity mutants, except those marked with a *, which were determined by the approach used for low affinity mutants. K_D ratio is calculated from cGMP K_D/cAMP K_D; n, number of repetitions.

2.3.2. Double mutants

Overall, our mutant screening analysis (Table 2.1) shows that, although some of the single mutants tested greatly reduce the CNB domain's selectivity for cAMP over cGMP, none of these mutations could invert selectivity. We decided therefore to combine mutations and to analyse their effect on the ligand binding properties. We first combined V288S, which caused a reduction in cAMP affinity by more than 8-fold, with A352S, which shows increased affinity for cGMP. This double mutant displays reasonably high affinity for both nucleotides (K_D cAMP: 690 ± 72 nM; K_D cGMP: 749 ±75 nM) but it still does not

show a preference for cGMP (Table 2.2). We then combined V288S with A352D, a single mutant that also showed increased affinity for cGMP. Strikingly, the double mutant V288S/A352D displayed a preference for cGMP over cAMP (~0.6x for cAMP) with K_D cAMP: 547 ± 111 nM and K_D cGMP: 351 ± 95 nM (Table 2.2).

Table 2.2: K_D values relative to cAMP and cGMP for CNB domain double mutants.

Mutant	cAMP K_D (nM)	cGMP K_D (nM)	K_Ds ratio	N
V288S/A352S	691 ± 72	749 ± 75	1.1	3
V288S/A352D	547 ± 111	351 ± 95	0.64	3

K_Ds were determined as described for high-affinity mutants. K_D ratio is calculated from cGMP K_D/cAMP K_D; n, number of repetitions.

2.3.3. A triple mutant with inverted ligand selectivity

2.3.3.1. Binding properties

To increase cGMP selectivity further, we combined the V288S/A352D double mutant with a mutation in another part of the ligand binding pocket. Although T284S decreases cGMP affinity slightly, it decreases cAMP affinity even more. As expected, the triple mutant T284S/V288S/A352D increases the preference for cGMP even further by decreasing cAMP affinity (K_D cAMP: 2190 ± 347 nM), while not affecting cGMP affinity (K_D cGMP: 336 ±126 nM) (Table 2.3). This results in a 6.5x preference for cGMP (0.15x for cAMP, for comparison with previous values). Binding affinities for inosine 3', 5'-cyclic monophosphate (cIMP) and cytidine 3', 5'-cyclic monophosphate (cCMP) were also determined for wild-type and T284S/V288S/A352D (Table 2.3). For each ligand, the variation in the K_Ds was within 2-fold, showing that the combination of the three mutations affects specifically the binding of cAMP and cGMP.

Table 2.3: Comparison of the K_D values of cAMP, cGMP, cIMP and cCMP for the wild-type and triple mutant CNB domain.

Mutant	cAMP K_D (nM) (n=6)	cGMP K_D (nM) (n=6)	K_Ds ratio	cIMP K_D (µM) (n=3)	cCMP K_D (µM) (n=3)
WT	148 ± 22	1731 ± 264	11.7	11.4 ± 1.8	78.6 ± 9.4
T284S/V288S/A352D	2190 ± 347	336 ± 126	0.15	20.0 ± 1.3 *	34.3 ± 4.9 *

K_Ds were determined as described for high affinity mutants, except those marked with a *, which were determined by the approach used for low affinity mutants. K_D ratio is calculated from cGMP K_D/cAMP K_D; n, number of repetitions.

2.3.3.2. Activity of MlotiK1 T284S/V288S/A353D in the full-length channel

Full-length MlotiK1 is studied through a radioactive uptake assay (Nimigean, 2006). In this assay, we used $^{86}Rb^+$, which also permeates through potassium channels.

The experimental setup is the following. Freshly purified potassium channel is reconstituted in liposomes in the presence of a high potassium ion concentration. Before the experiments, a potassium gradient is formed by passing the liposomes through a desalting resin equilibrated in a buffer solution where the potassium concentration is 7500-fold lower and replaced with sorbitol. The concentration gradient will drive potassium efflux out of the liposomes through the potassium channel. Potassium efflux creates an electrical gradient across the membrane, due to the excess of positive charges outside the liposomes. $^{86}Rb^+$ is then added and the electrical gradient will drive its uptake into the liposomes through the reconstituted potassium channel. Uptake is stopped by loading aliquots of liposomes to a cation exchange column that removes external $^{86}Rb^+$. Radioactivity inside the liposomes is then quantified in a scintillation counter and reflects the activity of the channel. However, reconstitution efficiency or liposome density may vary between experiments. Therefore, it is necessary to normalize the data for the total liposome volume accessible to the channels, by adding the potassium ionophore valinomycin, which renders all liposomes permeable to $^{86}Rb^+$ (Nimigean, 2006).

Using the $^{86}Rb^+$ uptake assay described above, activation of the triple mutant by the two ligands was compared. $K_{1/2}$ of activation of 0.58 ± 0.13 and 7.4 ± 3.3 µM were obtained for cGMP and cAMP, respectively (Fig. 2.5). These values contrast with the corresponding $K_{1/2}$ values of 0.92 ± 0.11 µM and 0.11 ± 0.02 µM for cGMP and cAMP in the wild-type (Altieri et al., 2008). This shows that the alterations in cAMP and cGMP affinities for the CNB domain are also reflected in channel function.

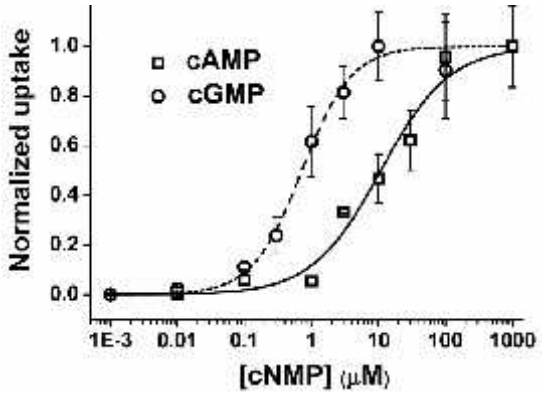

Figure 2.5: Functional analysis of MlotiK1 T284S/V288S/A352D using a $^{86}Rb^{+}$ uptake assay. Normalized uptake by channel reconstituted in liposomes as a function of ligand concentration (cGMP: circles, cAMP: squares) was fitted with a Hill equation (cGMP, $K_{1/2}$ = 0.6 ± 0.1 μM, Hill coefficient (n) = 1.3; cAMP: $K_{1/2}$ = 7.4 ± 3.3 μM, n = 0.84).

2.3.3.3. Crystal structure of MlotiK1 CNB domain T284S/V288S/A352D

To understand the molecular details behind the inversion of ligand selectivity, the X-ray crystal structure of the mutant CNB domain in complex with cGMP was determined by Dr. Fátima Fonseca, from our group. The assymetric unit contains two protein molecules that are identical except in the N-terminal linker, which occupies different positions. Superposing this structure with the wild-type structure in complex with cGMP reveals several differences. First, the αC helix extends to residues 354 or 355 (depending on the molecule considered); while in the previous structures the helix is disordered after residue 349. Second, the β4-β5 hairpin adopts a diferent conformation, collapsing towards the binding pocket (Fig. 2.6).

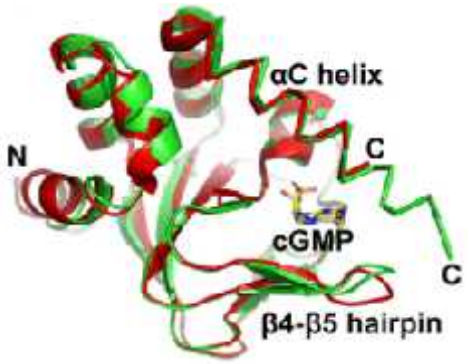

Figure 2.6: Superposition of triple mutant (green) and wild-type (red) CNB domain structures in complex with cGMP. Ligands are represented in stick and some structural elements of the binding pocket are indicated.

2.3.3.4. The binding pocket

The structure shows that D352 forms hydrogen bonds with the N1 and N2 groups of cGMP, explaining the gain in affinity for cGMP (Fig. 2.7 A). This is consistent with a crystal structure of the a mutant CNB domain from the HCN2 channel, which also shows an aspartate in an identical position forming identical hydrogen bonds with the nucleotide (Flynn et al., 2007). Interestingly, the two other substitutions, S288 and S284, have no direct or only long distance contacts with the ligand. Instead, they participate with water molecules in a hydrogen bond network that “bridges” the ligand to the S284, N286 and S288 residues of the β4-β5 hairpin. This network is formed by four water molecules (A to D) (Fig. 2.7 A), three of which were already present in the wild-type structure (Fig. 2.7 B).

Comparison of the binding pockets of MlotiK1 T284S/V288S/A352D and MlotiK1 wild-type clearly shows that in the wild type the water-mediated hydrogen bond network is much less extensive. It is formed only between the O6 and N7 atoms of the ligand and water molecules A, B and C (Fig. 2.7 B). The cGMP-selective binding pocket is therefore more hydrophilic than the cAMP-selective binding pocket.

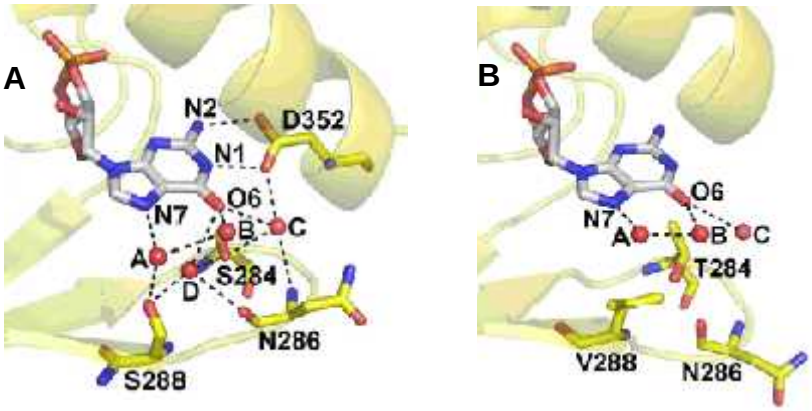

cGMP-selective cAMP-selective

Figure 2.7: Comparison of the binding pockets of MlotiK1 (A) T284S/V288S/A352D mutant and (B) Wild-type. cGMP and important residues in the binding pocket are represented in stick. Water molecules are represented by red spheres. The network of water-mediated hydrogen bonds is represented as black dashed lines.

2.3.4. Molecular dynamics simulations

To further explore the triple mutant crystal structure, our collaborator Dr. Simone Furini, from Siena University, Italy, performed molecular dynamics (MD) simulations. Both

the wild-type and triple mutant structures in complex with cGMP were used in this analysis. Results showed an interesting difference between both. While the wild-type structure remained essentially unaltered during the simulation time, in the triple mutant structure, the β4-β5 hairpin was shown to be mobile, alternating between three main conformations (Fig. 2.8). Such conformations are a closed one (Fig. 2.8 A), in which the β4-β5 hairpin moves towards the ligand base and residues S288, N286 and S284 establish direct interactions with the ligand, without obvious participation of water molecules. The second conformation, semiclosed, is quite similar to the crystal structure (Fig. 2.8 B). In the third conformation, open, the β4-β5 hairpin is clearly shifted away from the ligand base and the water content is higher, resulting in a larger water-mediated hydrogen bond network (Fig. 2.8 C). Importantly, the structural variability observed during the simulation is restricted to the β4-β5 hairpin, as the positions of the ligand and the αC helix are essentially unaltered (Fig. 2.8 D). These results suggest that due to crystal packing restrictions, the second conformation was selected among the three sampled by the domain during crystal formation. The MD simulations provide therefore a more complete picture of the dynamic structure of the triple mutant CNB domain in solution.

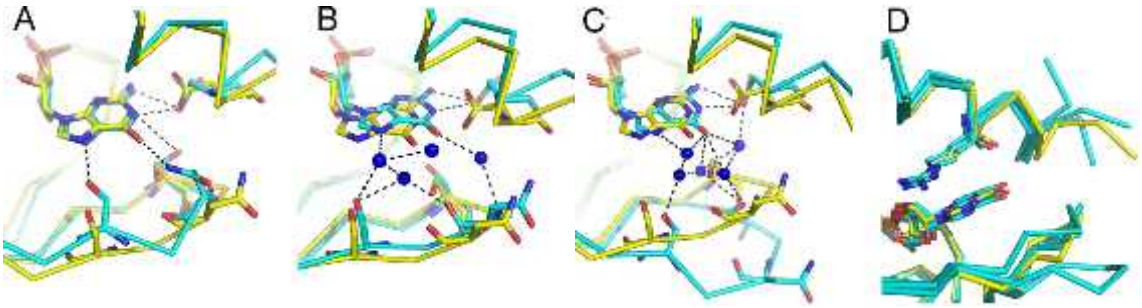

Figure 2.8: MD simulation conformations. View of the superposed ligand binding pockets from the triple mutant crystal structure (yellow stick) and from MD simulation snapshot models (cyan) in the (A) closed, (B) semiclosed and (C) open conformations. Structures are shown as Cα traces, with ligands in yellow (crystal structure) or cyan (MD simulation models). Only waters that mediate protein-ligand interactions are shown (as blue spheres). Dashed lines connect some of the atoms within hydrogen bond distance. D) Superposition of crystal structure and MD simulation snapshot structures in the difference conformations. View of the ligand binding pocket with cGMP and R348 shown as stick.

2.4. Discussion

Prior to this work, our understanding of the determinants of ligand selectivity in CNB domains was based on studies where a single point mutant inverted selectivity. It was clear also that these single point mutations were not sufficient to explain the selectivity in the majority of CNB domains. In this work, a large set of MlotiK1 CNB domain point mutants was tested for binding to cAMP and cGMP and their binding affinities were compared. As a control to use for comparison with the point mutants tested, binding affinities were also determined in wild-type MlotiK1 CNB domain. The domain is 12-fold selective for cAMP. None of the single mutants tested could invert ligand selectivity. The single mutants T284S, V288S and A352D were selective for cAMP; however they were less selective than the wild-type, with selectivity ratios of 6, 2 and 3, respectively. Inversion of ligand selectivity in MlotiK1 CNB domain was achieved through the combined effect of the three mutations T284S, V288S and A352D.

The crystal structure of T284S/V288S/A352D CNB domain showed a more hydrophilic binding pocket, with an extensive network of hydrogen bonds. D352 forms direct hydrogen bonds with the ligand base. The other two mutated residues, S284 and S288, also form hydrogen bonds with the ligand; however, those are mediated by four water molecules. These water molecules form “bridges” between polar groups of the cGMP base and polar groups of the residues S284, N286 and S288. MD simulations performed with this structure revealed three conformations of the binding pocket. The different conformations show the β4-β5 hairpin in different positions and a variable number of water molecules in the binding pocket. Taken together, the conformations show that the triple mutant, cGMP-selective binding pocket has increased flexibility in comparison to the wild-type. Such flexibility is determined by the increased mobility of the β4-β5 hairpin.

The crystal structure and the MD simulation results indicate two novel aspects that contribute to the increased affinity for cGMP in the triple mutant. One is the polar environment of the binding pocket, which results in polar interactions (direct or water-mediated) with the ligand base. This finding is supported by computational simulations that showed that dehydration should have a higher energetic penalty for cGMP than for cAMP (Zhou and Siegelbaum, 2007). The other aspect is the increased structural variability in the mutant, which suggests that higher entropy associated to the cGMP-bound state in the mutant also contributes to its higher affinity for the ligand. This unexpected factor contributes greatly for understanding the difficulty of predicting ligand selectivity in CNB domains by sequence analysis. Factors such as stabilization of water

molecules and flexibility of the binding pocket are not directly extracted from simple analysis of the amino acid sequence of the protein.

3. Visualizing the conformational change by atomic force microscopy (Paper II)

The present section describes a collaborative study of the conformational change induced by cAMP in full-length MlotiK1.

3.1. Introduction

The structures of the isolated CNB domain have revealed the different conformations of the bound and unbound states of the domain (Clayton et al., 2004; Altieri et al., 2008). How the CNB domain conformation changes in the full-length channel is still unknown. Atomic force microscopy (AFM) is a highly versatile technique for visualization of molecular surfaces and for studying conformational changes in membrane proteins. The use of AFM to study the conformational change in full-length MlotiK1 reconstituted into two-dimensional (2D) crystals is described in the present section. Before discussion of the results obtained, a brief introduction about AFM and 2D crystals will be presented.

3.1.1. The atomic force microscope (AFM) precursor: the scanning tunneling microscope (STM)

AFM evolved from STM (Binning, 1982). STM uses a sharp metallic tip to obtain structural information about the surface of a sample attached to a support. The principle is the following: an electric current can be generated between two electrodes of opposite charges if they are connected by a conductive material. However, when the distance between the electrodes is in the nanometer range, electrons can “jump” from one electrode to the other without any conductive material on the way. This phenomenon is called tunnel current. The intensity of such current decreases as the distance between the electrodes increases. STM is based on this phenomenon and the electrodes are the tip and the sample. The sample is scanned by the tip and the distance between them is kept constant in the nanometer range, to generate constant tunnel current (Binning, 1982) As the sample is usually not atomically flat, the tip position has to be permanently adjusted. Such adjustments can be converted into a surface profile of the sample. The technique was first tested on gold and $CaIrSn_4$ surfaces, allowing visualizing individual atoms for the first time (Binning, 1982). However, this technique has an important limitation: only conducting materials can be studied. Few years after its invention, STM was improved to overcome this limitation, and AFM was developed (Binnig et al., 1986). In both techniques, if the sample is static, the tip position is accurately adjusted. In STM it is to

keep tunnel current constant; in AFM it is to keep constant the force exerted by the tip over the sample surface, as there is physical contact between both (Binnig et al., 1986).

3.1.2. Operating principle of an AFM microscope

"About three decades ago few would have believed that a single atom could be visualized simply by touching it" (Frederix et al., 2009).

Prior to analysis, sample is adsorbed onto a chemically inert hydrophilic and flat surface by changing pH and/or ionic strength. The most appropriate materials are mica, molybdenium dissulfide, graphite, gold or platinum. They should be freshly cleaved before use, to ensure that they are completely clean (Frederix et al., 2009).

Essential components of any AFM microscope are a sharp tip mounted on the edge of a flexible cantilever, a laser and a laser detector that records laser deflection (Fig. 3.1). The tip contours the sample surface, applying a constant force over it in the piconewton (pN) range. The sample topography determines the amplitude of the cantilever oscillations. A laser beam is deflected by hitting a reflective surface on the cantilever backside. The laser deflection profile is therefore correlated to the sample topography. The microscope is also equipped with a piezoelectric scanner. Piezoelectric materials contract and expand very slightly depending on the voltage applied. The piezoelectric scanner, which can be attached to the sample support or to the cantilever, allows the tip position to be controlled very accurately in all three dimensions (Whited and Park, 2014).

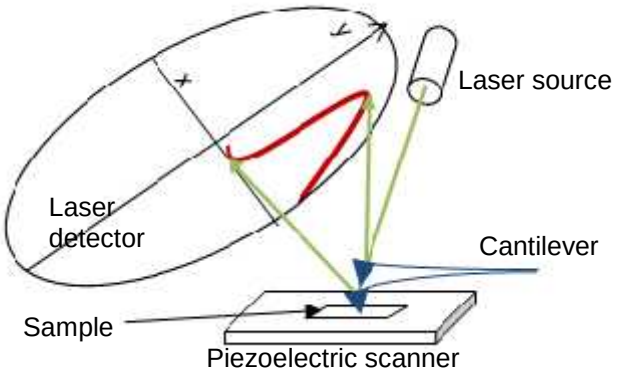

Figure 3.1: Schematic representation of the essential components of an AFM microscope (adapted from (Whited and Park, 2014).

The most important characteristics of a cantilever are its chemical composition and spring constant, which is a measure of its stiffness. The best cantilevers should be short and have low spring constants (Safenkova et al., 2012).

The instrument must be isolated from sound and vibrations (Fotiadis, 2012). There are two modes of imaging: contact mode and tapping mode. In contact mode, the tip is dragged over the sample surface and cantilever deflection is monitored. In tapping mode, the cantilever is oscillated so the tip touches the sample intermittently. In both modes, the amplitude of the cantilever oscillations is related to the sample height. Tapping mode is more adequate to avoid damage in fragile or loosely attached samples (Whited and Park, 2014).

An ideal sample for high-resolution AFM is a fairly flat surface containing shallow cavities. Deep and/or narrow clefts decrease the resolution limit, as they are difficult to penetrate and contour by the tip. Resolution is primarily determined by the tip dimensions. Lateral resolution is determined by the tip apex and vertical resolution by thermal fluctuations of the cantilever (Frederix et al., 2009). After being in contact with the sample, the tip gets contaminated with it, so it has to be replaced frequently.

Under AFM, samples are analyzed in their native aqueous environment. Standard deviations show not only the reproducibility of the height measurements but also the flexible regions of the molecules in the sample (Stahlberg et al., 2001).

3.1.3. The versatility of AFM

AFM is considered as the instrument of choice for studying native membranes structure, as well as conformational changes and dynamics of membrane proteins (Muller, 2008; Fotiadis, 2012). The AFM signal-to-noise ratio is superior to that of any optical microscopic technique (Muller, 2008) and this instrument is the only that allows imaging biological structures at nanometer resolution in a hydrated environment (Frederix et al., 2009).

Conventional AFM typically requires more than one minute for complete acquisition of an image (Picco, 2007) (Fotiadis, 2012). For visualization of rapid biological processes, high-speed AFM was developed. One of the solutions found was the simultaneous use of multiple cantilevers to generate composite images (Picco, 2007). The most common one is based on high-speed scanners and small cantilevers of high resonant frequency and low spring constant in tapping mode (Viani et al., 1999). Such approach allows very high scanning speeds and acquisition of a new image every 80 milisseconds (Ando et al., 2001).

The capabilities of AFM extend far beyond just making images. AFM is also used for studying intermolecular interactions and single-molecule force spectroscopy. The tip can be used to break chemical bonds, mechanically unfold proteins or dissociate complexes. The forces measured provide insights concerning the nature of the molecular interactions disrupted (Muller, 2008). In mechanical unfolding, the tip is pressed over an immobilized protein to form a chemical bond. Then, the tip is retracted and the protein is stretched, beginning to unfold. The graph of force produced by the cantilever as function of the retraction distance is known as the force spectrum. In these spectra, each peak represents the force required for unfolding a particular region of the protein, providing insights about the relative stability and conformational variability of each region. If a ligand has a stabilizing effect on the protein, force spectra obtained with and without the ligand can provide insights about the protein regions stabilized by a ligand (Whited and Park, 2014).

Despite other approaches, which characterize the binding properties in average, AFM is able, not only to visualize individual molecules, but also to measure individual intermolecular interactions (Whited and Park, 2014). This is particularly useful when the binding equilibrium under study is complex, with multiple binding or formation of complexes with variable composition. Some of the successful applications of AFM for studying molecular interactions were in the context of antigen-antibody, enzyme-inhibitor, nucleic acid-nucleic acid, or nucleic acid-protein interactions (Safenkova et al., 2012).

Recent developments are showing that the AFM microscope can still be improved, as well as sample preparation methods. Such improvements will increase even further its potential.

3.1.4. Some achievements brought by AFM: from photosynthesis to medicine

Shortly after its invention, the AFM microscope was shown to visualize molecules in solution (Drake et al., 1989). The first biological process visualized by AFM was thrombin-catalysed polymerization of fibrinogen into fibrin, which is involved in blood clotting. From 9 to 33 minutes after addition of thrombin, the gradual assembly of a fibre, followed by its increase in thickness could be clearly seen (Drake et al., 1989). Hepatic gap junctions, which are intercellular pores in the plasma membrane involved in cell-to-cell communication, were the first native structure to be disassembled and measured by AFM (Hoh et al., 1991). The opening and closing of gap junctions in both sides was shown by AFM to be stimulated by changes in pH (Muller et al., 2002; Yu et al., 2007).

The GPCR rhodopsin, involved in vision, is densely packed *in vivo*. AFM allowed visualization of the packed dimeric arrangement of these light receptors in native mouse rod membranes, providing clues about the mechanism of light transduction in vertebrates (Fotiadis et al., 2003).

Surfaces of membranes, obtained directly from cells or prepared in the lab, can be studied by AFM, as any nanometer scale structure that can be adsorbed onto an appropriate surface. Large molecules or supramolecular structures can be studied as well. AFM has revealed much about organization, complexes and biological processes of native membranes (Frederix et al., 2009). A remarkable example is the contribution to understand the structure, functional assembly, interactions and light adaptation of the photosynthetic machinery in purple bacteria (Liu and Scheuring, 2013)).

AFM can also monitor physical properties of individual living cells in real time and follow their dynamics after stimuli. AFM has medical applications and renal physiology is an exemplary case. The effect of antihypertensive compounds in kidney cells can be studied by measuring forces between a cell and the tip. It is possible to follow changes in mechanical properties, surface adhesion and stiffness of the cells before and after treatment (Jeong and Lee, 2012).

3.1.5. Two-dimensional crystals: a platform for AFM (and electron crystallography)

A membrane protein two-dimensional (2D) crystal is a planar assembly of a densely packed membrane protein arranged in a two dimensional lattice. The protein molecules are immersed in a phospholipid bilayer. These assemblies should be large, well-ordered and single-layered. For preparation of 2D crystals, freshly purified membrane protein is mixed with phospholipids (dissolved in detergent) at high protein to lipid ratios. Such high ratios prevent closure of phospholipid assemblies into vesicles, keeping them as planar bilayers and favouring formation of protein-protein contacts in the lattice. The crystals are formed by removal of the detergent, which can be done by different methods: dialysis, adsorption onto polystyrene particles (such as “BioBeads”) or dilution of the mixture (to dilute detergent below the critical micelle concentration) (Levy et al., 2001; Stahlberg et al., 2001).

2D membrane protein crystals can be studied not only by AFM, but also by electron crystallography. Importantly, the membrane protein is in its native lipid state. AFM allows imaging of the protein surface and its dynamics, providing insights concerning conformational changes and mechanism. Electron crystallography provides 3D or 2D

electron density maps. If 2D crystals of the same protein are analyzed by the two techniques, atomic structure and surface dynamics can be explored (Stahlberg et al., 2001).

3.2. Materials and methods

3.2.1. Protein expression and purification

Protein expression and purification were based on the procedure described previously (Clayton, 2009). Full-length wild type MlotiK1 was expressed in *E. coli* C41 (DE3) cells after induction (at OD_{600}, ~1.0) for 5 h with 0.3 µg/mL anhydrotetracycline (Fluka). Cells were lysed in PBS buffer, and membranes containing MlotiK1 were harvested by ultracentrifugation (257,000 g, 90 min). MlotiK1 was extracted from membranes with PBS buffer containing 25 mM n-decyl-β-D-maltopyranoside (DM), 5 mM β-mercaptoethanol, 200 µM cAMP. The histidine-tagged MlotiK1 was bound to Ni-NTA agarose beads (Qiagen) and eluted with 500 mM imidazole. The histidine tag was cleaved off with thrombin (HIT) and MlotiK1 was twice purified in a Superdex 200 (Amersham Pharmacia Biotech) size-exclusion chromatography column equilibrated in 20 mM Tris-HCl (pH 7.5), 150 mM KCl, 200 µM cAMP, 3 mM DTT, and 5 mM lauryldimethylamine-N-oxide (LDAO). The same procedure was used for the MlotiK1 R348A mutant, where the cAMP concentration was kept at 400 µM throughout purification (if not stated otherwise).

3.2.2. Reconstituting densely packed MlotiK1 membranes

MlotiK1 was reconstituted into lipid membranes forming densely packed assemblies using *E. coli* polar lipid extract (Avanti) as described previously (Clayton et al., 2009). Lipids were dissolved in 20 mM Tris-HCl (pH 7.5), 150 mM KCl, 200 µM cAMP, 3 mM DTT, 5 mM LDAO, and 60 mM n-octyl-β-D-glucopyranoside. Samples were prepared by mixing protein and lipids at the lipid/protein ratios (mg/mg) of 1.5, 1.6, 1.7, or 1.8 (final volume was 109–111 µL). Mixtures were incubated at 30 °C for 1 h with agitation. Membranes were formed by dialyzing the samples against 2 L of a solution composed by 20 mM Tris-HCl (pH 7.5), 50 mM KCl, 200 µM cAMP for the wild type channel and 600 µM cAMP for the mutant, 2 mM DTT, and 0.02 % sodium azide using Slide-A-Lyzer MINI Dialysis units (Thermo Scientific) with a 10 KDa cutoff. Dialysis was continued for 2–3 d at

31 °C. To prepare MlotiK1 channels without cyclic nucleotide, the membranes were formed in the presence of cAMP as described above, but then the dialysis buffer was changed for a dialysis solution without cAMP, and the dialysis was extended for 2 d at 31 °C. After this time, the temperature was changed to 20 °C, and the dialysis was continued for additional 7 d during which the cAMP-free dialysis solution was changed once. The expected nucleotide concentration after these dialysis steps was <300 pM for mutant and <100 pM for wt MlotiK1. These concentrations are well below the cAMP affinities of the channel (K_D (wild type), ~80 nM; K_D (mutant), ~18 µM). Fresh DTT was added every 2 d. Reconstituted membranes were stored at 4 °C until AFM analysis.

3.2.3. Radioactive flux assay

The $^{86}Rb^+$ uptake assay was performed as described previously (Clayton et al., 2004; Nimigean, 2006). Briefly, MlotiK1 was reconstituted in proteoliposomes in the presence of high concentration of K^+. K^+ was removed from the external solution, $^{86}Rb^+$ was added, and after incubating for 90 min, the radioactivity associated with the proteoliposomes was measured. Normalized radioactivity levels of liposomes where MlotiK1 was reconstituted was plotted as a function of ligand concentration and fitted with the following Hill equation:

$$y = \frac{x^n}{k_{1/2} + x^n},$$

where y is the normalized uptake, x is the ligand concentration and n is the Hill coefficient. The $K_{1/2}$ of activation was determined. The data presented here display decreased baseline noise by comparison with our previous study (Clayton et al., 2004). We attribute this to decreased contamination by other proteins, achieved by incremental improvements of multiple purification steps.

3.2.4. Atomic force microscopy

The AFM (Nanocope IIe; Veeco) was equipped with a fluid cell and oxide sharpened Si_3N_4 cantilevers (OMCL TR400PSA; Olympus) having nominal spring constants of ~0.09 N/m. Reconstituted MlotiK1 membranes were adsorbed onto freshly cleaved mica (Muller et al., 1997) in 200 mM KCl, 20 mM Tris-HCl (pH 7.5), and at cAMP concentrations indicated. After an adsorption time of ~30 min, the sample was gently rinsed with the imaging buffer to remove nonadsorbed membranes. Imaging buffer

solutions were either 50 mM KCl; 200, 600, or 900 µM cAMP; and 20 mM Tris-HCl (pH 7.5); or 50 mM KCl and 20 mM Tris-HCl (pH 7.5). All buffer solutions were freshly made using nano-pure water (18.2 MΩ/cm) and pro analysi (>98.5%) purity-grade reagents from Sigma and Merck. Upon buffer exchange, the AFM setup was thermally equilibrated for ~30 min. When changing cAMP-containing buffer for cAMP-free buffer, the sample was incubated for >3 h before imaging. High-resolution contact-mode AFM topographs were recorded at room temperature and at imaging forces of ~50 pN that do not to perturb the native membrane protein structure (Muller and Engel, 2007; Muller, et al., 1997). Imaging forces were manually adjusted to compensate for thermal drift (Muller and Engel, 2007). Proportional and integral gains were adjusted manually to minimize the error (deflection) signal and to maximize the height signal. When approaching a lateral resolution of ~2 nm, the scanning speed of the AFM stylus was between 500 and 1500 nm/s. To prove the reproducibility of the experimental findings, we repeated every experimental condition for wild type and mutant MlotiK1 in at least 12 independent experiments. In every experiment, we recorded between 20 and 60 AFM topographs of MlotiK1 membranes and channels. For every experimental condition, the statistical height analysis of MlotiK1 membranes was determined from membranes imaged in at least 12 independent experiments. All experiments conducted were consistent and showed that the height changes observed upon cAMP-binding and cAMP-unbinding of mutant MlotiK1 channels were fully reproducible.

3.2.5. Image processing and averaging

AFM topographs (512 × 512 pixels) were selected by the structural details of the reproducibly imaged MlotiK1 surface and when showing identical structural features in the simultaneously monitored trace and retrace scanning directions. Correlation averaging was performed using the SEMPER image processing system (Saxton et al., 1979; Saxton and Baumeister, 1982). Single particles were translationally and rotationally aligned to a reference MlotiK1 and averaged. This correlation average was used as a reference for refinement cycles. Correlation-averaged unit cells of the MlotiK1 tetramer were 4-fold symmetrized. To assess the standard deviation (SD), $\sigma_{k,l}$, individual unit cells were aligned angularly, as well as translationally, before single-particle averaging (Frank et al., 1988). The SD was then calculated from the averaged topograph $\mu_{k,l}$ for each pixel (k, l) for x^i particles:

$$\pm^{2}_{k,l} = \frac{1}{N}\sum_{i-1}^{N}\left(X^{i}_{k,l} - \ll_{k,l}\right)^{2}$$

SD maps are displayed as image in a one-to-one pixel correspondence with the correlation-averaged topograph.

3.3. Results

3.3.1. Visualizing the bound state

The 2D crystal samples, whose preparation was described above, were studied by our collaborators Dr. Stefania A. Mari and Dr. Daniel J. Müller at the Department of Biosystems Science and Engineering of the Swiss Federal Institute, in Basel, Switzerland. Samples prepared in the presence of cAMP were adsorbed onto mica plates and analyzed by AFM at room temperature in a buffered solution. Low resolution images show whole 2D crystals (Fig. 3.2 A). The largest ones had several tens of micrometers in length.

When samples were imaged at higher resolution, structural details became visible (Figs. 3.2 B to 3.2 D). The crystals are formed by rows of four-fold symmetric molecules that protrude 3.2 ± 0.5 nm above the lipid surface separated by rows of proteins with a shallow protein surface, protruding only 1.8 ± 0.5 nm (Fig. 3.2 B). Since MlotiK1 packs into 2D crystals in an alternate up and down orientation (Chiu et al., 2007; Clayton et al., 2009), the “tall” standing four-fold symmetric surfaces correspond to the cytoplasmic surface of the channel and the low lying surface corresponds to the extracellular surface of the channel (Fig. 3.2 B). The four-fold arrangement on the cytoplasmic surface are the CNB domains in the bound state, with a vestibule at the centre. The total height of MlotiK1 membranes measured above the mica surface was 10.2 ± 0.8 nm. The CNB domains protrude 3.2 ± 0.5 nm above the lipid surface and their total diameter is between 8 and 10 nm. These dimensions are consistent with previous structural data of MlotiK1 CNB domain (Clayton et al., 2004; Chiu et al., 2007). The vestibule has an inner diameter of approximately 1.5 ± 0.5 nm and a depth near 1.4 ± 0.3 nm.

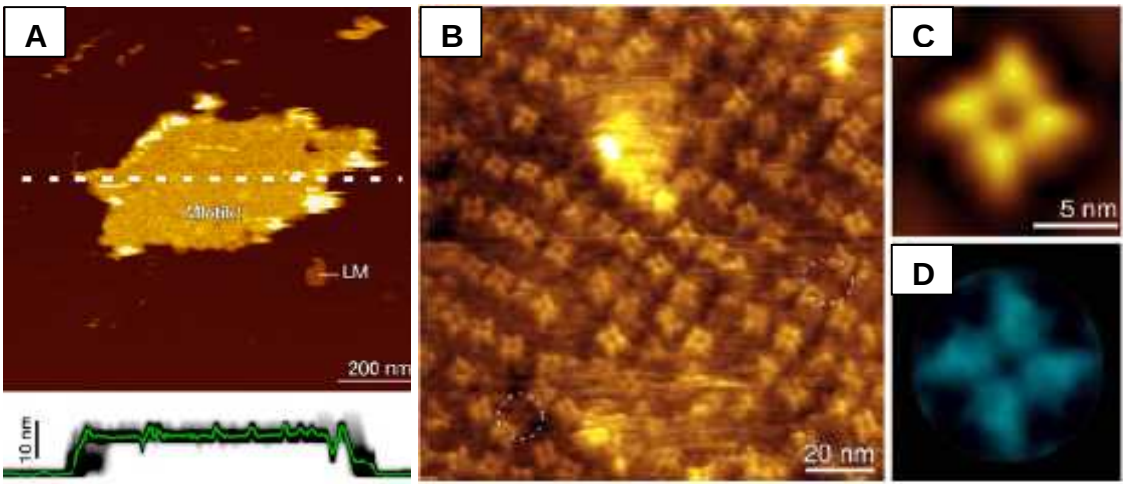

Figure 3.2: A densely packed lipid membrane containing wild-type MlotiK1 in the presence of cAMP. (A) Overview at low resolution. The brown background represents the surface of the mica plate where the sample was adsorbed. The sample is represented in yellow due to its height above the surface. “LM” refers to “lipid membrane”, a phospholipid bilayer without protein, whose height is lower in comparison to a membrane containing MlotiK1 and is therefore represented in light-brown. Below the image there is a height profile represented by a green line and respective standard deviation in black. The height profile was taken along the white dashed line. (B) High-resolution topograph of a crystal identical to the one shown in (A). In (B), each collored tetramer corresponds to a MlotiK1 channel imaged from the cytoplasmic side. Individual protrusions correspond to individual CNB domains. Two channels with the extracellular side facing the viewer are highligted with dashed circles. (C) and (D) average and standard deviation, respectively, of MlotiK1 channels with the cytoplasmic side facing the viewer.

3.3.2. R348A, a mutant with lower affinity for cAMP

After characterizing the bound state, we studied the unbound state. To do so, cAMP was excluded from the sample buffer by extensive dialysis. In contrast with previously electron crystallography studies (Clayton et al., 2009), extensive dialysis did not result in structural changes that could be visualized by AFM. We attributed this to the high affinity binding of cAMP (Cukkemane et al., 2007) and to the densely packed MlotiK1 molecules in the 2D crystals. We hypothesize that such fact increased the association rate of the ligand to the binding pocket, complicating its removal.

We overcame this problem by employing a point mutant with decreased affinity for cAMP. R348A was our choice, as its K_D for cAMP is approximately 200-fold higher (Cukkemane et al., 2007) and has a good purification yield. The choice of a lower affinity

mutant raised the question of whether the mutatant was functionally active. Using the radioactive flux assay described in the previous section, Stephen Altieri (at Yale University, New Haven, CT, USA) could show that the R348A mutant is still active in the presence of cAMP. Its $K_{1/2}$ of activation of 10.0 ± 4.4 µM is 100-fold higher in relation to the wild-type and its maximum activity under saturating cAMP concentration is lower, in comparison to the wild-type channel (Fig. 3.3).

After this study was completed, a recent report showed that the cAMP association rate is identical both in the wild-type and in R348A; however, the dissociation rate is over than 500-fold higher in the mutant (Peuker et al., 2013). This provides an explanation for the difficulty in removing cAMP from wild-type MlotiK1 in comparison to R348A.

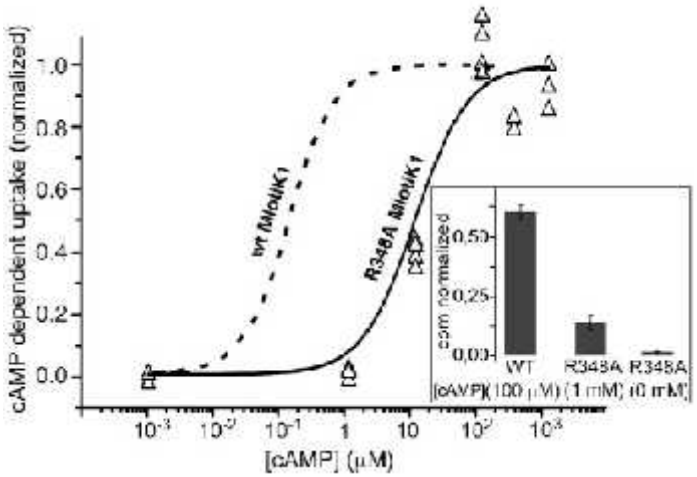

Figure 3.3: Functional analysis of MlotiK1 R348A using a $^{86}Rb^{+}$ uptake assay. Normalized uptake by channel reconstituted in liposomes as a function of cAMP concentration was fitted (solid curve) with a Hill equation, yielding a $K_{1/2}$ of activation of 10.0 ± 4.4 µM and a Hill coefficient (n) = 1.1 ± 0.6. The dashed curve illustrates the fitted curve for an identical analysis of wild-type MlotiK1, which has a $K_{1/2}$ of activation of 100 nM and n = 1.3. The inset shows normalized radioactivity values for wild-type and mutant MlotiK1 at saturating cAMP concentrations (100 µM for wt; 1 mM for R348A) or in the absence of cAMP (R348A, 0 mM). The wild-type data were taken from Clayton et al. 2004.

3.3.3. Visualizing the unbound state

The R348A mutant was assembled into 2D crystals in the presence of cAMP and imaged in the presence of 900 µM of ligand (a saturating concentration). Within the resolution attained, its topography was indistinguishable of that of the wild-type under the same conditons, with a total height of 10.2 ± 0.8 nm (Figs. 3.4 A to 3.4 C). This is

consistent with the fact that this mutant is functionally active. When cAMP was removed from the imaging solution and re-imaged after three hours, the membranes increased their heights in approximately 1.7 nm, protruding 11.8 ± 0.8 nm. Mutant membranes prepared in the presence of cAMP and extensively dialyzed against cAMP-depleted solution showed an even higher height of 13.5 ± 0.7 nm. While interpreting the height measurements, we took into consideration the fact that the total height measured varies whether cAMP is added or removed in only one or in the two sides of the sample. The ligand could not be added or removed to the CNB domains located on the side of the membrane that was adsorbed onto the mica plate. The unbound state visualized in R348A was quite different of the bound state: the CNB domains become totally unorganized, the vestibule disappears and the height of the CNB domains increases from the original 3.2 ± 0.5 nm by approximately 1.7 nm (Figs. 3.4 D to 3.4 F). No individual CNB domains or any sub-structure can be reproducibly identified. The height increase in the CNB domains in the unbound state could result from the conformational change induced by cAMP release from the binding pocket and also from a repositioning of the linker that connects the CNB domains to the transmembrane region. The “disappearance” of the vestibule could simply be a consequence of the increased structural variability or flexibility of the unbound state. The standard deviation of the unbound state is also larger than that of the bound state, consistent with its increased structural variability (Figs. 3.4 C and 3.4 F).

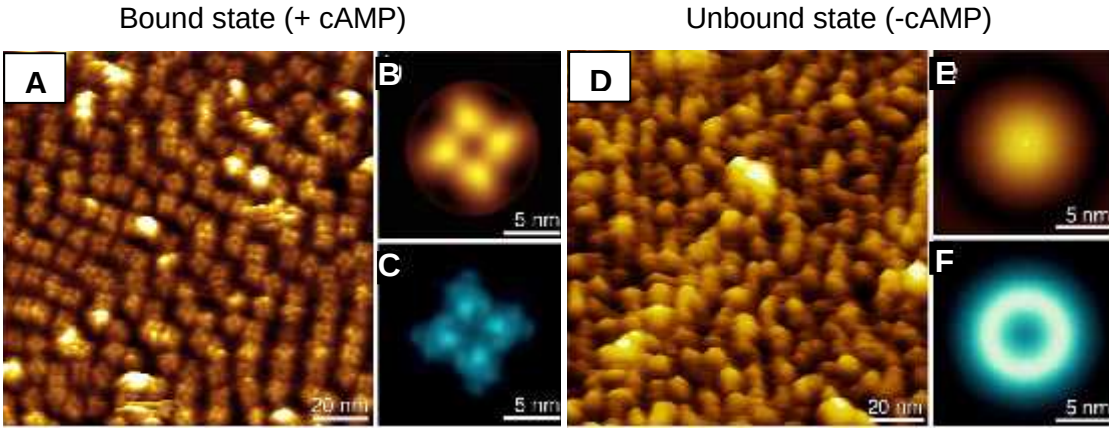

Figure 3.4: AFM images of MlotiK1 R348A-packed membranes in the presence (A to C) and in the absence (D to F) of cAMP. (A) and (D): membrane overviews; (B) and (E): average; (C) and (F): standard deviation.

3.3.4. The reversibility of the changes observed

Importantly, the observed structural changes in the CNB domains are reversible. A sample of R348A prepared in the presence of cAMP was imaged. CNB domains were organized in the four-fold arrangement (Fig. 3.5 A). When cAMP was excluded from the medium, they became unorganized (Fig. 3.5 B). When a saturating cAMP concentration of 900 µM was re-added to the medium, the four-fold arrangement was recovered in 99 % of the channels (Fig. 3.5 C). However, when the re-added concentration was 600 µM, which is high but not saturating, the bound conformation was recovered only partially (data not shown). After several repetitions of this experiment, it was concluded that the conformational change observed is reversible and cAMP-dependent. It is summarized in Fig. 3.5 D. In conclusion, cAMP binding has a clear effect in decreasing the structural variability of MlotiK1 CNB domains.

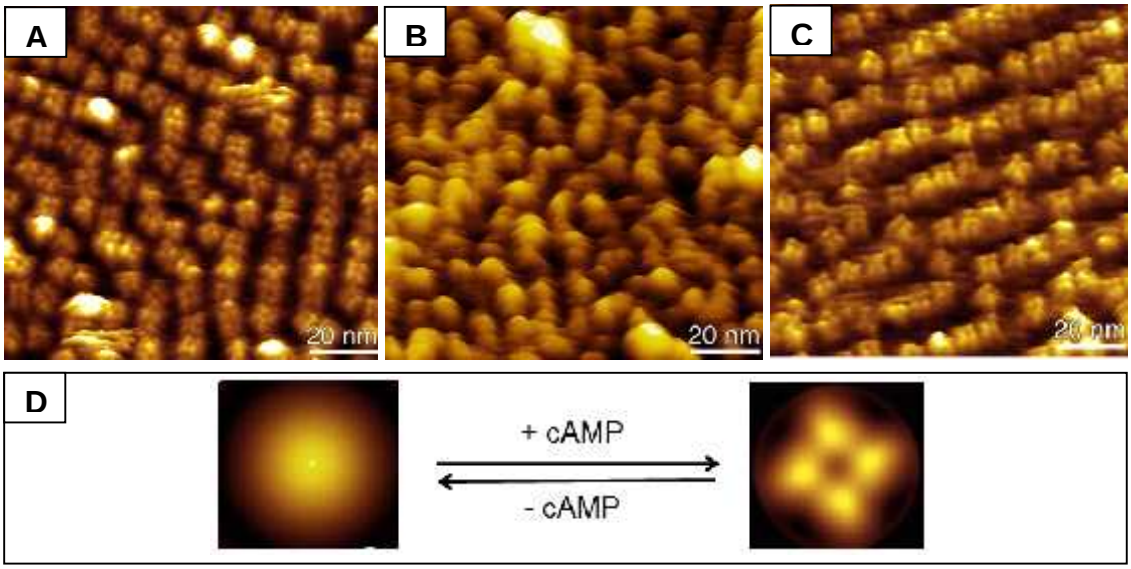

Figure 3.5: AFM images of MlotiK1 R348A-packed membranes prepared in the presence of cAMP (A) before, (B) after removal of cAMP and (C) after readdition of cAMP. (D) Schematic representation of the reversible change in MlotiK1 CNB domains arrangement induced by cAMP binding (+cAMP) and unbinding (-cAMP). Images are single particle averages.

3.4. Discussion

Our work has contributed significantly to understand the cAMP-dependent conformational change in MlotiK1. Using densely packed MlotiK1 membranes and AFM,

we could show that gating of MlotiK1 affects the arrangement of the CNB domains in the full-length channel. First, we imaged wild-type channel in the presence of cAMP. Under such condition, the CNB domains were found to be positioned in a four-fold arrangement, with a vestibule at the center. Removal of the ligand from solution did not result in any detectable changes in the wild-type protein, indicating that the ligand was tightely bound and extensive dialysis failed to remove it. The low affinity, functionally active R348A mutant was used to overcome this difficulty. This mutant was first imaged in the presence of cAMP. The CNB domins showed an identical arrangement to the wild-type channel. Ligand was then removed from solution by dialysis and an unexpected difference was found: the CNB domains have become totally unorganized and could not be visualized separately. No structural details could be identified in the absence of cAMP. Additionally, their total height of the CNB domains measured from the membrane surface increased. This transition, from an organized bound state to an unorganized unbound state, was found to be fully reversible and dependent on ligand concentration. Interestingly, the increase in structural variability in the unbound state has also been seen in the crystal structures of the isolated CNB domain (Clayton et al., 2004; Altieri et al., 2008). Using AFM, we could, for the first time, visualize the rearrangement of the CNB domains in an ion channel regulated by cyclic nucleotides. Such rearrangement provides insights regarding the cyclic nucleotide gating mechanism in this family of ion channels.

4. General discussion

In the present project, the MlotiK1 potassium channel was used as a model to explore the molecular features that determine ligand selectivity in CNB domains, as well as the conformational changes that occur upon ligand binding in cyclic nucleotide-regulated ion channels.

CNB domains are found not only in ion channels, but also in protein kinases, guanine nucleotide exchange factors and transcription factors (Rehmann et al., 2007). Some of these effector proteins are activated by cAMP, others by cGMP. For example, the eukaryotic guanine nucleotide exchange factor Epac and the prokaryotic transcription factor CAP are both activated by cAMP, CNG channels involved in vision are activated by cGMP, whereas CNG channels involved in olfaction are unselective (Kaupp and Seifert, 2002). Function of these cyclic nucleotide effectors is therefore dependent on their ligand selectivity. In the cell, this property confers the ability for similar proteins to be specifically activated by different cyclic nucleotides and therefore, by different signalling pathways. It is reasonable to assume that ligand selectivity is largely determined by molecular features of the CNB domain. These features are only partially understood.

To explore this property, we inverted ligand selectivity in the 12-fold cAMP-selective MlotiK1. To achieve this objective, we started by comparing crystal structures of MlotiK1 CNB domain in complex with cAMP and cGMP. These structures suggested residues that might affect ligand discrimination. A large set of single point mutations was generated in order to test different properties on such residues. None of the single mutants tested could invert ligand selectivity, but some had a mild effect in decreasing it. The V288S mutant became only about 2-fold selective. In T284S and A352D, selectivity was decreased to about 6 and 3-fold, respectively. These three mutations were combined and a triple mutant was generated, which was about 7-fold selective for cGMP. Although in an olfactory channel it was possible to invert ligand selectivity using a single mutant (Altenhofen, 1991), in our studies, only after combining three point mutations the same effect could be achieved.

The first studies of ligand selectivity in CNB domains were usually restricted to mutagenesis followed by a functional assay (Altenhofen et al., 1991; Varnum et al., 1995). In our study, this classic approach was complemented by structural and computational analyses of the CNB domain triple mutant, using X-ray crystallography and molecular dynamics (MD) simulations. The structural basis of the inversion in ligand selectivity was revealed by the T284S/V288S/A352D CNB domain crystal structure. The structure showed the molecular interactions between cGMP and the binding pocket. Whereas D352 establishes direct hydrogen bonds with the ligand, as predicted (Varnum et al., 1995), the two other mutated residues are involved in a water-mediated hydrogen bond network with cGMP. The combination of the three mutated residues changed the chemical character of

the binding pocket. Whereas the wild-type binding pocket was predominately hydrophobic (Clayton et al., 2004; Altieri et al., 2008), the triple mutant binding pocket showed an increase in its hydrophilic environment. The fact that the S284 and S288 residues establish interactions with the ligand that are not direct, but mediated by water molecules, was an unexpected finding. The β4-β5 hairpin, where S284 and S288 are located, was identified as a novel region in CNB domains involved in ligand selectivity.

Additionally and to overcome a common limitation of crystal structures, we performed MD simulations. Protein molecules are dynamic in solution, frequently displaying different conformations; however, during crystal growth, only one conformation is usually selected by the crystal lattice. Therefore, the crystal structures tend to show only one conformation in cases where multiple conformations are possible. To uncover such putative conformations, both wild type (cAMP-selective) and triple mutant (cGMP-selective) structures were studied by MD simulations. An additional difference was found. In the wild-type structure (in complex with cGMP), only one conformation was obtained, whereas in the triple mutant three different conformations were identified. Their basic difference was restricted to the β4-β5 hairpin, which was found to be highly flexible in the cGMP-selective structure. In our study, the crystal structure of the triple mutant CNB domain showed one conformation and the MD simulations were able to uncover other conformations. Together, these results have shown that the change in ligand selectivity from cAMP-selective to cGMP-selective involves not only and increase in the hydrophilic character of the binding pocket, but also an increase in flexibility of the β4-β5 hairpin. Such flexibility increase could not be predicted from the protein sequence. This fact helps to understand the difficulties in establishing general rules to define the determinants of ligand selectivity in CNB domains.

Our conclusions are corroborated by independent studies. Structural and functional studies in two HCN channels have shown that at least some of the residues that are determinants of ligand selectivity in MlotiK1 have conserved roles in ligand selectivity in CNB domains (Flynn et al., 2007; Zhou and Siegelbaum, 2007). The recent determination of the crystal structure of a cGMP-selective CNB domain from protein kinase G (Huang et al., 2014) is also of interest. The binding pocket is highly accessible to the solvent and there is an arginine at the position of V288 in MlotiK1. This arginine forms hydrogen bonds with cGMP, resembling the interactions with two water molecules found in the MlotiK1 CNB domain triple mutant structure. These features show that this highly cGMP-selective CNB domain also has a highly hydrophilic binding pocket. This fact supports our finding that a more hydrated binding pocket favors cGMP binding relative to cAMP. Of special interest is the fact that this structure does not have any residue at the

position of A352 in MlotiK1. Therefore, an aspartate at this position, although favourable, is not a universal requirement for cGMP-selectivity.

Besides ligand selectivity, another important aspect of cyclic nucleotide regulation in cyclic nucleotide regulated ion channels is the conformational change induced by the ligand. Crystal structures of the isolated CNB domain were determined in the absence and presence of cAMP (Clayton et al., 2004), showing the structural differences between both states in the isolated domain. How the conformational change affects the full-length channel was still unclear. The conformational change of cytoplasmic domains has been characterized in few potassium channels. Using spectroscopic approaches, it was shown that the cytoplasmic domains of the inwardly rectifier potassium channel KirBac3.1 have different positions in both states, being more separated and closer to the membrane in the open state (Gupta et al., 2010). In addition, functional studies have shown that the cytoplasmic RCK domain subunits of a BK calcium activated potassium channel also display well defined conformations in both states (Krishnamoorthy et al., 2005).

To study the cAMP-induced conformational change in full-length MlotiK1, we took advantage of the versatility of atomic force microscopy (AFM). AFM showed that in the presence of cAMP, the CNB domains were arranged in a symmetric four-fold arrangement, with a vestibule at the center. Using a low affinity, functionally active mutant, R348A, we were able to visualize a change in the arrangement of the CNB domains in the full-length channel that is ligand dependent. In the presence of cAMP, the mutant channel showed a similar arrangement of the CNB domains, which, within the resolution attained by AFM, is identical to the wild-type protein. In the absence of cAMP, large changes were observed. The CNB domains became unorganized and the distance that separates from the membrane leaflet increased. This transition between an organized bound state and an unorganized unbound state was found to be dependent on cAMP concentration, since it was reversible. In contrast with other potassium channels (Krishnamoorthy et al., 2005; Gupta et al., 2010), in MlotiK1, the unbound state does not have a well-defined conformation. We do not know if in other channels there are also unorganized conformations that are important for gating.

The recent determination of 3D structures of full-length MlotiK1 in the absence and presence of cAMP by electron crystallography (Kowal et al., 2014) provided information concerning the conformational change in the transmembrane region, complementing our study. The gating mechanism seems to involve a twist of the pore domain helices and a tilt and shift of the voltage sensor-like domains helices. However, it is not totally clear if the unbound state was really obtained. In both structures, the CNB domains are ordered and the height increase upon ligand removal is lower than in our AFM study. The method used to confirm the removal of cAMP from solution is not able to confirm the total removal of the

ligand from the protein. Removal of cAMP from wild-type MlotiK1 is frequently a slow and inefficient process. In our study, one week of dialysis with buffer changes failed to remove it. We overcame this issue by using the R348A mutant. Another limitation of the study by Kowal et al., (2014) concerns an advantage of AFM over electron crystallography. AFM provides single-particle images (which can be averaged), revealing the behavior of individual molecules.

The prokaryotic MlotiK1 is a model to understand cyclic nucleotide regulation in its eukaryotic relatives. An important difference between MlotiK1 and CNG or HCN channels is the length of the linker connecting the pore domain to the CNB domain. While in CNG and HCN channels it contains approximately 80 amino acids, in MlotiK1 it contains only about 20 residues (Clayton et al., 2008). This difference in length may partially affect the gating mechanism and represents a limitation of MlotiK1 as a model to understand this process in its eukaryotic homologues.

By exploring the molecular basis of ligand selectivity and conformational change, we gained insights concerning two essential aspects of ligand regulation in cyclic nucleotide activated ion channels. Since CNB domains are found also in other proteins and are highly conserved, the molecular basis of discrimination between cAMP and cGMP should be valid for other CNB domains, whether they belong to a protein kinase, a transcription factor, a nucleotide exchange factor or an ion channel.

5. Concluding remarks

In the present project, the bacterial cyclic nucleotide regulated potassium channel MlotiK1 was studied in the context of its ligand selectivity and conformational change.

Using MlotiK1 as a model, we reached a better understanding of the molecular determinants of ligand selectivity in CNB domains (Paper I). In addition to the regions of CNB domains known to determine discrimination between cAMP and cGMP, an additional region was identified: the β4-β5 hairpin. After screening a comprehensive set of point mutations in the binding pocket of this cAMP-selective CNB domain, we generated a cGMP-selective triple mutant domain. The crystal structure of the triple mutant CNB domain and molecular dynamics simulations showed a hydrophilic and more flexible binding pocket, especially in the β4-β5 hairpin. The polar character of the binding pocket was found to be essential for ligand selectivity. A more apolar binding pocket favours cAMP, whereas a strongly hydrophilic one favous cGMP.

Before the beginning of this project, our knowledge concerning the conformational change was restricted to the bound and unbound structures of the isolated CNB domain. AFM has shown that gating of the channel is correlated to large alterations in the orientation of the CNB domains (Paper II). They are organized in a four-fold arrangement in the bound state and unorganized in the unbound state. Importantly, the R348A mutant used to visualize the unbound state was shown to be functional. The alterations visualized by AFM were found to be reversible and dependent on cAMP concentration.

MlotiK1 has been an effective model channel for structural studies. This potassium channel has helped in our understanding of the molecular determinants of ligand selectivity in CNB domains. AFM provided insights concerning its conformational change. Our studies have contributed to better understand the molecular details of cyclic nucleotide regulation in a potassium channel.

6. Apendix

This final section describes three preliminary experiments.

6.1. Exploring the equilibrium between the bound inactive and bound active states of the CNB domain

Ligand binding induces a conformational change in a CNB domain. Nevertheless, the existence of two bound states with different conformations, bound active and bound inactive, is generally accepted. In the bound inactive state, the ligand is bound, but the protein conformation still corresponds to the unbound state; however, in the bound active state, the domain has undergone a change in conformation. The effect of two R348 (in αC helix) mutations in the equilibrium distribution between these two states was studied in the MlotiK1 CNB domain. The approach used was the comparison of cysteine accessibility in the CNB domain under different conditions. Accessibility was monitored using a cysteine-reacting probe and reaction kinetics were quantified in the absence of ligand and in the presence of saturating ligand concentrations. Differences in reaction kinetics are dependent on differences in cysteine accessibility, which are related to the average protein conformation at the experimental conditions.

6.1.1. 5,5'-dithiobis-(2-nitrobenzoic acid), DTNB

To measure the accessibity of different positions in the CNB domain we have adapted a spectrophotometric assay that uses 5,5'-dithiobis-(2-nitrobenzoic acid) (DTNB), also known as Ellman's reagent (Ellman, 1959). DTNB reaction is represented in Fig. 6.1. When DTNB reacts with a reduced thiol group, the compound is split in two. One half remains attached to the thiol group, while the other is released into solution. The latter has a higher absorbance at 412 nm than unreacted DTNB. Common applications of DTNB include quantification of glutathione in blood samples (Sedlak and Lindsay, 1968) and quantification of the number of cysteines in a protein (Riener et al., 2002). In proteins, the kinetics of reaction depends on the accessibility of the cysteine residue.

Figure 6.1: Representation of the reaction between DTNB and a reduced thiol group (R-SH).

6.1.2. Estimation of the percentage of saturation

For estimating the percentage of protein containing ligand (% saturation) at the ligand concentration used, a general protein-ligand binding equilibrium was considered. In a protein (P) and ligand (L) binding reaction, in which a protein-ligand complex (PL) is formed:

$$P + L \rightleftharpoons PL$$

K_D is given by:

$$K_D = \frac{|P|_{free}|L|_{free}}{|PL|}$$

Knowing that $|L|_{free}$ = $|L|_{total}$ - $|PL|$ and that $|P|_{free}$ = $|P|_{total}$ - $|PL|$, $|P|_{free}$ and $|L|_{free}$ can be replaced in the above equation:

$$K_D = \frac{\left(|P|_{total} - |PL|\right)\left(|L|_{total} - |PL|\right)}{|PL|}$$

Substituting the parameters K_D (previously determined), $|P|_{total}$ (10 µM) and the $|L|_{total}$ used, $|PL|$ can be determined. A $|PL|$ value between 9.90 and 9.99 µM will correspond to a % saturation of 99.0-99.9 %.

6.1.3. Data fitting

The time constant of each reaction was quantified by fitting an equation to the averaged curve, which was expressed in terms of absorbance (A) as function of time (t). An exponential decay is expressed by:

$$A = A_{\max} e^{-kt}$$

Where A_{max} is the maximum absorbance and k is the rate constant. Similarly, an exponential growth that tends to A_{max} is given by:

$$A = A_{\max}\left(1 - e^{-kt}\right)$$

The time constant τ is the inverse of k. Additionally, t was substituted by (t-t_0), since the initial absorbance value recorded was usually not zero. Data were fit with the following equation:

$$A = A_{\max}\left(1 - e^{-\frac{t-to}{2}}\right)$$

6.1.4. Validating the assay: C263V (αB helix) and C263V C331V M299C (αC helix)

MlotiK1 CNB domain has two cysteine residues, C263 and C331. Since C331 is located in the αB helix (Fig. 6.2 A), then, the C263V mutant can be used to monitor the cysteine accessibility at the αB helix. Importantly, C331 is more shielded in the bound state than in the unbound (Figs. 6.2 A and 6.2 B). Additionally, we generated the C263V C331V M299C mutant, which has a single cysteine, located close to the cyclic nucleotide (Fig. 6.2 B). Closing down of the αC helix upon ligand binding should decrease accessibility to M299C (Figs. 6.2 A and 6.2 B).

Cysteine accessibility of both mutants was probed with DTNB in the absence of ligand and in the presence of saturating concentrations of cAMP, cGMP, cIMP and cCMP. Time constants were determined (Table 6.1). For the two mutants described above, the reaction was faster in the unbound state than in the presence of each of the four ligands (Figs. 6.2 C and 6.2 D), as expected from structural data. This provides support for the use of this assay. cAMP, cGMP and cIMP have identical effects in the accessibility of αB and αC helices. Interestingly, the cCMP induced accessibility at αB and αC is not as reduced as with other nucleotides.

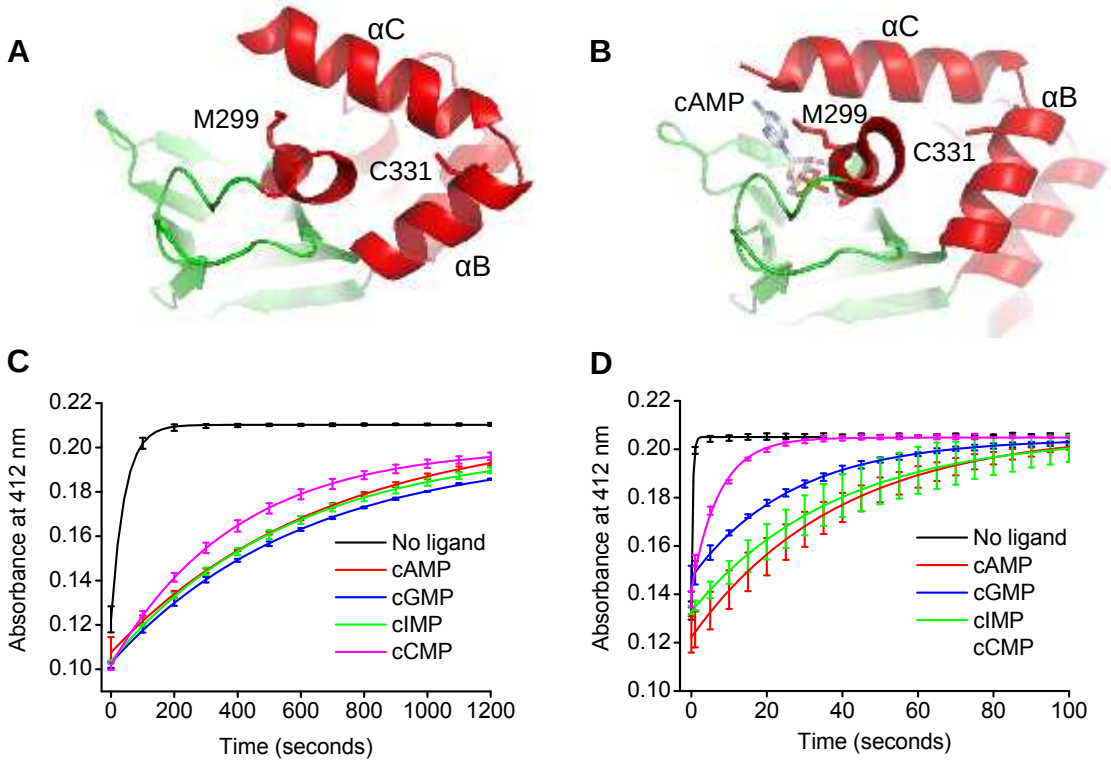

Figure 6.2: Accessibility alterations at C331 and M299. (A) and (B) Structures of MlotiK1 CNB domain in the (A) unbound and (B) bound states. In both structures, C331 and M299 are prepresented in stick. In (B), cAMP is also represented in stick. (C) and (D) DTNB reactions of (C) C263V and (D) C263V C331V M299C, for comparing accessibilities of C331 and M299, respectively. Cysteine accessibility in both mutants was monitored in the absence of ligand and in the presence of saturating concentrations of the cyclic nucleotides indicated below the curves.

Table 6.1: Time constants in seconds (n=3) for MlotiK1 CNB domain mutants.

Ligand	**Monitoring αB** C263V	**Monitoring αC** C263V C331V M299C
(no ligand)	42.0 ± 0.1	0.40 ± 0.02
cAMP	678.9 ± 0.7	37.7 ± 0.1
cGMP	629.0 ± 0.9	26.1 ± 0.1
cIMP	571.7 ± 0.6	38.5 ± 0.1
cCMP	398.8 ± 0.3	8.06 ± 0.05

6.1.5. The effect of R348 in the bound inactive and bound active distribution

The C263V mutation was combined with R348A and R348N. Accessibilities were compared in the unbound state and in the presence of cAMP or cGMP (Fig. 6.3) and time constants were determined (Table 6.2). In the unbound state, time constants are identical, 44.0 ± 0.5 seconds and 48.8 ± 0.2 seconds for C263V R348A and C263V R348N respectively. In the presence of cAMP, however, results were different, with time constant of 100.4 ± 0.2 seconds for R348A and 172.6 ± 0.5 seconds for R348N. With cGMP, time constants were again lower for R348A than for R348N, 46.4 ± 0.2 seconds versus 92.6 ± 0.8 seconds, respectively. In identical conditions, accessibility in the presence of ligands is higher in C263V R348A than in C263V R348N.

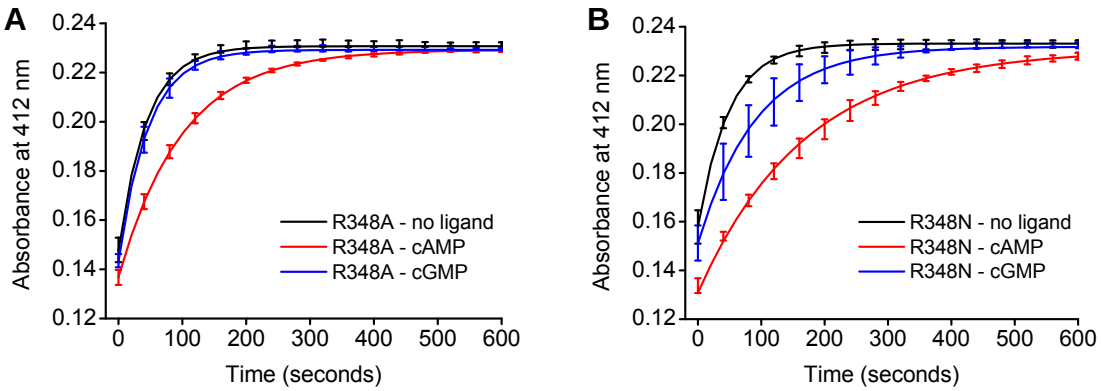

Figure 6.3: (A) and (B) DTNB reactions of (A) C263V R348A and (B) C263V R348N. In both mutants, accessibility of C263V was monitored in the absence of ligand and in the presence of saturating concentrations of the cyclic nucleotides indicated below the curves.

Table 6.2: Time constants in seconds (n=3) for MlotiK1 CNB domain mutants.

Ligand	C263V R348A	C263V R348N
(no ligand)	44.0 ± 0.5	48.8 ± 0.2
cAMP	100.4 ± 0.2	172.6 ± 0.5
cGMP	46.4 ± 0.2	92.6 ± 0.8

Considering that a binding equilibrium has three states: unbound, bound inactive and bound active:

Unbound ⇌ Bound Inactive ⇌ Bound Active

The equilibrium between unbound and bound states (active and inactive) is controlled by ligand concentration. However, the two bound states are different in terms of conformational change. In the bound inactive state, the ligand is bound, but the protein conformation still corresponds to the unbound state. In the bound active state, the domain has undergone a change in conformation. Due to their different conformations, the two bound states have different accessibilities. In the case of C263V R348A and C263V R348N, different accessibilities may result from a different distribution between the equilibrium positions of the bound inactive and the bound active states. Alternatively, they may have different static conformations between both states. C263V R348A appears to favour more the bound inactive state relative to the bound active than the C263V R348N mutant. With this simple accessibility assay, we could get insights concerning the effect of two R348 mutations in the equilibrium distribution between the bound inactive and bound active states.

Table 6.3: Ligand concentrations, K_D and % saturation used for each mutant.

	C263V			C263V C331V M299C		
	Conc.	K_D	% sat.	Conc.	K_D	% sat.
cAMP	80	0.057 ± 0.011	99.9	80	0.197 ± 0.036	99.7
cGMP	310	0.347 ± 0.031	99.9	310	2.241 ± 0.200	99.3
cIMP	2100	1.60 ± 0.069	99.9	2100	17.8 ± 2.1	99.2
cCMP	1500	8.17 ± 0.74	99.5	15000	135.0 ± 14.3	99.1

Concentrations and K_Ds (determined from triplicate measurements) are expressed in µM. K_Ds were determined by the method used for high-affinity mutants (described in section 2).

Table 6.4: Ligand concentrations, K_D and % saturation used for each mutant.

	C263V R348A			C263V R348N		
	Conc.	K_D	% sat.	Conc.	K_D	% sat.
cAMP	1900	29.6 ± 1.6	98.5	1900	16.8 ± 1.1	99.1
cGMP	2200	8.37 ± 0.63	99.6	2200	8.29 ± 0.84	99.6

Concentrations and K_Ds (determined from triplicate measurements) are expressed in µM. K_Ds were determined by the method used for low-affinity mutants (described in section 2).

6.2. A preliminary electron microscopy study of MlotiK1 in NABB particles

Here, an initial structural study of MlotiK1 incorporated into nanoscale apolipoprotein-bound bilayer (NABB) particles, using electron microscopy (EM) is described. Nanodisc technology has been revolutionizing the membrane protein research field. We incorporated MlotiK1 into NABB particles, a variant of nanodiscs, and explored the potential of these particles for structure determination. Before the description of the experiment, a short theoretical background concerning nanodiscs/NABB particles will be presented.

6.2.1. Nanodisc technology

Nanodiscs (Bayburt, 2002) consist of a patch of a phospholipid bilayer surrounded by a membrane scaffold protein (MSP). The MSP keeps the bilayer in a disc-like arrangement, by protecting the phospholipid acyl groups from the solvent. The phospholipid portion of each nanodisc particle can accommodate a membrane protein into the bilayer, mimicking a biological membrane (Fig. 6.4) and can keep an integral membrane protein soluble in a detergent-free solution, while still incorporated into a phospholipid bilayer (Borch and Hamann, 2009).

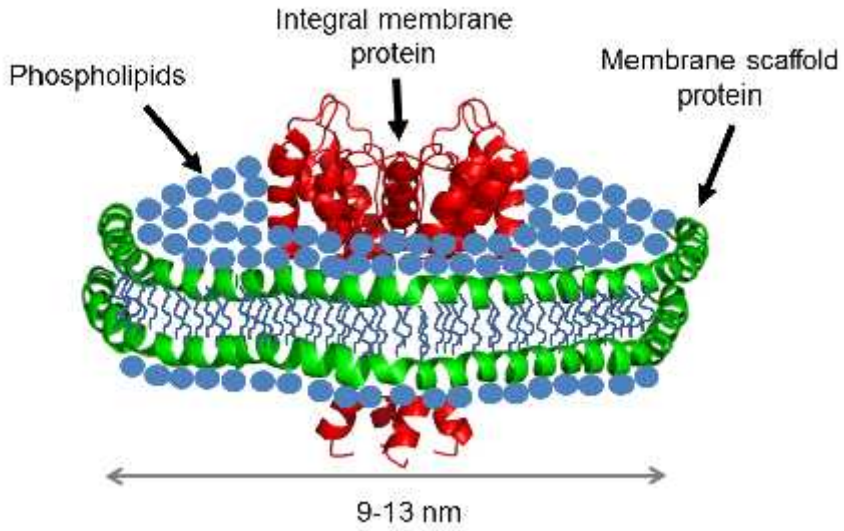

Figure 6.4: Structural model of a nanodisc containing a membrane protein.

5.2.1.1. Biological basis

Nanodiscs are based on nascent discoidal high-density lipoprotein (ndHDL) particles, which are the direct precursors of high-density lipoprotein (HDL) particles. In vertebrates, the main role of HDL particles is the reverse cholesterol transport, a process consisting in cholesterol harvest throughout the organism and its delivery into the liver, for further excretion. ndHDL particles are formed when two apolipoprotein A-1 (Apo A-1) molecules enclose serum phospholipids, forming discoidal bilayer particles. These particles then incorporate cholesterol through an ATP-dependent process, becoming speroidal (Nelson, 2005). Their role in the prevention of artherosclerosis gives HDL particles and apo A-1 great medical interest.

Human Apo A-1 is α-helical and has lipid-free and lipid-bound conformations. While in the lipid-free conformation it forms two helical bundles (Fig. 6.5 A; Ajees et al., 2006), in the lipid-bound conformation the protein adopts a horseshoe-like shape (Borhani et al., 1997). Such shape results of the kinks inserted into the helices by its several proline residues (Fig. 6.5 B). Changes in lipid concentration determine the turnover between the lipid free and lipid-bound conformations (Narayanaswami and Ryan, 2000). Truncating the N-terminal α-helix favours the lipid-bound conformation, as the lipid-bound structure was determined with such truncation (Borhani et al., 1997). MSPs are based on Apo A-1 or other apolipoproteins (Borch and Hamann, 2009), where the N-terminal helix was removed.

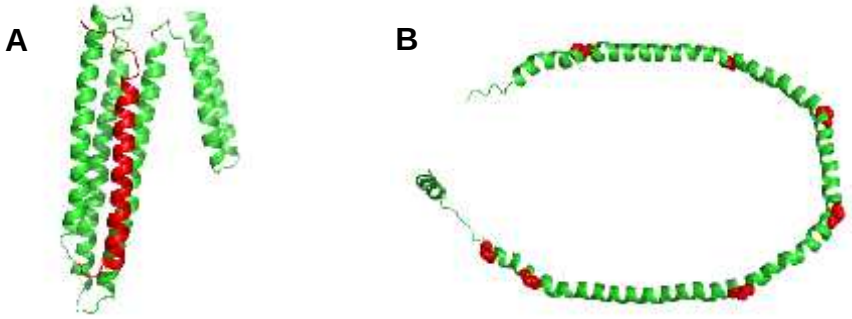

Figure 6.5: Crystal structures of human Apo A-1. (A) Full-length protein (PDB code: 2A01) and (B) Δ43 N-terminal truncation, where proline residues are represented by red spheres (PDB code: 1AV1). The portion truncated in (B) is represented in red in (A).

5.2.1.3. Properties and applications of nanodiscs

The first report describes preparation of nanodiscs by mixing a MSP and phospholipids in a detergent solution at appropriate molar ratios, followed by detergent removal by dialysis (Bayburt, 2002). Similarly to ndHDL particles, each nanodisc particle contains two MSP molecules wrapping around the edges of the particle, each one covering the hydrophobic chains of a leaflet (Bayburt and Sligar, 2010). Nanodisc diameter is between 9 and 13 nanometers and is fine-tuned by engineering the MSP to adjust its length and optimizing the lipid content (Denisov et al., 2004).

Nanodiscs can be adsorbed or attached to a surface via a tag in the MSP (Borch and Hamann, 2009; Bayburt and Sligar, 2010). Nanodiscs seem to be a promising tool for NMR studies of small membrane proteins (Lyukmanova et al., 2008; Gluck et al., 2009). By stabilizing a membrane protein into a lipid bilayer, nanodiscs keep it monodisperse and soluble in the absence of detergent. Additionally, both sides are equally accessible. If the membrane protein has multiple oligomeric states, a specific state can be selected (Bayburt and Sligar, 2010).

Several membrane proteins have been incorporated into nanodiscs, including bacteriorhodopsin (Bayburt and Sligar, 2003), the protomer of the SecYEG peptide translocating complex (Alami et al., 2007), KcsA (Shenkarev et al., 2009), cytochrome P450 and some GPCRs (Nath et al., 2007; Bayburt and Sligar, 2010). Nanodiscs can also be used for delivery of hydrophobic drugs and contrast agents used in medical imaging (Ryan, 2010).

5.2.1.4. Nanoscale apolipoprotein bound bilayer (NABB) particles

Danio rerio (zebrafish) apo A-1 was also shown to form discoidal particles identical to nanodiscs, called nanoscale apolipoprotein bound bilayer (NABB) particles. Bovine rhodopsin was shown to be functional when inserted into such particles (Banerjee et al., 2008), as well as the plant light-harvesting complex II (Pandit et al., 2011). NABB particles contain a HisTag, which can be used to immobilize the particle onto a surface containing nickel ions (Zaitseva et al., 2010). It has also been shown that NABB particles can be applied for delivering the KcsA channel into the lipid bilayer used in the ion channel electrical recordings chamber (Banerjee and Nimigean, 2011).

6.2.2. Incorporation of MlotiK1 into NABB particles

MlotiK1 was incorporated into NABB particles by mixing freshly purified MllotiK1 in detergent with Zap1 and POPC. Detergent was removed by dialysis and the dialysed sample was analyzed by size exclusion chromatography. The chromatogram obtained and 15 % SDS-PAGE analysis of fractions collected are shown in Fig. 6.6. The elution volumes of the three main peaks are indicated. Pure Zap1 elutes at 16.8 ml in the same column (data not shown), therefore, the third peak was not analyzed by SDS-PAGE. The major peak was eluted at 14.8 ml and SDS-PAGE analysis shows that it contains both Zap1 and MlotiK1. Additionally, pure MlotiK1 in detergent solution is eluted at 14.8 ml in the same column (data not shown). Since detergent was removed from the preparation, these findings indicate that Zap1 has associated with MlotiK1, forming a larger structure that elutes at a lower elution volume (14.8 ml) than Zap1 alone. There is also a “shoulder” at approximately 13.2 ml, with the same protein composition as the peak at 14.8 ml, which indicates that NABB particles have some tendency to aggregate.

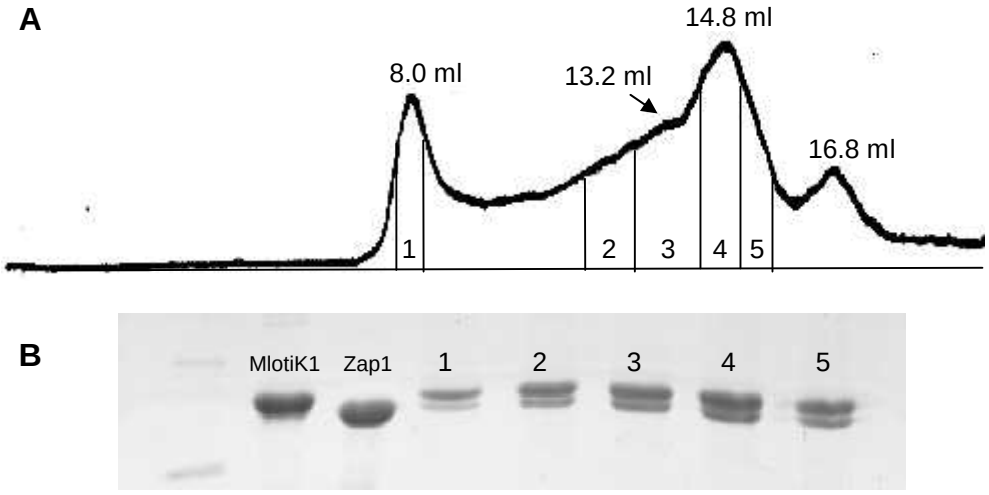

Figure 6.6: Analysis of MlotiK1 incorporated into NABB particles (A) Gel filtration chromatogram where the elution volumes are indicated above the respective peaks and the fractions collected are numbered from 1 to 5 (B) 15 % SDS-PAGE analysis of the fractions collected in (A).

6.2.3. EM data and structural model

“The case for cryoEM of membrane proteins and 3-D particle reconstructions using Nanodiscs has also seen recent success” (Bayburt and Sligar, 2010).

At the Rudolf Virchow Center, in Würzburg, Germany, samples corresponding to the protein peak eluted at 14.8 ml (Fig. 6.6) were analyzed with EM by Christian Kraft (technician) and the data collected were processed by Dr. Shashi Bhushan. Only two kinds of particles were expected to be found: empty NABB particles and NABB particles containing MlotiK1. Views of empty NABB particles will correspond to top and side views. In contrast, NABB particles containing MlotiK1 will probably appear in either two top views (with the extracellular or cytoplasmic channel faces facing the viewer) or in a side view. All class averages (obtained by superposition of identical single particle images) should correspond to different orientations of these two kinds of particles.

A pool of single particle images was obtained and some of those are shown in Fig. 6.7 A. Single particle images were automatically grouped into ten class averages (Fig. 6.7 B). Due to their low resolution, interpretation of the class averages obtained was not obvious. Nevertheless, some assumptions could be made. Class averages #2 and #8 could represent side views of NABB particles without MlotiK1 incorporated, due to their slightly elongated shape. Class averages displaying round shapes, such as #3, #5, #7 or #10, might represent top views of the particle, with the membrane surface parallel to the plane. It is not evident wheter MlotiK1 is present or if the CNB domains are facing the viewer or not. Class averages #4 and #9 seem to represent side views of NABB particles containing MlotiK1, due to their irregular electron density. Class averages #1 and #6 have an irregular shape; therefore no interpretation could be done.

Class average #3 (Fig. 6.7 C) was the most interesting, since it provides more details, allowing a more complete interpretation. Such interpretation is sketched in Fig. 6.7 D. In this class average, two of the CNB domains appear to stand out of the NABB disc formed by the Zap1 proteins. In this class average, dimensions of the putative CNB domains are approximately 2.4 nm and the disc region is approximately 7.8 nm long. MlotiK1 has four-fold symmetry and its symmetry axis is located through the channel pore. An axis was placed between the putative CNB domains, in a perpendicular orientation to the disc region. The four-fold symmetric arrangement of MlotiK1 in the bound state (Paper II) allowed applying a four-fold symmetry operation through the axis. Using such operation, a structural model was generated (Fig. 6.7 E). For this preliminary model, resolution was not calculated.

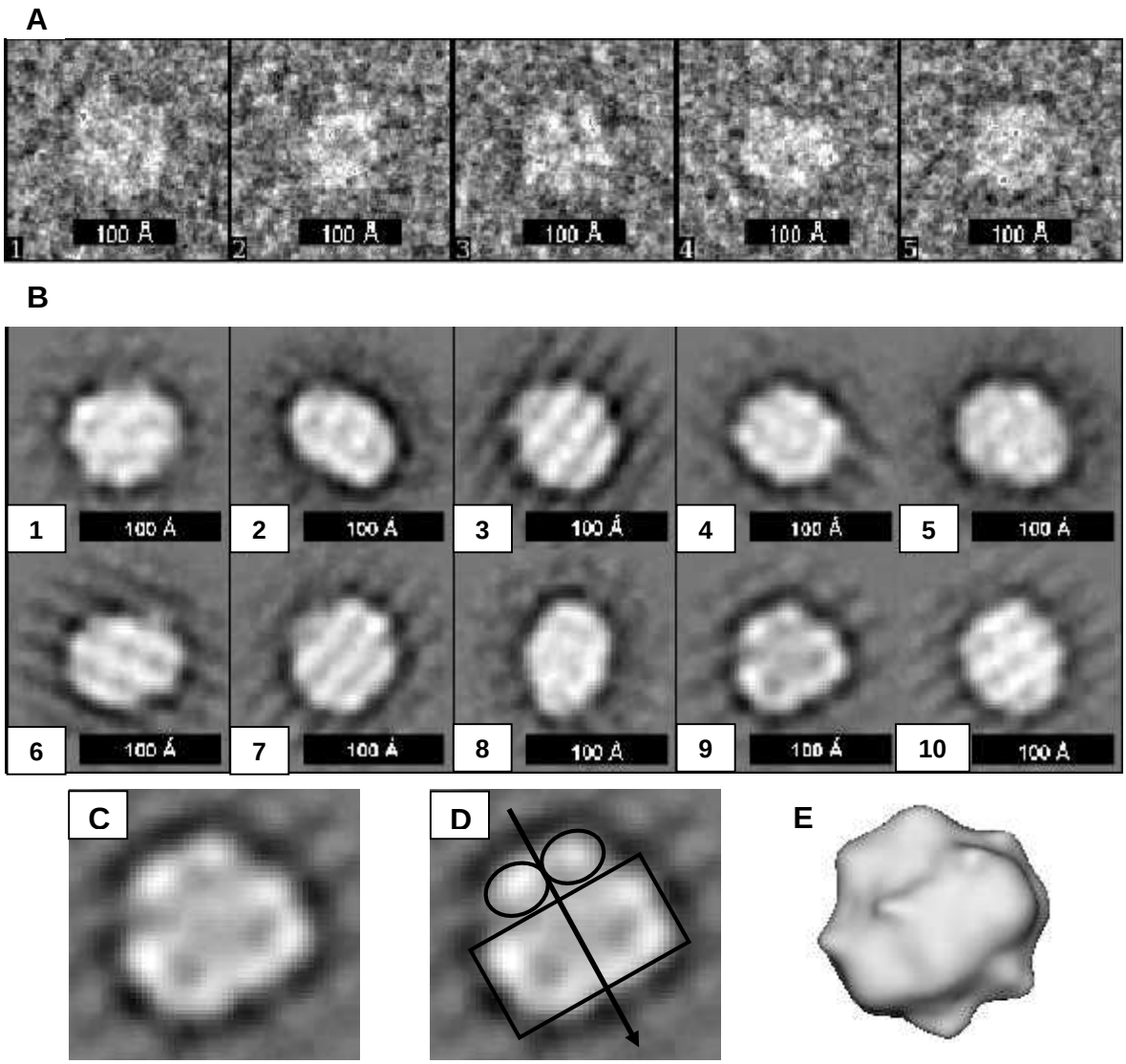

Figure 6.7: EM sample imaging and model buiding of MlotiK1 reconstituted in NABB particles. (A) Examples of single particle images. (B) Class averages (numbered from 1 to 10) obtained from the total pool of single particle images. In (A) and (B), scale bars in black were added, representing 100 Å (10.0 nm). (C) Magnification of class average #9 (D) Interpretation of class average #9, where putative structural elements are identified. Arrow: symmetry axis running through the channel pore; rectangle: protein transmembrane region surrounded by the NABB particle; circles: CNB domains. (E) Model generated from (D) represented in the same orientation.

6.2.4. Analysis of the model obtained

The small dimensions of MlotiK1 required the use of negative staining, which limited the resolution attainable. The dimensions of the structural model obtained were

estimated using the software UCSF Chimera (Pettersen et al., 2004). As a guideline, the diameter of MlotiK1 transmembrane region was measured in the crystal structure, resulting in values of 8.7 and 7.0 nm, between opposite and neighbouring subunits, respectively (Fig. 6.8 A). In the EM electron density maps, the contour of the particles is not well defined, affecting therefore the accuracy of measurements. In the EM model obtained, particle diameter measured between neighbouring and opposite edges was approximately 8.8 and 10.8 nm, respectively (Fig. 6.8 B). These values are consistent with the maximal Stokes diameter of empty NABB particles, 10.0 to 12.5 nm, determined by gel filtration chromatography (Banerjee et al., 2008). After rotating the structural model into a side view (Fig. 6.8 C), its total height was also measured, 9.3 nm. By AFM, the total height of MlotiK1 was approximately 8.9 nm in the bound state and 10.6 nm in the unbound state (Paper II). The thickness of a nanodisc/NABB particle is approximately 4.3 nm (Frauenfeld et al., 2011). Considering this value, a rectangle of a width representing 4.3 nm was placed in the figure to indicate the expected location of Zap1 (Fig. 6.8 C). The side view image shows two regions separated by the disc region. Their heights above and below the membrane level were approximately 1.9 and 3.1 nm. In our AFM study, the heights of the extracellular side and CNB domains of MlotiK1 were 1.8 and 3.2 nm, respectively (Paper II). Based on this previous data, the extracellular side and the CNB domains were assigned to the heights of 1.9 and 3.0 nm, respectively. One of the complicating factors in this interpretation is that the overal dimensions of NABB particles containing MlotiK1 (height: 9.4 nm; diameter: 8.8 or 10.8 nm) are similar, increasing therefore the difficulty in distinguishing particles in different orientations.

Comparison of the structural model obtained with another one previously determined at 16 Å also by EM, but in detergent solution, shows that resolution was lower in the presence of the NABB particle than in its absence (Fig. 6.9). It is well known that resolution is strongly determined by sample quality. In NABB particles, resolution obtained was clearly lower than in detergent solution. Although other factors, such as the equipment used and operators involved, were different, one may hypothesize that lower resolution resulted also of increased structural heterogeneity due to the presence of Zap1. This hypothesis is supported by a recent study. A chimera containing the MlotiK1 CNB domains attached to the KcsA channel was incorporated into NABB particles and imaged by EM. The resolution achieved, 26 Å (McCoy et al., 2014), was lower than that of MlotiK1 obtained in detergent solution, 16 Å (Chiu et al., 2007). Also of interest was the fact that the cAMP binding affinity of the chimera increased 10-fold upon incorporation into NABB particles (McCoy et al., 2014).

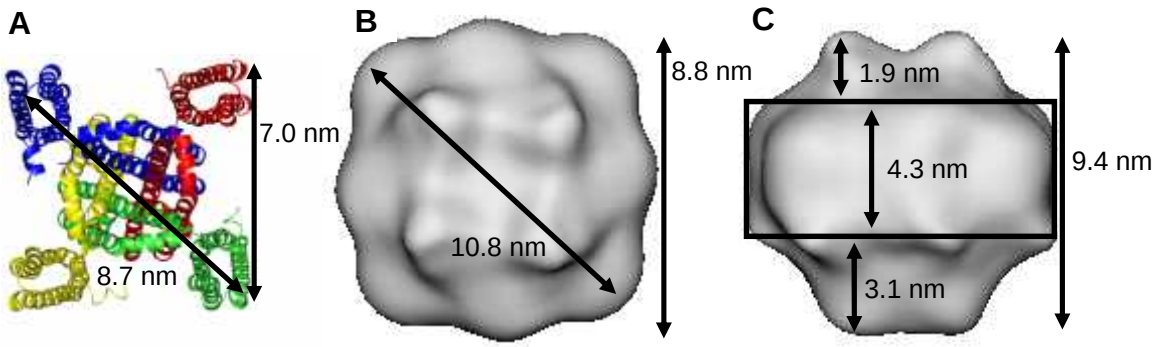

Figure 6.8: Approximate dimensions of MlotiK1. (A) Top view of the transmembrane region crystal structure (PDB code: 3BEH). MlotiK1 incorporated into NABB particles in a (B) top view and (C) side view. In the side view, a rectangle indicates the expected location of the MlotiK1 transmembrane region surrounded by the NABB particle.

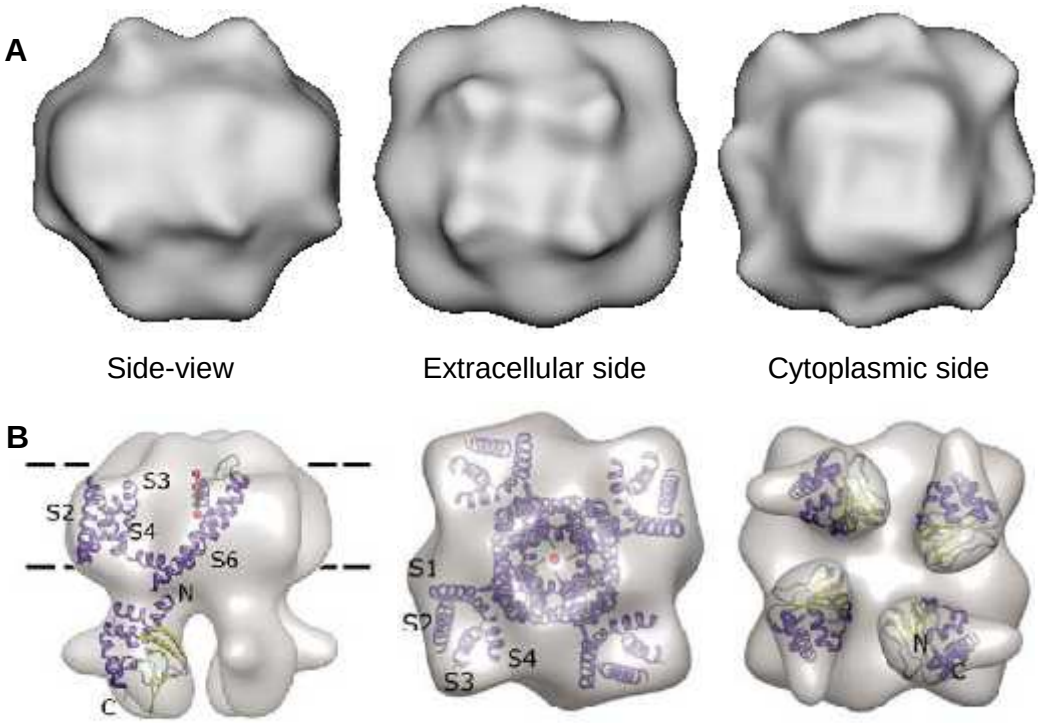

Figure 6.9: Structural models of MlotiK1 by EM in different orientations. (A) MlotiK1 incorporated in NABB particles. (B) Published structural model at 16 Å, where crystal structures of MlotiK1 CNB domain and a voltage-gated potassium channel were superposed (Chiu et al., 2007).

6.3. A fluorescence-based activity assay for potassium channels

Here, our effort in developing a new functional assay for MlotiK1 is described. Such assay is a non-radioactive alternative to the $^{86}Rb^{+}$ uptake assay currently used (Nimigean, 2006). Besides the specific safety requirements in any radioactive work, the rubidium uptake assay shows large deviations within replicates of the same condition, requiring a large number of repetitions for a reliable quantitative result. In addition, ^{86}Rb has to be used within two monts after production, due to its relatively low half-lfe (approximately 18 days). After such period, it becomes contaminated with ^{86}Rb decay products, which may affect the data. Due to these drawbacks, we decided to try developing an alternative assay to use with MlotiK1 and other potassium channels that fail to be studied by electrical recordings.

6.3.1. Potassium-binding benzofuran isophthalate (PBFI)

Potassium-binding benzofuran isophthalate (PBFI, Molecular Probes, Fig. 6.10 A) is a fluorophore that binds potassium ions through a crown ether chemical group. Upon potassium binding, its intrinsic fluorescence is significantly enhanced (Fig. 6.10 B). PBFI has been used for functional studies of several potassium transport systems, including a potassium/proton antiporter (Jezek et al., 1990) and an ATP-dependent potassium channel (Paucek et al., 1992). It has also been used for quantification of intracellular potassium concentration (Andersson et al., 2006). Functional studies based on fluorescent probes have also been used for other ions, such as for sodium and calcium (Li et al., 1992). These facts provided some hope concerning the possibility of developing a novel functional assay for potassium channels using PBFI as a fluorescent probre.

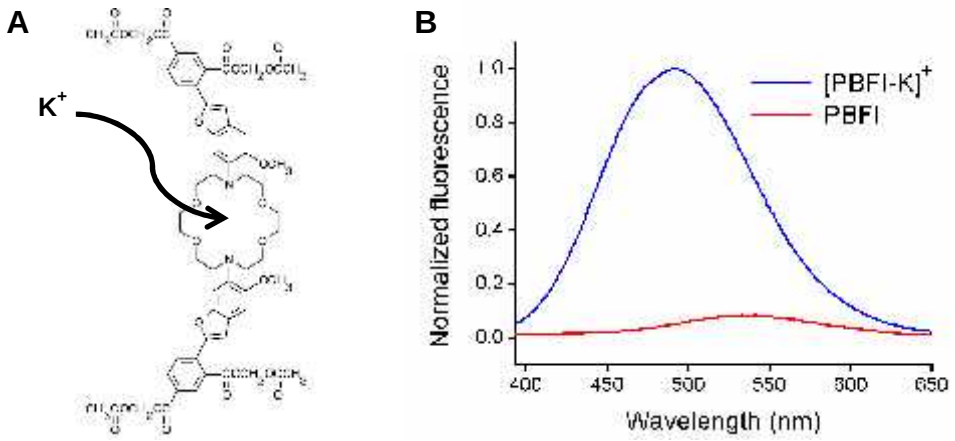

Figure 6.10: PBFI. (A) Chemical structure, where the potassium-binding site is indicated. (B) Emission spectra of apo-PBFI (red) and PBFI in complex with 15 mM KCl (blue).

6.3.1.1. Characterization of PBFI binding properties

We started by characterizing PBFI binding to potassium and to sodium, obtaining K_D values of 5.7 ± 0.3 mM and 17.1 ± 1.3 mM for potassium and sodium, respectively (Fig. 6.11). The potassium binding curve shows that fluorescence increases rapidly between 0 and 15 mM potassium, starting to saturate at 30 mM (Fig. 6.11 A). PBFI fluorescence is very sensitive to potassium concentration between 0 and 15 mM, therefore we chose to use in the assay a 0 to 15 mM potassium ion concentration gradient between the inside and the outside of the liposomes. Since PBFI affinity for sodium is approximately 3-fold lower (Fig. 6.11 B), we do not expect that traces of sodium ions in solution should interfere.

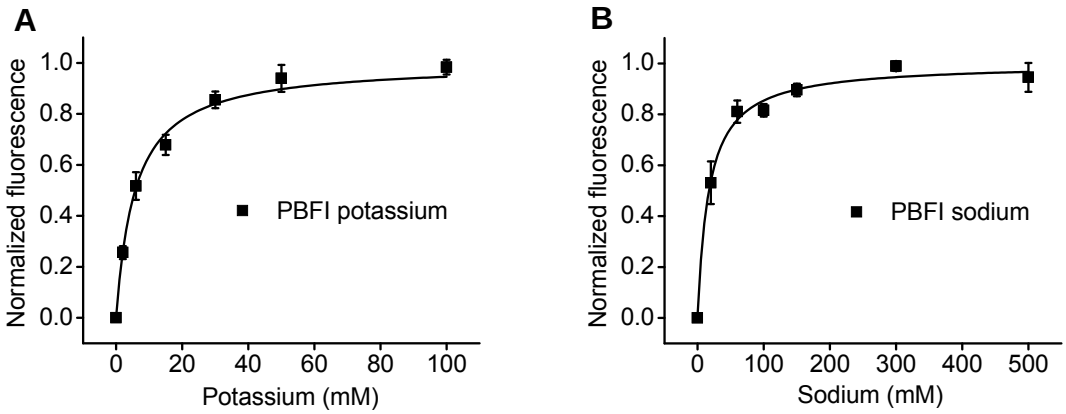

Figure 6.11: PBFI fluorescence as a function of (A) potassium or (B) sodium concentration. K_D values determined were 5.7 ± 0.3 mM and 17.1 ± 1.3 mM for potassium and sodium, respectively.

6.3.2. Setup of the assay

The final objective of this work was to develop an activity assay based on PBFI fluorescence enhancement in the presence of potassium. The KcsA channel was chosen for testing the assay, since it is stable, easy to purify and has a high permeation rate (Heginbotham et al., 1998).

Liposomes containing 15 mM KCl were prepared in a buffer with pH 7.4 and then destabilized with detergent, in order to enable membrane protein insertion into the liposomes membrane. The potassium channel was added and detergent was removed by hydrophobic adsorption. PBFI was then added and samples were freeze-thawed and sonicated, to allow PBFI to penetrate the liposomes. The liposomes were further loaded into a desalting column equilibrated in a buffer of pH 7.0 depleted of KCl, to remove external PBFI and create KCl and pH gradients. Proteoliposomes were eluted in the void volume. Osmotic pressure was kept close to zero by adding N-methyl-β-D-glucamine (NMG) to both buffers. This compound was used to adjust total concentrations to 155 mM.

The fluorescence signal due to the $[PBFI\text{-}K]^+$ complex remains reasonably stable even after creating the concentration gradient, because the KcsA potassium channel is highly selective for potassium and therefore the chemical equilibrium between K^+ and $[PBFI\text{-}K]^+$ is not significantly disturbed. The efflux of K^+, a positive charge, requires the influx of another cation, which was chosen to be H^+, to compensate for the establishment of a difference in electrical potential. When the proteon ionophore carbonyl cyanide 3-chlorophenyl hydrazone (CCCP) is added, liposomes become selectively permeable to protons, allowing the influx of these positive charges, since pH is lower outside the liposomes. This allows efflux of potassium ions though the potassium channel, causing therefore their displacement from PBFI and a consequent fluorescence decrease. Finally, when the potassium ionophore valinomycin is added, there is a total potassium efflux from the liposomes and maximal fluorescence decrease (Fig. 6.12 A).

A representative result is shown in Fig. 6.12 B. Here, liposomes samples were destabilized with 13 mM [(3-Cholamidopropyl)dimethylammonio]-1-propanesulfonate hydrate (CHAPS) and reconstituted with KcsA at protein to lipid ratios (w/w) of 1/150 and 1/500. There are two negative controls without KcsA: one in which liposomes were destabilized with detergent and another in which they were not. All curves were normalized and superposed. Addition of CCCP (500 seconds after the beginning of the measurement) did not cause any fluorescence decrease in samples containing KcsA. When valinomycin was added (1400 seconds after the beginning of the measurement), a

rapid decrease in fluorescence was observed in all conditions. This is consistent with a rapid displacement of potassium from PBFI, caused by its efflux, which resulted in a rapid decrease in its concentration inside the liposomes.

Upon addition of CCCP, fluorescence should have decreased in samples containing KcsA, fact that was consistently not observed. The main reason behind such lack of detectable effect could be the low sensitivity of the assay. This lack of sensitivity in combination with the low open probability of the channel would make the signal indistinguishable from the control conditions. The intrinsic leakiness of the liposomes, reflected in the tendency of the baseline to lower over time, might have also contributed. Moreover, the baseline usually showed some “bumps”, complicating even further the assay. Additionally, reconstitution efficiency was not evaluated. Consequently, the lack of signal could also be caused by decreased reconstitution efficiency. In the end, we could not overcome the problems encountered and the assay was abandoned.

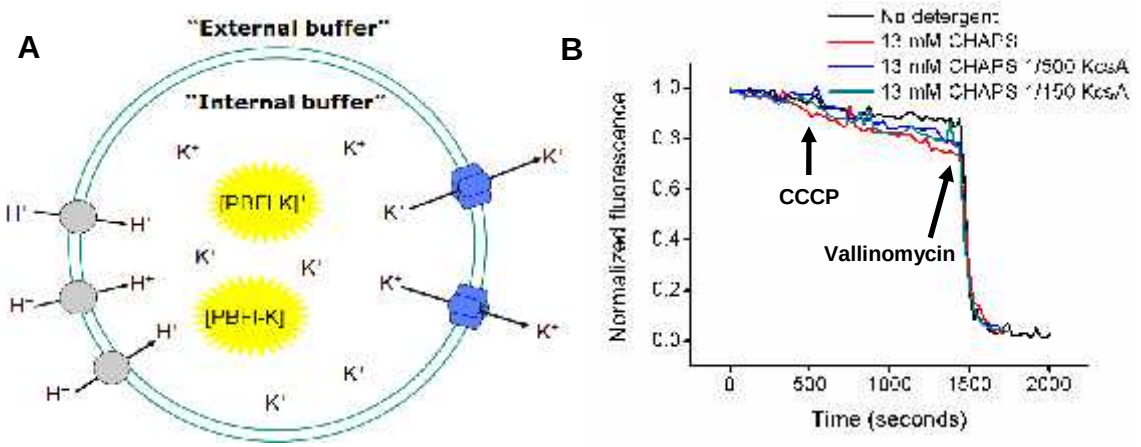

Figure 6.12: The fluorescence-based activity assay (A) Setup of the assay, where a liposome is represented as a large circle containing K^+ ions and the $[PBFI\text{-}K]^+$ complex. CCCP, which provides permeability ot H^+ ions, and KcsA are represented in grey and blue, respectively. “Internal buffer”: 20 mM HEPES-HCl pH 7.4, 120 mM NMG-HCl, 80 µM PBFI, 15 mM KCl; “Extrernal buffer”: 20 mM HEPES-HCl pH 7.0, 135 mM NMG-HCl (B) Time-course graph of potassium efflux in liposomes where the pH and potassium gradients were created as described above. CCCP and valinomycin were added at 500 and 1400 seconds after the beginning of the measurement, respectively (indicated by arrows). Data were normalized to the valinomycin-induced potassium efflux.

6.4. Materials and methods

6.4.1. DTNB assay

MlotiK1 CNB domain C263V and C263V C331V M299C were expressed and purified as described (Clayton et al., 2004; Altieri et al., 2008). Gel fitration chromatography was performed in a Superdex 75 column and cAMP was removed as described in Paper I for other CNB domain mutants. Refolded MlotiK1 CNB domain mutants were pre-incubated overnight at 4 ºC with 1 mM tris(2-carboxyethyl)phosphine (TCEP) and 10 mM dithiothreitol (DTT), which were later removed by desalting in a HiTrap desalting column. DTNB (Invotrogen) reactions were carried out in 50 mM sodium phosphate pH 7.4, 100 mM NaCl, 1 mM EDTA. The procedure was based on (Vopel et al., 2009). 10 µM of single cysteine protein mutant were reacted with 200 µM DTNB in the absence of any ligand or in the presence of the ligand concentrations indicated in Tables 5.3 and 5.4. K_D values were determined as described in Paper I for other CNB domain mutants. Absorbance was recorded at 412 nm over time and temperature was kept at 25 ºC. For recording fast reactions, such as C263V C331V M299C in the absence and presence of cCMP, a stopped-flow apparatus was attached to the spectrophotometer. For each condition, the reaction was carried out in triplicate and data were averaged.

6.4.2. Incorporation of MlotiK1 into NABB particles and EM

The MSP used was Zap1 (Banerjee et al., 2008), provided by Prof. Thomas P. Sakmar (Rockefeller University, New York, NY, USA). Zap1 was expressed and purified as described (Banerjee et al., 2008) with the exception that protein was expressed in BL21 (DE3) RIL cells and a Superose 6 gel filtration column was used. 1-palmitoyl-2-oleoyl-sn-glycero-3-phosphocholine (POPC, Avanti) was prepared as described (Banerjee and Nimigean, 2011). Prepared Zap1 and POPC were stored at -80 and -20 ºC, respectively. Full-length MlotiK1 was expressed and purified according to Paper II, with the exception that protein was loaded once onto a Superose 6 gel filtration column.

NABB particles were prepared by mixing Zap1, freshly purified MlotiK1 and POPC at the molar ratios 2:1:25, respectively, in a total volume of 200 µl. Buffer used was 20 mM Tris-HCl pH 7.5, 100 mM KCl, 3 mM DTT, 5 mM n-decyl-β-D-maltopyranoside (DM, Anatrace), 200 µM cAMP. The mixture was incubated on ice for 30–40 minutes and transferred to Slide-A-Lyzer MINI Dialysis units (Thermo Scientific) with a 10 kDa cutoff. The detergent was removed by dialysis during three days against 200 ml DM-depleted

buffer. Self-assembled NABB particles were loaded onto a Superose 6 gel filtration column equilibrated in dialysis buffer. Samples were collected at different elution volumes and analyzed by SDS-PAGE.

Sample was analyzed at the Rudolf Virchow Center, Würzburg, Germany, by Christian Kraft and Dr. Shashi Bhushan. 3.5 µl of 10-fold diluted sample were applied to 10 nm carbon-coated grids and stained with uranyl acetate. Sample was imaged under low-dose conditions (25 electrons/$Å^2$) on a Tecnai T12 transmission electron microscope operated at 120 kV and cooled with liquid nitrogen. 67,000x nominal magnification at a defocus in the range of 1.0-1.5 µm were used. Micrographs were obtained using a 4K CCD camera, corresponding each pixel to 2.2 Å. The data was processed with image processing package EMAN2 (Tang et al., 2007). About 2,000 particles were used for 2D classification and model building. Model was visualized and its dimensions were measured using UCSF Chimera (Pettersen et al., 2004).

6.4.3. Fluorescence-based activity assay

PBFI concentration was determined by absorption at 346 nm, using the molar extinction coefficient of 42000 $M^{-1}cm^{-1}$, provided by the manufacturer. All fluorescence measurements were carried out in a Horiba Fluoromax-4 (Jobin Yvon) spectrofluorometer. For binding assays, solutions containing 80 nM PBFI and increasing concentrations of potassium or sodium were prepared. Spectra were collected with excitation at 340 nm and emission between 390 and 650 nm. $[PBFI\text{-}K]^+$ and $[PBFI\text{-}Na]^+$ K_Ds were determined using the procedure described in Paper I for 8-NBD cAMP binding to CNB domain mutants.

Liposomes were prepared from *E. coli* Polar Lipid Extract (Avanti) purchased in a chloroform solution. Solvent was evaporated and lipids ressuspended in 15 mM KCl, 120 mM NMG, 20 mM HEPES-NMG pH 7.4 to a lipid concentration of 4 mg/ml. Phospholipid aggregates were disrupted by sonication in a water bath, followed by freeze-thawing (four times) and extrusion through a 400 nm filter. Extruded lipssomes were stored at 4 ºC and used within three days.

KcsA was expressed and purified as described (Heginbotham et al., 1997). Liposomes were aliquoted to 100 µl portions and solubilized with 13 mM CHAPS for 120 minutes. Freshly purified KcsA was added at protein to lipid ratios (w/w) of 1/500 and 1/150. CHAPS concentration corresponds to the detergent-to-lipid ratio used in the $^{86}Rb^+$ uptake assay. Detergent was removed by hydrophobic adsorption using Bio-Beads (Bio-Rad), using the procedure described in Paper I for the uptake assay. After detergent

removal, 80 µM PBFI was added to liposome suspension, which was further freeze-thawed four times and sonicated in water bath for 3 x 5 seconds. Liposomes were loaded onto a 5 ml HiTrap desalting column attached to an ÄKTA purifier system, equilibrated in 135 mM NMG, 20 mM HEPES-NMG pH 7.0, to remove external PBFI and create a pH gradient.

Kinetic measurements were performed immediately after the gradients were formed. Temperature was set at 20 ºC and a 1.5 ml Hellma quartz cuvette with agitation was used. Excitation and emission wavelengths were set at 340 and 494 nm, respectively, with both slit widths at 7 nm. Shutter was controlled in the “anti-photobleaching” mode. Integration time was 0.5 seconds. After the beginning of each measurement, 200 nM CCCP and 90 nM valinomycin were added after 500 and 1400 seconds, respectively.

7. References

Adelman, J.P., J. Maylie, and P. Sah. 2012. Small-conductance Ca2+-activated K+ channels: form and function. *Annual review of physiology*. 74:245-269.

Adelman, W.J., Jr., and R.J. French. 1978. Blocking of the squid axon potassium channel by external caesium ions. *The Journal of physiology*. 276:13-25.

Afonine, P.V., R.W. Grosse-Kunstleve, N. Echols, J.J. Headd, N.W. Moriarty, M. Mustyakimov, T.C. Terwilliger, A. Urzhumtsev, P.H. Zwart, and P.D. Adams. 2012. Towards automated crystallographic structure refinement with *phenix.refine*. *Acta Crystallogr. D Biol. Crystallogr.* 68:352–367.

Alami, M., K. Dalal, B. Lelj-Garolla, S.G. Sligar, and F. Duong. 2007. Nanodiscs unravel the interaction between the SecYEG channel and its cytosolic partner SecA. *The EMBO journal*. 26:1995-2004.

Alioua, A., Y. Tanaka, M. Wallner, F. Hofmann, P. Ruth, P. Meera, and L. Toro. 1998. The large conductance, voltage-dependent, and calcium-sensitive K+ channel, Hslo, is a target of cGMP-dependent protein kinase phosphorylation in vivo. *The Journal of biological chemistry*. 273:32950-32956.

Altenhofen, W., J. Ludwig, E. Eismann, W. Kraus, W. Bönigk, U.B. Kaupp. 1991.Control of ligand specificity in cyclic nucleotide-gated channels from rod photoreceptors and olfactory epithelium. *Proceedings of the National Academy of Sciences of the United States of America*. 88:9868-9872.

Altieri, S.L., G.M. Clayton, W.R. Silverman, A.O. Olivares, E.M. De la Cruz, L.R. Thomas, and J.H. Morais-Cabral. 2008. Structural and energetic analysis of activation by a cyclic nucleotide binding domain. *Journal of molecular biology*. 381:655-669.

Anand, G.S., C.A. Hughes, J.M. Jones, S.S. Taylor, and E.A. Komives. 2002. Amide H/2H exchange reveals communication between the cAMP and catalytic subunit-binding sites in the R(I)alpha subunit of protein kinase A. *Journal of molecular biology*. 323:377-386.

Andersson, B., V. Janson, P. Behnam-Motlagh, R. Henriksson, and K. Grankvist. 2006. Induction of apoptosis by intracellular potassium ion depletion: using the fluorescent dye PBFI in a 96-well plate method in cultured lung cancer cells. *Toxicology in vitro : an international journal published in association with BIBRA*. 20:986-994.

Ando, T., N. Kodera, E. Takai, D. Maruyama, K. Saito, and A. Toda. 2001. A high-speed atomic force microscope for studying biological macromolecules. *Proceedings of the National Academy of Sciences of the United States of America*. 98:12468-12472.

Aravind, L., and C.P. Ponting. 1997. The GAF domain: an evolutionary link between diverse phototransducing proteins. *Trends in biochemical sciences*. 22:458-459.

Armstrong, C.M. 1971. Interaction of tetraethylammonium ion derivatives with the potassium channels of giant axons. *The Journal of general physiology*. 58:413-437.

Armstrong, C.M., F. Bezanilla, and E. Rojas. 1973. Destruction of sodium conductance inactivation in squid axons perfused with pronase. *The Journal of general physiology*. 62:375-391.

Armstrong, C.M., and B. Hille. 1972. The inner quaternary ammonium ion receptor in potassium channels of the node of Ranvier. *The Journal of general physiology*. 59:388-400.

Ashman, D.F., R. Lipton, M.M. Melicow, and T.D. Price. 1963. Isolation of adenosine 3', 5'-monophosphate and guanosine 3', 5'-monophosphate from rat urine. *Biochemical and biophysical research communications*. 11:330-334.

Baker, N.A., D. Sept, S. Joseph, M.J. Holst, and J.A. McCammon. 2001. Electrostatics of nanosystems: Application to microtubules and the ribosome. *Proceedings of the National Academy of Sciences of the United States of America*. 98:10037–10041.

Banerjee, S., T. Huber, and T.P. Sakmar. 2008. Rapid incorporation of functional rhodopsin into nanoscale apolipoprotein bound bilayer (NABB) particles. *Journal of molecular biology*. 377:1067-1081.

Banerjee, S., and C.M. Nimigean. 2011. Non-vesicular transfer of membrane proteins from nanoparticles to lipid bilayers. *The Journal of general physiology*. 137:217-223.

Bayburt, T.H., and S.G. Sligar. 2003. Self-assembly of single integral membrane proteins into soluble nanoscale phospholipid bilayers. *Protein science : a publication of the Protein Society*. 12:2476-2481.

Bayburt, T.H., and S.G. Sligar. 2010. Membrane protein assembly into Nanodiscs. *FEBS letters*. 584:1721-1727.

Bayburt, T.H.G., Y. V.; Sligar, S. G. 2002. Self-assembly of discoidal phospholipid bilayer nanoparticles with membrane scaffold proteins. *Nano Lett.* 2:853-856.

Beavo, J.A., M. Conti, and R.J. Heaslip. 1994. Multiple cyclic nucleotide phosphodiesterases. *Molecular pharmacology*. 46:399-405.

Bell, D.C., H. Yao, R.C. Saenger, J.H. Riley, and S.A. Siegelbaum. 2004. Changes in local S4 environment provide a voltage-sensing mechanism for mammalian hyperpolarization-activated HCN channels. *The Journal of general physiology*. 123:5-19.

Bellanda, M., S. Mammi, S. Geremia, N. Demitri, L. Randaccio, Q.B. Broxterman, B. Kaptein, P. Pengo, L. Pasquato, and P. Scrimin. 2007. Solvent polarity controls the

helical conformation of short peptides rich in Calpha-tetrasubstituted amino acids. *Chemistry (Weinheim an der Bergstrasse, Germany)*. 13:407-416.

Benarroch, E.E. 2013. HCN channels: function and clinical implications. *Neurology*. 80:304-310.

Berthet, J., T.W. Rall, and E.W. Sutherland. 1957. The relationship of epinephrine and glucagon to liver phosphorylase. IV. Effect of epinephrine and glucagon on the reactivation of phosphorylase in liver homogenates. *The Journal of biological chemistry*. 224:463-475.

Binnig, G., C.F. Quate, and C. Gerber. 1986. Atomic force microscope. *Physical review letters*. 56:930-933.

Binning, G.R., H.; Gerber, C.; Weibel, E. 1982. Surface studies by scanning tunneling microscopy. *Phys. Rev. Lett.* 49:57-61.

Borch, J., and T. Hamann. 2009. The nanodisc: a novel tool for membrane protein studies. *Biological chemistry*. 390:805-814.

Borhani, D.W., D.P. Rogers, J.A. Engler, and C.G. Brouillette. 1997. Crystal structure of truncated human apolipoprotein A-I suggests a lipid-bound conformation. *Proceedings of the National Academy of Sciences of the United States of America*. 94:12291-12296.

Canaves, J.M., and S.S. Taylor. 2002. Classification and phylogenetic analysis of the cAMP-dependent protein kinase regulatory subunit family. *Journal of molecular evolution*. 54:17-29.

Chiu, P.L., M.D. Pagel, J. Evans, H.T. Chou, X. Zeng, B. Gipson, H. Stahlberg, and C.M. Nimigean. 2007. The structure of the prokaryotic cyclic nucleotide-modulated potassium channel MloK1 at 16 A resolution. *Structure (London, England : 1993)*. 15:1053-1064.

Clayton, G.M., S.G. Aller, J. Wang, V. Unger, and J.H. Morais-Cabral. 2009. Combining electron crystallography and X-ray crystallography to study the MlotiK1 cyclic nucleotide-regulated potassium channel. *Journal of structural biology*. 167:220-226.

Clayton, G.M., S. Altieri, L. Heginbotham, V.M. Unger, and J.H. Morais-Cabral. 2008. Structure of the transmembrane regions of a bacterial cyclic nucleotide-regulated channel. *Proceedings of the National Academy of Sciences of the United States of America*. 105:1511-1515.

Clayton, G.M., W.R. Silverman, L. Heginbotham, and J.H. Morais-Cabral. 2004. Structural basis of ligand activation in a cyclic nucleotide regulated potassium channel. *Cell*. 119:615-627.

Cole, K.S., and H.J. Curtis. 1939. ELECTRIC IMPEDANCE OF THE SQUID GIANT AXON DURING ACTIVITY. *The Journal of general physiology*. 22:649-670.

Cook, N.J., W. Hanke, and U.B. Kaupp. 1987. Identification, purification, and functional reconstitution of the cyclic GMP-dependent channel from rod photoreceptors. *Proceedings of the National Academy of Sciences of the United States of America*. 84:585-589.

Corbin, J.D., P.H. Sugden, L. West, D.A. Flockhart, T.M. Lincoln, and D. McCarthy. 1978. Studies on the properties and mode of action of the purified regulatory subunit of bovine heart adenosine 3':5'-monophosphate-dependent protein kinase. *The Journal of biological chemistry*. 253:3997-4003.

Costache, A., N. Bucurenci, and A. Onu. 2013. Adenylate cyclases involvement in pathogenicity, a minireview. *Roumanian archives of microbiology and immunology*. 72:63-86.

Craven, K.B., and W.N. Zagotta. 2006. CNG and HCN channels: two peas, one pod. *Annual review of physiology*. 68:375-401.

Cukkemane, A., B. Gruter, K. Novak, T. Gensch, W. Bonigk, T. Gerharz, U.B. Kaupp, and R. Seifert. 2007. Subunits act independently in a cyclic nucleotide-activated K(+) channel. *EMBO reports*. 8:749-755.

Cukkemane, A., D. Nand, S. Gradmann, M. Weingarth, U.B. Kaupp, and M. Baldus. 2012. Solid-state NMR [13C,15N] resonance assignments of the nucleotide-binding domain of a bacterial cyclic nucleotide-gated channel. *Biomolecular NMR assignments*. 6:225-229.

de Rooij, J., H. Rehmann, M. van Triest, R.H. Cool, A. Wittinghofer, and J.L. Bos. 2000. Mechanism of regulation of the Epac family of cAMP-dependent RapGEFs. *The Journal of biological chemistry*. 275:20829-20836.

de Rooij, J., F.J. Zwartkruis, M.H. Verheijen, R.H. Cool, S.M. Nijman, A. Wittinghofer, and J.L. Bos. 1998. Epac is a Rap1 guanine-nucleotide-exchange factor directly activated by cyclic AMP. *Nature*. 396:474-477.

Denisov, I.G., Y.V. Grinkova, A.A. Lazarides, and S.G. Sligar. 2004. Directed self-assembly of monodisperse phospholipid bilayer Nanodiscs with controlled size. *Journal of the American Chemical Society*. 126:3477-3487.

Diller, T.C., Madhusudan, N.H. Xuong, and S.S. Taylor. 2001. Molecular basis for regulatory subunit diversity in cAMP-dependent protein kinase: crystal structure of the type II beta regulatory subunit. *Structure (London, England : 1993)*. 9:73-82.

Doyle, D.A., J. Morais Cabral, R.A. Pfuetzner, A. Kuo, J.M. Gulbis, S.L. Cohen, B.T. Chait, and R. MacKinnon. 1998. The structure of the potassium channel: molecular basis of K+ conduction and selectivity. *Science (New York, N.Y.)*. 280:69-77.

Drake, B., C.B. Prater, A.L. Weisenhorn, S.A. Gould, T.R. Albrecht, C.F. Quate, D.S. Cannell, H.G. Hansma, and P.K. Hansma. 1989. Imaging crystals, polymers, and processes in water with the atomic force microscope. *Science (New York, N.Y.)*. 243:1586-1589.

Ellman, G.L. 1959. Tissue sulfhydryl groups. *Archives of biochemistry and biophysics*. 82:70-77.

Emmer, M., B. deCrombrugghe, I. Pastan, and R. Perlman. 1970. Cyclic AMP receptor protein of E. coli: its role in the synthesis of inducible enzymes. *Proceedings of the National Academy of Sciences of the United States of America*. 66:480-487.

McCoy, A.J., R.W. Grosse-Kunstleve, P.D. Adams, M.D. Winn, L.C. Storoni, and R.J. Read. 2007. Phaser crystallographic software. *Jounal of Applied Crystallography.* 40:658–674.

Evans, P. 2006. Scaling and assessment of data quality. *Acta Crystallogr. D Biol. Crystallogr.* 62:72–82.

Feller, S.E., Y.H. Zhang, R.W. Pastor, and B.R. Brooks. 1995. Constant pressure molecular dynamics simulation: The Langevin piston method. *Journal of Chemical Physics.* 103:4613–4621.

Flynn, G.E., and W.N. Zagotta. 2001. Conformational changes in S6 coupled to the opening of cyclic nucleotide-gated channels. *Neuron*. 30:689-698.

Fotiadis, D. 2012. Atomic force microscopy for the study of membrane proteins. *Current opinion in biotechnology*. 23:510-515.

Fotiadis, D., Y. Liang, S. Filipek, D.A. Saperstein, A. Engel, and K. Palczewski. 2003. Atomic-force microscopy: Rhodopsin dimers in native disc membranes. *Nature*. 421:127-128.

Francis, S.H., J.L. Busch, J.D. Corbin, and D. Sibley. 2010. cGMP-dependent protein kinases and cGMP phosphodiesterases in nitric oxide and cGMP action. *Pharmacological reviews*. 62:525-563.

Frank, J., Bretaudiere, J.-P., Carazo, J.-M., Veschoor, A., and Wagenknecht, T. 1987. Classification of images of biomolecular assemblies: A study of ribosomes and ribosomal subunits of Escheria coli. *Journal of microscopy*. 150: 99–115

Frauenfeld, J., J. Gumbart, E.O. Sluis, S. Funes, M. Gartmann, B. Beatrix, T. Mielke, O. Berninghausen, T. Becker, K. Schulten, and R. Beckmann. 2011. Cryo-EM structure of the ribosome-SecYE complex in the membrane environment. *Nature structural & molecular biology*. 18:614-621.

Frederix, P.L., P.D. Bosshart, and A. Engel. 2009. Atomic force microscopy of biological membranes. *Biophysical journal*. 96:329-338.

Friebe, A., and D. Koesling. 2003. Regulation of nitric oxide-sensitive guanylyl cyclase. *Circulation research*. 93:96-105.

Fukuhara, S., A. Sakurai, H. Sano, A. Yamagishi, S. Somekawa, N. Takakura, Y. Saito, K. Kangawa, and N. Mochizuki. 2005. Cyclic AMP potentiates vascular endothelial cadherin-mediated cell-cell contact to enhance endothelial barrier function through an Epac-Rap1 signaling pathway. *Molecular and cellular biology*. 25:136-146.

Furini, S., P. Barbini, and C. Domene. 2013. DNA-recognition process described by MD simulations of the lactose repressor protein on a specific and a non-specific DNA sequence. *Nucleic Acids Research.* 41:3963–3972.

Gloerich, M., and J.L. Bos. 2010. Epac: defining a new mechanism for cAMP action. *Annual review of pharmacology and toxicology*. 50:355-375.

Gluck, J.M., M. Wittlich, S. Feuerstein, S. Hoffmann, D. Willbold, and B.W. Koenig. 2009. Integral membrane proteins in nanodiscs can be studied by solution NMR spectroscopy. *Journal of the American Chemical Society*. 131:12060-12061.

Goldberg, N.D., S.B. Dietz, and A.G. O'Toole. 1969. Cyclic guanosine 3',5'-monophosphate in mammalian tissues and urine. *The Journal of biological chemistry*. 244:4458-4466.

Gross-Langenhoff, M., K. Hofbauer, J. Weber, A. Schultz, and J.E. Schultz. 2006. cAMP is a ligand for the tandem GAF domain of human phosphodiesterase 10 and cGMP for the tandem GAF domain of phosphodiesterase 11. *The Journal of biological chemistry*. 281:2841-2846.

Gupta, S., V.N. Bavro, R. D'Mello, S.J. Tucker, C. Vénien-Bryan, M.R. Chance. 2010. Conformational changes during the gating of a potassium channel revealed by structural mass spectrometry. *Structure.* 18:839-846.

Hanoune, J., and N. Defer. 2001. Regulation and role of adenylyl cyclase isoforms. *Annual review of pharmacology and toxicology*. 41:145-174.

Hardman, J.G., and E.W. Sutherland. 1969. Guanyl cyclase, an enzyme catalyzing the formation of guanosine 3',5'-monophosphate from guanosine trihosphate. *The Journal of biological chemistry*. 244:6363-6370.

Heginbotham, L., L. Kolmakova-Partensky, and C. Miller. 1998. Functional reconstitution of a prokaryotic K+ channel. *The Journal of general physiology*. 111:741-749.

Heginbotham, L., Z. Lu, T. Abramson, and R. MacKinnon. 1994. Mutations in the K+ channel signature sequence. *Biophysical journal*. 66:1061-1067.

Heginbotham, L., E. Odessey, and C. Miller. 1997. Tetrameric stoichiometry of a prokaryotic K+ channel. *Biochemistry*. 36:10335-10342.

Herberg, F.W., W.R. Dostmann, M. Zorn, S.J. Davis, and S.S. Taylor. 1994. Crosstalk between domains in the regulatory subunit of cAMP-dependent protein kinase:

influence of amino terminus on cAMP binding and holoenzyme formation. *Biochemistry*. 33:7485-7494.

Hibino, H., A. Inanobe, K. Furutani, S. Murakami, I. Findlay, and Y. Kurachi. 2010. Inwardly rectifying potassium channels: their structure, function, and physiological roles. *Physiological reviews*. 90:291-366.

Hille, B. 1973. Potassium channels in myelinated nerve. Selective permeability to small cations. *The Journal of general physiology*. 61:669-686.

Hille, B. 1992. Ionic Channels of Excitable Membranes. Second.ed. Sinauer Associates Inc., Sunderland, MA, USA.

Hille, B., and W. Schwarz. 1978. Potassium channels as multi-ion single-file pores. *The Journal of general physiology*. 72:409-442.

Hodgkin, A.L., and A.F. Huxley. 1952a. The components of membrane conductance in the giant axon of Loligo. *The Journal of physiology*. 116:473-496.

Hodgkin, A.L., and A.F. Huxley. 1952b. Currents carried by sodium and potassium ions through the membrane of the giant axon of Loligo. *The Journal of physiology*. 116:449-472.

Hodgkin, A.L., and A.F. Huxley. 1952c. A quantitative description of membrane current and its application to conduction and excitation in nerve. *The Journal of physiology*. 117:500-544.

Hodgkin, A.L., and R.D. Keynes. 1955. The potassium permeability of a giant nerve fibre. *The Journal of physiology*. 128:61-88.

Hofmann, F. 1980. Apparent constants for the interaction of regulatory and catalytic subunit of cAMP-dependent protein kinase I and II. *The Journal of biological chemistry*. 255:1559-1564.

Hoh, J.H., R. Lal, S.A. John, J.P. Revel, and M.F. Arnsdorf. 1991. Atomic force microscopy and dissection of gap junctions. *Science (New York, N.Y.)*. 253:1405-1408.

Holmgren, M., P.L. Smith, and G. Yellen. 1997. Trapping of organic blockers by closing of voltage-dependent K+ channels: evidence for a trap door mechanism of activation gating. *The Journal of general physiology*. 109:527-535.

Ishikawa, E., S. Ishikawa, J.W. Davis, and E.W. Sutherland. 1969. Determination of guanosine 3',5'-monophosphate in tissues and of guanyl cyclase in rat intestine. *The Journal of biological chemistry*. 244:6371-6376.

Jeong, K.H., and S.H. Lee. 2012. A new technical approach to monitor the cellular physiology by atomic force microscopy. *Electrolyte & blood pressure : E & BP*. 10:7-11.

Jezek, P., F. Mahdi, and K.D. Garlid. 1990. Reconstitution of the beef heart and rat liver mitochondrial K+/H+ (Na+/H+) antiporter. Quantitation of K+ transport with the novel fluorescent probe, PBFI. *The Journal of biological chemistry*. 265:10522-10526.

Johnson, D.A., P. Akamine, E. Radzio-Andzelm, M. Madhusudan, and S.S. Taylor. 2001. Dynamics of cAMP-dependent protein kinase. *Chemical reviews*. 101:2243-2270.

Jorgensen, W.L., J. Chandrasekhar, J.D. Madura, R.W. Impey, and M.L. Klein. 1983. Comparison of simple potential functions for simulating liquid water. *Journal of chemical physics.* 79:926–935.

Kabsch, W. 2010. XDS. *Acta Crystallogr. D Biol. Crystallogr.* 66:125–132.

Kaneko, T., Y. Nakamura, S. Sato, E. Asamizu, T. Kato, S. Sasamoto, A. Watanabe, K. Idesawa, A. Ishikawa, K. Kawashima, T. Kimura, Y. Kishida, C. Kiyokawa, M. Kohara, M. Matsumoto, A. Matsuno, Y. Mochizuki, S. Nakayama, N. Nakazaki, S. Shimpo, M. Sugimoto, C. Takeuchi, M. Yamada, and S. Tabata. 2000. Complete genome structure of the nitrogen-fixing symbiotic bacterium Mesorhizobium loti. *DNA research : an international journal for rapid publication of reports on genes and genomes*. 7:331-338.

Karle, I.L., J.L. Flippen-Anderson, R. Gurunath, and P. Balaram. 1994. Facile transition between 3(10)- and alpha-helix: structures of 8-, 9-, and 10-residue peptides containing the -(Leu-Aib-Ala)2-Phe-Aib- fragment. *Protein science : a publication of the Protein Society*. 3:1547-1555.

Kaupp, U.B., T. Niidome, T. Tanabe, S. Terada, W. Bonigk, W. Stuhmer, N.J. Cook, K. Kangawa, H. Matsuo, T. Hirose, and et al. 1989. Primary structure and functional expression from complementary DNA of the rod photoreceptor cyclic GMP-gated channel. *Nature*. 342:762-766.

Kaupp, U.B., and R. Seifert. 2001. Molecular diversity of pacemaker ion channels. *Annual review of physiology*. 63:235-257.

Kaupp, U.B., and R. Seifert. 2002. Cyclic nucleotide-gated ion channels. *Physiological reviews*. 82:769-824.

Kawasaki, H., G.M. Springett, N. Mochizuki, S. Toki, M. Nakaya, M. Matsuda, D.E. Housman, and A.M. Graybiel. 1998. A family of cAMP-binding proteins that directly activate Rap1. *Science (New York, N.Y.)*. 282:2275-2279.

Klein, P.S., T.J. Sun, C.L. Saxe, 3rd, A.R. Kimmel, R.L. Johnson, and P.N. Devreotes. 1988. A chemoattractant receptor controls development in Dictyostelium discoideum. *Science (New York, N.Y.)*. 241:1467-1472.

Kowal, J., M. Chami, P. Baumgartner, M. Arheit, P.L. Chiu, M. Rangl, S. Scheuring, G.F. Schroder, C.M. Nimigean, and H. Stahlberg. 2014. Ligand-induced structural

changes in the cyclic nucleotide-modulated potassium channel MloK1. *Nature communications*. 5:3106.

Kraemer, A., H.R. Rehmann, R.H. Cool, C. Theiss, J. de Rooij, J.L. Bos, and A. Wittinghofer. 2001. Dynamic interaction of cAMP with the Rap guanine-nucleotide exchange factor Epac1. *Journal of molecular biology*. 306:1167-1177.

Krishnamoorthy, G., J. Shi, D. Sept, J. Cui. 2005. The NH2 terminus of RCK1 domain regulates Ca2+-dependent BK(Ca) channel gating. *The Journal of general physiology*. 126:227-241.

Krishnan, M.N., J.P. Bingham, S.H. Lee, P. Trombley, and E. Moczydlowski. 2005. Functional role and affinity of inorganic cations in stabilizing the tetrameric structure of the KcsA K+ channel. *The Journal of general physiology*. 126:271-283.

Kuo, J.F., and P. Greengard. 1969a. An adenosine 3',5'-monophosphate-dependent protein kinase from Escherichia coli. *The Journal of biological chemistry*. 244:3417-3419.

Kuo, J.F., and P. Greengard. 1969b. Cyclic nucleotide-dependent protein kinases. IV. Widespread occurrence of adenosine 3',5'-monophosphate-dependent protein kinase in various tissues and phyla of the animal kingdom. *Proceedings of the National Academy of Sciences of the United States of America*. 64:1349-1355.

Kuo, J.F., and P. Greengard. 1970. Cyclic nucleotide-dependent protein kinases. VI. Isolation and partial purification of a protein kinase activated by guanosine 3',5'-monophosphate. *The Journal of biological chemistry*. 245:2493-2498.

Lakowicz, J.R. 2006. Principles of fluorescence spectroscopy. Third.ed. Springer, New York, NY, USA.

Levy, D., M. Chami, and J.L. Rigaud. 2001. Two-dimensional crystallization of membrane proteins: the lipid layer strategy. *FEBS letters*. 504:187-193.

Lewis, A.S., and D.M. Chetkovich. 2011. HCN channels in behavior and neurological disease: too hyper or not active enough? *Molecular and cellular neurosciences*. 46:357-367.

Li, W., Z. Shariat-Madar, M. Powers, X. Sun, R.D. Lane, and K.D. Garlid. 1992. Reconstitution, identification, purification, and immunological characterization of the 110-kDa Na+/Ca2+ antiporter from beef heart mitochondria. *The Journal of biological chemistry*. 267:17983-17989.

Lincoln, T.M., and J.D. Corbin. 1977. Adenosine 3':5'-cyclic monophosphate- and guanosine 3':5'-cyclic monophosphate-dependent protein kinases: possible homologous proteins. *Proceedings of the National Academy of Sciences of the United States of America*. 74:3239-3243.

Lipkin, D.C., W. H.; Markham, R. 1959. Adenosine-3′:5′-phosphoric acid: a proof of structure. *J. Am. Chem. Soc.* 81:6198-6203.

Liu, L.N., and S. Scheuring. 2013. Investigation of photosynthetic membrane structure using atomic force microscopy. *Trends in plant science*. 18:277-286.

Liu, Y., M. Holmgren, M.E. Jurman, and G. Yellen. 1997. Gated access to the pore of a voltage-dependent K+ channel. *Neuron*. 19:175-184.

Loboda, A., A. Melishchuk, and C. Armstrong. 2001. Dilated and defunct K channels in the absence of K+. *Biophysical journal*. 80:2704-2714.

Long, S.B., E.B. Campbell, and R. Mackinnon. 2005. Voltage sensor of Kv1.2: structural basis of electromechanical coupling. *Science (New York, N.Y.)*. 309:903-908.

Long, S.B., X. Tao, E.B. Campbell, and R. MacKinnon. 2007. Atomic structure of a voltage-dependent K+ channel in a lipid membrane-like environment. *Nature*. 450:376-382.

Lyukmanova, E.N., Z.O. Shenkarev, A.S. Paramonov, A.G. Sobol, T.V. Ovchinnikova, V.V. Chupin, M.P. Kirpichnikov, M.J. Blommers, and A.S. Arseniev. 2008. Lipid-protein nanoscale bilayers: a versatile medium for NMR investigations of membrane proteins and membrane-active peptides. *Journal of the American Chemical Society*. 130:2140-2141.

MacKerell, A.D., D. Bashford, M. Bellott, R.L. Dunbrack, J.D. Evanseck, M.J. Field, S. Fischer, J. Gao, H. Guo, S. Ha, et al. 1998. All-atom empirical potential for molecular modeling and dynamics studies of proteins. *J. Phys. Chem. B*. 102:3586–3616.

MacKinnon, R. 1991. Determination of the subunit stoichiometry of a voltage-activated potassium channel. *Nature*. 350:232-235.

MacKinnon, R. 2003. Potassium channels. *FEBS letters*. 555:62-65.

MacKinnon, R., S.L. Cohen, A. Kuo, A. Lee, and B.T. Chait. 1998. Structural conservation in prokaryotic and eukaryotic potassium channels. *Science (New York, N.Y.)*. 280:106-109.

Manganiello, V.C., T. Murata, M. Taira, P. Belfrage, and E. Degerman. 1995. Diversity in cyclic nucleotide phosphodiesterase isoenzyme families. *Archives of biochemistry and biophysics*. 322:1-13.

Martyna, G.J., D.J. Tobias, and M.L. Klein. 1994. Constant pressure molecular dynamics algorithms. *J. Chem. Phys.* 101:4177–4189.

Matulef, K., and W.N. Zagotta. 2003. Cyclic nucleotide-gated ion channels. *Annual review of cell and developmental biology*. 19:23-44.

McCoy, J.G., and C.M. Nimigean. 2012. Structural correlates of selectivity and inactivation in potassium channels. *Biochimica et biophysica acta*. 1818:272-285.

McCoy, A.J., R.W. Grosse-Kunstleve, P.D. Adams, M.D. Winn, L.C. Storoni, and R.J. Read. 2007. Phaser crystallographic software. *J. Appl. Cryst.* 40:658–674.

McCoy, J.G., R. Rusinova, D.M. Kim, J. Kowal, S. Banerjee, A. Jaramillo Cartagena, A.N. Thompson, L. Kolmakova-Partensky, H. Stahlberg, O.S. Andersen, and C.M. Nimigean. 2014. A KcsA/MloK1 chimeric ion channel has lipid-dependent ligand-binding energetics. *The Journal of biological chemistry*. 289:9535-9546.

McKay, D.B., and T.A. Steitz. 1981. Structure of catabolite gene activator protein at 2.9 A resolution suggests binding to left-handed B-DNA. *Nature*. 290:744-749.

McKay, D.B., I.T. Weber, and T.A. Steitz. 1982. Structure of catabolite gene activator protein at 2.9-A resolution. Incorporation of amino acid sequence and interactions with cyclic AMP. *The Journal of biological chemistry*. 257:9518-9524.

Menini, A. 1995. Cyclic nucleotide-gated channels in visual and olfactory transduction. *Biophysical chemistry*. 55:185-196.

Miyamoto, E., J.F. Kuo, and P. Greengard. 1969. Cyclic nucleotide-dependent protein kinases. 3. Purification and properties of adenosine 3',5'-monophosphate-dependent protein kinase from bovine brain. *The Journal of biological chemistry*. 244:6395-6402.

Miyamoto, S., and P.A. Kollman. 1992. Settle: An analytical version of the SHAKE and RATTLE algorithm for rigid water molecules. *J. Comput. Chem.* 13:952–962.

Morais-Cabral, J.H., Y. Zhou, and R. MacKinnon. 2001. Energetic optimization of ion conduction rate by the K+ selectivity filter. *Nature*. 414:37-42.

Muller, D.J. 2008. AFM: a nanotool in membrane biology. *Biochemistry*. 47:7986-7998.

Muller, D.J., Amrein, M, and Engel, A. (1997) Adsorption of biological molecules to a solid support for scanning probe microscopy. Journal of structural biology. 119:172–188.

Muller, D. J., and Engel, A. (2007) Atomic force microscopy and spectroscopy of native membrane proteins. *Nature Protocols* 2:2191–2197.

Muller, D.J., G.M. Hand, A. Engel, and G.E. Sosinsky. 2002. Conformational changes in surface structures of isolated connexin 26 gap junctions. *The EMBO journal*. 21:3598-3607.

Nakamura, T., and G.H. Gold. 1987. A cyclic nucleotide-gated conductance in olfactory receptor cilia. *Nature*. 325:442-444.

Narayanaswami, V., and R.O. Ryan. 2000. Molecular basis of exchangeable apolipoprotein function. *Biochimica et biophysica acta*. 1483:15-36.

Nath, A., W.M. Atkins, and S.G. Sligar. 2007. Applications of phospholipid bilayer nanodiscs in the study of membranes and membrane proteins. *Biochemistry*. 46:2059-2069.

Nelson, D.L.C., M. M. 2005. Lehninger Principles of Biochemistry. Fourth.ed. W. HO. Freeman, New York, NY, USA.

Nimigean, C.M. 2006. A radioactive uptake assay to measure ion transport across ion channel-containing liposomes. *Nature protocols*. 1:1207-1212.

Nimigean, C.M., and M.D. Pagel. 2007. Ligand binding and activation in a prokaryotic cyclic nucleotide-modulated channel. *Journal of molecular biology*. 371:1325-1337.

Nimigean, C.M., T. Shane, and C. Miller. 2004. A cyclic nucleotide modulated prokaryotic K+ channel. *The Journal of general physiology*. 124:203-210.

Nishida, M., and R. MacKinnon. 2002. Structural basis of inward rectification: cytoplasmic pore of the G protein-gated inward rectifier GIRK1 at 1.8 A resolution. *Cell*. 111:957-965.

Pandit, A., N. Shirzad-Wasei, L.M. Wlodarczyk, H. van Roon, E.J. Boekema, J.P. Dekker, and W.J. de Grip. 2011. Assembly of the major light-harvesting complex II in lipid nanodiscs. *Biophysical journal*. 101:2507-2515.

Paucek, P., G. Mironova, F. Mahdi, A.D. Beavis, G. Woldegiorgis, and K.D. Garlid. 1992. Reconstitution and partial purification of the glibenclamide-sensitive, ATP-dependent K+ channel from rat liver and beef heart mitochondria. *The Journal of biological chemistry*. 267:26062-26069.

Pettersen, E.F., T.D. Goddard, C.C. Huang, G.S. Couch, D.M. Greenblatt, E.C. Meng, and T.E. Ferrin. 2004. UCSF Chimera--a visualization system for exploratory research and analysis. *Journal of computational chemistry*. 25:1605-1612.

Peuker, S., A. Cukkemane, M. Held, F. Noe, U.B. Kaupp, and R. Seifert. 2013. Kinetics of ligand-receptor interaction reveals an induced-fit mode of binding in a cyclic nucleotide-activated protein. *Biophysical journal*. 104:63-74.

Phillips, J.C., R. Braun, W. Wang, J. Gumbart, E. Tajkhorshid, E. Villa, C. Chipot, R.D. Skeel, L. Kalé, and K. Schulten. 2005. Scalable molecular dynamics with NAMD. *Journal of computational chemistry.* 26:1781–1802.

Picco, L.M.B., L.; Ulcinas, A.; Engledew, D. J.; Antognozzi, M.; Horton, M. A. and Miles, M. J. 2007. Breaking the speed limit with atomic force microscopy. *Nanotechnology*. 18:044030.

Podda, M.V., and C. Grassi. 2013. New perspectives in cyclic nucleotide-mediated functions in the CNS: the emerging role of cyclic nucleotide-gated (CNG) channels. *Pflugers Archiv : European journal of physiology*.

Pongs, O., N. Kecskemethy, R. Muller, I. Krah-Jentgens, A. Baumann, H.H. Kiltz, I. Canal, S. Llamazares, and A. Ferrus. 1988. Shaker encodes a family of putative potassium channel proteins in the nervous system of Drosophila. *The EMBO journal*. 7:1087-1096.

Postea, O., and M. Biel. 2011. Exploring HCN channels as novel drug targets. *Nature reviews. Drug discovery*. 10:903-914.

Rall, T.W., and E.W. Sutherland. 1958. Formation of a cyclic adenine ribonucleotide by tissue particles. *The Journal of biological chemistry*. 232:1065-1076.

Rall, T.W., and E.W. Sutherland. 1962. Adenyl cyclase. II. The enzymatically catalyzed formation of adenosine 3',5'-phosphate and inorganic pyrophosphate from adenosine triphosphate. *The Journal of biological chemistry*. 237:1228-1232.

Ranganathan, R., J.H. Lewis, and R. MacKinnon. 1996. Spatial localization of the K+ channel selectivity filter by mutant cycle-based structure analysis. *Neuron*. 16:131-139.

Rehmann, H., E. Arias-Palomo, M.A. Hadders, F. Schwede, O. Llorca, and J.L. Bos. 2008. Structure of Epac2 in complex with a cyclic AMP analogue and RAP1B. *Nature*. 455:124-127.

Rehmann, H., J. Das, P. Knipscheer, A. Wittinghofer, and J.L. Bos. 2006. Structure of the cyclic-AMP-responsive exchange factor Epac2 in its auto-inhibited state. *Nature*. 439:625-628.

Rehmann, H., B. Prakash, E. Wolf, A. Rueppel, J. de Rooij, J.L. Bos, and A. Wittinghofer. 2003. Structure and regulation of the cAMP-binding domains of Epac2. *Nature structural biology*. 10:26-32.

Rehmann, H., A. Wittinghofer, and J.L. Bos. 2007. Capturing cyclic nucleotides in action: snapshots from crystallographic studies. *Nature reviews. Molecular cell biology*. 8:63-73.

Riener, C.K., G. Kada, and H.J. Gruber. 2002. Quick measurement of protein sulfhydryls with Ellman's reagent and with 4,4'-dithiodipyridine. *Analytical and bioanalytical chemistry*. 373:266-276.

Roosild, T.P., S. Castronovo, S. Miller, C. Li, T. Rasmussen, W. Bartlett, B. Gunasekera, S. Choe, and I.R. Booth. 2009. KTN (RCK) domains regulate K+ channels and transporters by controlling the dimer-hinge conformation. *Structure (London, England : 1993)*. 17:893-903.

Rothberg, B.S. 2012. The BK channel: a vital link between cellular calcium and electrical signaling. *Protein & cell*. 3:883-892.

Roux, B., and R. MacKinnon. 1999. The cavity and pore helices in the KcsA K+ channel: electrostatic stabilization of monovalent cations. *Science (New York, N.Y.)*. 285:100-102.

Ryan, R.O. 2010. Nanobiotechnology applications of reconstituted high density lipoprotein. *Journal of nanobiotechnology*. 8:28.

Safenkova, I.V., A.V. Zherdev, and B.B. Dzantievf. 2012. Application of atomic force microscopy for characteristics of single intermolecular interactions. *Biochemistry. Biokhimiia*. 77:1536-1552.

Saxton, W.O., Pitt, T.J., and Horner, M. (1979) Digital image processing: The semper system. Ultramicroscopy 4:343–354.

Saxton, W.O., and Baumeister, W. (1982) The correlation averaging of a regularly arranged bacterial cell envelope protein. J Microsc 127:127–138.

Schrempf, H., O. Schmidt, R. Kummerlen, S. Hinnah, D. Muller, M. Betzler, T. Steinkamp, and R. Wagner. 1995. A prokaryotic potassium ion channel with two predicted transmembrane segments from Streptomyces lividans. *The EMBO journal*. 14:5170-5178.

Schunke, S., J. Lecher, M. Stoldt, U.B. Kaupp, and D. Willbold. 2010. Resonance assignments of the nucleotide-free wildtype MloK1 cyclic nucleotide-binding domain. *Biomolecular NMR assignments*. 4:147-150.

Schunke, S., K. Novak, M. Stoldt, U.B. Kaupp, and D. Willbold. 2007. Resonance assignment of the cyclic nucleotide binding domain from a cyclic nucleotide-gated K(+) channel in complex with cAMP. *Biomolecular NMR assignments*. 1:179-181.

Schunke, S., M. Stoldt, J. Lecher, U.B. Kaupp, and D. Willbold. 2011. Structural insights into conformational changes of a cyclic nucleotide-binding domain in solution from Mesorhizobium loti K1 channel. *Proceedings of the National Academy of Sciences of the United States of America*. 108:6121-6126.

Schunke, S., M. Stoldt, K. Novak, U.B. Kaupp, and D. Willbold. 2009. Solution structure of the Mesorhizobium loti K1 channel cyclic nucleotide-binding domain in complex with cAMP. *EMBO reports*. 10:729-735.

Sedlak, J., and R.H. Lindsay. 1968. Estimation of total, protein-bound, and nonprotein sulfhydryl groups in tissue with Ellman's reagent. *Analytical biochemistry*. 25:192-205.

Shabb, J.B., and J.D. Corbin. 1992. Cyclic nucleotide-binding domains in proteins having diverse functions. *The Journal of biological chemistry*. 267:5723-5726.

Shenkarev, Z.O., E.N. Lyukmanova, O.I. Solozhenkin, I.E. Gagnidze, O.V. Nekrasova, V.V. Chupin, A.A. Tagaev, Z.A. Yakimenko, T.V. Ovchinnikova, M.P. Kirpichnikov, and A.S. Arseniev. 2009. Lipid-protein nanodiscs: possible application in high-resolution NMR investigations of membrane proteins and membrane-active peptides. *Biochemistry. Biokhimiia*. 74:756-765.

Shibasaki, T., H. Takahashi, T. Miki, Y. Sunaga, K. Matsumura, M. Yamanaka, C. Zhang, A. Tamamoto, T. Satoh, J. Miyazaki, and S. Seino. 2007. Essential role of Epac2/Rap1 signaling in regulation of insulin granule dynamics by cAMP.

Proceedings of the National Academy of Sciences of the United States of America. 104:19333-19338.

Silverman, W.R., and L. Heginbotham. 2007. The MlotiK1 channel transports ions along the canonical conduction pore. *FEBS letters*. 581:5024-5028.

Stahlberg, H., D. Fotiadis, S. Scheuring, H. Remigy, T. Braun, K. Mitsuoka, Y. Fujiyoshi, and A. Engel. 2001. Two-dimensional crystals: a powerful approach to assess structure, function and dynamics of membrane proteins. *FEBS letters*. 504:166-172.

Sutherland, E.W. 1972. Studies on the mechanism of hormone action. *Science (New York, N.Y.)*. 177:401-408.

Sutherland, E.W., and T.W. Rall. 1958. Fractionation and characterization of a cyclic adenine ribonucleotide formed by tissue particles. *The Journal of biological chemistry*. 232:1077-1091.

Sutherland, E.W., T.W. Rall, and T. Menon. 1962. Adenyl cylase. I. Distribution, preparation, and properties. *The Journal of biological chemistry*. 237:1220-1227.

Tang, C.Y., and D.M. Papazian. 1997. Transfer of voltage independence from a rat olfactory channel to the Drosophila ether-a-go-go K+ channel. *The Journal of general physiology*. 109:301-311.

Tang, G., L. Peng, P.R. Baldwin, D.S. Mann, W. Jiang, I. Rees, and S.J. Ludtke. 2007. EMAN2: an extensible image processing suite for electron microscopy. *Journal of structural biology*. 157:38-46.

Tao, X., J.L. Avalos, J. Chen, and R. MacKinnon. 2009. Crystal structure of the eukaryotic strong inward-rectifier K+ channel Kir2.2 at 3.1 A resolution. *Science (New York, N.Y.)*. 326:1668-1674.

Tesmer, J.J. 2008. Guanylyl cyclase sees the light. *Journal of biology*. 7:31.

Theurkauf, W.E., and R.B. Vallee. 1982. Molecular characterization of the cAMP-dependent protein kinase bound to microtubule-associated protein 2. *The Journal of biological chemistry*. 257:3284-3290.

Thompson, A.N., I. Kim, T.D. Panosian, T.M. Iverson, T.W. Allen, and C.M. Nimigean. 2009. Mechanism of potassium-channel selectivity revealed by Na(+) and Li(+) binding sites within the KcsA pore. *Nature structural & molecular biology*. 16:1317-1324.

Titani, K., T. Sasagawa, L.H. Ericsson, S. Kumar, S.B. Smith, E.G. Krebs, and K.A. Walsh. 1984. Amino acid sequence of the regulatory subunit of bovine type I adenosine cyclic 3',5'-phosphate dependent protein kinase. *Biochemistry*. 23:4193-4199.

Tombola, F., M.M. Pathak, and E.Y. Isacoff. 2006. How does voltage open an ion channel? *Annual review of cell and developmental biology*. 22:23-52.

Torres, Y.P., F.J. Morera, I. Carvacho, and R. Latorre. 2007. A marriage of convenience: beta-subunits and voltage-dependent K+ channels. *The Journal of biological chemistry*. 282:24485-24489.

Trudeau, M.C., and W.N. Zagotta. 2003. Calcium/calmodulin modulation of olfactory and rod cyclic nucleotide-gated ion channels. *The Journal of biological chemistry*. 278:18705-18708.

Vaandrager, A.B., and H.R. de Jonge. 1996. Signalling by cGMP-dependent protein kinases. *Molecular and cellular biochemistry*. 157:23-30.

Varnum, M.D., K.D. Black, and W.N. Zagotta. 1995. Molecular mechanism for ligand discrimination of cyclic nucleotide-gated channels. *Neuron*. 15:619-625.

Viani, M.B., T.E. Schäffer, A. Chand, M. Rief, H.E. Gaub, and P.K. Hansma. 1999. Small cantilevers for force spectroscopy of single molecules. *J. Appl. Phys.* 86:2258-2262.

Vieira-Pires, R.S., and J.H. Morais-Cabral. 2010. 3(10) helices in channels and other membrane proteins. *The Journal of general physiology*. 136:585-592.

Vopel, T., S. Kunzelmann, and C. Herrmann. 2009. Nucleotide dependent cysteine reactivity of hGBP1 uncovers a domain movement during GTP hydrolysis. *FEBS letters*. 583:1923-1927.

Walsh, D.A., J.P. Perkins, and E.G. Krebs. 1968. An adenosine 3',5'-monophosphate-dependant protein kinase from rabbit skeletal muscle. *The Journal of biological chemistry*. 243:3763-3765.

Wedel, B., and D. Garbers. 2001. The guanylyl cyclase family at Y2K. *Annual review of physiology*. 63:215-233.

White, A.A., and G.D. Aurbach. 1969. Detection of guanyl cyclase in mammalian tissues. *Biochimica et biophysica acta*. 191:686-697.

Whited, A.M., and P.S. Park. 2014. Atomic force microscopy: a multifaceted tool to study membrane proteins and their interactions with ligands. *Biochimica et biophysica acta*. 1838:56-68.

Wolfe, L., S.H. Francis, and J.D. Corbin. 1989. Properties of a cGMP-dependent monomeric protein kinase from bovine aorta. *The Journal of biological chemistry*. 264:4157-4162.

Yellen, G. 2002. The voltage-gated potassium channels and their relatives. *Nature*. 419:35-42.

Yu, J., C.A. Bippes, G.M. Hand, D.J. Muller, and G.E. Sosinsky. 2007. Aminosulfonate modulated pH-induced conformational changes in connexin26 hemichannels. *The Journal of biological chemistry*. 282:8895-8904.

Zaitseva, E., M. Saavedra, S. Banerjee, T.P. Sakmar, and R. Vogel. 2010. SEIRA spectroscopy on a membrane receptor monolayer using lipoprotein particles as carriers. *Biophysical journal*. 99:2327-2335.

Zelman, A.K., A. Dawe, C. Gehring, and G.A. Berkowitz. 2012. Evolutionary and structural perspectives of plant cyclic nucleotide-gated cation channels. *Frontiers in plant science*. 3:95.

Zhao, J., E. Hoye, S. Boylan, D.A. Walsh, and J. Trewhella. 1998. Quaternary structures of a catalytic subunit-regulatory subunit dimeric complex and the holoenzyme of the cAMP-dependent protein kinase by neutron contrast variation. *The Journal of biological chemistry*. 273:30448-30459.

Zhou, L., and S.A. Siegelbaum. 2007. Gating of HCN channels by cyclic nucleotides: residue contacts that underlie ligand binding, selectivity, and efficacy. *Structure (London, England : 1993)*. 15:655-670.

Zhou, Y., and R. MacKinnon. 2003. The occupancy of ions in the K+ selectivity filter: charge balance and coupling of ion binding to a protein conformational change underlie high conduction rates. *Journal of molecular biology*. 333:965-975.

Zhou, Y., J.H. Morais-Cabral, A. Kaufman, and R. MacKinnon. 2001. Chemistry of ion coordination and hydration revealed by a K+ channel-Fab complex at 2.0 A resolution. *Nature*. 414:43-48.

Zoraghi, R., J.D. Corbin, and S.H. Francis. 2004. Properties and functions of GAF domains in cyclic nucleotide phosphodiesterases and other proteins. *Molecular pharmacology*. 65:267-278.

Zubay, G., D. Schwartz, and J. Beckwith. 1970. Mechanism of activation of catabolite-sensitive genes: a positive control system. *Proceedings of the National Academy of Sciences of the United States of America*. 66:104-110.

8. Publications

Published June 30, 2014

Determinants of ligand selectivity in a cyclic nucleotide–regulated potassium channel

João Pessoa,[1,2] Fátima Fonseca,[1] Simone Furini,[3] and João H. Morais-Cabral[1]

[1]Instituto de Biologia Molecular e Celular and [2]Instituto de Ciências Biomédicas Abel Salazar, Universidade do Porto, 4150-180 Porto, Portugal

[3]Department of Medical Biotechnologies, University of Siena, 53100 Siena, Italy

Cyclic nucleotide–binding (CNB) domains regulate the activity of channels, kinases, exchange factors, and transcription factors. These proteins are highly variable in their ligand selectivity; some are highly selective for either cAMP or cGMP, whereas others are not. Several molecular determinants of ligand selectivity in CNB domains have been defined, but these do not provide a complete view of the selectivity mechanism. We performed a thorough analysis of the ligand-binding properties of mutants of the CNB domain from the MlotiK1 potassium channel. In particular, we defined which residues specifically favor cGMP or cAMP. Inversion of ligand selectivity, from favoring cAMP to favoring cGMP, was only achieved through a combination of three mutations in the ligand-binding pocket. We determined the x-ray structure of the triple mutant bound to cGMP and performed molecular dynamics simulations and a biochemical analysis of the effect of the mutations. We concluded that the increase in cGMP affinity and selectivity does not result simply from direct interactions between the nucleotide base and the amino acids introduced in the ligand-binding pocket residues. Rather, tighter cGMP binding over cAMP results from the polar chemical character of the mutations, from greater accessibility of water molecules to the ligand in the bound state, and from an increase in the structural flexibility of the mutated binding pocket.

INTRODUCTION

The cyclic nucleotides cAMP and cGMP are important secondary messengers in several signal transduction pathways, including those of vision and olfaction (Zhang and Cote, 2005; Rehmann et al., 2007; Pifferi et al., 2010). Action of these small molecules is, in many cases, dependent on binding to a cyclic nucleotide–binding (CNB) domain. Ligand binding induces a conformational change in the CNB domain, which is propagated to an effector domain leading to a functional alteration (Rehmann et al., 2007). Among the proteins with cyclic nucleotide–dependent activity, there are three families of cation tetrameric channels (Fig. S1): the eukaryotic CNG channels (Craven and Zagotta, 2006); the eukaryotic hyperpolarization-activated CNG (HCN) channels (Craven and Zagotta, 2006); and the bacterial cyclic nucleotide–regulated channels, which include the MlotiK1 potassium channel (Clayton et al., 2004; Nimigean et al., 2004). All of these channels have subunits with six transmembrane helices and a C-terminal cytoplasmic CNB domain.

The ligand-binding pocket in CNB domains (Fig. 1 A) has a shallow cavity, formed by residues from several structural motifs (the β4–β5 hairpin, the αP helix, and loop of the phosphate-binding cassette [PBC]) and a lid that closes over the nucleotide (Rehmann et al., 2007). In MlotiK1, the lid is formed by the C-terminal αC helix and includes an arginine (R348) that interacts directly with the nucleotide base (Clayton et al., 2004). Strikingly, cyclic nucleotide selectivity varies greatly among proteins with CNB domains, with some proteins strongly favoring cAMP while others favor cGMP. For example, the bovine rod photoreceptor and olfactory CNG channels are ∼40 times more sensitive to cGMP than to cAMP, as measured from the ratio of the $K_{1/2}$ for channel activation (Altenhofen et al., 1991). In the olfactory channel, mutation of a threonine at the C-terminal end of the PBC to alanine was sufficient to invert selectivity from a 40-fold preference for cGMP to a 3.3-fold preference for cAMP. However, the equivalent mutation in the rod photoreceptor channel, although reducing affinity for cGMP, did not invert selectivity. However, mutation of an aspartate present in the αC helix of the bovine rod CNG channel to a non-negatively charged residue resulted in the inversion of the efficacy of cGMP versus cAMP to act as agonists (Varnum et al., 1995). Nimigean and Pagel (2007) analyzed the effect of equivalent mutations in the MlotiK1 channel. They found that mutations S308V, equivalent to the threonine in the PBC, and A352D, equivalent to the aspartate in αC helix,

Correspondence to João H. Morais-Cabral: jcabral@ibmc.up.pt

Abbreviations used in this paper: CNB, cyclic nucleotide–binding; HCN, hyperpolarization-activated CNG; MD, molecular dynamics; PBC, phosphate-binding cassette; RMSD, root-mean-square deviation.

The Rockefeller University Press $30.00
J. Gen. Physiol. Vol. 144 No. 1 41–54
www.jgp.org/cgi/doi/10.1085/jgp.201311145

Supplemental Material can be found at:
http://jgp.rupress.org/content/suppl/2014/06/26/jgp.201311145.DC1.html

Published June 30, 2014

altered the affinity for cAMP and cGMP, as predicted previously. However, these changes were relatively small, and channel ligand selectivity was not inverted. The inability to define general rules that explain selectivity in CNB domains (Cukkemane et al., 2011) is a reflection of our incomplete understanding of this mechanism, and it probably results from several factors: the difficulty of many studies to distinguish the impact of mutated residues on functional selectivity versus binding selectivity, the lack of structural analysis to complement the biochemical or functional studies, and the inexhaustive exploration of all the residues in the binding pocket of CNB domains.

The MlotiK1 channel is particularly amenable for defining the determinants of cyclic nucleotide selectivity. This channel has been well characterized at a structural, functional, and biochemical level (Clayton et al., 2004, 2008; Nimigean et al., 2004; Chiu et al., 2007; Cukkemane et al., 2007; Nimigean and Pagel, 2007; Altieri et al., 2008; Schünke et al., 2009, 2011; Peuker et al., 2013), and, by studying the isolated CNB domain, it is possible to separate ligand binding from, at least, the final steps of the mechanism of channel activation. We performed an extensive mutagenesis analysis of the residues involved in the structural interaction with the nucleotide base and evaluated the impact of these mutations on the binding of cAMP and cGMP. Ligand-binding selectivity was inverted only after three different mutations were combined; a structural analysis of this triple mutant reveals how these mutations alter the molecular details of the nucleotide-binding pocket.

MATERIALS AND METHODS

Preparation of CNB domain without ligand

MlotiK1 CNB domain mutants were expressed and purified as described previously (Clayton et al., 2004). PBS buffer containing 2 mM DTT (purification buffer) was used throughout purification. Size-exclusion chromatography was performed in a Superdex 75 column (GE Healthcare). For preparation of apo-domain, freshly purified protein was incubated overnight with cAMP agarose beads (Sigma-Aldrich), and bound protein was extensively washed with purification buffer. cAMP-free protein was eluted by unfolding with purification buffer that included 3 M guanidinium chloride (unfolding buffer). cAMP removal was monitored by determining the OD_{260}/OD_{280} ratio, as described previously (Peuker et al., 2013). Typical values varied between 0.65 and 0.90 for nucleotide-free CNB domain. Protein was first diluted to 0.3 mg/ml with unfolding buffer and then diluted threefold into refolding buffer (100 mM NaCl, 10 mM sodium phosphate, pH 7.0, 5 mM glutathione [reduced], 0.5 mM glutathione [oxidized], 0.5 mM L-arginine, and 10 mM EDTA) (Cukkemane et al., 2007) to a final concentration of 0.1 mg/ml protein and 1 M guanidinium chloride. This solution was gently stirred at 4°C for 3 h, and then the protein was concentrated to ∼0.3 mg/ml. The refolded protein was further dialyzed against refolding buffer to lower guanidinium chloride concentration to ∼50 mM. Dialyzed protein was concentrated and loaded onto a Superdex 75 size-exclusion column to remove misfolded protein (Peuker et al., 2013) (folded protein elutes at 12.0–12.5 ml, and misfolded protein elutes at 16.0–17.0 ml). Finally, refolded apo-protein was dialyzed against 10 mM HEPES buffer, pH 7.5, and 100 mM NaCl before binding assays.

Cyclic nucleotide–binding assays

Dissociation constants were determined at room temperature in 10 mM HEPES, pH 7.5, and 100 mM NaCl, with a fluorescence assay that uses the fluorescent nucleotide analogue 8-NBD cAMP (Biolog) (Cukkemane et al., 2007; Altieri et al., 2008). Cyclic nucleotides (cAMP and cGMP [both from Sigma-Aldrich], cIMP [Sigma-Aldrich], and cCMP [Biolog]) were purchased as acids or as sodium salts. For each mutant, the K_d of the fluorescent analogue was determined by titrating 50 nM 8-NBD cAMP with increasing protein concentrations and collecting fluorescence emission spectra (excitation at 471 nm) in a spectrofluorometer (Fluoromax-4; Horiba Scientific). For each protein concentration tested, emission at 536 nm was normalized as described previously (Altieri et al., 2008), and data were fitted with the following equation:

$$y = \frac{1}{1 + \frac{2}{-1 - \frac{L}{K} + \frac{P}{K} + \sqrt{\left(1 + \frac{L}{K} - \frac{P}{K}\right)^2 + 4 \times \frac{P}{K}}}},$$

where y is the normalized fluorescence intensity, K is the dissociation constant of 8-NBD cAMP, P is protein concentration, and L is 8-NBD cAMP concentration.

For determination of the dissociation equilibrium constants of cAMP or cGMP, the above assay was repeated in the presence of a competing fixed concentration of cAMP or cGMP in each sample. For determination of the competing concentration, the protein concentration that resulted in 70–80% of the maximum signal was selected and titrated with increased ligand concentrations. The ligand concentration that decreased the signal to 40–50% was then chosen for the competition assay. Data were fitted with the following equation:

$$y = G \times L1 \times \frac{2\sqrt{a^2 - 3b}\cos\left(\frac{c}{3}\right) - a}{3K1 + 2\sqrt{a^2 - 3b}\cos\left(\frac{c}{3}\right) - a} + y0,$$

where,

$$a = K1 + K2 + L1 + L2 - P$$
$$b = K2(L1 - P) + K1(L2 - P) + K1K2$$
$$c = \arccos\frac{-2a^3 + 9ab + 27K1K2P}{2\sqrt{(a^2 - 3b)^3}},$$

where y is the fluorescence intensity, $K1$ is the dissociation constant of 8-NBD cAMP, $K2$ is the dissociation constant of cAMP or cGMP, $L1$ is the 8-NBD cAMP concentration, P is total protein concentration, $L2$ is total concentration of cAMP or cGMP, G is signal gain, and $y0$ is signal offset.

For mutants displaying 8-NBD cAMP dissociation constants higher than 5 µM, a modified assay was used (Altieri et al., 2008). The concentrations of the protein and 8-NBD cAMP were fixed at approximately the K_d value and two times the K_d value, respectively, and titrated with increasing cAMP or cGMP concentrations. Data were fitted with the previous equation but with a varying cyclic nucleotide concentration.

Published June 30, 2014

Expression and purification of full-length MlotiK1 channel

Full-length MlotiK1 T284S/V288S/A352D was expressed, purified, and reconstituted as described previously for the wild-type channel (Clayton et al., 2004; Nimigean et al., 2004). In brief, MlotiK1 expressed in C41 (DE3) cells was extracted at 4°C for 30 min with PBS buffer, pH 7.4, containing 50 mM *n*-decyl-β-D-maltopyranoside (DM; Anatrace), 200 µM cAMP, 5 mM β-mercaptethanol. During purification and until gel filtration, the same buffer was used, but cAMP was excluded and the DM concentration decreased to 5 mM, unless stated otherwise. Detergent-extracted proteins were incubated with nickel beads and first washed with 50 mM imidazole to remove nonspecifically bound proteins, followed by a 200-ml wash in 2 mM DM. This ensured that cAMP bound to the triple mutant channel, which has micromolar affinity for cAMP, would dissociate from the protein. MlotiK1 was eluted in 500 mM imidazole and further purified by gel filtration on a Superdex 200 column (GE Healthcare) equilibrated in 20 mM Tris-HCl, pH 7.5, 150 mM KCl, 5 mM DM, and 3 mM DTT. Protein was immediately reconstituted in the presence of different ligand concentrations.

Liposome reconstitution and radioactive uptake assay

Proteoliposome preparation followed previously described procedures (Clayton et al., 2004; Nimigean et al., 2004; Altieri et al., 2008). In brief, 7.5 µg MlotiK1 protein was mixed with 1.5 mg *Escherichia coli* polar lipids (Avanti Polar Lipids, Inc.) in 10 mM HEPES, 5 mM *N*-methyl-β-D-glucamine (NMG), pH 7.6, and 150 mM KCl for a total volume of 150 µl. The detergent was removed by hydrophobic adsorption using Bio-Beads SM-2 (Bio-Rad Laboratories). Samples were gently stirred for 1 h at room temperature at a Bio-Beads/detergent (wt/wt) ratio of 10-15. This step was repeated twice and followed by an overnight incubation at 4°C with at a Bio-Beads/detergent (wt/wt) ratio of 20-30. Proteoliposomes were not frozen at any stage. A potassium concentration gradient was established by exchanging the external buffer to 10 mM HEPES, 5 mM NMG, pH 7.6, 20 µM KCl, and 150 mM sorbitol (sorbitol buffer) in the presence of the appropriate cAMP or cGMP concentrations, using spin columns. Uptake assays (Nimigean, 2006) were started by mixing one third of the final reaction volume of buffer-exchanged proteoliposomes with two thirds of sorbitol buffer containing 5 cps/µl $^{86}Rb^{+}$ (PerkinElmer) and the appropriate ligand concentration. Uptake was monitored after 90 min in 100-µl aliquots and normalized as described previously (Nimigean, 2006).

Purification and crystallization of T284S/V288S/A352D mutant CNB domain

Expression and purification of T284S/V288S/A352D CNB domain was performed as described previously for the wild-type domain (Clayton et al., 2004). For nucleotide removal, the protein bound to GST beads was washed with 200 ml buffer (PBS buffer containing 3 mM DTT) before incubation with thrombin. Size-exclusion chromatography was performed on a Superdex 75 column equilibrated in 10 mM Tris, pH 7.0, 100 mM NaCl, and 4 mM DTT.

Crystals of T284S/V288S/A352D mutant domain were grown using the vapor diffusion method in 24-well hanging-drop trays with a 500-µl reservoir solution of 0.15 M sodium citrate, pH 5.6, 0.9 M ammonium sulfate, and 100 mM lithium sulfate. Protein at 10 mg/ml was combined with cGMP (final concentration of 1.5 mM) and mixed with the reservoir solution at a 1:1 ratio for a final drop volume of 4 µl. Crystals appeared within 10 d at 25°C. Crystals were cryoprotected in well solution supplemented with 25% glycerol and 1.5 mM cGMP before flash cooling in liquid nitrogen. Diffraction data were collected at 100 K at the beamline 14-4 of the European Synchrotron Radiation Facility (ESRF) and processed with XDS (Kabsch, 2010) and SCALA (Evans, 2006). Mutant CNB domain crystals grew in space group $P2_12_12_1$ with two molecules in the asymmetric unit. The structure of the mutant CNB domain–cGMP complex was solved by molecular replacement with Phaser (McCoy et al., 2007) using chain A of the cGMP-bound structure (Protein Data Bank accession no. 3CL1) (Altieri et al., 2008) as the search model. Model building and refinement were performed with Coot (Emsley et al., 2010) and Phenix (Afonine et al., 2012), respectively. Ligand restraints were generated using Phenix. Figures were generated using PyMOL software (Schrödinger, LLC).

Molecular dynamics (MD) simulations

Two models were defined as corresponding to the CNB domain of wild-type MlotiK1 and of the T284S/V288S/A352D mutant, respectively. The atomic coordinates of the wild-type domain were taken from the Protein Data Bank (accession no. 3CL1) (Altieri et al., 2008). Residues 350–354 are missing in 3CL1, whereas their structure was solved in the mutant. Because these residues are close to the nucleotide-binding site, we decided to include them in both models. The initial structure of residues 350–354 in the wild-type domain was defined as an elongation of the αC helix. The final models included residues 320–354 for the wild-type CNB domain and residues 314–355 for the T284S/V288/A352 mutant domain. N and C terminals were acetylated and amidated. The default protonation state was assumed for all the ionizable residues, and histidine residues were protonated at the epsilon position. All of the water molecules that are present in the crystallographic structures were retained. The systems were solvated by ∼6,000 water molecules, and the necessary number of chloride ions was added to guarantee electrical neutrality. The atomic models were first equilibrated in the NVT ensemble (600 ps), with harmonic restraints applied to all of the heavy atoms of the protein, of cGMP, and of the crystallographic water molecules. The harmonic restraints were gradually removed in the course of 10-ns equilibration trajectories in the NPT ensemble. Production trajectories of 100 ns followed.

MD trajectories were simulated using NAMD version 2.9 (Phillips et al., 2005), with the CHARMM27 force field with CMAP corrections (MacKerell et al., 1998), and the TIP3P model for water molecules (Jorgensen et al., 1983). Pressure was kept at 1 atm by the Nosé–Hoover Langevin piston method (Martyna et al., 1994; Feller et al., 1995), with a damping time constant of 50 fs and a period of 100 fs. Temperature was kept at 300 K by coupling the system to a Langevin thermostat, with a damping coefficient of 5 ps^{-1} (Feller et al., 1995). Electrostatic interactions were treated by the particle mesh Ewald algorithm, with a grid spacing below 1 Å (Essmann et al., 1995). Van der Waals interactions were truncated at 12 Å and smoothed at 10 Å. Hydrogen atoms were restrained by the SETTLE algorithm (Miyamoto and Kollman, 1992). A time step of 2 fs was adopted to integrate the equations of motion.

Energy calculations

The energy of binding, ΔG, is defined as:

$$\Delta G = G_{complex} - G_{protein} - G_{cGMP},$$

where $G_{complex}$, $G_{protein}$, and G_{cGMP} are the energies of the complex, the isolated protein, and the nucleic acid, respectively. These energies were estimated with the MM-PBSA approach, using the single-trajectory paradigm; i.e., the structures of complex, protein, and nucleic acid were taken from the same MD trajectory. As a general rule, the single-trajectory paradigm provides accurate energy estimates only if the ligands and the protein do not change structure upon binding. However, in this study, we are interested only in energetic differences between the wild-type and the triple mutant, and not in the absolute value of the binding energies. Therefore, a less stringent condition applies to MM-PBSA calculations with the single-trajectory paradigm. Even if the structure of

Published June 30, 2014

the protein or of the ligand changes upon binding, the estimated difference in binding energy between the wild type and the mutant is still accurate, provided that these structural changes have similar energetic effects in the two systems.

The free energy of each species was calculated as:

$$G = E_{VDW} + G_{SA} + E_{COUL} + G_{PB},$$

where E_{VDW} is the Van der Waals energy, E_{COUL} is the coulombic energy, and G_{PB} and G_{SA} are polar and apolar contributions to the solvation energy. The apolar contribution to the binding energy is given by the sum of E_{VDW} and G_{SA}, whereas the sum of E_{COUL} and G_{PB} defines the polar component of the binding energy. Solvation energies were calculated with the APBS software (Baker et al., 2001). The probe radius for the definition of the molecular surfaces was 1.4 Å. The relative dielectric constants were 80 and 2, respectively, for solvent and solutes. The apolar solvation energy was assumed proportional to the solvent-accessible surface area, with proportionality constant equal to 0.0072 kcal mol^{-1} $Å^{-2}$. Binding energies were calculated as average values over the 100-ns MD trajectories. The time series of the various energy terms was tested for the presence of correlation with the Ljung–Box lack of correlation statistical test with a confidence level of 95%, as described in Furini et al. (2013). A sampling period for the MD trajectories equal to 1 ns guaranteed lack of correlation among samples in the time series of all the energy terms. This lack of correlation is necessary for defining a safe (over) estimation of the standard error affecting the calculated binding energies.

Accession numbers

The coordinates and structure factors of the mutant CNB domain–cGMP complex from the MlotiK1 channel were deposited at the Protein Data Bank under the accession number 4MUV.

Online supplemental material

Table S1 shows statistics of crystallographic data and refinement. Fig. S1 shows the sequence alignment of CNB domains from the MlotiK1, HCN2, and CNGA-1 channels, and the CNB β domain from the cGMP-dependent kinase I and CNB homology domains from the ELK and EAG1 channels. Figs. S2 and S3 illustrate two stereo views of the ligand-binding pocket of the triple mutant CNB domain from the MlotiK1 channel. Fig. S4 shows a mutant cycle analysis of mutations V288S and A352D. Fig. S5 shows representations of the ligand-binding pocket in the structure of the cGMP-bound CNB β domain from the cGMP-dependent protein kinase I. The online supplemental material is available at http://www.jgp.org/cgi/content/full/jgp.201311145/DC1.

RESULTS

Inverting ligand selectivity in the MlotiK1 channel

We determined the constants of dissociation of cAMP and cGMP for the MlotiK1 channel CNB domain (K_d: 148 ± 22 nM, $n = 6$, for cAMP; 1,731 ± 264 nM, $n = 6$, for cGMP) (Fig. 1, B–D, and Table 1); these values are

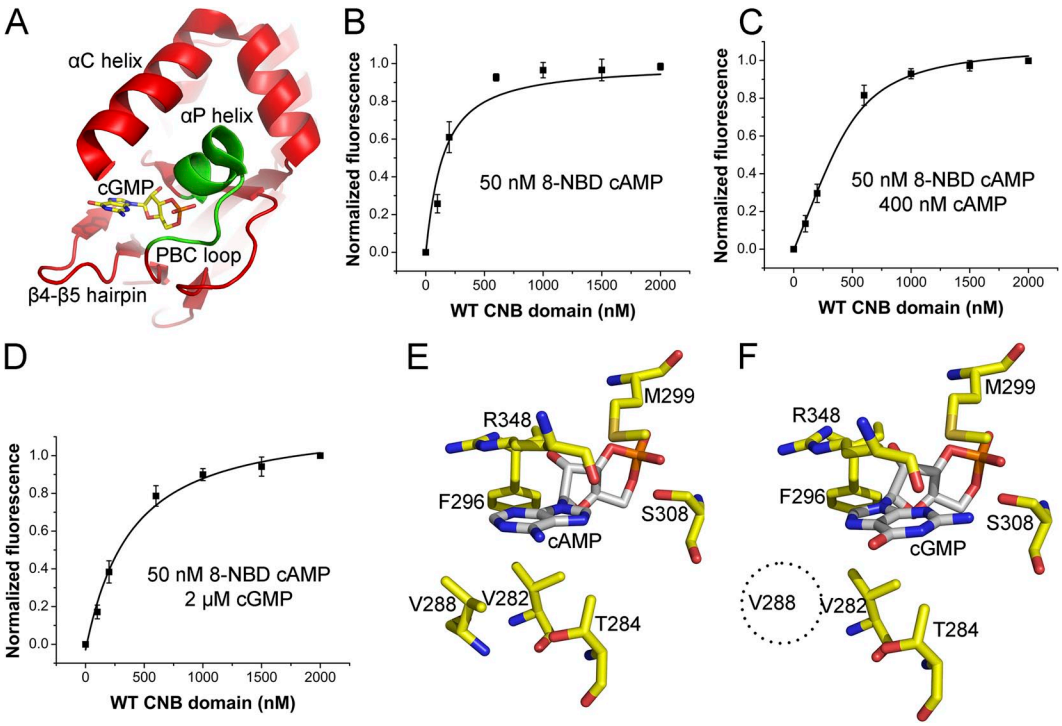

Figure 1. Cyclic nucleotide binding in the MlotiK1 CNB domain. (A) View of the CNB domain bound to cGMP. Structural elements (in red and green) that form the ligand-binding pocket are indicated. cGMP is shown as stick. (B–D) Fluorescence binding curves of the CNB domain protein titrated against 50 nM 8-NBD cAMP, (B) in the absence of competitor, and in the presence of (C) 400 nM cAMP or (D) 2 µM cGMP. K_d values determined were 171 ± 20 nM for 8-NBD cAMP, 148 ± 22 nM for cAMP, and 1,731 ± 264 nM for cGMP. Error bars indicate standard deviation of error. Experiments involve six replicates from two different protein batches. (E and F) View of residues interacting directly with ligand bases in the wild-type MlotiK1 CNB crystal structures bound to (E) cAMP (Protein Data Bank accession no. 1VP6) and (F) cGMP (Protein Data Bank accession no. 3CL1). Dotted circle indicates that V288 is one of the residues not interacting with cGMP.

Published June 30, 2014

TABLE 1

cAMP and cGMP K_ds for the wild-type and CNB domain mutants

Structural motif	Mutant	cAMP K_d	cGMP K_d	K_d ratio	*n*
		nM	*nM*		
	Wild type	148 ± 22	1,731 ± 264	11.7	6
β4–β5 hairpin	V282L	1,008 ± 53	8,951 ± 743	8.9	3
	T284N	342 ± 41	6,556 ± 633	19.2	3
	T284Q	731 ± 90	6,952 ± 1312	9.5	3
	T284S	464 ± 58	2,984 ± 379	6.4	6
	V288A	393 ± 50	2,544 ± 355	6.5	3
	V288L	201 ± 19	996 ± 163	5.2	3
	V288I	138 ± 39	797 ± 118	5.8	6
	V288S	1,205 ± 160	2,105 ± 128	1.7	4
αP helix	M299C	501 ± 99	2,942 ± 357	5.9	3
	M299Q	734 ± 134	11,649 ± 2,621	15.9	3
C terminus	A352S	174 ± 23	727 ± 160	4.2	3
	A352D	256 ± 29	850 ± 121	3.3	6
αC helix	R348A	24,822 ± 3182[a]	38,781 ± 2,449[a]	1.6	3
	R348N	19,142 ± 507[a]	32,106 ± 3,844[a]	1.7	3
	R348Q	25,097 ± 2,216[a]	46,062 ± 5,609[a]	1.8	3
	R348K	16,446 ± 842[a]	23,547 ± 982[a]	1.4	3
	R348Y	24,174 ± 2,214[a]	33,172 ± 4,771[a]	1.4	3
V288S/A352S		691 ± 72	749 ± 75	1.1	3
V288S/A352D		547 ± 111	351 ± 95	0.64	3
T284S/V288S/A352D		2,190 ± 347	336 ± 126	0.15	6

K_ds were determined by competition at a constant ligand concentration and with variable protein concentration; except for those marked with footnote a. K_d ratio is calculated from (cGMP K_d/cAMP K_d); *n*, number of repetitions.

[a]K_ds were determined by competition at a constant protein concentration and with variable ligand concentration.

larger than the values reported by others (Cukkemane et al., 2007), but the discrepancy does not alter the conclusions of our study, as we are interested in understanding the molecular basis of the relative preference of one nucleotide over the other, and we have used the same procedure throughout this study (exceptions are noted). Our measurements show that the domain is 12 times more selective for cAMP than for cGMP, as defined from the ratio of the experimentally determined affinities for the two ligands. This nucleotide preference is also reflected in the nucleotide concentration dependence of channel activity measured using an

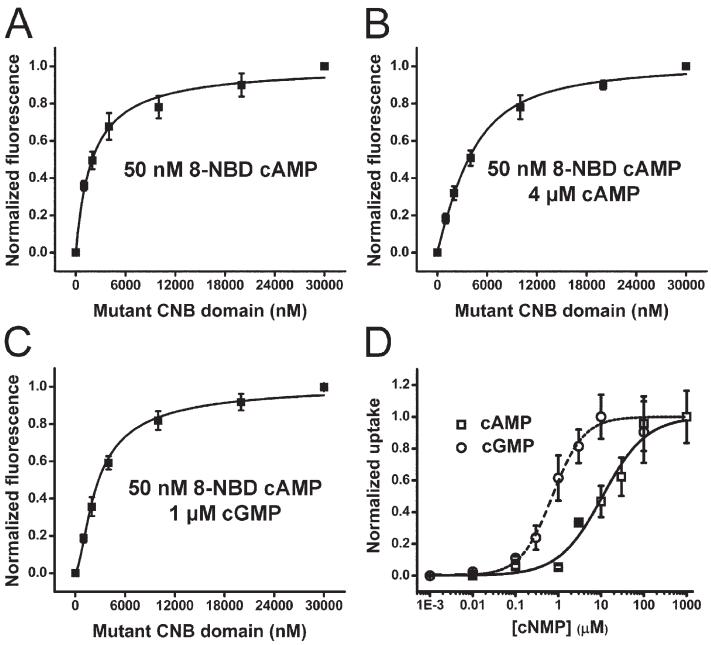

Figure 2. Titration experiments with the MlotiK1 T284S/V288S/A352D mutant. (A–C) Fluorescence binding curves of triple mutant CNB domain titrated against 50 nM 8-NBD cAMP, (A) in the absence of competitor and in the presence of (B) 4 µM cAMP or (C) 1 µM cGMP. The K_d values determined were 2,005 ± 160 nM for 8-NBD cAMP, 2,190 ± 347 nM for cAMP, and 336 ± 126 nM for cGMP. (D) Functional analysis of the T284S/V288S/A352D MlotiK1 potassium channel using an $^{86}Rb^+$ uptake assay. Normalized uptake by channel reconstituted in liposomes as a function of ligand concentration (circles, cGMP; squares, cAMP) was fitted with a Hill equation (cGMP: $K_{1/2}$ = 0.6 ± 0.1 µM and Hill coefficient = 1.3; cAMP: $K_{1/2}$ = 7.4 ± 3.3 µM and Hill coefficient = 0.84). Error bars indicate standard deviation of error. Data in fluorescence binding assays involved six replicates from two different protein batches. Radioactivity uptake assay involved three to eight replicates from three different protein batches.

Published June 30, 2014

$^{86}Rb^{+}$ flux assay; the channel has a higher sensitivity for cAMP ($K_{1/2}$ values of 110 ± 20 nM) than for cGMP (920 ± 110 nM) (Altieri et al., 2008).

A comparison of the MlotiK1 CNB domain structures bound to cAMP and cGMP (Fig. 1, E and F) shows that the residues that are within 4 Å of the nucleotide bases and which probably determine much of the binding properties of the domain are: V282 and T284 in the β4–β5 hairpin; F296, M299, and S308 in different sections of the PBC; and R348 in the αC helix, the lid of the binding pocket. The most obvious difference in the interactions established by cAMP and cGMP is V288. This residue is positioned in the β4–β5 hairpin and is within interacting distance of the cAMP base but not of cGMP (Fig. 1, E and F). Confirming the importance of these local interactions for the ligand-binding properties of the domain, we inverted ligand selectivity in the MlotiK1 CNB domain through a combination of mutations at three of these residues (T284S/V288S/A352D). This mutant domain shows a 6.5× preference for cGMP or, to allow a direct comparison with the wild-type value, a 0.15× preference for cAMP. Relative to the wild-type domain, these mutations decreased cAMP affinity (K_d cAMP: 2,190 ± 347 nM) and increased cGMP affinity (K_d cGMP: 336 ± 126 nM) (Fig. 2, A–C, and Table 1).

Reflecting the ligand-binding properties of the isolated mutant domain, the $K_{1/2}$ values for the concentration dependence of activity in the triple mutant channel show a functional preference for cGMP over cAMP ($K_{1/2}$ of ∼600 nM for cGMP and ∼7 µM for cAMP) (Fig. 2 D). Ligand efficacy in the wild-type and triple mutant channels was estimated by measuring the $^{86}Rb^{+}$ flux after 90 min in the presence of saturating concentrations of ligand (>100 times higher than the $K_{1/2}$). The maximum normalized flux for the wild-type channel is 0.29 ± 0.11 (n = 7) for cAMP and 0.18 ± 0.07 (n = 6) for cGMP. For the mutant, the values are 0.39 ± 0.07 (n = 6) for cAMP and 0.33 ± 0.05 (n = 6) for cGMP. Because of the limitations inherent to the assay, these values have to be considered carefully, but they show that unlike for ligand sensitivity, the three mutations do not appear to greatly alter the functional efficacy of the ligands.

Structure of the triple mutant

We determined the x-ray structure of the T284S/V288S/A352D mutant domain in complex with cGMP at 1.25 Å (Figs. 3, S2, and S3, and Table S1). These crystals contain two protein copies in the asymmetric unit, which are for the most part indistinguishable.

A comparison of the triple mutant structure to the wild-type domain structure in complex with cGMP (Protein Data Bank accession no. 3CL1) (Altieri et al., 2008) reveals high overall structural similarity (Fig. 3 A), with a backbone root-mean-square deviation (RMSD) of 0.60 Å.

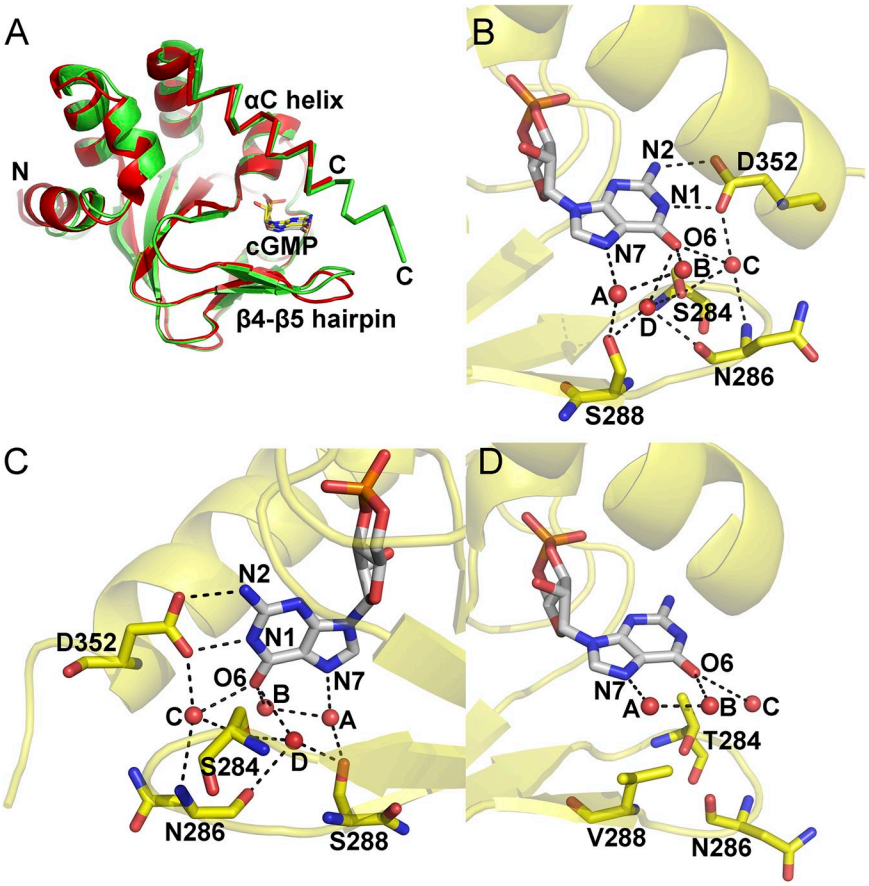

Figure 3. Structural characterization of the T284S/V288S/A352D MlotiK1 CNB domain mutant. (A) Superposition of triple mutant (green) and wild-type (red) CNB domain structures in complex with cGMP. Ligands are represented as stick. Some structural elements of the binding pocket are indicated. (B) Detail of the ligand-binding pocket of the triple mutant. cGMP is shown in white stick, with some of the residues in the pocket shown in yellow. Water molecules bound in the ligand-binding pocket are shown as red spheres. Dashed lines connect some of the atoms within hydrogen bond distance. The rest of the protein is shown in transparent cartoon. (C) As in B, but viewed from just below the β4–β5 hairpin. (D) View as in B of the ligand-binding pocket of one of the asymmetric unit protein molecules present in the cGMP-bound wild-type CNB domain crystals. Some of the residues in the hairpin and the three waters present in the binding pocket are shown.

Published June 30, 2014

There are, however, interesting differences in the binding pocket. First, the αC helix in the mutant, where A352D was introduced, is five to six residues longer and the domain structure ends at residue 354 or 355 (Fig. 3 A), depending on the asymmetric unit molecule considered. Second, the β4–β5 hairpin in the mutant, where the other two mutations were introduced, adopts a different conformation relative to the wild-type structure, closing further over the ligand (Fig. 3 A). Despite these differences, the nucleotides adopt the same *syn* conformation and are in similar positions.

A more detailed analysis of the triple mutant interactions between the protein and the nucleotide base shows that V282, M299, S308, and R348 interact with the ligand in the same way as in the wild-type structure. In one of the asymmetric unit mutant copies, the side-chain methyl groups of A309 and A351 are also within 4 Å of the base, but this is not observed in the other copy. More

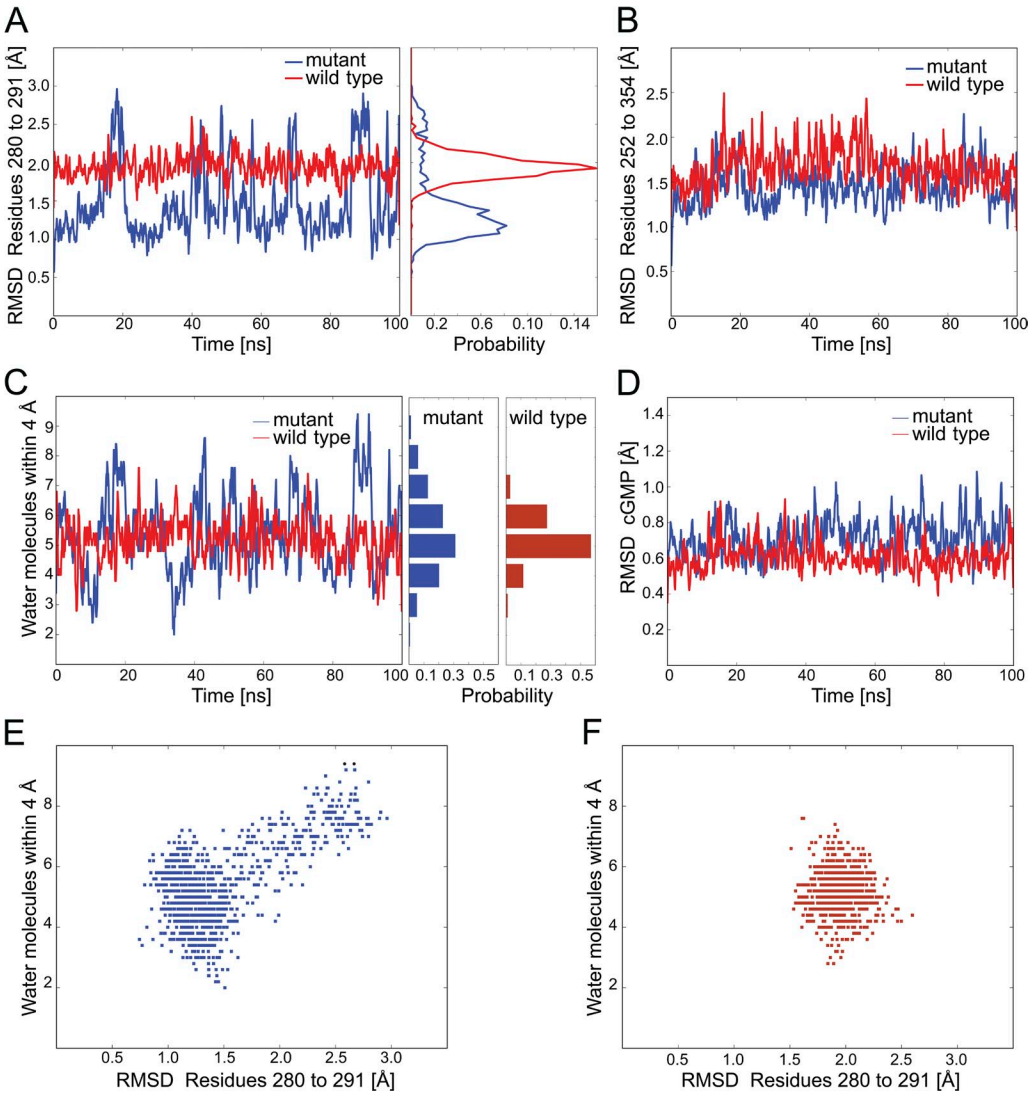

Figure 4. MD simulations of the MlotiK1 CNB domain. MD trajectories were sampled with a period of 10 ps. Data for the wild-type CNB domain and for the T284S/V288S/A352 mutant are shown, respectively, in red and in blue. (A) RMSD of the backbone atoms in the β4–β5 hairpin (residues 280–291). The probability histograms shown on the right side of the panel were calculated using a bin size of 0.05 Å. (B) RMSD of the backbone atoms of residues 252–354, corresponding to the whole CNB domain. In A and B, all of the MD snapshots were superimposed on the corresponding crystal structure, using the heavy atoms of cGMP as reference. (C) Number of water molecules closer than 4.0 Å from heavy atoms of the nucleotide base. At the beginning of the simulation, the structure contains six waters within 4.0 Å of the base. (D) RMSD of the heavy atoms of cGMP. All the MD snapshots were superimposed on the corresponding crystal structure, using the backbone atoms of residues 252–354 as reference. (E and F) Number of water molecules closer than 4.0 Å from heavy atoms of the nucleotide base as a function of the RMSD of the backbone atoms in the β4–β5 hairpin (residues 280–291), (E) in the mutant and (F) wild-type domains.

Published June 30, 2014

interesting are the differences in the structural roles of the three mutations (T284S, V288S, and A352D). The A352D side chain extends toward the nucleotide base, with the carboxylic group hydrogen bonding N1 and N2 of the guanine (Figs. 3, B and C, and S3) and anchoring the end of the αC helix to the body of the domain. This interaction mirrors a similar disposition seen in the I336D–HCN2 CNB domain structure (Flynn et al., 2007). In contrast, T284S and V288S are either beyond the 4-Å range for Van der Waals interactions with the nucleotide base or at the far end of this type of interaction, leading us to conclude that these residues do not establish close interactions with the nucleotide. Instead, T284S and V288S are involved in a hydrogen bond network with four water molecules present in the binding pocket (Fig. 3, B and C). Waters A and B are positioned along the rim of the guanine ring, whereas waters C and D are positioned between the β4–β5 hairpin and the nucleotide base. The B factors of the four waters and of the surrounding protein atoms are similar, indicating that these waters are stably bound in the crystal. This water network connects several residues in the binding pocket to each other and to the nucleotide base. Water A bridges V288S and N7 in the nucleotide base and is also within hydrogen-bonding distance of water B; water B also hydrogen bonds O6 in the nucleotide base. Water C is within hydrogen-bonding distance of the carboxylic group of A352D, of the hydroxyl in T284S, of O6 in the nucleotide, and of the main-chain amino group in N286 in the β4–β5 hairpin. Finally, water D is within hydrogen-bonding distance of O6 in the nucleotide base, of the hydroxyl groups in V288S and T284S, and of the carbonyl of N286. Analysis of the previously determined structures of the MlotiK1 CNB domain reveals that in one of the asymmetric unit protein copies of the cGMP-bound wild-type domain crystal structure (Fig. 3 D), there are water molecules in the binding pocket that are equivalent to waters A, B, and C. However, they do not form a hydrogen bond network in the ligand pocket, and they are not observed in the other protein copy.

Exploring the binding pocket interactions with MD simulations

To get a more complete view of the interactions between the ligand-binding pocket residues and the nucleotide, we performed MD simulations with the triple mutant and the wild-type CNB domain structures bound to cGMP.

Interestingly, a plot of β4–β5 hairpin backbone atom RMSD over the duration of the simulation revealed that the mutant structure hops repeatedly between two or three different conformations, corresponding to RMSDs of ∼1.1, ∼1.5, and 2.0–2.5 Å, whereas the wild-type structure oscillates around a more uniform average structure (Fig. 4 A). Further analysis reveals that, in the triple mutant simulations, there is a correlation between the number of waters and the different hairpin conformations (Fig. 4, A, C, and E) so that higher RMSD values correspond to a higher number of waters within 4 Å of the base. Thus, transition between the different conformations is accompanied by movement of water molecules

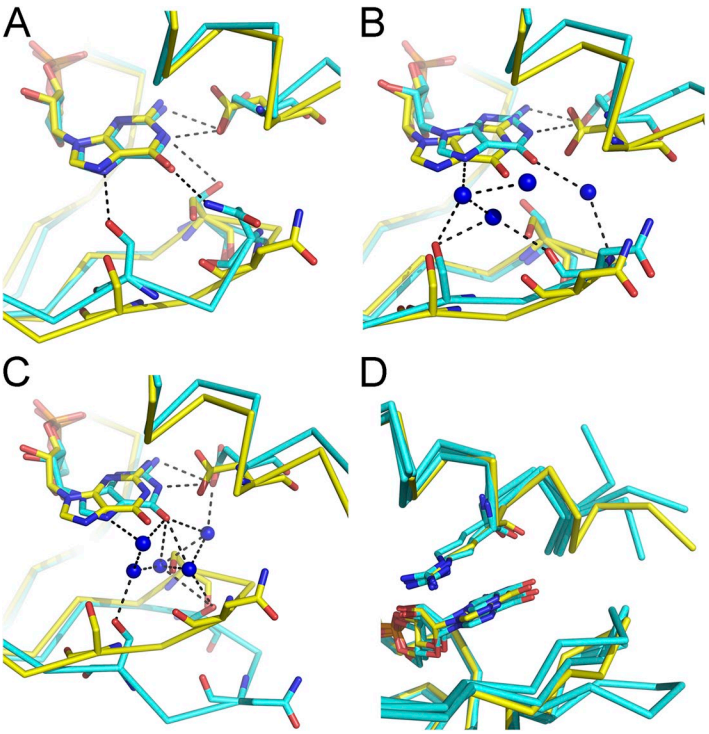

Figure 5. MD simulation conformational states. View of the superposed ligand-binding pockets from the triple mutant crystal structure (yellow stick) and from MD simulation snapshot models (cyan) in the (A) closed conformation, (B) semi-closed conformation, and (C) open conformation. Structures are shown as Cα traces, with ligands in yellow (crystal structure) or cyan (MD simulation models). Only waters that mediate protein–ligand interactions are shown (as blue spheres). Dashed lines connect some of the atoms within hydrogen bond distance. (D) Superposition of crystal structure and MD simulation snapshot structures in the different conformations. View of the ligand-binding pocket with cGMP and R348 shown as stick.

Published June 30, 2014

in and out of the nucleotide neighborhood. In contrast, a similar plot for the wild-type simulation shows a rapid fluctuation in the number of waters around the average value of five to six waters (Fig. 4 F).

Analysis of snapshot structures corresponding to the different conformations of the triple mutant revealed: a closed conformation in which the hairpin moves toward the base (Fig. 5 A), establishing closer interactions with the ligand base; a semi-closed conformation that strongly resembles the crystal structure (Fig. 5 B); and an open conformation where the hairpin moves away from the nucleotide base (Fig. 5 C). These conformations are associated with different numbers of water molecules in the binding pocket so that: the closed conformation has no or very few waters within hydrogen-bonding distance of the base; the semi-closed has approximately four waters within hydrogen-bonding distance of the base, just like the crystal structure; and the open conformation has a larger number of waters forming a network that connects the ligand and the protein. Importantly, the nucleotide and the αC helix remain stable throughout the simulation and in all of these conformations (Figs. 4 D and 5 D), indicating that the bound state of the domain is not affected by these conformational changes around the nucleotide, and that the ligand can be stabilized either by direct protein contacts or water-mediated contacts.

In addition, visual inspection of the triple mutant crystal lattice reveals that the β4–β5 hairpin is tightly packed against other protein molecules in the lattice. Therefore, it seems reasonable to conclude that during crystal formation there is a selection of one of the conformational states sampled by the ligand-binding pocket and that the MD simulation has uncovered the existence of other conformations.

The analysis of hydrogen bonds formed between the protein and the nucleotide base during the MD simulations shows that in the wild-type structure, there is an average of one hydrogen bond formed directly with protein atoms and one bond that is mediated by water (we did not consider interactions that might be mediated by more than one water molecule). In the triple mutant, the numbers are 2.5 for direct bonds and 1 for water mediated. A breakdown of these hydrogen bonds among the binding pocket residues is shown in Table 2. The direct hydrogen bond formed between S308 and N7 in the base is present both in the wild-type and mutant protein and is highly stable over the length of the simulations, agreeing well with the demonstrated importance of this residue for the stability of bound cGMP (Altenhofen et al., 1991; Flynn et al., 2007). The hydrogen bonds that are present in the mutant but not in the wild-type simulations are caused by A352D, which forms a long-lived interaction with the ligand through its carboxylic group, and V288S, which either forms a direct or a water-mediated hydrogen bond over a good fraction of the simulation time. The water-mediated interaction between V288S and the ligand is present in the crystal structure of the mutant (Fig. 3, B and C) as well as in the simulation semi-closed conformation (Fig. 5 B); the direct hydrogen bond involving this residue occurs in the simulation closed conformation, when the binding pocket loses water molecules and the hairpin approaches the nucleotide base (Fig. 5 A).

The analysis of the MD simulations suggests that there are two aspects that contribute favorably for the tighter binding of cGMP by the mutant. The detection in the triple mutant MD simulation of several conformations of the ligand-binding site, whereas in the wild-type domain only one conformation is observed, suggests that tighter binding of cGMP in the triple mutant involves a more favorable entropic component. In addition, several factors indicate that the tighter cGMP binding in

TABLE 2

Stability of hydrogen bonds formed between protein and ligand base during MD simulation

	Wild type		T284S/V288S/A352D	
Residue	Protein–cGMP h-bonds	Water-mediated h-bonds	Protein–cGMP h-bonds	Water-mediated h-bonds
284	2% (OG1)	23% (OG1)	—	10% (OG)
286	—	35% (ND2) +20% (N) +3% (O)	6% (ND2)	22% (O) +9% (N) +4% (ND2)
288	—	—	24% (OG)	35% (OG)
297	—	—	—	—
298	—	—	—	—
308	95% (OG)	3% (O)	93% (OG)	—
348	—	6% (NE) +2% (O)	—	2% (NE)
352	—	—	67% (OD2) +61%(OD1)	7% (OD1) +7% (OD2)

Percentages correspond to the fraction of time in the MD trajectory when a protein residue forms a hydrogen bond (h-bond) with the guanine group. The name of the protein atom participating to the h-bond is given in parentheses. Two atoms are considered part of an h-bond if donor and acceptor are closer than 3.5 Å and the donor–hydrogen–acceptor angle is below 35°.

Published June 30, 2014

the triple mutant is also the result of an increase in the polar chemical nature of the binding pocket: (a) all of the mutations introduced in the triple mutant have a strong polar chemical character, and (b) our analysis of both the crystal structure and MD simulation show that A352D and V288S are involved in polar interactions (direct or water mediated) with the nucleotide. An estimation of the polar energy contribution to the total energy of cGMP binding in the wild-type and mutant domains supports this proposal. A quantitative comparison of the estimated binding energies with experimental data is not possible because of the approximations applied; for example, the entropic contribution to the binding energy is not considered. Nevertheless, these approximations are not expected to affect greatly the main result of our energetic analyses (Table 3), which shows that the polar component of the binding energy is more favorable for cGMP binding in the mutant (−6.4 kcal/mol) than in the wild-type domain (−2.8 kcal/mol). In contrast, the apolar term is less favorable in the mutant than in the wild-type domain.

Impact of individual mutations in the triple mutant CNB domain

We also analyzed the role of the individual mutated residues on the stability of the mutant complex by measuring the ligand-binding properties of the single-point mutant domains (Table 1). The A352D single-point mutant has lower ligand selectivity than the wild-type domain (approximately three times preference for cAMP). This results from a decrease in cAMP affinity (K_d cAMP: 256 ± 29 nM) and an increase in cGMP affinity (K_d cGMP: 850 ± 121 nM). On the other hand, the V288S single-point mutant domain is almost nonselective (1.7× preference for cAMP) because of a large decrease in cAMP affinity (K_d cAMP: 1,205 ± 160 nM), with no effect on cGMP (K_d cGMP: 2,105 ± 128 nM). Similarly, the relatively neutral substitution of T284 for serine reduced cAMP affinity (K_d cAMP: 464 ± 58 nM) while having little effect on cGMP (K_d cGMP: 2,984 ± 379 nM), so that its overall selectivity decreased to an approximately six times cAMP preference.

The increased affinity for cGMP in the A352D mutant fits well with the close interaction between this residue and the ligand seen in the crystal and in the MD simulation. The almost neutral effect of T284S on cGMP binding also fits well with the structural and simulation data where no specific interactions are observed between this residue and cGMP. In contrast, the crystal structure and the MD simulations led us to expect that the V288S mutant would show tighter cGMP binding, but the affinity measurements in the V288S single mutant show no impact on cGMP binding. In addition, none of the single mutants alone causes the inversion in ligand selectivity, strongly suggesting that inversion in ligand selectivity is caused mainly by an effect that results from the combination of the three residue changes (T284S/V288S/A352D). To dissect the underlying details of this combination of mutations, we performed a mutant cycle energetic coupling analysis (Carter et al., 1984; Schreiber and Fersht, 1995; Ranganathan et al., 1996; Yifrach et al., 2009). More specifically, in a double mutant cycle analysis of ligand binding, a coupling energy above or below zero indicates that there is a difference in the energetic interaction of two side chains between the bound and unbound states.

After determining the affinity of the V288S/A352D double mutant for cAMP and cGMP (K_d cAMP: 547 ± 111 nM and K_d cGMP: 351 ± 95 nM [Table 1], corresponding to an ∼0.6× preference for cAMP), we calculated the coupling energies between these two residues. For cAMP binding, the coupling energy is −0.78 ± 0.18 kcal/mol, and for cGMP binding, it is −0.64 ± 0.20 kcal/mol. We also determined the coupling energies for the combination of T284S with V288S/A352D: 0.14 ± 0.19 kcal/mol for cAMP binding and −0.34 ± 0.29 kcal/mol for cGMP binding. The V288S/A352D plus T284S coupling energies are small and, within their associated error, close to zero, so we consider that they represent independent effects. In contrast, analysis of the mutant cycle for V288S and A352D (Fig. S4) shows that the impact of V288S in the absence or presence of A352D is different. V288S alone has no effect (0.12 ± 0.10 kcal/mol) in cGMP binding but has a stabilizing impact (−0.52 ± 0.18 kcal/mol) when combined with A352D. This stabilization fits nicely with the type of interactions observed in the crystal structure and MD simulations between this residue and the ligand. Additionally, it is worthwhile considering that in the triple mutant structure, these two residues are far from each other (∼8 Å) and, most likely, even further away in the unbound-state structures (Clayton et al., 2004; Altieri et al., 2008; Schünke et al., 2009, 2011); the coupling energies for this residue pair are therefore larger than the coupling energy values determined by Schreiber and Fersht (1995) for residue pairs separated by more than

TABLE 3

Binding energies estimated with MM/PBSA

CNB domain	E_{apolar}	E_{polar}	E_{tot}
	kcal/mol	*kcal/mol*	*kcal/mol*
Wild type	−49.1 ± 0.3	−2.8 ± 0.3	−51.9 ± 0.4
Mutant	−47.1 ± 0.4	−6.4 ± 0.3	−53.4 ± 0.4
ΔG(mutant)-ΔG(wild-type)	2.0 ± 0.7	−3.6 ± 0.6	−1.5 ± 0.8

Binding energies are reported as average values ± standard errors calculated over 100 samples (100-ns MD trajectories sampled with a period equal to 1 ns). The total binding energy (E_{tot}) is the sum of an apolar term (E_{apolar}; equal to the Van der Waals energy plus the apolar contribution to the solvation energy) and a polar term (E_{polar}; equal to the coulombic energy plus the polar contribution to the solvation energy).

Published June 30, 2014

7 Å (all <|0.5| kcal/mol) on the interface of the barstar–barnase protein complex. It is possible to envisage that a long-distance interaction between V288S and A352D could result from the stabilization of the water molecule network present in the binding pockets of the crystal and simulation structures. However, the V288S/A352D coupling energies are smaller than the |1| kcal/mol arbitrary barrier commonly used to define cooperative effects; therefore, we cautiously considered this residue combination as additive.

Exploring other residues in the binding pocket

In addition to the three mutations described above, we evaluated the impact of various other binding pocket mutations. We have summarized the results of this analysis in Table 1. Overall, this mutant screening shows that, although some of the tested single mutants greatly reduce the domain's preference for cAMP over cGMP, none of these single mutations (including those found to determine selectivity in other cyclic nucleotide–regulated channels) caused a reversal of selectivity, as defined by the ratio of the K_ds.

We have found specific effects that provide new insights into the general ligand-binding properties of CNB domains. The lack of a clear definition of which residues in the binding pocket favor cAMP binding explains in part our incomplete understanding of the molecular determinants of cyclic nucleotide binding in CNB domains. It has been shown in HCN2 channels that residues at the C-terminal end of the αC helix affect cAMP binding (Zhou and Siegelbaum, 2007), but these do not appear to interact directly with the nucleotide. We have now found that apolar residues (valine, leucine, isoleucine, and alanine) at position 288 of MlotiK1, in the β4–β5 hairpin and in the immediate neighborhood of the nucleotide base, favor cAMP binding. This conclusion results from finding that the presence of the apolar amino acids at this position maintains tight cAMP binding and cAMP preference over cGMP (Table 1), whereas the introduction of a serine (V288S) caused a large decrease in the affinity for cAMP and made the mutant almost nonselective (Table 1).

In addition, we have confirmed the importance of a negatively charged amino acid at the end of the αC helix (Varnum et al., 1995; Flynn et al., 2007) at position 352, for the increased stability of the cGMP complex (Table 1). Also, we showed that a serine, at this same position (A352S), increases cGMP affinity (K_d cGMP: 727 ± 170 nM) while not altering cAMP affinity (K_d cGMP: 174 ± 23 nM).

We also looked at substitutions in R348 (Table 1), a residue that has an important role in the closure of the αC helix over the ligand and therefore on the stabilization of the bound state of CNG (Puljung and Zagotta, 2013), HCN (Zhou and Siegelbaum, 2007), and MlotiK1 channels (Clayton et al., 2004; Altieri et al., 2008; Mari et al., 2011) (Fig. S1). In the MlotiK1 channel, this is illustrated by several observations within the CNB domain: the interactions established by the arginine in the nucleotide-bound domain structures (Clayton et al., 2004; Altieri et al., 2008; Schünke et al., 2009); the greatly reduced cAMP affinity of the R348A mutant domain (Cukkemane et al., 2007; Peuker et al., 2013); and in the channel, by the high $K_{1/2}$ for the nucleotide dependence of activation in the R348A mutant channel and by its lower flux activity at saturating concentrations of ligand (Mari et al., 2011).

We first confirmed that R348A is almost nonselective (K_d cAMP: 25 ± 3.2 µM; K_d cGMP: 39 ± 2.5 µM) and then tested other side chains at this position. In particular, we wondered whether residues with long polar side chains could replace the arginine by retaining the interactions with the nucleotide base and also the hydrogen bonding with residues in the binding pocket. Strikingly, mutations R348N, R348Q, and R348K have basically the same ligand-binding properties as R348A, with affinities for cAMP and cGMP that vary between 16 and 46 µM and are almost nonselective (1.4–1.8× for cAMP). Because of the low affinity for the fluorescent analogue displayed by all mutations of R348, we used a slightly different titration procedure (see Materials and methods and Table 1). We also evaluated if electronic delocalization in the side chain was a determining factor at this position by measuring ligand-binding affinities for the mutant R348Y; however, results are very similar to R348A (K_d cAMP: 24 ± 2.2 µM; K_d cGMP: 33 ± 4.8 µM). Collectively, these results show that R348, in the αC helix, is a major determinant of nucleotide affinity (both cAMP and cGMP), as it was the only residue where mutations caused K_d changes >10-fold and resulted in large changes in ligand selectivity. Our results mirror previous findings in other cyclic nucleotide–regulated channels (Craven and Zagotta, 2006; Flynn et al., 2007; Zhou and Siegelbaum, 2007; Puljung and Zagotta, 2013). Collectively, these results support the general importance of the αC helix arginine for the stabilization of the "bound-activated state" through closure of the αC lid over the nucleotide and show that the physical–chemical properties of the arginine side chain are essential for this role.

DISCUSSION

Our analysis in the MlotiK1, together with a study by Nimigean and Pagel (2007), confirmed the importance of specific binding pocket residues for cGMP binding (Table 1), a serine/threonine at the end of the PBC sequence, and an aspartate at the end of the αC helix. We also established that apolar residues on the β4–β5 hairpin favor cAMP binding.

In certain cyclic nucleotide–regulated proteins, the presence of one of the residues discussed above is sufficient

Published June 30, 2014

for determining preference for cGMP over cAMP. However, in the MlotiK1 CNB domain, and in many other cyclic nucleotide–regulated proteins, this is not true (Cukkemane et al., 2011), and it is clear that other factors (other residues and/or structural features) also play a role in ligand selectivity. We inverted ligand selectivity in the MlotiK1 channel with a combination of mutations at T284S, V288S, and A352D. The x-ray structure of our triple mutant shows that A352D establishes close contacts with the guanine group, whereas the other two residues are involved with a network of four water molecules that connect the protein and the ligand. Surprisingly, an MD simulation reveals that the conformation seen in the crystal is not unique; in the simulation, the crystal conformation (or semi-closed conformation) appears to be in equilibrium with two other conformations: a closed conformation where the β4–β5 hairpin is positioned closer to the nucleotide base and V288S forms direct interactions with the guanine group, and an open conformation where the hairpin has moved away from the ligand and contacts between the protein and the ligand involve a network of many waters. Importantly, all of these different conformations appear to correspond to a bound-activated state of the domain, as the nucleotide position and the position of the αC helix do not vary greatly over the length of the simulation. In contrast, the MD simulation of the cGMP-bound wild-type domain shows only one conformation.

The "structural freedom" of the triple mutant ligand-binding pocket observed in the MD simulation, involving multiple conformations of the β4–β5 hairpin and movement of solvent molecules in and out of the pocket, strongly suggests that the increased stability of the cGMP complex in this mutant is partly caused by an increase in the entropy of the bound state relative to the wild-type domain. In addition, our mutagenesis analysis together with the crystal structure and MD simulation also strongly indicates that there is a combined effect of the three mutations (T284S/V288S/A352D) to create a polar environment around the nucleotide base involving interactions of water molecules with the protein. This conclusion is based on several factors: the increased polar chemical character of all the substitutions; the larger number of hydrogen bonds established between the protein and the ligand in the simulation closed and semi-closed conformations relative to the wild-type domain; the larger number of water molecules that solvate the ligand in the simulation open conformation; and the calculated contribution of the polar energy to the total binding energy of the ligand. Importantly, the significance of the polar environment for defining cGMP preference in our mutant domain is supported by theoretical calculations that show that the cGMP hydration energy is greater than for cAMP (Zhou and Siegelbaum, 2008). This theoretical finding suggests that preference for cGMP binding in a CNB domain can be generally achieved through a binding pocket that either compensates for ligand dehydration or allows many of the solvation waters to be retained in the bound state. These are exactly the features that we have found in our analysis of the MlotiK1 triple mutant.

In this context, it is also interesting to analyze the recently published structure of the cGMP-bound CNB β domain from the cGMP-dependent protein kinase I (Protein Data Bank accession no. 4KU7) (Huang et al., 2014), a domain that is ∼250 times more selective for cGMP than cAMP (Figs. S1 and S5). Its binding pocket includes an arginine at a position that is equivalent to residue 288 in MlotiK1; importantly, it was shown that mutation of this residue to alanine strongly affects the selectivity properties of the domain. In the structure, the arginine hydrogen bonds N7 and O6 in the guanine base, resembling the interactions established between the waters A and B and the base in our triple mutant structure (Fig. S5, A and B). In addition, the ligand base is highly exposed to the bulk solvent (Fig. S5, C and D) because the αC helix is very short and the tip of the β4–β5 hairpin is disordered. Collectively, this analysis shows that the ligand-binding pocket of this strongly cGMP-selective CNB domain shares some of the polar environment characteristics described above in the MlotiK1 triple mutant domain.

Our conclusion that the polar character and the structural freedom of the ligand-binding pocket in the triple mutant are determining factors for cGMP preference also explains the difficulty in establishing rules for determining the selectivity properties of a CNB domain just from an amino acid sequence. These prediction rules cannot just consider the possible direct interactions between side chains and the nucleotide chemical groups. They have to consider that there are multiple mechanisms for establishing selectivity in a CNB domain, mechanisms that include more complex effects such as the stabilization of water molecules in the ligand-binding pocket or differences in the entropy of this pocket.

We thank Andras Szollosi, Nuno Mateus, Iva Fernandes, Ricardo S. Vieira-Pires, Enrique de la Cruz, Wenxiang Cao, and Carol Harley for their help. We also thank ESRF for access to ID14-4 through the Portuguese BAG.

We thank the Fundação para a Ciência e a Tecnologia for a PhD fellowship (SFRH/BD/60274/2009 to J. Pessoa) and a post-doctoral fellowship (SFRH/BPD/77040/2011 to F. Fonseca). This work was funded by FEDER Funds through the Operational Competitiveness Program– COMPETE and by national funds through FCT–Fundação para a Ciência e a Tecnologia under the project FCOMP-01-0124-FEDER-028185 (PTDC/BBB-BQB/1418/2012 awarded to J.H. Morais-Cabral). CINECA is acknowledged for providing high performance computing resources through Award N. HP10BX4MV5.

The authors declare no competing financial interests.

Sharona E. Gordon served as editor.

Submitted: 5 December 2013
Accepted: 10 June 2014

Published June 30, 2014

REFERENCES

Afonine, P.V., R.W. Grosse-Kunstleve, N. Echols, J.J. Headd, N.W. Moriarty, M. Mustyakimov, T.C. Terwilliger, A. Urzhumtsev, P.H. Zwart, and P.D. Adams. 2012. Towards automated crystallographic structure refinement with *phenix.refine*. *Acta Crystallogr. D Biol. Crystallogr.* 68:352–367. http://dx.doi.org/10.1107/S0907444912001308

Altenhofen, W., J. Ludwig, E. Eismann, W. Kraus, W. Bönigk, and U.B. Kaupp. 1991. Control of ligand specificity in cyclic nucleotide-gated channels from rod photoreceptors and olfactory epithelium. *Proc. Natl. Acad. Sci. USA.* 88:9868–9872. http://dx.doi.org/10.1073/pnas.88.21.9868

Altieri, S.L., G.M. Clayton, W.R. Silverman, A.O. Olivares, E.M. De la Cruz, L.R. Thomas, and J.H. Morais-Cabral. 2008. Structural and energetic analysis of activation by a cyclic nucleotide binding domain. *J. Mol. Biol.* 381:655–669. http://dx.doi.org/10.1016/j.jmb.2008.06.011

Baker, N.A., D. Sept, S. Joseph, M.J. Holst, and J.A. McCammon. 2001. Electrostatics of nanosystems: Application to microtubules and the ribosome. *Proc. Natl. Acad. Sci. USA.* 98:10037–10041. http://dx.doi.org/10.1073/pnas.181342398

Carter, P.J., G. Winter, A.J. Wilkinson, and A.R. Fersht. 1984. The use of double mutants to detect structural changes in the active site of the tyrosyl-tRNA synthetase (*Bacillus stearothermophilus*). *Cell.* 38:835–840. http://dx.doi.org/10.1016/0092-8674(84)90278-2

Chiu, P.L., M.D. Pagel, J. Evans, H.T. Chou, X. Zeng, B. Gipson, H. Stahlberg, and C.M. Nimigean. 2007. The structure of the prokaryotic cyclic nucleotide-modulated potassium channel MloK1 at 16 Å resolution. *Structure.* 15:1053–1064. http://dx.doi.org/10.1016/j.str.2007.06.020

Clayton, G.M., W.R. Silverman, L. Heginbotham, and J.H. Morais-Cabral. 2004. Structural basis of ligand activation in a cyclic nucleotide regulated potassium channel. *Cell.* 119:615–627. http://dx.doi.org/10.1016/j.cell.2004.10.030

Clayton, G.M., S. Altieri, L. Heginbotham, V.M. Unger, and J.H. Morais-Cabral. 2008. Structure of the transmembrane regions of a bacterial cyclic nucleotide-regulated channel. *Proc. Natl. Acad. Sci. USA.* 105:1511–1515. http://dx.doi.org/10.1073/pnas.0711533105

Craven, K.B., and W.N. Zagotta. 2006. CNG and HCN channels: Two peas, one pod. *Annu. Rev. Physiol.* 68:375–401. http://dx.doi.org/10.1146/annurev.physiol.68.040104.134728

Cukkemane, A., B. Grüter, K. Novak, T. Gensch, W. Bönigk, T. Gerharz, U.B. Kaupp, and R. Seifert. 2007. Subunits act independently in a cyclic nucleotide-activated K^+ channel. *EMBO Rep.* 8:749–755. http://dx.doi.org/10.1038/sj.embor.7401025

Cukkemane, A., R. Seifert, and U.B. Kaupp. 2011. Cooperative and uncooperative cyclic-nucleotide-gated ion channels. *Trends Biochem. Sci.* 36:55–64. http://dx.doi.org/10.1016/j.tibs.2010.07.004

Emsley, P., B. Lohkamp, W.G. Scott, and K. Cowtan. 2010. Features and development of Coot. *Acta Crystallogr. D Biol. Crystallogr.* 66:486–501. http://dx.doi.org/10.1107/S0907444910007493

Essmann, U., L. Perera, M.L. Berkowitz, T. Darden, H. Lee, and L.G. Pedersen. 1995. A smooth particle mesh Ewald method. *J. Chem. Phys.* 103:8577–8593. http://dx.doi.org/10.1063/1.470117

Evans, P. 2006. Scaling and assessment of data quality. *Acta Crystallogr. D Biol. Crystallogr.* 62:72–82. http://dx.doi.org/10.1107/S0907444905036693

Feller, S.E., Y.H. Zhang, R.W. Pastor, and B.R. Brooks. 1995. Constant pressure molecular dynamics simulation: The Langevin piston method. *J. Chem. Phys.* 103:4613–4621. http://dx.doi.org/10.1063/1.470648

Flynn, G.E., K.D. Black, L.D. Islas, B. Sankaran, and W.N. Zagotta. 2007. Structure and rearrangements in the carboxy-terminal region of SpIH channels. *Structure.* 15:671–682. http://dx.doi.org/10.1016/j.str.2007.04.008

Furini, S., P. Barbini, and C. Domene. 2013. DNA-recognition process described by MD simulations of the lactose repressor protein on a specific and a non-specific DNA sequence. *Nucleic Acids Res.* 41:3963–3972. http://dx.doi.org/10.1093/nar/gkt099

Huang, G.Y., J.J. Kim, A.S. Reger, R. Lorenz, E.W. Moon, C. Zhao, D.E. Casteel, D. Bertinetti, B. Vanschouwen, R. Selvaratnam, et al. 2014. Structural basis for cyclic-nucleotide selectivity and cGMP-selective activation of PKG I. *Structure.* 22:116–124. http://dx.doi.org/10.1016/j.str.2013.09.021

Jorgensen, W.L., J. Chandrasekhar, J.D. Madura, R.W. Impey, and M.L. Klein. 1983. Comparison of simple potential functions for simulating liquid water. *J. Chem. Phys.* 79:926–935. http://dx.doi.org/10.1063/1.445869

Kabsch, W. 2010. XDS. *Acta Crystallogr. D Biol. Crystallogr.* 66:125–132. http://dx.doi.org/10.1107/S0907444909047337

MacKerell, A.D., D. Bashford, M. Bellott, R.L. Dunbrack, J.D. Evanseck, M.J. Field, S. Fischer, J. Gao, H. Guo, S. Ha, et al. 1998. All-atom empirical potential for molecular modeling and dynamics studies of proteins. *J. Phys. Chem. B.* 102:3586–3616. http://dx.doi.org/10.1021/jp973084f

Mari, S.A., J. Pessoa, S. Altieri, U. Hensen, L. Thomas, J.H. Morais-Cabral, and D.J. Müller. 2011. Gating of the MlotiK1 potassium channel involves large rearrangements of the cyclic nucleotide-binding domains. *Proc. Natl. Acad. Sci. USA.* 108:20802–20807. http://dx.doi.org/10.1073/pnas.1111149108

Martyna, G.J., D.J. Tobias, and M.L. Klein. 1994. Constant pressure molecular dynamics algorithms. *J. Chem. Phys.* 101:4177–4189. http://dx.doi.org/10.1063/1.467468

McCoy, A.J., R.W. Grosse-Kunstleve, P.D. Adams, M.D. Winn, L.C. Storoni, and R.J. Read. 2007. Phaser crystallographic software. *J. Appl. Cryst.* 40:658–674. http://dx.doi.org/10.1107/S0021889807021206

Miyamoto, S., and P.A. Kollman. 1992. Settle: An analytical version of the SHAKE and RATTLE algorithm for rigid water molecules. *J. Comput. Chem.* 13:952–962. http://dx.doi.org/10.1002/jcc.540130805

Nimigean, C.M. 2006. A radioactive uptake assay to measure ion transport across ion channel-containing liposomes. *Nat. Protoc.* 1:1207–1212. http://dx.doi.org/10.1038/nprot.2006.166

Nimigean, C.M., and M.D. Pagel. 2007. Ligand binding and activation in a prokaryotic cyclic nucleotide-modulated channel. *J. Mol. Biol.* 371:1325–1337. http://dx.doi.org/10.1016/j.jmb.2007.06.030

Nimigean, C.M., T. Shane, and C. Miller. 2004. A cyclic nucleotide modulated prokaryotic K^+ channel. *J. Gen. Physiol.* 124:203–210. http://dx.doi.org/10.1085/jgp.200409133

Peuker, S., A. Cukkemane, M. Held, F. Noé, U.B. Kaupp, and R. Seifert. 2013. Kinetics of ligand-receptor interaction reveals an induced-fit mode of binding in a cyclic nucleotide-activated protein. *Biophys. J.* 104:63–74. http://dx.doi.org/10.1016/j.bpj.2012.11.3816

Phillips, J.C., R. Braun, W. Wang, J. Gumbart, E. Tajkhorshid, E. Villa, C. Chipot, R.D. Skeel, L. Kalé, and K. Schulten. 2005. Scalable molecular dynamics with NAMD. *J. Comput. Chem.* 26:1781–1802. http://dx.doi.org/10.1002/jcc.20289

Pifferi, S., A. Menini, and T. Kurahashi. 2010. Signal transduction in vertebrate olfactory cilia. *In* The Neurobiology of Olfaction. CRC Press, Boca Raton, FL. 203–224.

Puljung, M.C., and W.N. Zagotta. 2013. A secondary structural transition in the C-helix promotes gating of cyclic nucleotide-regulated ion channels. *J. Biol. Chem.* 288:12944–12956. http://dx.doi.org/10.1074/jbc.M113.464123

Ranganathan, R., J.H. Lewis, and R. MacKinnon. 1996. Spatial localization of the K^+ channel selectivity filter by mutant cycle-based structure analysis. *Neuron.* 16:131–139. http://dx.doi.org/10.1016/S0896-6273(00)80030-6

Published June 30, 2014

Rehmann, H., A. Wittinghofer, and J.L. Bos. 2007. Capturing cyclic nucleotides in action: snapshots from crystallographic studies. *Nat. Rev. Mol. Cell Biol.* 8:63–73. http://dx.doi.org/10.1038/nrm2082

Schreiber, G., and A.R. Fersht. 1995. Energetics of protein-protein interactions: Analysis of the Barnase-Barstar interface by single mutations and double mutant cycles. *J. Mol. Biol.* 248:478–486. http://dx.doi.org/10.1016/S0022-2836(95)80064-6

Schünke, S., M. Stoldt, K. Novak, U.B. Kaupp, and D. Willbold. 2009. Solution structure of the *Mesorhizobium loti* K1 channel cyclic nucleotide-binding domain in complex with cAMP. *EMBO Rep.* 10:729–735. http://dx.doi.org/10.1038/embor.2009.68

Schünke, S., M. Stoldt, J. Lecher, U.B. Kaupp, and D. Willbold. 2011. Structural insights into conformational changes of a cyclic nucleotide-binding domain in solution from *Mesorhizobium loti* K1 channel. *Proc. Natl. Acad. Sci. USA.* 108:6121–6126. http://dx.doi.org/10.1073/pnas.1015890108

Varnum, M.D., K.D. Black, and W.N. Zagotta. 1995. Molecular mechanism for ligand discrimination of cyclic nucleotide-gated channels. *Neuron.* 15:619–625. http://dx.doi.org/10.1016/0896-6273(95)90150-7

Yifrach, O., N. Zandany, and T. Shem-Ad. 2009. Examining cooperative gating phenomena in voltage-dependent potassium channels: Taking the energetic approach. *Methods Enzymol.* 466:179–209. http://dx.doi.org/10.1016/S0076-6879(09)66008-0

Zhang, X., and R.H. Cote. 2005. cGMP signaling in vertebrate retinal photoreceptor cells. *Front. Biosci.* 10:1191–1204. http://dx.doi.org/10.2741/1612

Zhou, L., and S.A. Siegelbaum. 2007. Gating of HCN channels by cyclic nucleotides: Residue contacts that underlie ligand binding, selectivity, and efficacy. *Structure.* 15:655–670. http://dx.doi.org/10.1016/j.str.2007.04.012

Zhou, L., and S.A. Siegelbaum. 2008. Pathway and endpoint free energy calculations for cyclic nucleotide binding to HCN channels. *Biophys. J.* 94:L90–L92. http://dx.doi.org/10.1529/biophysj.108.130872

Pessoa et al., http://www.jgp.org/cgi/content/full/jgp.201311145/DC1

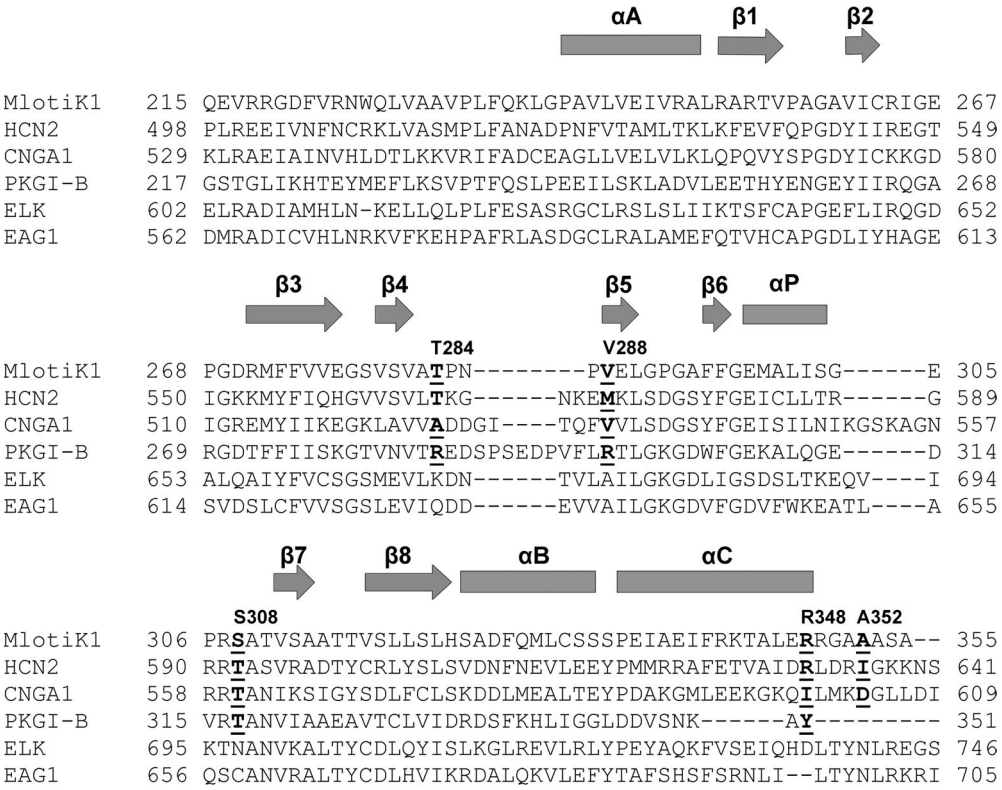

Figure S1. Sequence alignment of CNB domains from the MlotiK1 (UniProt accession no. Q98GN8), HCN2 (RefSeq accession no. NP_032252), and CNGA-1 channels (UniProt accession no. Q00194); CNB β domain from the cGMP-dependent kinase I (UniProt accession no. Q13976); and CNB homology domains from the ELK (RefSeq accession no. XP_001919436) and EAG1 (RefSeq accession no. NP_034730) channels. Secondary structure elements of MlotiK1CNB domain are shown as arrows (β strand) or rectangles (α helix). Residues that are discussed in the main text are shown in bold.

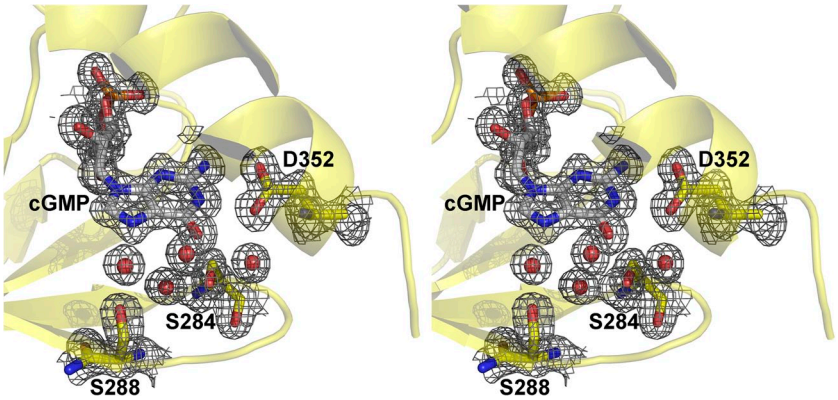

Figure S2. Stereo view of the 2Fo-Fc electron density map at 1.25-Å resolution covering the binding pocket of the T284S/V288S/A352D MlotiK1 CNB domain. cGMP and side chains of S288, D352, and S384 are represented as stick. Water molecules A–D are represented in red spheres. Electron density around these elements is represented by a gray mesh.

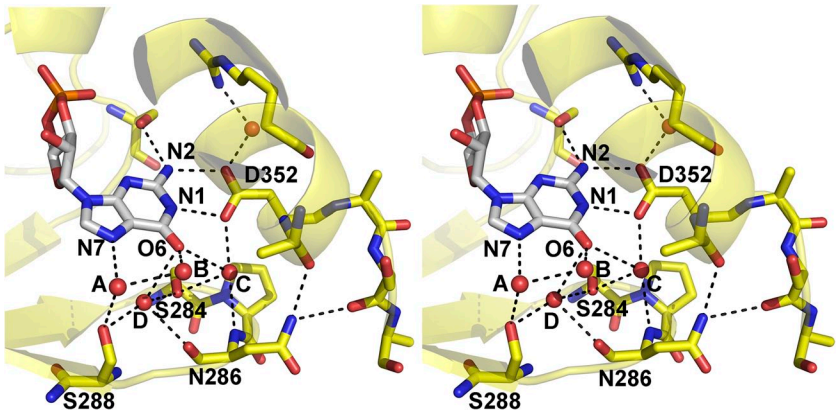

Figure S3. Stereo view of the ligand-binding pocket in the triple mutant. Water molecules are represented by red spheres, and the ligand (in white) and some residues (in yellow) are represented as stick. Residues and atoms discussed in the main text are labeled. The hydrogen bond network is represented by dashed lines.

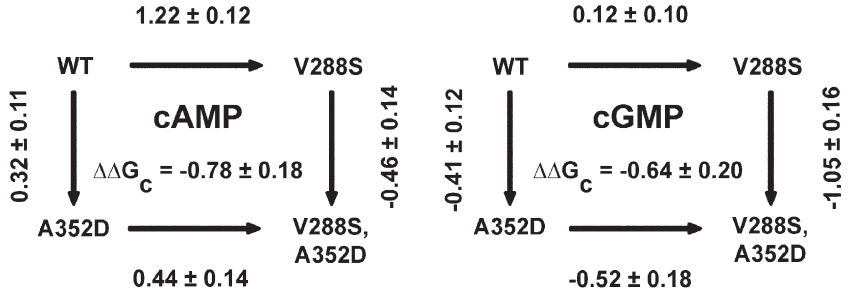

Figure S4. Mutant cycle energetic analysis. Mutant cycle of the V288S and A352D combination for cAMP (left) and cGMP binding (right). Corners correspond to wild-type, single, and double mutant CNB domain. Changes in ligand-binding energy (in kcal/mol) between different protein forms are indicated along the arrows connecting the corners. Coupling energy (ΔΔGc; in kcal/mol) is shown at the center of each panel.

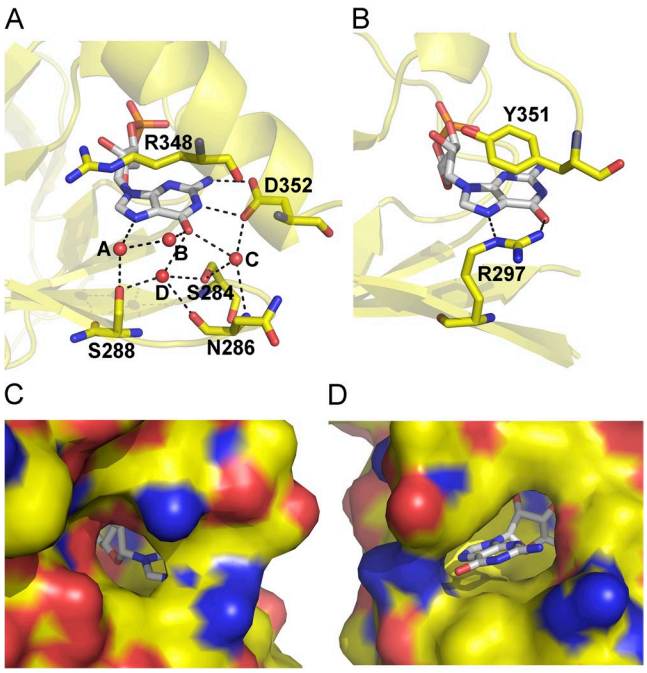

Figure S5. The CNB β domain from the cGMP-dependent protein kinase I. Identical views of the ligand-binding pocket in (A) the triple mutant domain from the MlotiK1 channel and in (B) the CNB β domain from the cGMP-dependent protein kinase I (Protein Data Bank accession no. 4KU7). Waters and some of the residues surrounding the nucleotide are labeled and shown as spheres and sticks, respectively. (C and D) Two views of the ligand-binding pocket in the CNB β domain from the cGMP-dependent protein kinase I, with the protein shown as a solvent-accessible surface. The figure shows that in this domain, the ligand is very exposed to the bulk solvent through two large water-accessible tunnels.

Table S1
Statistics of crystallographic data and refinement

Parameter	Value
Data collection	
Space group	P 2_1 2_1 2_1
Cell dimensions a, b, c (Å)	a = 60.05, b = 61.57, c = 67.84
Cell angles α, β, γ (°)	α, β, γ = 90.00
Resolution (Å)	42.99–1.22 (1.29–1.22)
R_{merge}	0.033 (0.646)
Total reflections	260,877 (33,195)
Unique reflections	74,662 (10,447)
$I/\sigma I$	20.9 (1.8)
Completeness (%)	99.0 (98.5)
Multiplicity	3.5 (3.2)
Refinement:	
Resolution (Å)	42.99–1.25 (1.27–1.25)
No. reflections	66,278 (3,514)
R_{work} / R_{free}	13.7/17.2
Number of atoms:	
Protein	4,402
Ligands	74
Solvent	355
Average B factor (all atoms) (Å^2)	18.0
RMSDs:	
Bond lengths (Å)	0.013
Bond angles (°)	1.56

Values in parentheses refer to the highest resolution shell.

Gating of the MlotiK1 potassium channel involves large rearrangements of the cyclic nucleotide-binding domains

Stefania A. Mari[a], João Pessoa[b,c], Stephen Altieri[d], Ulf Hensen[a], Lise Thomas[e], João H. Morais-Cabral[b,1], and Daniel J. Müller[a,1]

[a]Department of Biosystems Science and Engineering, Eidgenössische Technische Hochschule (ETH) Zurich, 4058 Basel, Switzerland; [b]Instituto de Biologia Molecular e Celular, Universidade do Porto, Rua do Campo Alegre 823, 4150-180 Porto, Portugal; [c]Instituto de Ciências Biomédicas Abel Salazar, Universidade do Porto, Largo Professor Abel Salazar 2, 4150-003 Porto, Portugal; [d]Department of Molecular Biophysics and Biochemistry, Yale University, New Haven, CT 06517; and [e]Department of Biological Sciences, Quinnipiac University, Hamden, CT 06517

Edited by Christopher Miller, Howard Hughes Medical Institute, Brandeis University, Waltham, MA, and approved November 2, 2011 (received for review July 12, 2011)

Cyclic nucleotide-regulated ion channels are present in bacteria, plants, vertebrates, and humans. In higher organisms, they are closely involved in signaling networks of vision and olfaction. Binding of cAMP or cGMP favors the activation of these ion channels. Despite a wealth of structural and studies, there is a lack of structural data describing the gating process in a full-length cyclic nucleotide-regulated channel. We used high-resolution atomic force microscopy (AFM) to directly observe the conformational change of the membrane embedded bacterial cyclic nucleotide-regulated channel MlotiK1. In the nucleotide-bound conformation, the cytoplasmic cyclic nucleotide-binding (CNB) domains of MlotiK1 are disposed in a fourfold symmetric arrangement forming a pore-like vestibule. Upon nucleotide-unbinding, the four CNB domains undergo a large rearrangement, stand up by ∼1.7 nm, and adopt a structurally variable grouped conformation that closes the cytoplasmic vestibule. This fully reversible conformational change provides insight into how CNB domains rearrange when regulating the potassium channel.

conformational changes | cyclic nucleotide gating | membrane protein | MloK1 | single-molecule imaging

Potassium channels are tetrameric membrane proteins that facilitate the permeation of potassium ions through the membrane with high specificity and high-throughput rates. These channels are central to the electrical activity of cells in humans and are, therefore, of fundamental importance for the function of nervous and muscular systems. The major mode of functional regulation in potassium channels is gating, a conformational change that occurs on the intracellular regions of the ion pore domain and involves an iris-like movement of the C-terminal transmembrane helices and a widening of the intracellular pore. Gating in potassium channels is induced by a variety of stimuli, including membrane voltage, intracellular calcium concentration, and cyclic nucleotide levels (1). These stimuli are sensed by a separate domain from the ion pore domain, inducing a conformational change that is then propagated to the gate of the channel.

The MlotiK1 potassium channel, from the bacterium *Mesorhizobium loti*, belongs to the family of channels that is regulated by cyclic nucleotides and includes eukaryotic cyclic nucleotide-gated (CNG) and hyperpolarization activated cyclic nucleotide-gated (HCN) channels (2, 3). These channels have C-terminal cytoplasmic cyclic nucleotide-binding (CNB) domains and upon binding of cAMP or cGMP, these domains undergo a conformational change that favors the opening of the gate of the channel. The major difference between the MlotiK1 channel and the CNG or HCN channels is the linker that connects the gate to the CNB domains. This helical linker (C linker) is roughly 80 residues long in CNG and HCN channels and only ∼20 residues long in the MlotiK1 channel.

The MlotiK1 channel has been the focus of structural and functional studies with the aim of understanding channel regulation by cyclic nucleotides. X-ray and NMR structures of the CNB domain in the cAMP-bound and -unbound conformations have been reported (4–6). Together with other CNB domain structures (7–9), the MlotiK1 studies have provided molecular details of ligand-binding and defined associated conformational changes. The structure of the full-length MlotiK1 channel, in detergent, has been reported at 3.1 Å resolution. This X-ray structure revealed the membrane-buried channel regions in the closed state, whereas the disordered CNB domains could not be observed (10). Electron microscopy of full-length channels in the presence of cAMP, either as 2D crystals in lipid bilayers or as single particles solubilized in detergent, produced a 9-Å resolution projection map (11) and a 16-Å resolution 3D structural model (12), respectively. The single-particle reconstruction shows the ligand-binding domains disposed in a fourfold symmetric arrangement. Despite this structural information, there is still a lack of understanding about the conformational changes that occur in the MlotiK1 channel upon ligand-binding.

Atomic force microscopy (AFM) has been established to observe the surfaces of membrane proteins at high resolution (0.5–2 nm) in their native state (13, 14). Importantly for biological applications, AFM requires no labeling or staining and allows imaging of membrane proteins in the lipid membrane, in buffer solution, and at ambient temperature (15, 16). With time-lapse AFM, it is possible to image single-membrane proteins at work (15, 17–19), as well as diffusing and assembling into higher complexes (20, 21).

To better understand the mechanism of gating in full-length cyclic nucleotide-regulated channels, we applied time-lapse AFM to characterize the conformational changes induced in the MlotiK1 channel by ligand-binding and -unbinding. AFM topographs show that upon cAMP-unbinding, the CNB domains of MlotiK1 undergo large conformational changes and move ∼1.7 nm. These conformational changes are reversed upon rebinding of cyclic nucleotide.

Author contributions: S.A.M., S.A., L.T., J.H.M.-C., and D.J.M. designed research; S.A.M., S.A., and L.T. performed research; J.P., J.H.M.-C., and D.J.M. contributed new reagents/analytic tools; S.A.M., S.A., U.H., L.T., J.H.M.-C., and D.J.M. analyzed data; U.H. created the structural models; and S.A.M., J.P., J.H.M.-C., and D.J.M. wrote the paper.

The authors declare no conflict of interest.

This article is a PNAS Direct Submission.

Freely available online through the PNAS open access option.

[1]To whom correspondence may be addressed. E-mail: daniel.mueller@bsse.ethz.ch or jcabral@ibmc.up.pt.

This article contains supporting information online at www.pnas.org/lookup/suppl/doi:10.1073/pnas.1111149108/-/DCSupplemental.

Results

High-Resolution AFM Imaging of Bound-State MlotiK1 Channels. Wild-type (wt) MlotiK1 channels reconstituted at high protein: lipid ratio in polar *Escherichia coli* lipid membranes were adsorbed onto freshly cleaved mica and imaged by AFM in the presence of cAMP (Fig. S1). AFM topographs showed the 3D surface of lipid membranes, having diameters up to several tens of micrometers and islands of densely packed MlotiK1 channels. The height of the lipid membranes above the mica support was 4.0 ± 0.5 nm (n = 81), whereas the height of MlotiK1 containing membranes was 10.2 ± 0.8 nm (n = 176).

At higher resolution, AFM topographs of the densely packed protein assemblies revealed single MlotiK1 channels (Fig. 1) that showed a fourfold symmetric arrangement protruding 3.2 ± 0.5 nm (n = 100) from the lipid surface. Previous structural studies suggest that only the relatively large cytoplasmic CNB domains can protrude that far from the membrane surface (4, 11, 12). In contrast, the extracellular surface of MlotiK1 is expected to protrude less. Indeed, AFM topographs showed shallow fourfold symmetric protein surfaces that protruded only 1.8 ± 0.5 nm (n = 48) between the higher protruding tetrameric MlotiK1 channels (Fig. 1*B* and Fig. S2). This alternate disposition of MlotiK1 channels exposing either their cytoplasmic or extracellular surface is consistent with the previously described "up-and-down" packing of MlotiK1 channels reconstituted into 2D crystals (11, 12). A schematic figure (Fig. S3) shows the arrangement of the MlotiK1 channels and the heights measured by AFM. From these observations, we conclude that the four high protrusions of MlotiK1 represent the cytoplasmic cAMP-binding domains.

To gain further insights into the disposition of CNB domains, we calculated a correlation-averaged topography of the MlotiK1 tetramer (Fig. 1*C*). The average shows that each CNB domain is oriented radially from the axis of the tetramer. At the center, the tetramer shows a vestibule with an inner diameter of ~1.5 ± 0.5 nm and a depth of ~1.4 ± 0.3 nm (n = 54). The SD map (22) shows the structural variability of the CNB domains (Fig. 1*D*).

MlotiK1 Membranes Increase Thickness in the Absence of cAMP. It is expected that changing the functional state of MoltiK1 because of binding or unbinding of cyclic nucleotide causes the potassium channel to undergo a conformational change. Unfortunately, we could not use the wt MlotiK1 channel for imaging this change. The CNB domain of the wt MlotiK1 channel shows a high binding affinity for cAMP (K_D, ~80 nM) (23). Therefore, removal of nucleotide from the CNB domain by dialysis or by exchanging the buffer is an extremely slow and inefficient process (4, 6, 23). Accordingly, wt MlotiK1 membranes showed no significant changes in the absence of cAMP (Fig. S1 *a–c*). This observation was not altered after extensive washing steps and storage of wt MlotiK1 membranes for 4 d in cAMP-free buffer solution at room temperature (Fig. S4). High-resolution AFM topographs of wt MlotiK1 channels recorded in the absence of cAMP did not reveal conformational changes (Figs. S4*b* and S5). wt MlotiK1 membranes that were dialyzed for 9 d against cAMP-free buffer (*Materials and Methods*) showed no structural changes as well (Fig. S6*a*).

To study the conformational change that occurs upon ligand-binding and -unbinding, we used the R348A mutant of MlotiK1 that has lower affinity for cAMP (K_D, ~18 μM) and can be prepared both in the bound and unbound states (23). We had previously reported that this mutant was not activated by cAMP (4), but by decreasing the background noise of the radioactivity uptake assay, we are now able to detect nucleotide-dependent channel activity (Fig. 2 and *Materials and Methods*). R348A mutant channel has a substantially lower maximal activity than the wt channel (Fig. 2, inset), with a $K_{1/2}$ of activation (10.0 ± 4.4 μM) 100-fold higher than wt MlotiK1 (Fig. 2). These results are consistent with previous cAMP-binding studies that show the CNB domain of the R348A mutant to bind cAMP at lower affinity (23).

We first imaged the R348A mutant in the presence of a saturating concentration of 900 μM cAMP (Fig. 3 *A–C*). Within the resolution achieved (1.5–2 nm), the mutant channel is indistinguishable from wt MlotiK1 (Fig. 1). Additionally, these mutant

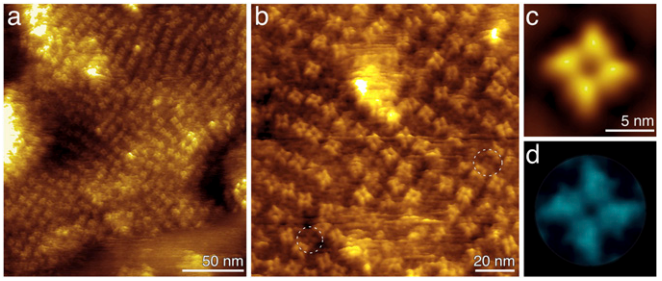

Fig. 1. High-resolution AFM topographs of the wt cyclic nucleotide-regulated potassium channel MlotiK1. (*A*) Overview of a membrane patch of densely packed MlotiK1 channels. (*B*) MlotiK1 channels imaged at higher resolution. Each of the light colored tetramers corresponds to a channel viewed from the cytoplasmic side. Individual protrusions correspond to individual CNB domains that protrude 3.2 ± 0.5 nm (n = 100) from the lipid bilayer. In between the highly protruding (or light colored) channels, lower-lying tetramers (dashed circles) exposing the extracellular surface of the channel can be observed. These lower tetramers protrude 1.8 ± 0.5 nm (n = 48) from the lipid bilayer. A gallery of these lower-protruding MlotiK1 channels is shown in Fig. S2. Correlation average (*C*) and SD map (*D*) calculated from 54 highly protruding MlotiK1 tetramers show details of the CNB domains. AFM topographs show full-color levels corresponding to vertical height scale of 12 nm (*A*), 5 nm (*B*), 4 nm (*C*), and 0.6 nm (*D*). Imaging buffer was 50 mM KCl, 200 μM cAMP, and 20 mM Tris-HCl (pH 7.5).

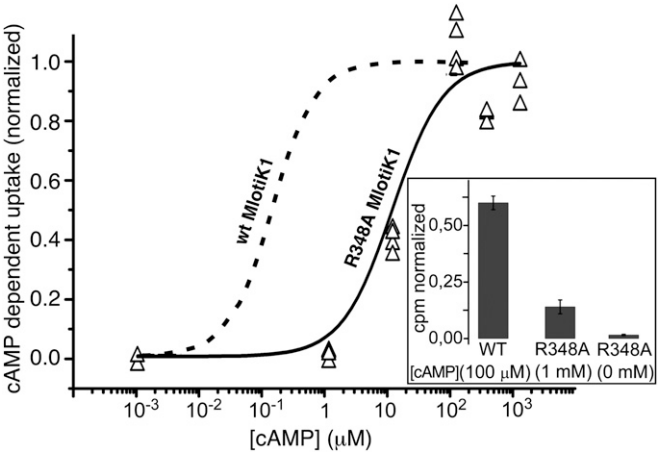

Fig. 2. cAMP-dependent activity of the wt and R348A mutant MlotiK1 channels. Uptake of $^{86}Rb^+$ into liposomes containing R348A mutant channel was measured in dependence of cAMP. The uptake activity was examined in duplicate at each cAMP concentration, from a common stock of liposomes. Raw values were first normalized by valinomycin uptake in the same vesicles and subsequently normalized by uptake at the maximum value (1 mM cAMP). The experiment was conducted twice (with different purifications), yielding four data points at each concentration. The solid curve shows a fit of the R348A data (triangles) with a Hill equation, yielding a $K_{1/2}$ of activation of 10 ± 4 μM and Hill coefficient of 1.1 ± 0.6. The dashed curve illustrates the fitted curve of similar experiments published on wt MlotiK1 (5), with $K_{1/2}$ of 110 nM and Hill coefficient of 1.3. The inset shows normalized radioactivity cpm for wt and mutant MlotiK1 at saturating cAMP concentrations (100 μM for wt; 1 mM for R348A) or in the absence of cAMP (R348A, 0 mM). The raw data (R348A) show mean values, and bars indicate SEs. The wt data were taken from ref. 4.

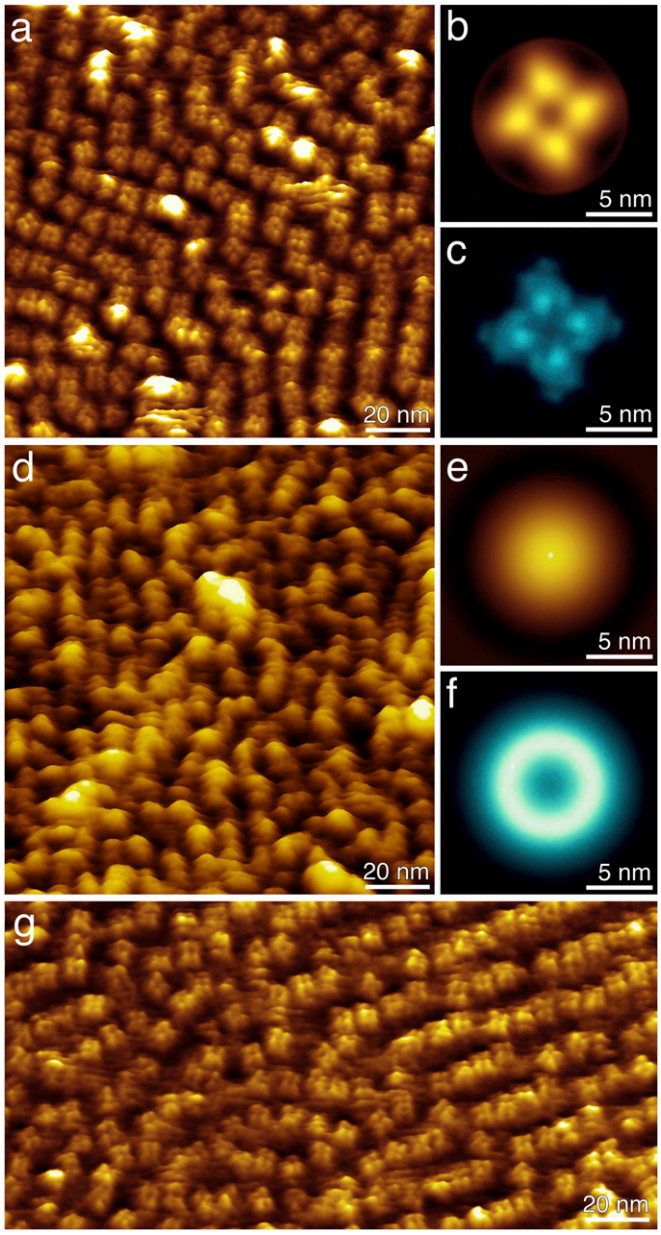

Fig. 3. High-resolution AFM topographs of the R348A mutant cyclic nucleotide-regulated potassium channel MlotiK1. (*A*) Mutant potassium channels imaged in the presence of cAMP. Single MlotiK1 tetramers protrude 3.1 ± 0.5 nm (n = 57) from the lipid bilayer. (*B* and *C*) Correlation average (*B*) and SD map (*C*) of 73 MlotiK1 tetramers showing details of the CNB domains. (*D*) Mutant potassium channels imaged in the absence of cAMP. The topograph shows single protrusions that correspond to individual MlotiK1 tetramers and extend 4.9 ± 0.6 nm (n = 148) from the lipid bilayer. (*E*) Single-particle average of 256 protrusions. (*F*) SD map of *E* showing the high structural variability of the protrusions in the unbound state. (*G*) Mutant Mlotik1 imaged after readdition of cAMP shows single tetramers that protrude 3.2 ± 0.5 nm (n = 45) from the lipid bilayer. AFM topographs have full-color levels corresponding to vertical height scales of 4 nm (*A*, *B*, and *G*), 0.6 nm (*C*), 6 nm (*D* and *E*) and 1.5 nm (*F*). Imaging buffer was 50 mM KCl, 900 μM cAMP (*A* and *G*), no cAMP (*D*), and 20 mM Tris-HCl (pH 7.5).

MlotiK1 membranes showed the same height 10.1 ± 0.8 nm (n = 156) as observed for wt MlotiK1 membranes (Fig. S1*D*). This agrees with the functional characterization that shows that the mutant is active (Fig. 2). To characterize the changes induced by cAMP release, we replaced the AFM imaging buffer for a cAMP-free buffer and reimaged the mutant MlotiK1 membranes after an incubation time of >3 h (Fig. S1 *d* and *e*). Mutant MlotiK1 membranes significantly increased heights (~1.7 nm) upon removal of cAMP, protruding 11.8 ± 0.8 nm (n = 147) from the mica support. This height change was reversed by the addition of 900 μM cAMP (Fig. S1*f* and Table S1).

We also imaged mutant MlotiK1 membranes that underwent a long dialysis step (9 d, with several dialysis-buffer changes) against cAMP-free buffer after protein reconstitution and before adsorption to the mica support. These membranes, imaged in cAMP-free buffer, showed an even larger height increase relative to the bound-state channel membranes, now protruding 13.5 ± 0.7 nm (n = 153) from the support (Fig. S6*b*). The cAMP-dependent height differences of the differently prepared mutant samples (Table S1) depend on the adsorption to mica. In samples already adsorbed to the mica support, the CNB domains in contact with the mica (Fig. S3) are hardly accessible to buffer exchange, do not loose the ligand, and, therefore, do not undergo a conformational change. Accordingly, removal of cAMP causes a ~1.7 nm height increase per membrane leaflet. Table S1 gives an overview of all heights measured for wt and mutant MlotiK1 membranes, and Fig. S7 illustrates the nucleotide-dependent height changes of the membrane leaflets.

Nucleotide-Binding Domains Undergo Drastic Conformational Changes. To characterize in detail the structural changes occurring with ligand-unbinding, we imaged the membranes containing mutant MlotiK1 channels at higher resolution. In cAMP-free buffer, we observed that the potassium channels protruded by 4.9 ± 0.6 nm (n = 148) from the lipid surface (Fig. 3*D* and Figs. S8 and S9). The characteristic fourfold symmetric structure of MlotiK1 observed in the cAMP-bound state (Figs. 1 and 3 *A* and *B* and Fig. S5), with four CNB domains surrounding the vestibule, was lost and each channel showed a single protrusion (Fig. 3 *D* and *E*). Importantly, at the single-molecule level, the protrusions do not show any obvious structural feature. This was reflected in the correlation-averaged topography (Fig. 3*E*). The SD map of the cAMP-unbound CNB domains showed much higher values (Fig. 3*F*) than that observed in presence of cAMP (Fig. 3*C*). This indicates an increased structural variability (or conformational flexibility) (22) of the CNB domains in the absence of ligand. Possibly because of this flexibility, substructural details of nucleotide-free MlotiK1 could not be contoured by the scanning AFM tip. Moreover, the AFM topographs showed that some protrusions appear to become more continuous between neighboring channels as if the CNB domains in the cAMP-unbound state could group with CNB domains from adjacent channels (Fig. 3*D* and Figs. S8 and S9). This change probably reflects an enhanced structural flexibility of the CNB domains, which allows them to explore a larger area and to interact with adjacent CNB domains provided by the densely packed potassium channels.

Upon readdition of saturating cAMP concentrations of 900 μM (Fig. 2), all CNB domains (~99%) collapsed back onto the membrane and adopted the cAMP-bound conformation (Fig. 3*G*). To image densely packed MlotiK1 membranes that show both bound and unbound channel conformations, we incubated mutant MlotiK1 membranes with cAMP-free buffer. Verification that the CNB domains switched to their cAMP-unbound conformation was performed by AFM imaging the height changes of MlotiK1 membranes. After this, we readded 600 μM cAMP, which did not fully saturate the CNB domains, and imaged the mutant MlotiK1 channels at a higher resolution (Figs. S8 and S9). It was observed that the majority, but not all, of channels collapsed back to the cAMP-bound conformation. The AFM topographs showing the coexistence of both cAMP-unbound and cAMP-bound conformations suggest that the conformational change of MlotiK1 channels is not cooperative between neighboring channels. Most importantly, however, these topographs directly show the height difference between the cAMP-unbound and cAMP-bound mutant

MlotiK1 channels of ~1.7 nm (Figs. S8 and S9) and confirm the same height difference detected upon switching the conformation of all mutant channels of a membrane by cAMP (Fig. 3 and Tables S1 and S2).

Table S2 summarizes the heights measured for wt and mutant MlotiK1 channels in the presence and absence of cAMP. Every experiment from which we calculated the average heights was repeated 12 times (see *Materials and Methods*). In every experiment that involved removing cAMP from the buffer solution, we observed that the mutant channels switched from the cAMP-bound to the cAMP-unbound conformation, and upon adding cAMP to the buffer solution, the mutant channels readopted the cAMP-bound conformation. However, these nucleotide-dependent conformational changes could not be recorded for wt MlotiK1 channels. In summary, these results show that the conformational changes observed for mutant MlotiK1 are fully reversible and dependent on cyclic nucleotide. They further support the idea that these changes are involved in the gating mechanism of the cyclic nucleotide-regulated potassium channel MlotiK1.

Discussion

Using AFM, we have imaged at the single molecule level two different conformational states of the cyclic nucleotide-regulated potassium channel MlotiK1 in a lipid membrane. For these experiments, we used wt MlotiK1 and the R348A point mutant MlotiK1. Consistent with previous reports (4, 6, 23), the wt MlotiK1 channel could only be imaged in the cAMP-bound state. In contrast, the mutant channel is activated at a higher cAMP concentration, allowing us to visualize both the unbound and bound states. Importantly, the conformations of the bound state of wt and mutant MlotiK1 were indistinguishable. In the bound state, the cytoplasmic CNB domains are clearly discernible and organized in a fourfold arrangement (Figs. 1 *B* and *C* and 3 *A* and *B*), matching the symmetry of the membrane-buried regions of the channel (10). This disposition of the CNB domains was previously observed by electron microscopy (12). Strikingly, with AFM, it was possible to image a vestibule at the center of the tetrameric arrangement (Figs. 1*C* and 3*B* and Fig. S5*b*).

We compared the AFM topograph of the channel in the bound state to a model generated (Fig. 4 *C*, *E*, and *G*) with MlotiK1 X-ray structures of the transmembrane channel regions [Protein Databank (PDB) code 3BEH] (10) and of the cAMP-bound domain (PDB code 1VP6) (4). Because residues 219–224 of MlotiK1 are present in a α-helical conformation in both crystal structures, the four CNB domains could be docked to the transmembrane channel region (Fig. 4 *E* and *G*). The CNB domains were then rotated outward to minimize steric clashes with the long S2–S3 channel loops and between the four CNB domains. Superimposing the CNB domain X-ray structure to the AFM topograph of the cAMP-bound state (Fig. 4 *A* and *C*) confirms that the four protrusions contoured by AFM are the cytoplasmic CNB domains. The model also shows the presence of a vestibule created by the CNB domains and the helical linker (C linker) that connects the domains to the transmembrane regions of the channel.

AFM imaging revealed that removal of cAMP from the buffer solution caused a dramatic conformational change in the mutant MlotiK1 channel. In the unbound state, the well-defined arrangement of the CNB domains is lost and a single large protrusion without reproducible substructures is detected (Figs. 3*D* and 4 *B* and *D*). The protrusion stands out ~1.7 nm relative to the CNB domains in their cAMP-bound conformation. The topographs also show that during the structural rearrangement, the cytoplasmic vestibule has disappeared. Moreover, AFM detected an increased structural variability of CNB domains that was not observed for the nucleotide-bound state. This variability could result from the ability of the four CNB domains in a single MlotiK1 channel to adopt distinct positions from each other. Importantly, this conformational change was reversible, and upon addition of cAMP, the CNB domains converted back to the bound state (Fig. 3*G* and Figs. S8 and S9). In their rebound state, the CNB domains adopted the same structural conformation and regained the reduced structural flexibility observed before removal of cAMP.

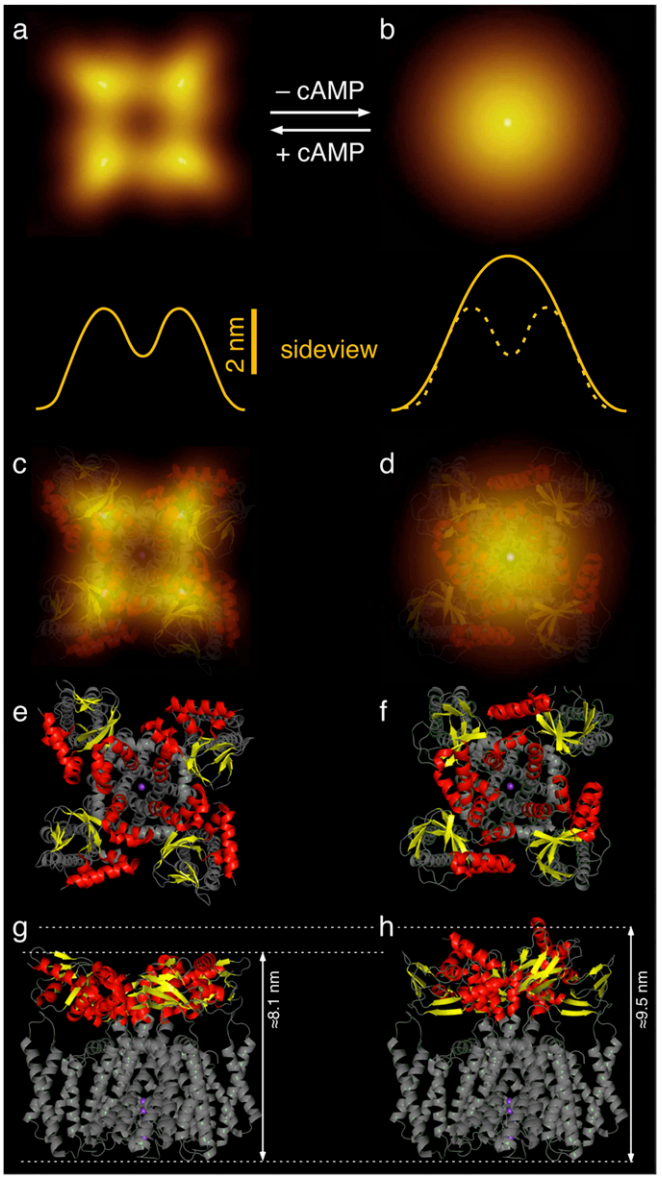

Fig. 4. Model of the conformational change gating the cyclic nucleotide-regulated potassium channel MlotiK1. Correlation-averaged AFM topographs of the cAMP-bound (*A*) and -unbound (*B*) conformations of the cytoplasmic surface of the MlotiK1 channel. Yellow lines represent height profiles of cross-sections along the averaged topographs. The dashed yellow line is that of the MlotiK1 channel in the cAMP-bound state. (*C* and *D*) Superimposition of averaged topograph and structural models for the cAMP-bound (*C*) and -unbound (*D*) conformations. Cytoplasmic CNB domains of the MlotiK1 channel are shown in red and yellow (see *E* and *F*); transmembrane domains are shown in gray. (*E*–*H*) Top (*E* and *F*) and side (*G* and *H*) view of structural models.

Unlike for the bound state, the molecular interpretation of the AFM topographs of the channel in the unbound state is not straightforward, mainly because it is not possible to identify individual CNB domains. However, we can use what is known about the structural properties of the MlotiK1 channel to try to understand the changes detected by AFM. The transition between cAMP-bound and -unbound states involves the disappearance of the cytoplasmic vestibule and an increase in the height of the CNB

domains. A possible explanation for the height change between the two states is revealed by creating a molecular model with the MlotiK1 X-ray structures of the transmembrane channel regions (PDB code 3BEH) (10) and of the cAMP-unbound CNB domain (PDB code 1U12) (4). A comparison between the model created with the cAMP-unbound CNB domains (Fig. 4 *F* and *H*) and the one created with cAMP-bound CNB domains (Fig. 4 *E* and *G*) shows a height difference of ∼1.6–1.9 nm, a value that compares very well with the height change measured by AFM between the channel bound and unbound states (Fig. 4 *A* and *B*). This comparison reveals that the height increase detected by AFM could result from the conformational change that occurs in the CNB domains upon ligand-unbinding, a change that has been well characterized by X-ray crystallography and NMR (4–6).

An intriguing aspect detected in the transition between the bound to the unbound state is the increase in the structural variability (or flexibility) of the CNB domains. This increase was assessed from a series of features revealed by AFM. (i) The SD map of the unbound-state protrusions (Fig. 3*F*) shows much larger values than similar maps for the bound state (Figs. 1*D* and 3*C*). This reflects a larger structural variability between protrusions of individual MlotiK1 channels. (ii) The averaged single protrusion in the unbound state lacks structural details; (iii) the CNB domains of single MlotiK1 channels in the unbound state are no longer distinguishable (Fig. 3*D* and Figs. S8 and S9*a*); and (iv) the protrusions of some channels in the unbound state can group with protrusions of neighboring MlotiK1 channels, indicating that the CNB domains are free to extend and to establish contacts with CNB domains from adjacent channels (Fig. 3*D* and Figs. S8 and S9).

Structural variability had been previously associated with the MlotiK1 CNB domains: (i) in the X-ray structure of the full-length MlotiK1, with partial ligand occupancy (10), the linker connecting the domains to the last transmembrane helix was clearly defined, but the CNB domains were crystallographically disordered and not observed; and (ii) in a comparison between different cAMP-unbound domain structures (5), the helices on the surface of the CNB domain, including the C-linker helix that connects to the channel gate, adopted different positions reflecting accessibility to multiple conformational states. In contrast, different X-ray structures in the cAMP-bound state were basically identical.

The conformational change observed for the CNB domains upon cAMP release is associated with an apparent volume increase of the cytoplasmic MlotiK1 surface. This increase is illustrated by the height profiles of the correlation averages (Fig. 4*B*). Based on the AFM topographs, we estimate that the apparent increase in volume is between 16–31 nm^3, depending on whether or not we consider that the cytoplasmic vestibule is filled with protein. Using as rule of thumb an average volume of 0.14 nm^3 for each amino acid (24), this apparent volume increase corresponds to 114–220 residues more in the cytoplasmic region in the unbound state relative to the bound state. From everything we know about potassium channels, a conformational change involving the transfer of these many amino acids from the transmembrane region to the cytoplasm is not possible. One possible explanation is that the apparent volume increase results from the conformational change of CNB domains that upon cAMP-unbinding increase height and distance from the transmembrane MlotiK1 domain, thereby creating a dome-like structure.

In conclusion, with AFM imaging of the MlotiK1 channel in two different functional states, we have shown that CNB domains in their cAMP-bound conformation are close to the membrane surface and adopt a well-defined conformation, whereas in the cAMP-unbound conformation, the CNB domains extend considerably from the transmembrane channel. A central characteristic of this ligand-induced conformational change is an order-to-disorder transition where in the bound state, CNB domains are ordered, and in the unbound, state the domains display a clear increase in their structural variability.

Materials and Methods

Protein Expression and Purification. Protein expression and purification were based on the procedure described previously (11). Full-length wt MlotiK1 was expressed in *E. coli* C41 (DE3) cells after induction (at OD_{600}, ∼1.0) for 5 h with 0.3 μg/mL anhydrotetracycline (Fluka). Cells were lysed in PBS buffer, and membranes containing MlotiK1 were harvested by ultracentrifugation (257,000 × *g*, 90 min). MlotiK1 was extracted from membranes with PBS buffer containing 25 mM n-decyl-β-D-maltopyranoside (DM), 5 mM β-mercaptoethanol, 200 μM cAMP. The histidine-tagged MlotiK1 was bound to Ni-NTA agarose beads (Qiagen) and eluted with 500 mM imidazole. The histidine tag was cleaved off with thrombin (HIT) and MlotiK1 was twice purified in a Superdex 200 (Amersham Pharmacia Biotech) size-exclusion chromatography column equilibrated in 20 mM Tris-HCl (pH 7.5), 150 mM KCl, 200 μM cAMP, 3 mM DTT, and 5 mM lauryldimethylamine-*N*-oxide (LDAO). The same procedure was used for the MlotiK1 R348A mutant, where the cAMP concentration was kept at 400 μM throughout purification (if not stated otherwise).

Reconstituting Densely Packed MlotiK1 Membranes. MlotiK1 was reconstituted into lipid membranes forming densely packed assemblies using *E. coli* polar lipid extract (Avanti) as described previously (11). Lipids were dissolved in 20 mM Tris-HCl (pH 7.5), 150 mM KCl, 200 μM cAMP, 3 mM DTT, 5 mM LDAO, and 60 mM n-octyl-β-D-glucopyranoside. Samples were prepared by mixing protein and lipids at the lipid/protein ratios (mg/mg) of 1.5, 1.6, 1.7, or 1.8 (final volume was 109–111 μL). Mixtures were incubated at 30 °C for 1 h with agitation. Membranes were formed by dialyzing the samples against 2 L of a solution composed by 20 mM Tris-HCl (pH 7.5), 50 mM KCl, 200 μM cAMP for the wt channel and 600 μM cAMP for the mutant, 2 mM DTT, and 0.02% sodium azide using Slide-A-Lyzer MINI Dialysis units (Thermo Scientific) with a 10 kDa cutoff. Dialysis was continued for 2–3 d at 31 °C.

To prepare MlotiK1 channels without cyclic nucleotide, the membranes were formed in the presence of cAMP as described above, but then the dialysis buffer was changed for a dialysis solution without cAMP, and the dialysis was extended for 2 d at 31 °C. After this time, the temperature was changed to 20 °C, and the dialysis was continued for additional 7 d during which the cAMP-free dialysis solution was changed once. The expected nucleotide concentration after these dialysis steps was <300 pM for mutant and <100 pM for wt MlotiK1. These concentrations are well below the cAMP affinities of the channel (K_D (wt), ∼80 nM; K_D (mutant), ∼18 μM). Fresh DTT was added every 2 d. Reconstituted membranes were stored at 4 °C until AFM analysis.

Radioactive Flux Assay. The $^{86}Rb^+$ uptake assay was performed as described previously (4, 25). Briefly, MlotiK1 was reconstituted in proteoliposomes in the presence of high concentration of K^+. K^+ was removed from the external solution, $^{86}Rb^+$ was added, and after incubating for 90 min, the radioactivity associated with the proteoliposomes was measured. The data presented here display decreased baseline noise by comparison with our previous study (4). We attribute this to decreased contamination by other proteins, achieved by incremental improvements of multiple purification steps.

AFM. The AFM (Nanocope IIe; Veeco) was equipped with a fluid cell and oxide-sharpened Si_3N_4 cantilevers (OMCL TR400PSA; Olympus) having nominal spring constants of ∼0.09 N/m. Reconstituted MlotiK1 membranes were adsorbed onto freshly cleaved mica (26) in 200 mM KCl, 20 mM Tris-HCl (pH 7.5), and at cAMP concentrations indicated. After an adsorption time of ∼30 min, the sample was gently rinsed with the imaging buffer to remove nonadsorbed membranes. Imaging buffer solutions were either 50 mM KCl; 200, 600, or 900 μM cAMP; and 20 mM Tris-HCl (pH 7.5); or 50 mM KCl and 20 mM Tris-HCl (pH 7.5). All buffer solutions were freshly made using nano-pure water (18.2 MOhm/cm) and pro analysi (>98.5%) purity-grade reagents from Sigma and Merck. Upon buffer exchange, the AFM setup was thermally equilibrated for ∼30 min. When changing cAMP-containing buffer for cAMP-free buffer, the sample was incubated for >3 h before imaging. High-resolution contact-mode AFM topographs were recorded at room temperature and at imaging forces of ∼50 pN that do not to perturb the native membrane protein structure (13, 27). Imaging forces were manually adjusted to compensate for thermal drift (13). Proportional and integral gains were adjusted manually to minimize the error (deflection) signal and to maximize the height signal. When approaching a lateral resolution of ∼2 nm, the scanning speed of the AFM stylus was between 500 and 1500 nm/s.

To prove the reproducibility of the experimental findings, we repeated every experimental condition for wt and mutant MlotiK1 in at least 12 independent experiments. In every experiment, we recorded between 20 and 60 AFM topographs of MlotiK1 membranes and channels. For every experimental condition, the statistical height analysis of MlotiK1 membranes (Table S1) was

determined from membranes imaged in at least 12 independent experiments. All experiments conducted were consistent and showed that the height changes observed upon cAMP-binding and cAMP-unbinding of mutant MlotiK1 channels were fully reproducible (Tables S1 and S2).

Image Processing and Averaging. AFM topographs (512 × 512 pixels) were selected by the structural details of the reproducibly imaged MlotiK1 surface and when showing identical structural features in the simultaneously monitored trace and retrace scanning directions. Correlation averaging was performed using the SEMPER image processing system (28, 29). Single particles were translationally and rotationally aligned to a reference MlotiK1 and averaged. This correlation average was used as a reference for refinement cycles. Correlation-averaged unit cells of the MlotiK1 tetramer were fourfold symmetrized. To assess the SD, $\sigma_{k,l}$, individual unit cells were aligned angularly, as well as translationally, before single-particle averaging (30). The SD was then calculated from the averaged topograph $\mu_{k,l}$ for each pixel (k, l) for x^i particles:

$$\sigma^2_{k,l} = \frac{1}{N}\sum_{i-1}^{N}\left(x^i_{k,l} - \mu_{k,l}\right)^2$$

SD maps are displayed as image in a one-to-one pixel correspondence with the correlation-averaged topograph.

ACKNOWLEDGMENTS. We thank P. Bosshart for discussions and C. Bippes for experimental advice. This study was supported by the Deutsche Forschungsgemeinschaft; European Union; European Life Scientist Organization; Klaus Tschira Stiftung; Swiss National Science Foundation; Fundação para a Ciência e a Tecnologia (PhD Fellowship SFRH/BD/60274/2009 to J.P.); and European Molecular Biology Organization for an installation grant to J.H.M.-C.

1. Kaupp UB, Seifert R (2001) Molecular diversity of pacemaker ion channels. *Annu Rev Physiol* 63:235–257.
2. Kaupp UB, Seifert R (2002) Cyclic nucleotide-gated ion channels. *Physiol Rev* 82: 769–824.
3. Matulef K, Zagotta WN (2003) Cyclic nucleotide-gated ion channels. *Annu Rev Cell Dev Biol* 19:23–44.
4. Clayton GM, Silverman WR, Heginbotham L, Morais-Cabral JH (2004) Structural basis of ligand activation in a cyclic nucleotide regulated potassium channel. *Cell* 119: 615–627.
5. Altieri SL, et al. (2008) Structural and energetic analysis of activation by a cyclic nucleotide binding domain. *J Mol Biol* 381:655–669.
6. Schünke S, Stoldt M, Lecher J, Kaupp UB, Willbold D (2011) Structural insights into conformational changes of a cyclic nucleotide-binding domain in solution from *Mesorhizobium loti* K1 channel. *Proc Natl Acad Sci USA* 108:6121–6126.
7. Kim C, Xuong NH, Taylor SS (2005) Crystal structure of a complex between the catalytic and regulatory (RIalpha) subunits of PKA. *Science* 307:690–696.
8. Sharma H, Yu S, Kong J, Wang J, Steitz TA (2009) Structure of apo-CAP reveals that large conformational changes are necessary for DNA binding. *Proc Natl Acad Sci USA* 106:16604–16609.
9. Taraska JW, Puljung MC, Olivier NB, Flynn GE, Zagotta WN (2009) Mapping the structure and conformational movements of proteins with transition metal ion FRET. *Nat Methods* 6:532–537.
10. Clayton GM, Altieri S, Heginbotham L, Unger VM, Morais-Cabral JH (2008) Structure of the transmembrane regions of a bacterial cyclic nucleotide-regulated channel. *Proc Natl Acad Sci USA* 105:1511–1515.
11. Clayton GM, Aller SG, Wang J, Unger V, Morais-Cabral JH (2009) Combining electron crystallography and X-ray crystallography to study the MlotiK1 cyclic nucleotide-regulated potassium channel. *J Struct Biol* 167:220–226.
12. Chiu PL, et al. (2007) The structure of the prokaryotic cyclic nucleotide-modulated potassium channel MloK1 at 16 A resolution. *Structure* 15:1053–1064.
13. Müller DJ, Engel A (2007) Atomic force microscopy and spectroscopy of native membrane proteins. *Nat Protoc* 2:2191–2197.
14. Frederix PL, Bosshart PD, Engel A (2009) Atomic force microscopy of biological membranes. *Biophys J* 96:329–338.
15. Engel A, Müller DJ (2000) Observing single biomolecules at work with the atomic force microscope. *Nat Struct Biol* 7:715–718.
16. Müller DJ, Dufrêne YF (2008) Atomic force microscopy as a multifunctional molecular toolbox in nanobiotechnology. *Nat Nanotechnol* 3:261–269.
17. Müller DJ, Hand GM, Engel A, Sosinsky GE (2002) Conformational changes in surface structures of isolated connexin 26 gap junctions. *EMBO J* 21:3598–3607.
18. Yu J, Bippes CA, Hand GM, Muller DJ, Sosinsky GE (2007) Aminosulfonate modulated pH-induced conformational changes in connexin26 hemichannels. *J Biol Chem* 282: 8895–8904.
19. Mari SA, et al. (2010) pH-induced conformational change of the beta-barrel-forming protein OmpG reconstituted into native E. coli lipids. *J Mol Biol* 396:610–616.
20. Müller DJ, et al. (2003) Observing membrane protein diffusion at subnanometer resolution. *J Mol Biol* 327:925–930.
21. Yamashita H, et al. (2009) Dynamics of bacteriorhodopsin 2D crystal observed by high-speed atomic force microscopy. *J Struct Biol* 167:153–158.
22. Müller DJ, Fotiadis D, Engel A (1998) Mapping flexible protein domains at subnanometer resolution with the AFM. *FEBS Lett* 430:105–111.
23. Cukkemane A, et al. (2007) Subunits act independently in a cyclic nucleotide-activated K(+) channel. *EMBO Rep* 8:749–755.
24. Harpaz Y, Gerstein M, Chothia C (1994) Volume changes on protein folding. *Structure* 2:641–649.
25. Nimigean CM (2006) A radioactive uptake assay to measure ion transport across ion channel-containing liposomes. *Nat Protoc* 1:1207–1212.
26. Müller DJ, Amrein M, Engel A (1997) Adsorption of biological molecules to a solid support for scanning probe microscopy. *J Struct Biol* 119:172–188.
27. Müller DJ, Engel A (1999) Voltage and pH-induced channel closure of porin OmpF visualized by atomic force microscopy. *J Mol Biol* 285:1347–1351.
28. Saxton WO, Pitt TJ, Horner M (1979) Digital image processing: The semper system. *Ultramicroscopy* 4:343–354.
29. Saxton WO, Baumeister W (1982) The correlation averaging of a regularly arranged bacterial cell envelope protein. *J Microsc* 127:127–138.
30. Frank J, Bretaudiere J-P, Carazo J-M, Veschoor A, Wagenknecht T (1987) Classification of images of biomolecular assemblies: A study of ribosomes and ribosomal subunits of *Escheria coli*. *J Microsc* 150:99–115.

Supporting Information

Mari et al. 10.1073/pnas.1111149108

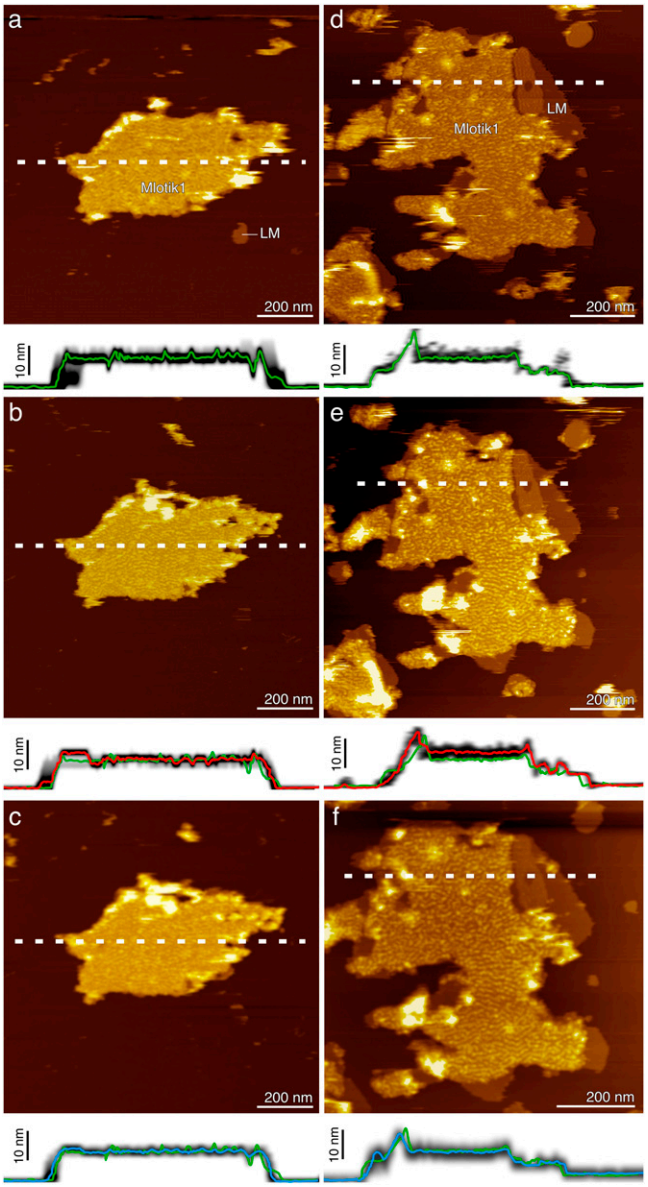

Fig. S1. Overview AFM topographs of wt and mutant R348A MlotiK1 reconstituted into membranes of *E. coli* polar lipid extract. Overviews of wt MlotiK1 channel (*a–c*) and mutant MlotiK1 channel (*d–f*) membranes prepared in the presence of cAMP (see *Materials and Methods*), and adsorbed and imaged in the presence of 200 μM cAMP (*a*) and 900 μM cAMP (*d*) after removing cAMP (*b* and e), and after the readdition of 200 μM cAMP (*c*) or 900 μM cAMP (*f*). Lipid membranes (LM) and densely packed MlotiK1 are clearly visible. Below each topograph is the height profile taken along the dashed lines. Every height profile represents the superimposition of 10 height lines and shows the height average (colored line) and height variation (gray shading). In the presence of cAMP, lipid membranes protruded 4.0 ± 0.5 nm (average ± SD; $n = 81$), wt MlotiK1 membrane patches protruded 10.2 ± 0.8 nm ($n = 176$) and mutant MlotiK1 patches protruded 10.1 ± 0.8 nm ($n = 156$) from the supporting mica. Imaging the same membranes in the absence of cAMP revealed no changes for wt MlotiK1 patches (*b*). Extending the incubation time in cAMP-free buffer solution to 4 d did not change the appearance and height (10.3 ± 0.6 nm; $n = 163$) of wt MlotiK1 membranes (compare with Fig. S4). In the absence of cAMP, mutant MlotiK1 membranes increased their height from 10.1 ± 0.8 nm (*d*) to 11.8 ± 0.8 nm ($n = 147$) (*e*). For better comparison, we superimposed the average height lines recorded in presence of cAMP (green lines) and height lines recorded in absence of cAMP (red lines) (*e*). Upon readding cAMP, wt MlotiK1 membranes showed no change in height (*c*), whereas mutant MlotiK1 membranes reduced their height back to that measured initially in the presence of cAMP (*f*). For better comparison, we superimposed the average height lines recorded in presence of readded cAMP (blue lines) and height lines recorded before depletion of cAMP (green lines) (*f*). Imaging buffers were 50 mM KCl and 20 mM Tris-HCl (pH 7.5) with cAMP concentrations as indicated. All heights for wt and mutant MlotiK1 measured in the presence of cAMP, in the absence of cAMP, and upon readding cAMP are given in Table S1. *n* gives the number of lipid membranes or MlotiK1 membranes measured.

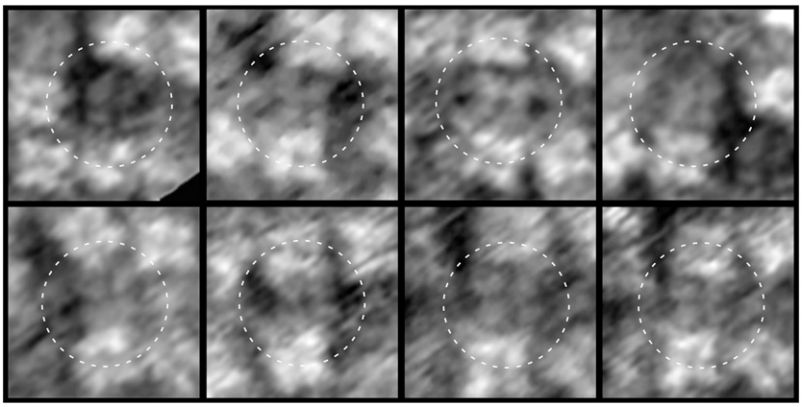

Fig. S2. Gallery of high-resolution AFM topographs of the extracellular surface of the wt MlotiK1 channel. AFM topographs revealed shallow tetrameric surfaces (outlined by dashed circles) between the highly protruding cytoplasmic surfaces of MlotiK1 channels. Different channels are shown at slightly different magnifications. The shallow tetramers protrude 1.8 ± 0.5 nm (n = 48) from the lipid bilayer, whereas the highly protruding tetramers protrude 3.2 ± 0.5 nm (n = 100) from the lipid membrane. On average, both the shallow and the highly protruding tetramers have an outer diameter of ~8–10 nm. AFM topographs show a gray level range corresponding to a vertical height scale of 4.5 nm. Imaging buffer was 50 mM KCl, 200 μM cAMP, and 20 mM Tris-HCl (pH 7.5). n gives the number of MlotiK1 tetramers measured.

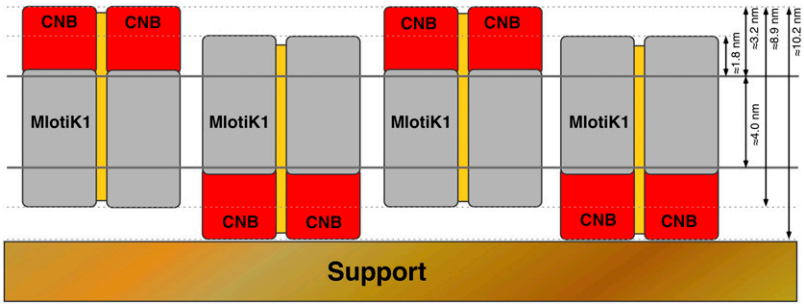

Fig. S3. Measured heights of the reconstituted wt MlotiK1 membrane. Schematic drawing showing a side view of the reconstituted MlotiK1 channels in an up-and-down orientation. Height values are average values measured from wt MlotiK1 in the presence of 50 mM KCl, 200 μM cAMP, and 20 mM Tris-HCl (pH 7.5).

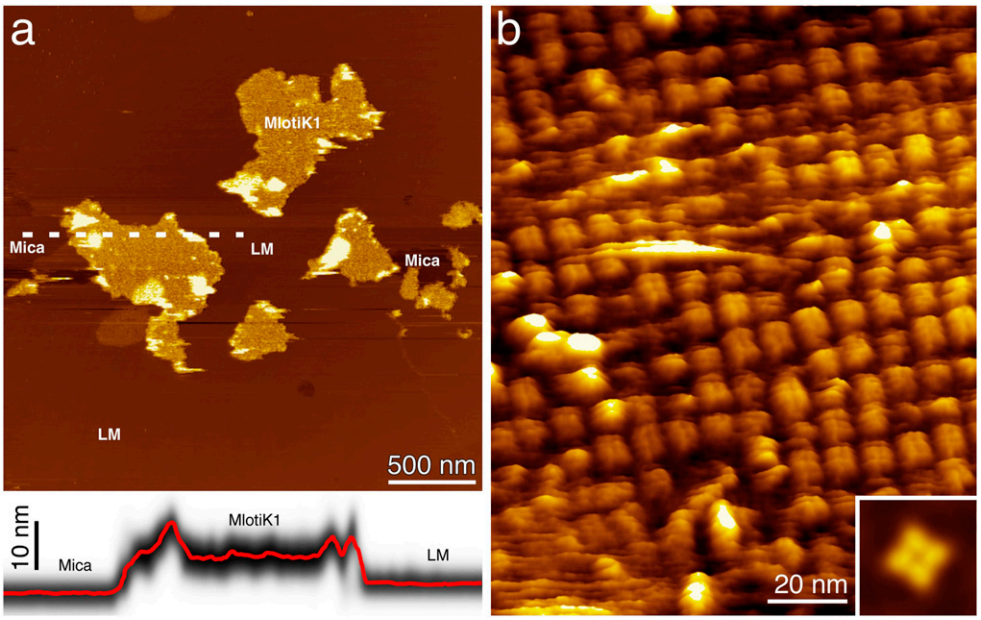

Fig. S4. AFM topographs of wt MlotiK1 membranes incubated for 4 d in cAMP-free buffer solution. (*a*) Overview topograph of wt MlotiK1 membranes. Lipid membranes (LM) embedding densely packed MlotiK1 are clearly visible. The height profile taken along the dashed line indicated in the topograph is shown at the bottom. The height profile represents the superimposition of 10 height lines and shows their average height (red line) and variation (gray shading). Lipid membranes protruded 3.6 ± 0.7 nm (n = 61), and MlotiK1 channels protruded 10.3 ± 0.6 nm (n = 163) from the support and 3.3 ± 0.5 nm (n = 117) from the lipid membrane. n gives the number of MlotiK1 membranes or channels measured. These average heights were not significantly different from average heights of wt MlotiK1 membranes recorded in the presence of cAMP (Fig. S1 *a* and *c* and Table S1). (*b*) High-resolution topograph showing wt MlotiK1 channels after incubation for 4 d in cAMP-free buffer at room temperature. The inset shows the correlation average of 117 MlotiK1 channels. Incubation and imaging buffer was 50 mM KCl and 20 mM Tris-HCl (pH 7.5). AFM topographs show full-color levels corresponding to vertical height scale of 20 nm (*a*) and 4.5 nm (*b*).

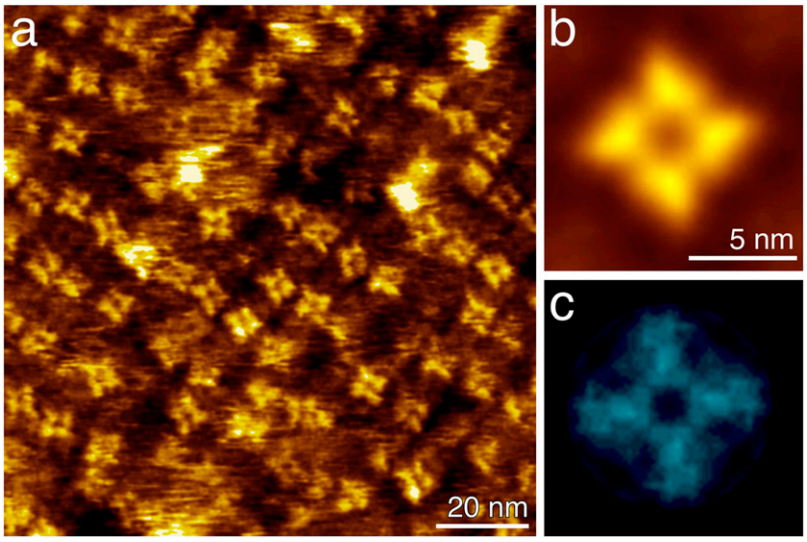

Fig. S5. High-resolution AFM topograph of wt MlotiK1 incubated for 12 h in cAMP-free buffer solution at room temperature. (*a*) Topograph showing single MlotiK1 channels with clearly visible CNB domains. Correlation average of 54 MlotiK1 tetramers showing the arrangement of the four CNB domains (*b*) and corresponding SD map showing the structural variability of the domains (*c*). As revealed from the AFM topographs, the appearance of wt MlotiK1 did not change when removing cAMP (compare Fig. 1 and Fig. S4). In absence of cAMP, the wt MlotiK1 channels protruded 3.2 ± 0.5 nm (n = 54) from the lipid bilayer. n gives the number of MlotiK1 channels measured. Images have full-color levels corresponding to vertical height scales of 5 nm (*a*), 4.5 nm (*b*), and 0.6 nm (*c*). Imaging buffer was 50 mM KCl and 20 mM Tris-HCl (pH 7.5).

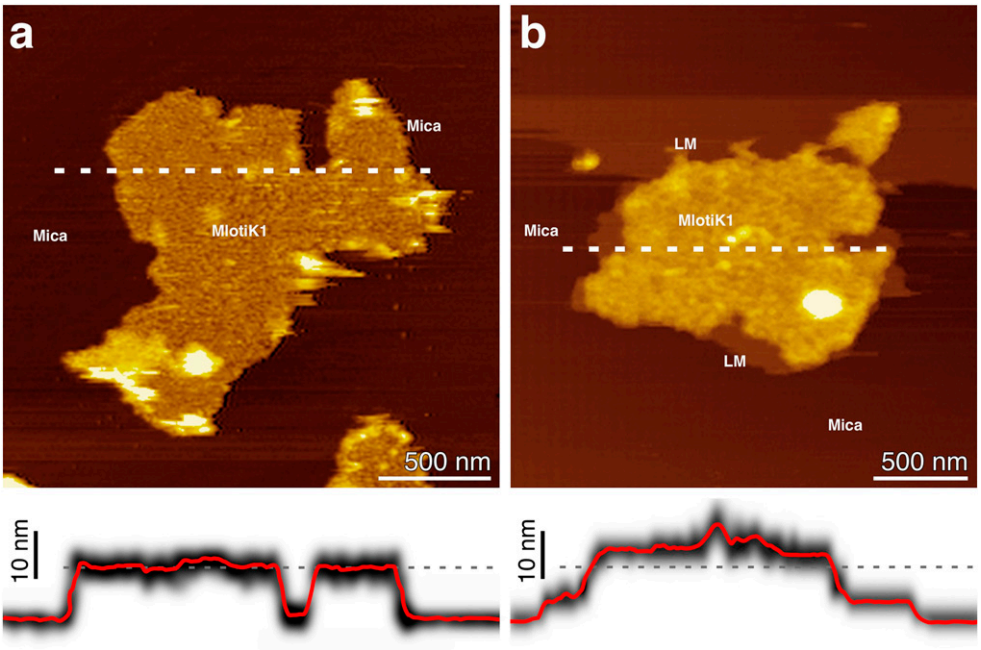

Fig. S6. AFM topographs of wt and mutant R348A MlotiK1 membranes prepared, adsorbed, and imaged in cAMP-free buffer solution. (*a*) Overview topograph of wt MlotiK1 membranes. The average height determined from 105 membranes was 10.0 ± 0.7 nm. (*b*) Overview topograph of a mutant MlotiK1 membrane. Lipid membranes (LM) embedding densely packed MlotiK1 are clearly visible. Lipid membranes protruded 3.9 ± 0.6 nm (n = 47) and MlotiK1 membranes protruded 13.5 ± 0.7 nm (n = 153) from the support. Below each topograph is the height profile taken along the dashed line. Each height profile is a superimposition of 10 height lines and shows their average (red line) and variation (gray shading). The gray dashed line indicates a height of 10 nm. Before adsorption to the supporting mica, the MlotiK1 membranes underwent a long dialysis step (9 d, with several dialysis-buffer changes) against cAMP-free buffer (see *Materials and Methods*). After dialysis the membranes were adsorbed to the mica and imaged by AFM using cAMP-free buffer solution [50 mM KCl and 20 mM Tris-HCl (pH 7.5)]. n gives the number of membranes measured.

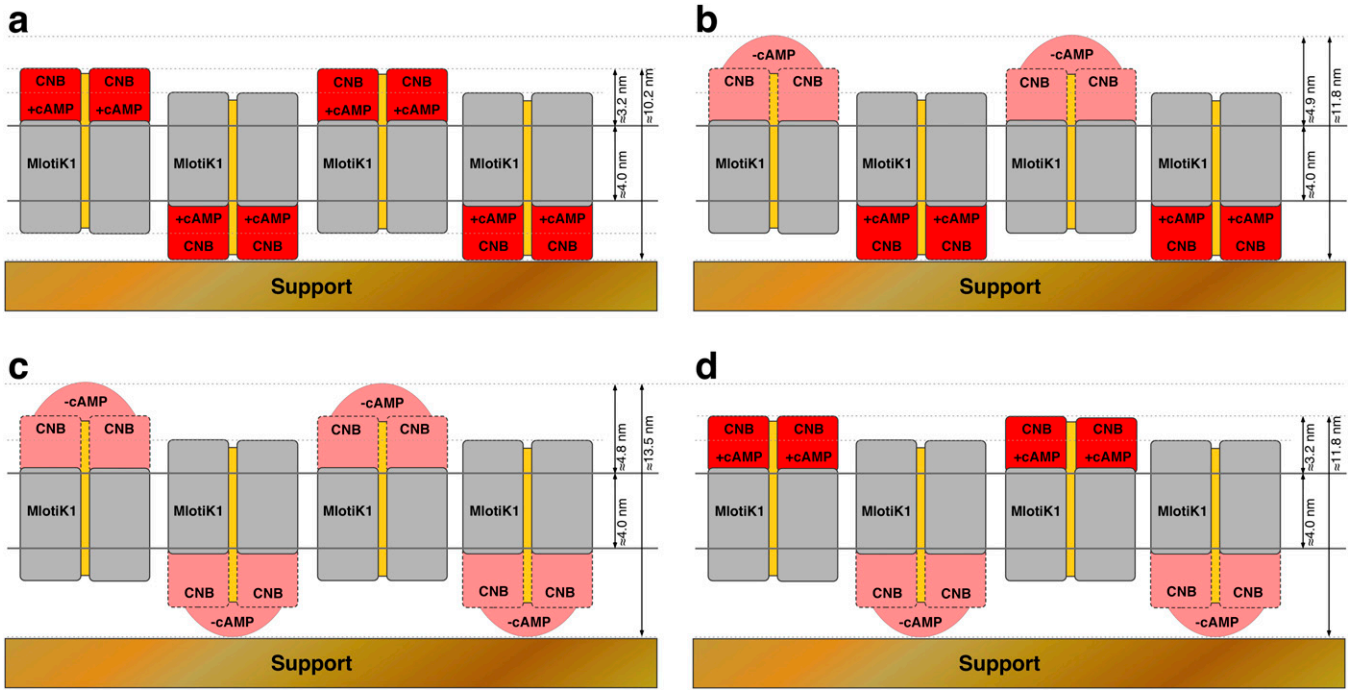

Fig. S7. Heights measured for reconstituted wt and mutant R348A MlotiK1 in the presence and absence of cAMP. (*a*) When prepared, adsorbed, and imaged in the presence of cAMP, wt and mutant MlotiK1 show the same heights within the errors of the AFM measurements (see Figs. S1 *a* and *d* and S3 and Table S1). The heights of wt MlotiK1 do not change after incubation and imaging in cAMP-free buffer (Figs. S1 *a*–*c*, S4, S5, and S6*a* and Table S1). (*b*) Mutant MlotiK1 membranes prepared and adsorbed in the presence of saturating cAMP concentrations but imaged in the absence of cAMP show an increased height of ∼11.8 nm (Fig. S1e and Table S1). This height change is attributable to conformational changes of the CNB domains facing the buffer solution (Fig. 3*D* and Figs. S8 and S9 and Table S1). Reincubating the cAMP-free mutant MlotiK1 (*b*) with cAMP reduces the membrane height to that measured for mutant and wt MlotiK1 membranes in the presence of cAMP (Figs. 3 *A* and *G*, Figs. S1*f* and S8 and Table S1). (*c*) When prepared, adsorbed, and imaged in the absence of cAMP, mutant MlotiK1 membranes show a height of ∼13.5 nm (Fig. S6*b* and Table S1). (*d*) Upon incubating the cAMP-free mutant MlotiK1 membranes (*c*) with saturating cAMP concentrations, the membranes show a height of ∼11.8 nm.

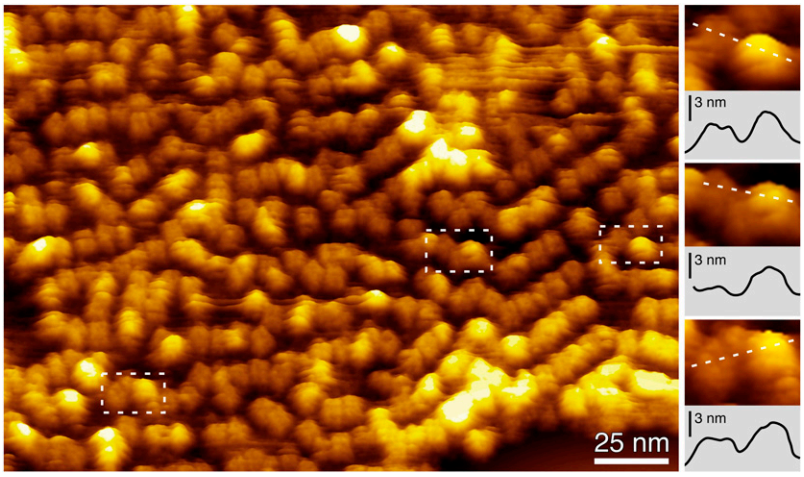

Fig. S8. High-resolution AFM topograph of mutant R348A MlotiK1 recorded after readdition of 600 μM cAMP. After adsorption to the supporting mica, cAMP-bound mutant MlotiK1 membranes were incubated in cAMP-free buffer solution [50 mM KCl and 20 mM Tris-HCl (pH 7.5)] for several hours. In the absence of cAMP, the MlotiK1 tetramers undergo a conformational change and increase height (Fig. 3*D*). After this, the membranes were incubated with 600 μM cAMP that was insufficient to saturate mutant MlotiK1. The AFM topograph shows an overview of MlotiK1 tetramers that coexist in two different conformational states. The lower protruding MlotiK1 tetramers (compare Figs. 1 and 3*A*) represent the cAMP-bound conformations, whereas the higher protrusions having the diameter of approximately one MlotiK1 tetramer (∼8–10 nm) represent the cAMP-unbound conformations. At fully saturating cAMP concentrations, all MlotiK1 tetramers (∼95%) are in the cAMP-bound conformation (Fig. 3*G*). The image on the right shows selected regions of the topograph at larger scale. These regions were taken from dashed rectangles indicated in the topograph. Below every selected region, we show a height profile (noise-filtered) that has been taken along the dashed line indicated. The height difference between lower-protruding (cAMP-bound) and higher-protruding (cAMP-unbound) MlotiK1 channels corresponds to ∼1.7 nm. The topographs show a full-color level corresponding to vertical height scale of 6 nm. The height analysis of cAMB-bound and cAMP-unbound mutant MlotiK1 channels is shown in Table S2. Imaging was 50 mM KCl, 600 μM cAMP, and 20 mM Tris-HCl (pH 7.5).

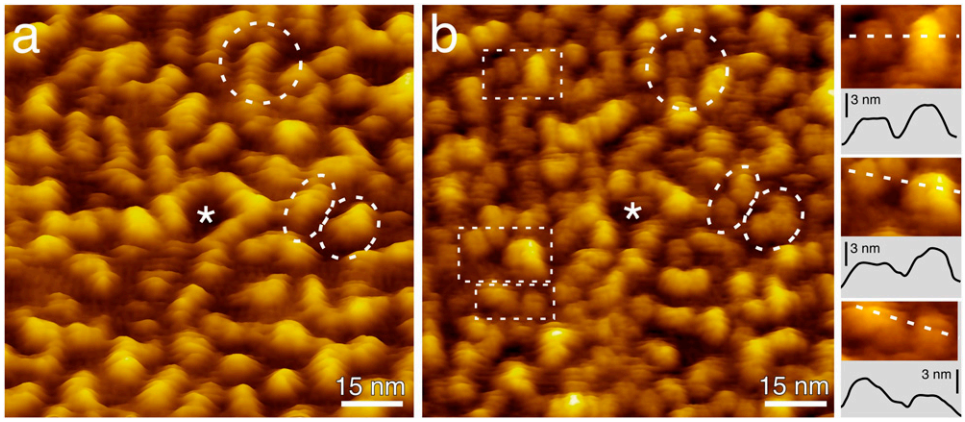

Fig. S9. Time-lapse AFM topographs of mutant R348A MlotiK1 recorded in the absence and presence of cAMP. (*a*) Mutant MlotiK1 channels recorded in cAMP-free buffer solution. After an incubation time of ~3 h all channels increased height by ~1.7 nm (see Fig. 3*D* and Table S2). (*b*) The same mutant MlotiK1 channels as in *a* recorded ~150 min after readdition of 600 μM cAMP. The asterisk highlights a reference area, and the dashed circles and ellipses highlight conformational changes of the same membrane area imaged in absence and presence of cAMP. The lower-protruding MlotiK1 tetramers represent the cAMP-bound conformations (compare Figs. 1 and 3*A* and Fig. S8), whereas the higher protrusions having the diameter of about one MlotiK1 tetramer represent the cAMP-unbound conformations (compare Fig. 3D and Fig. S8). Because mutant MlotiK1 was not fully saturated at 600 μM cAMP, not all channels have re-adopted the cAMP-bound conformation. The image on the right shows selected regions of the MlotiK1 membrane at larger scale. These regions were taken from dashed rectangles indicated in the topograph *b*. Below every selected region, we show a height profile (noise-filtered) that has been taken along the dashed line indicated. The height difference between lower-protruding (cAMP-bound) and higher-protruding (cAMP-unbound) MlotiK1 channels corresponds to ~1.7 nm. Topographs have full-color levels corresponding to a vertical height scale of 6 nm. Imaging buffer was 50 mM KCl, no cAMP (*a*), 600 μM cAMP (*b*), and 20 mM Tris-HCl (pH 7.5).

Table S1. Heights measured for wt and mutant R348A MlotiK1 membranes protruding from the mica support in the presence and absence of cAMP

Preparation/imaging	wt MlotiK1	Mutant MlotiK1
+cAMP/+cAMP/+cAMP	10.2 ± 0.8 nm (*n* = 176)	10.1 ± 0.8 nm (*n* = 156)
+cAMP/+cAMP/−cAMP	10.3 ± 0.6 nm (*n* = 163)*	11.8 ± 0.8 nm (*n* = 147)†
−cAMP/−cAMP/−cAMP	10.0 ± 0.7 nm (*n* = 105)*	13.5 ± 0.7 nm (*n* = 153)†
−cAMP/−cAMP/+cAMP	—	12.1 ± 0.8 nm (*n* = 39)†

Average heights and SDs measured from a number (*n*) of MlotiK1 membranes imaged by AFM. Sample preparation, adsorption, and imaging conditions were as follows:

+cAMP/+cAMP/+cAMP: MlotiK1 membranes were prepared in the presence of cAMP (see *Materials and Methods*), adsorbed in cAMP-containing buffer, and imaged in cAMP-containing buffer [200 μM cAMP (wt MlotiK1) or 900 μM cAMP (mutant MlotiK1)].

+cAMP/+cAMP/−cAMP: MlotiK1 membranes were prepared in the presence of cAMP (see *Materials and Methods*), adsorbed in cAMP-containing buffer [200 μM cAMP (wt MlotiK1) or 900 μM cAMP (mutant MlotiK1)], and imaged in cAMP-free buffer.

−cAMP/−cAMP/−cAMP: MlotiK1 membranes were prepared in the absence of cAMP (see *Materials and Methods*), adsorbed in cAMP-free buffer, and imaged in cAMP-free buffer.

−cAMP/−cAMP/+cAMP: MlotiK1 membranes were prepared in the absence of cAMP (see *Materials and Methods*), adsorbed in cAMP-free buffer, and imaged in cAMP-containing buffer (900 μM cAMP for mutant MlotiK1).

For every experimental condition listed, the statistical height analysis of MlotiK1 membranes was taken from membranes imaged in at least 12 independent experiments. For each experiment between 20 and 60 AFM, topographs of membranes have been recorded.

*Indicates that the average height is not significantly different (Student *t* test) from the average height shown at the top of the row. Adsorption buffer: 200 mM KCl, 20 mM Tris-HCl (pH 7.5), and cAMP concentrations as indicated. Imaging buffer: 50 mM KCl, 20 mM Tris-HCl (pH 7.5), and cAMP concentrations as indicated.

†Indicates that the average height is significantly different (Student *t* test) from the average height shown at the top of the row (+cAMP/+cAMP/+cAMP).

Table S2. Heights measured for wt and mutant R348A MlotiK1 channels protruding with their CNB domains from the lipid bilayer

Preparation/imaging	wt MlotiK1	Mutant MlotiK1
+cAMP/+cAMP/+cAMP	3.2 ± 0.5 nm (*n* = 100)	3.1 ± 0.5 nm (*n* = 57)
+cAMP/+cAMP/−cAMP	3.3 ± 0.5 nm (*n* = 117)*	4.9 ± 0.6 nm (*n* = 148)†
−cAMP/−cAMP/−cAMP	3.4 ± 0.6 nm (*n* = 78)*	4.9 ± 0.6 nm (*n* = 123)†
−cAMP/−cAMP/+cAMP	—	3.2 ± 0.5 nm (*n* = 45)*

Average heights and SDs measured from a number (*n*) of MlotiK1 channels imaged by AFM. Sample preparation, adsorption, and imaging conditions were as follows:

+cAMP/+cAMP/+cAMP: MlotiK1 membranes were prepared in the presence of cAMP (see *Materials and Methods*), adsorbed in cAMP-containing buffer, and imaged in cAMP-containing buffer [200 μM cAMP (wt MlotiK1) or 900 μM cAMP (mutant MlotiK1)].

+cAMP/+cAMP/−cAMP: MlotiK1 membranes were prepared in the presence of cAMP (see *Materials and Methods*), adsorbed in cAMP-containing buffer [200 μM cAMP (wt MlotiK1) or 900 μM cAMP (mutant MlotiK1)], and imaged in cAMP-free buffer.

−cAMP/−cAMP/−cAMP: MlotiK1 membranes were prepared in the absence of cAMP (see *Materials and Methods*), adsorbed in cAMP-free buffer, and imaged in cAMP-free buffer.

−cAMP/−cAMP/+cAMP: MlotiK1 membranes were prepared in the absence of cAMP (see *Materials and Methods*), adsorbed in cAMP-free buffer, and imaged in cAMP-containing buffer (900 μM cAMP for mutant MlotiK1).

*Indicates that the average height is not significantly different (Student *t* test) from the average height shown at the top of the row. Adsorption buffer: 200 mM KCl, 20 mM Tris-HCl (pH 7.5), and cAMP concentrations as indicated. Imaging buffer: 50 mM KCl, 20 mM Tris-HCl (pH 7.5), and cAMP concentrations as indicated.

†Indicates that the average height is significantly different (Student *t* test) from the average height shown at the top of the row (+cAMP/+cAMP/+cAMP).